Nanoscopic Surface Measurements on Metasurfaces and 2D Materials

Dissertation
zur Erlangung des Doktorgrades
der Naturwissenschaften

vorgelegt beim Fachbereich Physik
der Johann Wolfgang Goethe-Universität
in Frankfurt am Main

von
Frederik William Walla
aus Offenbach am Main

Frankfurt 2021
(D30)

vom Fachbereich Physik der

Johann Wolfgang Goethe-Universität als Dissertation angenommen.

Dekan:	Prof. Dr. Harald Appelshäuser
Gutachter:	Prof. Dr. Hartmut Roskos Dr. habil. Arash Rahimi-Iman

Datum der Disputation: 02.11.2022

List of Abbreviations

AFM	Atomic Force Microscope
c-AFM	Conductive Atomic Force Microscope
ATR	Attenuated Total Reflection
CMOS	Complementary Metal-Oxide Semiconductor
DBR	Distributed Bragg Reflector
EPM	Non-Local Empirical Pseudo Potential Method
FDTD	Finite Difference Time Domain
FIB	Focussed Ion Beam
hBN	hexagonal Boron Nitride
IMI	Insulator-Metal-Insulator
I-V	Current-Voltage
MOSFET	Metal Oxide Semiconductor Field-Effect Transistor
NDR	Negative Differential Resistance
SEM	Scanning Electron Microscopy
STM	Scanning Tunneling Microscopy
a-SNOM	Aperture-Type Scanning Near-Field Optical Microscope
s-SNOM	Scattering-Type Scanning Near-Field Optical Microscope
SPP	Surface Plasmon Polariton
LRSPP	Long-Range Surface Plasmon Polariton
TE	Transversal Electric
TM	Transversal Magnetic
TEPL	Tip-Enhanced Photoluminescence
TERS	Tip-Enhanced Raman Spectroscopy
TFET	Tunnel Field-Effect Transistor
TMDC	Transition Metal Dichalcogenide
WKB	Wentzel-Kramers-Brillouin

Contents

Appendix

Chapter 1

Introduction

1.1 Nanoplasmonics

Nanoplasmonics refers to a subfield of nanophotonics, which covers the generation, detection and manipulation of light at nanometre scales. The research field focusses on the interaction processes of light and conduction electrons at metal-dielectric interfaces or metallic nanostructures. It explores optical near-fields at sub-wavelength volumes and interactions between confined fields and matter. Its goals align with the trend in nanophotonics to establish miniaturized optical devices for applications in microscopy, optical communication and sensing [1].

With regards to potential applications, a major driver lies in the field of optical communication and data manipulation. Specifically, there is hope for higher calculation speeds than with electronics and simultaneously smaller footprints compared to photonic technologies. Fundamentally, the carrier frequencies for electronic signals are limited by RC-delay of the electronics and create an upper limit for the data transmission rate. Over longer distances, higher frequencies in the form of light are used for optical communication with optical fibres. However, optical waveguides for data transmission must be much larger in diameter as their cut-off diameter scales with the wavelength of the light (e.g. 1550 nm at telecom wavelengths). Combining nanoelectronic dimensions in the order of mere nanometres with optical frequencies of hundreds of terahertz would allow to replace some of the optical-to-electronic conversion at the information destination that creates bottlenecks in current data manipulation networks. [2, 3]

Moreover, scientific curiosity is driven by the fact that confinement of light into nanoscale dimensions leads to strong electromagnetic fields that allow for the investigation of light-matter interaction in a broad range of frequencies, from the visible to the terahertz regime. This interaction can be further enhanced by resonant structures, such as metallic nanoparticles, structured surfaces, metasurfaces and 2D materials. Controlling the interaction between light and matter at the nanoscale can be exploited to create new phenomena and material properties at the larger scale, such as negative refraction, sub-wavelength focussing and surface guiding of light. Furthermore, many optoelectronic applications, such as detectors, modulators and switches, as well as higher harmonics frequency generation are all based on the use of light-matter interaction. [4]

1.2 Metasurfaces and 2D materials

The field of metamaterials has been growing over the past 15 years and made the development of materials with novel electromagnetic and photonic properties a reality. Metamate-

rials are artificially fabricated periodic micro- or nanostructures, as illustrated in Fig. 1.1, that react resonantly to incident light. Due to their sub-wavelength building blocks, they can form macroscopic electromagnetic properties that cannot be found in natural materials. The design of their sub-wavelength components controls the effective material properties such as permittivity and permeability in a way that allows refractive index and the interaction with light to be designed in new ways. The most popular examples of these novel effects are superresolution imaging and negative refraction, with the most prominent application being the electromagnetic camouflage cloak [5]. However, many applications of this type are limited by high absorption losses and strong dispersion inherent to the resonant behaviour. Moreover, the fabrication of micro- and nanoscopic *three-dimensional* structures with existing techniques is particularly complex.

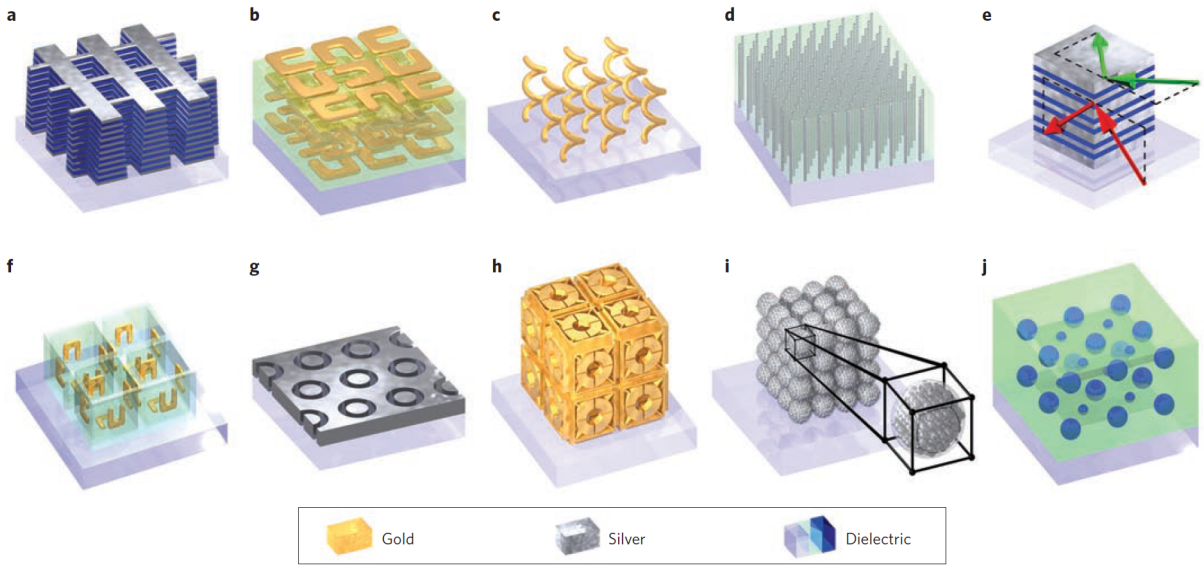

Figure 1.1: 3D photonic-metamaterial structures based on periodic metallic and dielectric "meta-atoms". Reprinted by permission from Springer Nature: Springer Nature, Nature Photonics **5**, 523-530, Ref.[6], Copyright (2011).

Currently, research is increasingly focusing on optical metasurfaces, as shown in Fig. 1.2. Metasurfaces are ultra-thin structures whose thickness lies far below the wavelength of light, which significantly minimizes optical losses. In contrast to three-dimensional metamaterials, they benefit from considerably simpler manufacturing processes based on established semiconductor technology, such as lithography and nanoprinting. The planar structures are of particular interest due to the prospect of integrating them directly into photonic micro- and nano-chips. This opens up an enormous application potential [7].

Two other aspects justify the particular interest in two-dimensional metasurfaces: The extremely thin layers use tiny resonators to directly control the phase of radiation and are able to shape wave fronts as desired. A new generation of ultra-thin optical elements could be created whose interaction with light is no longer based on the classical propagation of light waves [8]. Another promise are materials that transmit light far below its wavelength. Such waves with large wave vectors are usually characterized by evanescent fields and die out quickly. However, hyperbolic metasurfaces are designed to support the propagation of surface waves with extremely large wave vectors. This way, the diffraction limit of classical optics can be tricked and spatially compressed Surface Plasmon Polaritons (SPPs) may be realized. This motivates potential applications in nanophotonics, such as planar nanotransceivers, pure optical communication, signal processing and high-resolution sensors and

imaging [9].

SPPs are electromagnetic waves that can propagate at the interfaces between metallic and dielectric media, e.g. gold and air. A quasi-particle is formed from the coupling of an electromagnetic wave in the dielectric medium with a plasma wave in the metallic medium, whose behaviour and expansion is determined by the properties of both media. The prospect of using specially developed metasurfaces to exploit compressed and controllable surface plasmons with exotic properties has led to a fusion of the research fields of metamaterials and plasmonics into metaplasmonics in recent years [5, 10]. Research is driven by visionary questions: Can we develop nanoscopic circuits based on light instead of electricity? Can these nanocircuits be used as nanoradios in wireless applications? Is it possible to use nanocircuits directly with biological units as optical nanosensors? [11, 12]

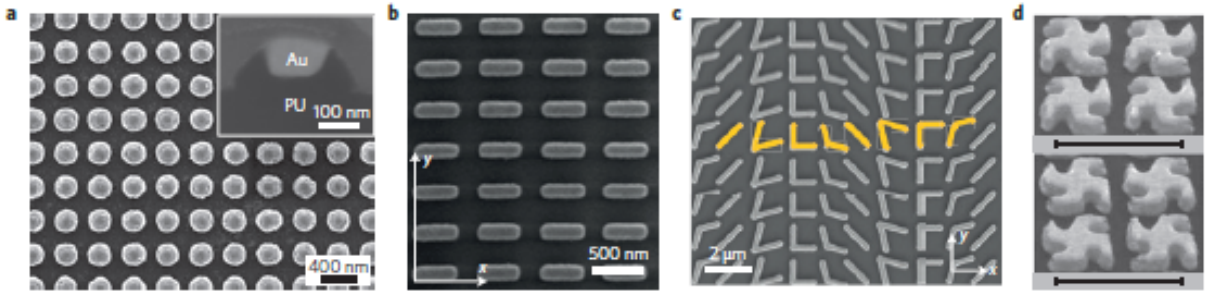

Figure 1.2: Scanning Electron Microscopy (SEM) images of metasurfaces. (a) Gold-nano discs on polyurethane, (b) Nano-printed rod antennas, (c) V-antennas produced by electron beam lithography, (d) Chiral metasurface (beam corresponds to 500 nm). Reprinted by permission from Springer Nature: Springer Nature, Nature Photonics **8**, 889-898, Ref.[13], Copyright (2014).

SPPs are not limited to noble metal surfaces and metasurfaces. Another important playing field for plasmonic effects are natural 2D materials like graphene, hexagonal Boron Nitride (hBN) or Transition Metal Dichalcogenides (TMDCs). These naturally occurring van-der-Waals crystals grow in weakly bound layers held together by intermolecular van-der-Waals forces. The individual layers can be mechanically exfoliated from the bulk crystal or directly grown in single or few layer form and thus offer themselves as surfaces that can be perfectly smooth down to the atomic level. These interfaces are well-suited for studying the coupling of light and matter, such as plasmons, electrons, excitons or phonons, in the form of polaritons. In fact, the successful exfoliation of graphene was so ground-breaking that it was awarded with the Noble Prize in Physics in 2010 [14]. Currently, TMDCs are gaining traction as another promising 2D material due to their semiconducting properties, direct band gap in the visible spectrum and strong spin-orbit coupling.

The combination of nanostructured surfaces and TMDC materials can be used to further increase the coupling between light and matter. Metasurfaces and nanoparticles, both with features on sub-wavelength scales, and photonic cavities with wavelength lengthscales are used to facilitate coupling between light and plasmonic or excitonic phenomena. The fact that most TMDC monolayers have a direct band gap in the visible frequency spectrum allows the coupling of visible light with its excitonic resonance. The coupling becomes apparent through absorption and re-emission of photons, showing visible photoluminescence. The control of this coupling through the use of resonant cavities or nanoparticles can be exploited to enhance the photoluminescence photon yield and even change the lifetime of the excitation. [15]

Another application that may exploit the two-dimensional nature of semiconducting

TMDC crystals are Tunnel Field-Effect Transistors (TFETs). These are motivated by the apparent quantum limitation of increasingly miniaturized conventional transistors. With gate oxides reaching critical thicknesses of about 1 nm, electrons begin to leak by tunnelling through. Tunnel transistors instead use the tunnelling of electrons as their working principle. The extremely thin semiconducting monolayers, multilayers and heterostructures serve as well-controlled tunnel barriers. Switching the device is done electrically or optically by modulating the probability of electrons to tunnel through this barrier. Obviously, the nanoscale integration of transistors based on two-dimensional semiconductors feeds into the domain of applying nanophotonic components to enhance microchip speeds and footprint. [16, 17]

Again, the understanding and control of light-matter interaction is a cornerstone of this development and tangles these seemingly frayed threads. The following section presents the current state of research in the field of metasurfaces in the context of surface wave control (i.e. metaplasmonics). Two-dimensional TMDC materials complement the discussion on polaritonic interfaces and connect to further applications of TMDCs in the context of tunnel devices. Lastly, the thesis branches off from *nanoscopic* light-matter coupling to non-linear light-matter interaction in bulk silicon, where it will be shown how a single charge carrier description is able to capture the valence band dynamics after excitation by intense terahertz pulses surprisingly well.

1.3 Milestones and state of the art

In recent years, metasurfaces have become one of the fastest developing domains of modern theoretical and applied research on electromagnetic effects [18]. For the development of the first directive antennas in the radio frequency range, dense cable grids were investigated as early as 1897 [19], which could be described as homogeneous effective media under the assumption of large wavelengths. For optical frequencies, initial studies on metasurfaces began in 1970 with so-called nano-island films for sensor applications. Resonant nano-metallic islands were used to increase the field of incident radiation. Still, the resulting anomalous absorption of the incident light could be described by an effective complex permittivity as for homogeneous materials [20].

Meanwhile, the central idea of transforming the phase front of an incident wave directly via interaction with individual sub-wavelength elements has developed into active research on “flat optics” [21]. Notable established metasurface-based ultra-thin optical elements in the scope of flat optics are Vortex plates, half and quarter wave plates, flat lenses and mirrors with anomalous reflection and refraction [22]. Ultra-thin smartphones, photography and fibre-integrated flat lenses for biomedical imaging are just a few of the applications that researchers are envisioning.

In contrast to research on metasurfaces for the direct manipulation of wave fronts, metasurfaces for the control of propagating near-field waves, such as surface plasmons, have only recently begun to attract more interest [23–26], as illustrated in Fig. 1.3. In particular, the investigation of extremely anisotropic metasurfaces, which permit surface waves with hyperbolic dispersion, is predicted to have a bright future because of their potential for the development of photonic chips [27]. For example, Liu et al. [22] theoretically showed how the propagation of SPPs can be controlled selectively between normal and anomalous diffraction. High et al. [28] later demonstrated hyperbolic dispersion in the visible frequency range on a silver nanostructure and confirmed the expected negative refraction and diffraction-free propagation experimentally. A further experimental characterization of a hyperbolic metasurface by Samusev et al. [26] could experimentally demonstrate polarization-dependent

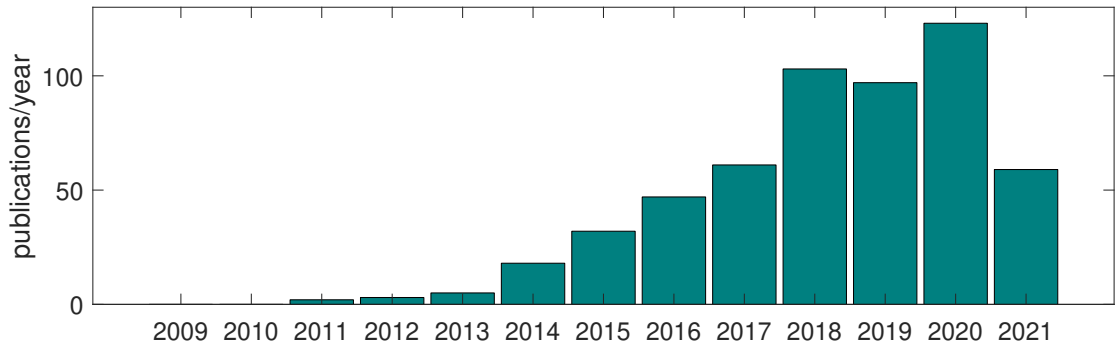

Figure 1.3: Relevance of the topic 'metasurface' and 'surface plasmon' in the last ten years measured by publications per year according to the citation database Web of Science Core Collection as of 09/2021.

excitation of different hyperbolic surface modes on a metasurfaces made up of elliptical gold discs. In both cases, far-field methods were used for characterization, specifically detection of the decoupled surface wave and Attenuated Total Reflection (ATR) spectroscopy, respectively.

Direct observation and imaging (direct mapping) of SPP at short wavelengths is especially challenging for strongly confined surface waves with compressed wavelengths and electrical fields that rapidly decay perpendicular to the surface. These properties demand that the near-field is detected in the vicinity of the surface with sub-wavelength resolution. A Scattering-Type Scanning Near-Field Optical Microscope (s-SNOM) is ideally suited for these requirements and well established for the measurement of surface plasmons on isotropic metallic films [29–31] and 2D materials [32–34]. With this optical near-field method, local material properties and surface fields with spatial resolution down to nanometres can be recorded. The method allows the direct observation of the electrical field amplitude and phase of surface plasmons and thus direct characterization of wave vector, dispersion, directivity, propagation width, divergence, reflection and refraction.

In connection with metamaterials, first s-SNOM studies have recently been published. For the terahertz frequency range, the directional control of surface plasmons on metasurfaces was demonstrated [35]. In the mid-infrared region, s-SNOM measurements on chiral metasurfaces helped clarify the origin of circular dichroism [36, 37]; moreover, SPPs on three-dimensional metamaterials [38] and the near-field characterization of ultra-flat phase controlling metasurfaces [39] were demonstrated. The visible and near-infrared spectral range has received less attention, even though it is particularly relevant for telecommunications and data transmission and thus promises potential applications in metaphotonics [40]. Still, several publications show impressive findings, e.g. direct near-field measurements of a plasmonic metal lens [41], the manipulation of surface waves by phased array structures [42], the propagation of SPPs on anisotropic metasurfaces [43] and along a one-dimensional photonic transmission lines at a telecom wavelength of 1550 nm [44].

The resurgence of research involving TMDC materials inspired even further studies in the context of nanophotonics and polaritonics. Notably, the first experimental demonstration of photoluminescence in MoS_2 monolayers in 2010 [45], which is exclusive to single layer crystals [46], fuelled scientific curiosity. One approach taken was using hybrid systems made of TMDC monolayer(s) on a gold interface, allowing coupling of the metal's SPP mode to an exciton resonance [47], leading to the emergence of exciton-plasmon-polaritons. A notable demonstration of these hybrid polaritons by Zhang et al. [48] combines nanopatterned TMDCs and metallic films, effectively enhancing the interaction with light of these

polaritonic modes. Pushing the nanopatterning to smaller scales, one quickly reaches the domain of TMDC metasurfaces, which can be exploited to efficiently access the strong light-matter non-linear interaction present in TMDCs [49]. The integration of two-dimensional layers with nanoresonators serves well to make use of the promising characteristics found in TMDC materials: nanometer thickness, direct bandgap, strong spin-orbit coupling and durable mechanical properties. From an application-driven perspective, there is a vast potential for research focusing on (exciton) optoelectronics, (flexible) electronics, nanophotonics [50], light generation, computing, sensing [48] and spin-valley physics [51, 52]. One such milestone was the demonstration of the first (encapsulated) single-layer MoS_2 transistor in 2011 [53]. Moreover, by stacking of two-dimensional layers heterostructures emerge that are destined for the application as vertical TFETs [17, 54, 55], suggested as candidates for post-CMOS technology.

1.4 Outline of this thesis

This thesis is structured along seven chapters. The introduction is meant to offer a brief overview across the driving forces behind a lot of research on nanophotonics on two-dimensional material systems. The common thread of probing light-matter interaction at thin material interfaces will be recognizable throughout the thesis. The second chapter details the experimental setup that was built to conduct all nanoscopic experiments for this thesis. Furthermore, several intricacies and challenges of achieving sub-wavelength optical (s-SNOM) and nano-electrical (c-AFM) measurements are covered. Through the following four chapters, the contributions made by this thesis to investigating light-matter interaction on the nanoscale from various perspectives are presented. Each chapter contains a brief introduction, a theory section, measured data or simulation results and the analysis; complemented by a concluding section.

Chapter 3 covers the direct observation of guided mode resonances on a metallic metasurface with a self-implemented s-SNOM. In Chapter 4, the s-SNOM technique is applied to a TMDC monolayer in combination with a resonant microcavity to trace the origin of enhanced photoluminescence. The setup is modified into a Conductive Atomic Force Microscope (c-AFM) for Chapter 5, facilitating the measurement of quantum tunnelling currents across microscopic terraces of vertical TMDC and graphene (hetero)stacks.

Chapter 6 contains a digression from the domain of nanophotonics. Instead, single-carrier time-domain simulations are presented that accompany experiments on carrier dynamics and terahertz higher harmonics generation in p-doped silicon. The common thread of probing light-matter interaction offers a loose connection to the central theme. Additionally, a certain conceptual resemblance will be apparent between the dynamic response of charge carriers to an electromagnetic field constrained by the periodic crystal potential and the electron gas description governing surface plasmonics.

Chapter 7 concludes the thesis by drawing together the different results.

Chapter 2

Experimental setup

2.1 Diffraction limit and beyond

In classcial microscopy, the minimum resolution Δr of an optical system cannot significantly surpass the wavelength λ used for imaging. This relationship is known as the diffraction limit and expressed by the Rayleight criterion

$$\Delta r = \frac{1.22\lambda}{\sin\theta_{max}} \tag{2.1}$$

where θ_{max} is the maximum angle of the cone of light that enters the lens.

This dependence on wavelength and angle can be understood in the angular spectrum representation. An electric field distribution is expressed as a superposition of plane waves propagating at different angles and amplitudes. Each plane wave has a total momentum of $k = \frac{2\pi}{\lambda}$. However, their projection k_i parallel and perpendicular to the direction of propagation depends on the angle θ_i. A plane wave propagating at angle θ_i can be expressed within these directions via

$$\vec{E}(\vec{k},\vec{r}) = \vec{E}_0(e^{i(k_x x + k_y y)}e^{ik_z z}) \tag{2.2a}$$

$$k = \sqrt{k_x^2 + k_y^2 + k_z^2} \equiv \sqrt{k_\parallel^2 + k_\perp^2} \tag{2.2b}$$

Diffraction occurs due to the finite aperture of the optical system. Fig. 2.1 illustrates the diffraction of the electric field passing through a subwavelength aperture. The near-field region, within which the object can still be resolved, is lost after less than a distance of λ. [56, p. 38ff]

The electric field of subwavelength objects diffracts in an analogous way and more drastically with decreasing feature size. Plane waves propagating at a large angle θ_i have higher lateral momenta $k_\parallel$ and contain the finer image features of a sample. Hence, resolution is lost when these plane waves traveling at large θ_i are cut off by a finite aperture in the far field. An imaging system with a large angular resolution collects plane waves with large lateral momenta $k_\parallel$. Large apertures are necessary to collect the high wavevector components necessary to image very small objects. Moreover, $k_\parallel$ has an upper limit expressed in equation 2.2b, which is defined by its wavelength via $k = \frac{2\pi}{\lambda}$, namely the fundamental resolution limit for far-field microscopy.

To surpass the fundamental resolution limit for far-field microscopy, one can exploit the near-field of the optical field that is characterized by evanescent waves. In fact, the "use of evanescent waves is the key to optics on the nanometer scale" [58, p.7]. Propagating waves are defined by real wavevectors k_i; on the other hand, evanescent waves are defined

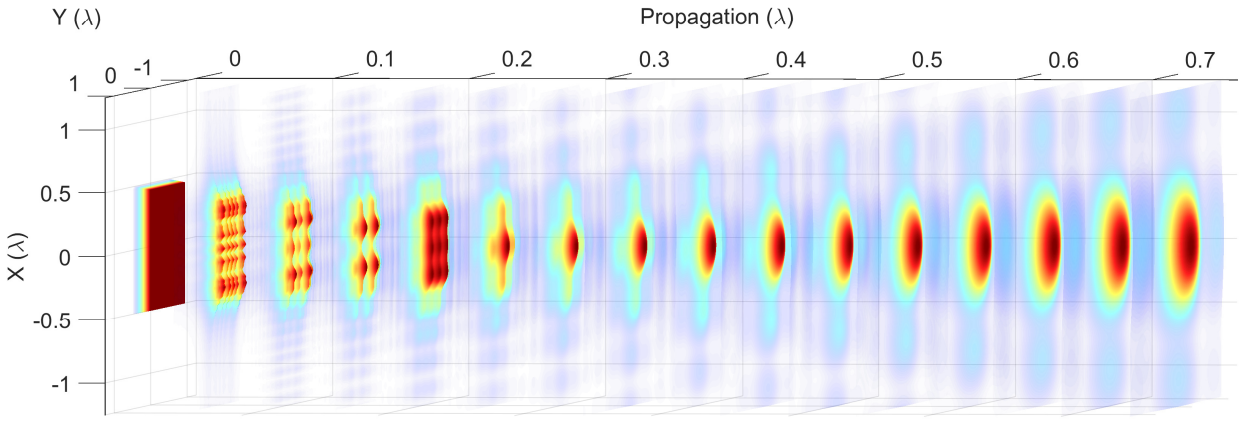

Figure 2.1: Fraunhofer diffraction for a subwavelength rectangular aperture of length $\lambda/2$ based on [57, p. 63].

by complex wavevector components k_z. Physically, these waves therefore quickly decay perpendicular to the surface. Eq. 2.3 shows that for complex values of k_z the wave decays quickly for large values of $|k_z|$

$$e^{i(k_z x + k_y y)} e^{ik_z z} = e^{i(k_x x + k_y y)} e^{-|k_z| z} \tag{2.3}$$

The consequence is that evanescent waves do not propagate into the far-field. The detection has to be performed in the vicinity of the surface. The advantage of measuring evanescent waves is that the use of complex k_z alleviates the limit on $k_{\|}$ imposed by equation 2.2b. Measuring closer to the surface lets one detect the field before it decays, hence more evanescent waves can be collected and a better resolution is achieved. The imaging resolution depends on the efficient detection of evanescent waves.

Experimentally, there are various approaches for detecting evanescent fields and facilitating near-field imaging: placing a detector close to the sample [59], using an Aperture-Type Scanning Near-Field Optical Microscope (a-SNOM), Tip-Enhanced Raman Spectroscopy (TERS), Tip-Enhanced Photoluminescence (TEPL) [58] or s-SNOM. The latter lies at the heart of this thesis and shall be presented further in this chapter.

2.2 Atomic force microscopy

The Atomic Force Microscope (AFM) serves as the foundation for the nanoscopic measurement techniques employed for this thesis: s-SNOM and c-AFM. It was invented in 1982 as a scanning probe microscope that uses a sharp tip to mechanically record the topography of a sample surface. [60] The measurement is based on the detection of miniscule forces between the sample and the probing tip. These tiny forces are resolved by monitoring a spring-like cantilever which is mechanically bent or whose vibration resonance frequency is shifted. The imaging resolution depends on the radius of the probing tip's apex. Nowadays, AFM resolution can reach down to atomic scales, imaging of atoms in molecules and even electron orbitals has been demonstrated [61].

2.2.1 Modes of operation

AFM is operated in three main sensing mechanisms: contact mode, tapping mode and non-contact mode. The forces between tip and sample change with distance and are governed

by Pauli exclusion repulsion and van-der-Waals attraction. For an uncharged interaction, the forces are described by the Lennard-Jones-Potential. The three AFM modes work in different regimes of this potential, that are characterized by repulsive (green) or attractive (purple) forces as illustrated in Fig. 2.2, respectively. [62]

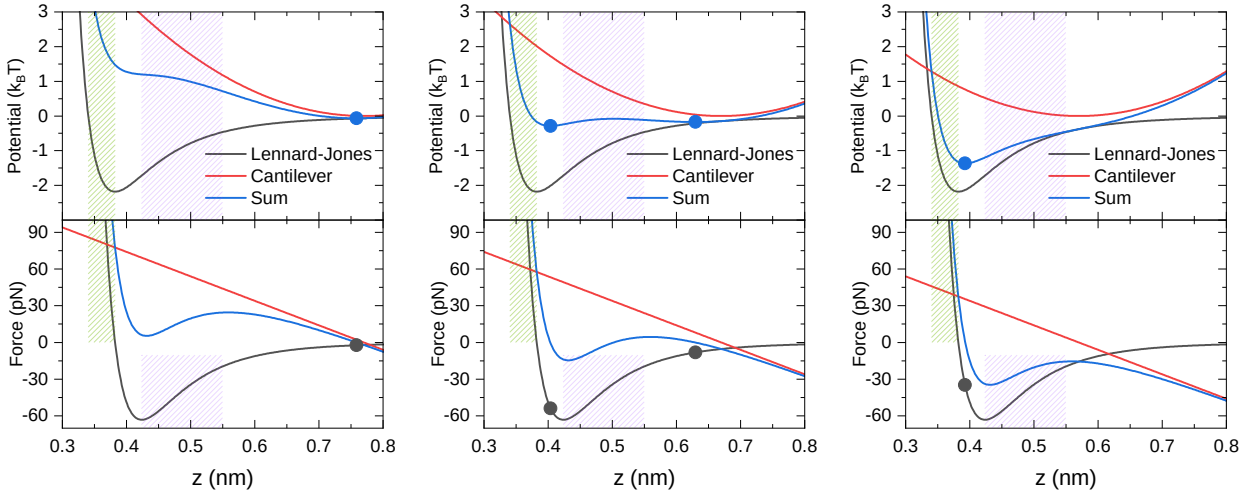

(a) $z_0 = 0.8\,\text{nm}$ (b) $z_0 = 0.7\,\text{nm}$ (c) $z_0 = 0.6\,\text{nm}$

Figure 2.2: Potential and Force of Lennard-Jones, Cantilever and total interaction for an AFM tip with three different relaxed tip-sample distances z_0. The dots mark the local minima of the total potential and thus the deflection of the flexed cantilever. Situations with multiple minima are subject to hysteresis (see Sect. 2.2.3). The shaded regions highlight the repulsive (green) and attractive (violet) force regimes associated with contact mode and non-contact mode respectively.

In contact mode, the distance is kept exclusively in the repulsive force regime and tip and sample are in direct contact. During a scan, the contact force is kept constant by controlling the sample height. This is achieved by monitoring the bending of the cantilever, typically via recording the position of a laser beam that is reflected off the cantilever's top surface.

In tapping mode, the cantilever is moved slightly away from the sample and oscillates at or close to its resonance frequency. The tip moves between the repulsive and attractive force regime and shortly taps the sample on each period. To keep the average force between tip and sample constant during a scan, the amplitude or phase of the cantilever oscillation is monitored optically by a deflected laser beam or piezo-electrically with a tuning fork.

In non-contact mode, tip and sample do not touch. The tip oscillates near its resonance frequency above the sample and stays in the attractive regime. The system is very sensitive to changes in the distance between tip and sample since slight changes in the attractive force affect the resonance frequency of the cantilever and are directly visible through a change in oscillation amplitude and phase.

2.2.2 Non-contact feedback

Keeping the tip-sample distance constant without being in contact thus requires a well-controlled feedback mechanism. The way in which mechanical amplitude and phase are affected by a changing distance is dependent on the force regime. The cantilever motion z

can be described by a 1-dimensional point mass m attached to the cantilever spring by [63]

$$m\ddot{z} + kz + \frac{m\omega_0}{Q}\dot{z} = F_{\mathrm{LJ}} + F_0 \cos(\omega t) \tag{2.4}$$

where F_0 and ω describe amplitude and frequency of the piezoelectric actuator. ω_0 and Q are resonance frequency and quality factor of the cantilever spring. F_{LJ} is the Lennard-Jones force. We can linearise the F_{LJ} over the tip oscillation around its equilibrium z_0', as can be seen from Fig. 2.2. Then F_{LJ} can be expanded as

$$F_{\mathrm{LJ}} = F_{\mathrm{LJ}}(z_0') + \frac{dF_{\mathrm{LJ}}}{dz}\Big|_{z_0'}(z - z_0') + ... \tag{2.5}$$

With these two Eqs. 2.4 and 2.5 an effective spring constant k_e and modified resonance frequency ω' can be obtained as

$$k_e = k - \frac{dF_{\mathrm{LJ}}}{dz}\Big|_{z_0'} \tag{2.6a}$$

$$\omega' = \sqrt{\frac{k_e}{m}} = \sqrt{\frac{k - \frac{dF_{\mathrm{LJ}}}{dz}|_{z_0'}}{m}} \tag{2.6b}$$

The gradient of the Lennard-Jones-Force in the non-contact regime (purple shaded) is positive ($\frac{dF_{\mathrm{LJ}}}{dz} > 0$), hence the resonance frequency ω' is reduced. A decrease in tip-sample distance z is observable as a further reduced resonance frequency ω'. For a set-point slightly above resonance, a reduction in distance thus shifts the resonance frequency away from the driven cantilever - a drop of the oscillation amplitude follows. [64, 65]

2.2.3 Force-distance curves and hysteresis

Typical force-distance curves for contact-mode AFM measurements with the setup used for this thesis are shown in Figs. 2.7 and 2.8 of Sect. 2.4.1. The graphs plot tip-sample interaction force over tip-sample distance. Upon approach, the cantilever is slightly bent down by the attractive forces before reaching the repulsive regime where it is bent upwards by the sample. A strong hysteresis occurs upon retract, since the position of the tip is given by the contribution of two potential: cantilever potential V_c and Lennard-Jones potential V_{LJ}. The sum of both is the effective potential. The cantilever will bend to remain in the local effective potential minimum while the relaxed tip-sample distance z_0 is swept. Fig. 2.2 highlights the local potential minima as dots. For certain intermediate distances, see Fig. 2.2b, multiple minima can exist. This causes a hysteresis that depends on approach/retract direction and creates a characteristic jump-off point, when the cantilever's current local potential minimum is resolved. [63]

The cantilever potential according to Hooke's law is

$$V_c(D) = \frac{k}{2}(z - z_0)^2 \tag{2.7}$$

where z is the real tip-sampe distance and z_0 the average tip-sample distance. Lennard-Jones potential is given by

$$V_{\mathrm{LJ}} = 4\epsilon\left((\frac{\sigma}{z})^{12} - (\frac{\sigma}{z})^{6}\right) \tag{2.8}$$

where values for adhesion work $\epsilon = 650 k_B$ and minimum separation $\sigma = 0.34\,\mathrm{nm}$ [66], and $\mathrm{k} = 0.2\,\mathrm{N/m}$ have been used to create Fig. 2.2.

For contact-mode AFM measurements it is important to calibrate an appropriate contact force prior to the measurement. This is done using a force-distance measurement and the cantilever spring constant, which is obtained from the manufacturer or calibration techniques, e.g. thermal tune method [67, 68]. A softer cantilever makes it easier to carefully control the contact force, while a stiff cantilever leads to lower force resolution. Moreover, a soft cantilever is necessary to keep the tip approached at low contact force without risking loss of contact. Common contact forces for contact-mode AFM vary between 50 nN and 500 nN [69]. Typically, soft cantilevers are not suitable for dynamic AFM operation due to their low resonance frequencies (ω_0 <20 kHz).

2.3 s-SNOM

The capability of AFM to keep a constant distance of several nanometers between a sample and a sharp probing tip provides a basis for optical measurements in the vicinity of the surface with nanoscopic resolution. In classical microscopy, the resolution of an image is limited by the wavelength of the light. Reaching beyond the diffraction limit of classical microscopy was proposed for the first time by Synge in 1928 [56], but could only be experimentally realized, firstly at a wavelength of 3 cm, in 1972 [70]. The first experimental proof at optical frequencies that the resolution limit is in fact penetrable was demonstrated in 1984 [71, 72]. The idea is based on the detection of quickly decaying evanescent components of the electric field that are confined to the surface. By scanning a detector, small aperture or scatterer in the vicinity of the surface, the evanescent fields can be detected or transferred to the far-field. Contrary to far-field radiation, evanescent waves contain highly-resolved detailed information on the sample surface far below their wavelength.

The transition from near-field to far-field region is determined by the wavelength λ and aperture or targeted resolution Δr, known as the Fraunhofer distance L

$$L = \frac{2(\Delta r)^2}{\lambda} \tag{2.9}$$

For the situation depicted in Fig. 2.1, with an object of size $\frac{\lambda}{2}$, the Fraunhofer distance is $L = \frac{\lambda}{2}$. For a typical tip size of 30 nm and $\lambda = 850$ nm, this evaluates to a tip-sample distance of below 3 nm. Consequently, near-field imaging at visible or near-infrared wavelengths has to be performed in close vicinity of the sample.

In s-SNOM, this is achieved by letting a sharp tip oscillate just above the surface (a setup identical to an AFM). Additionally, a laser beam is focussed onto the tip's apex, which functions as an optical probing antenna for both coupling and scattering of light. The tip is polarized by the electromagnetic field and the scattered light's magnitude and phase is affected by the interaction with the sample's dielectric constant.

The interaction can be modelled by two polarizable spheres that are affected by plane wave illumination. The origin of the contrast based on this approximation is detailed in Sect. 2.3.1. Moreover, using a more thorough treatment, the description can be extended to increasing levels of detail by including the geometry of the tip, the geometry of the sample (half space), reflections of the surface and beam parameters. [73, 74]

In short, the probe tip acts as a sub-wavelength scatterer for the near-field. It converts evanescent waves into propagating waves that can be detected in the far field. The intimate relationship between scattering dipole and scattering cross-section allows for an imaging resolution of the surface dielectric constant based on the tip size rather than wavelength. [58]

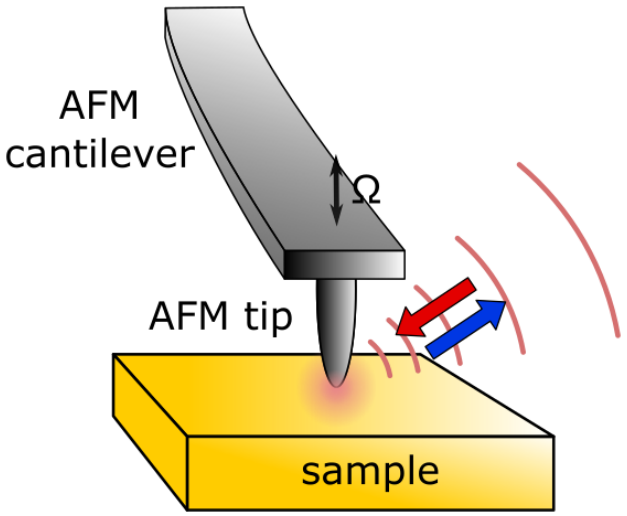

Figure 2.3: Light is focussed onto the AFM tip (red arrow). The strong field enhancement between tip apex and sample surface is modulated by the oscillation of the cantilever with frequency Ω. As a result, the scattered near-field (blue arrow=) carrier this (non-linear) modulation into the far-field, where it is detected.

2.3.1 Near-field signal generation

A common and easily accessible approach to model the tip-sample interaction and approximate the scattered magnitude and phase is the point-dipole model. The model assumes the tip to be a sphere with a point-dipole located at its center which induces a mirror dipole inside the sample. [75] For quantitative calculations an extended dipole model is often applied, which does a better job at avoiding underestimation of the tip's field enhacement. In this case, the tip is modelled as an elongated ellipsoid and the tip length enters the equation. [73] Several publications have introduced more advanced treatments of the tip-sample interaction [74, 76–80], including the effect of anisotropic samples [81, 82]. Though more exact, these models usually demand the introduction of several tunable geometric or empirical parameters, which ultimately requires fitting multiple parameters and complicates their predictive value [83].

In the following, the theory will cover the simple point-dipole model as it offers interesting qualitative insight into the signal origin that is sufficient for the analysis given in Chapter 3. Moreover, the approach of modelling the excitation of a polarizable sphere can be adapted to a dielectric sphere, which was used in Chapter 3 to excite surface waves on a metasurface. Yet another neat parallel is drawn in Sect. 3.2.2, where the derivation of the effective refractive index of a metasurface is based on the polarizability of subwavelength scatterers.

Within the point-dipole model the shape of the scanning probe is modelled as a small sphere with radius $a \ll \lambda$, as suggested in Fig. 2.4. As the object is so small, we may apply the quasi-static approximation to Maxwell's equations. The spherical tip forms a dipole moment $\vec{p}$ as it is polarized by the incoming field $\vec{E}_0$

$$\vec{p} = \alpha \vec{E}_0 \tag{2.10}$$

The polarizability α depends on the permittivities ϵ_i of tip and surrounding medium (air) and is given by [84]

$$\alpha = 4\pi\epsilon_0 a^3 \left(\frac{\epsilon_\mathrm{tip} - \epsilon_\mathrm{air}}{\epsilon_\mathrm{tip} + 2\epsilon_\mathrm{air}} \right) \tag{2.11}$$

Now, we use the electrostatic potential of a point dipole at distance $\vec{r}$ [84]

$$V(\vec{r}) = \frac{1}{4\pi\epsilon_0}\frac{\vec{r}\cdot\vec{p}}{r^3} \tag{2.12}$$

to calculate the electric field $\vec{E}$ generated by the tip

$$\vec{E} = -\vec{\nabla}V \tag{2.13a}$$

$$= -\frac{1}{4\pi\epsilon_0}\left(\frac{\vec{p}}{r^3}\vec{\nabla}\vec{r} + \vec{r}\cdot\vec{p}\vec{\nabla}r^{-3}\right) \tag{2.13b}$$

$$= \begin{cases} -\frac{1}{4\pi\epsilon_0}\vec{p}\left(\frac{1}{r^3} - \frac{3r^2}{r^5}\right) & = \frac{1}{2\pi\epsilon_0}\frac{\vec{p}}{r^3} \qquad \text{if } \vec{r} \parallel \vec{p} \\ -\frac{1}{4\pi\epsilon_0}\vec{p}\left(\frac{1}{r^3}\right) & = \frac{-1}{4\pi\epsilon_0}\frac{\vec{p}}{r^3} \qquad \text{if } \vec{r} \perp \vec{p} \end{cases} \tag{2.13c}$$

Since the vector $\vec{r}$ connects tip and mirror dipole, i.e. normal to the surface, the result depends on the polarization (s or p) of the incoming electric field relative to the surface.

The tip's dipole moment induces a mirror dipole p' in the sample given by the response of the surface.

$$\vec{p}' = \pm\frac{\epsilon_2 - 1}{\epsilon_2 + 1}\vec{p} \equiv \pm\beta\vec{p} \tag{2.14}$$

This induced dipole $\vec{p}'$ in turn is associated with a field $\vec{E}'$ according to Eq. 2.13c.

To obtain the effective dipole of the coupled system induced by both the incoming light $\vec{E}_0$ and the mirror dipole $\vec{E}'$, the contributions are added. For light polarized parallel to the tip, by applying Eq. 2.14 and substituting the distance between the dipole and its mirror image $r = 2(a + z)$, one obtains

$$\vec{p} = \alpha(\vec{E}_0 + \vec{E}') = \alpha\left(\vec{E}_0 + \frac{\vec{p}'}{2\pi\epsilon_0 r^3}\right) \tag{2.15a}$$

$$= \frac{\alpha}{1 - \frac{\alpha\beta}{2\pi\epsilon_0 r^3}}\vec{E}_0 \tag{2.15b}$$

$$= \frac{\alpha}{1 - \frac{\alpha\beta}{16\pi\epsilon_0(a+z)^3}}\vec{E}_0 = \alpha_{\text{eff},\parallel}\vec{E}_0 \tag{2.15c}$$

The result for light polarized perpendicular to the tip shaft is analogous. In this case, the dipole moments are oriented opposite to each other and the total scattering cross-section will be decreased to

$$\vec{p}_\perp = \frac{\alpha}{1 - \frac{\alpha\beta}{32\pi\epsilon_0(a+z)^3}}\vec{E}_0 = \alpha_{\text{eff},\perp}\vec{E}_0 \tag{2.16}$$

Naturally, parallel polarization is most common in s-SNOM experiments and Eq. 2.15c is mostly stated as the point-dipole model.

A simple extension can be used to further improve the model by including light $\vec{E}_{\text{s,r}}$ that is scattered by the tip towards the sample and then reaches the detector by specular reflection. Furthermore, the tip is excited additionally by incoming light that is first reflected off the surface and then reaches the tip. Both contributions are affected by the reflectivity of the sample. Phase delays are neglected due to the short optical paths relative to wavelength. The situation is depicted in Fig. 2.4. The additional electric fields are given by [85]

$$\vec{E}_{0,\text{r}} = r_\parallel\vec{E}_0 \tag{2.17a}$$

$$\vec{E}_{\text{s,r}} = r_\parallel\vec{E}_{\text{s}} \tag{2.17b}$$

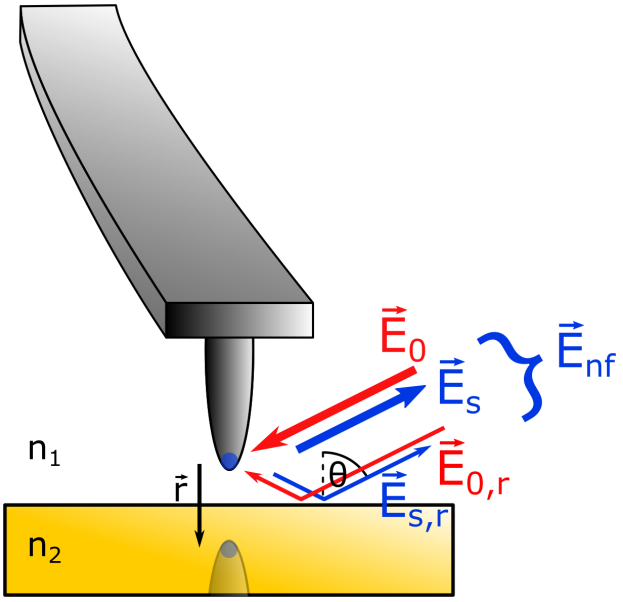

Figure 2.4: Incoming light $\vec{E}_0$ and scattered light $\vec{E}_s$ are the dominant waves. However, additional components reach the tip, $\vec{E}_{0,\mathrm{r}}$, and the detector $\vec{E}_{\mathrm{s,r}}$ via reflection off the sample. These contributions are added to obtain the total near-field signal $\vec{E}_{\mathrm{nf}}$.

The Fresnel coefficient $r_\parallel$ for non-magnetic media is given by

$$r_\parallel = \frac{n_1 \cos(\theta_2) - n_2 \cos(\theta_1)}{n_1 \cos(\theta_2) + n_2 \cos(\theta_1)} \tag{2.18}$$

where the refractive indices n_i and angles θ_i are connected via Snell's law

$$\frac{n_1}{n_2} = \frac{\sin(\theta_2)}{\sin(\theta_1)} \tag{2.19}$$

The tip-scattered field $\vec{E}_\mathrm{s}$ is thus composed of two components

$$\vec{E}_\mathrm{s} = \alpha_{\mathrm{eff},\parallel}(\vec{E}_0 + \vec{E}_{0,\mathrm{r}}) = \alpha_{\mathrm{eff}}(1 + r_\parallel)\vec{E}_0 \tag{2.20}$$

Finally, the field that reaches the detector is given by the sum of

$$\begin{aligned} \vec{E}_{\mathrm{nf}} = \vec{E}_\mathrm{s} + \vec{E}_{\mathrm{s,r}} &= (1 + r_\parallel)\vec{E}_\mathrm{s} \\ &= \alpha_{\mathrm{eff},\parallel}(1 + r_\parallel)^2 \vec{E}_0 \end{aligned} \tag{2.21}$$

Thus, the scattered light is proportional to the incoming light, with $\sigma = \alpha_{\mathrm{eff},\parallel}(1 + r_\parallel)^2$ being the scattering cross-section. This complex signal is measured in an s-SNOM experiment. Based of the model, one can determine the surface permittiviy from the acquired magnitude and phase of the scattered electric field.

It is noted in passing that while assuming negligible phase delays for reflection off tip and sample mostly improves agreement between data and model, it is not generally fulfilled. As reported by Walla et al. [Wal7], specular reflection of incoming radiation can result in the generation of SPPs on the sample surface with a non-negligible phase shift for certain (non-rotationally-symmetric) tip and sample geometries.

2.3.2 Pseudo-heterodyne detection

The focal spot size of the laser beam far exceeds the s-SNOM tip's size, due to the fundamental diffraction limit. The light that is scattered from the focal region thus contains near-field signal components and a considerable contribution of light that is scattered or reflected from the sample, top of the cantilever or the tip shaft. This leads to the central challenge in s-SNOM: the separation of the true near-field signal from these background components.

The background suppression is based on the modulation of the near-field component through harmonic modulation Ω of the tip-sample distance, i.e. oscillating the probing tip. The near-field term is strongly distance-dependent over length scales comparable to the tip size $a \ll \lambda$, see Eq. 2.15c. Harmonic modulation of the distance z thus generates higher harmonics at $n\Omega$. In contrast, the background-scattered light changes on scales of λ and is thus barely, and at most linearly, affected by the tip modulation. Different background-suppression schemes exist with varying complexity and effectiveness. These are non-interferometric (intensity), homodyne, heterodyne and pseudo-heterodyne detection. [86]

Non-interferometric and homodyne detection allow suppression of directly detected background-scattering (additive background) through lock-in amplification at a higher harmonic $n\Omega$. However, these methods cannot remove the effect of interference between near-field and background components (multiplicative background). On the other hand, heterodyne and pseudo-heterodyne detection make use of a frequency-shifted reference beam and theoretically allow the complete removal of background-scattered interference. At infrared and visible frequencies, pseudo-heterodyne detection is the more practical implementation of the two. It is therefore used in this work.

In pseudo-heterodyne detection, the s-SNOM signal E_{nf} is interfered with a sinusoidally phase modulated reference wave E_{R} at frequency $M < \Omega$

$$E_{\mathrm{R}} = E_{\mathrm{R},0} e^{i(\omega t + \gamma \sin(Mt) + \psi_R)} \tag{2.22}$$

where γ, M and ψ_R are the phase-modulation depth, frequency and phase offset, respectively. Phase-modulating the reference beam generates a frequency comb with equally spaced frequency components $\omega \pm mM$, phase shift of $\frac{\pi}{2}$ between neighbouring lines, and amplitudes $E_{R,0} J_m(\gamma)$, where J_m denotes the mth order Bessel function of the first kind.

The interference of the tip-scattered light E_{nf}, with frequency components $\omega \pm n\Omega$ at the higher harmonics of the cantilever oscillation, and the reference wave E_R creates sidebands with frequencies $f_{n,m} = n\Omega \pm mM$. This is depticted in Fig. 2.5. All doubly-modulated sidebands with $n, m \neq 0$ are now free of additive and multiplicative background contributions. Their amplitudes $u_{n,m}$ are [87]

$$u_{n,m} = 2\kappa E_{R,0} J_m(\gamma) E_{\mathrm{scat,n}} \cos(\phi_{\mathrm{scat},n} - \psi_R - m\frac{\pi}{2}) \tag{2.23}$$

where the detector sensitivity κ is introduced. The Bessel weighted functions of the first kind $J_m(\gamma) E_{\mathrm{scat,n}}$ are given in Fig. 2.5 for reference with a modulation depth $\gamma = 2.63$.

One can now use the first two sidebands $m = 1$ and $m = 2$ surrounding each harmonic nΩ. Their amplitude can be tuned to be equal by choosing an appropriate phase-modulation depth of $\gamma = 2.63$, yielding $J_1(\gamma) = J_2(\gamma)$. Moreover, the phase relationship between neighbouring lines can be used to yield the near-field amplitude and phase by combining

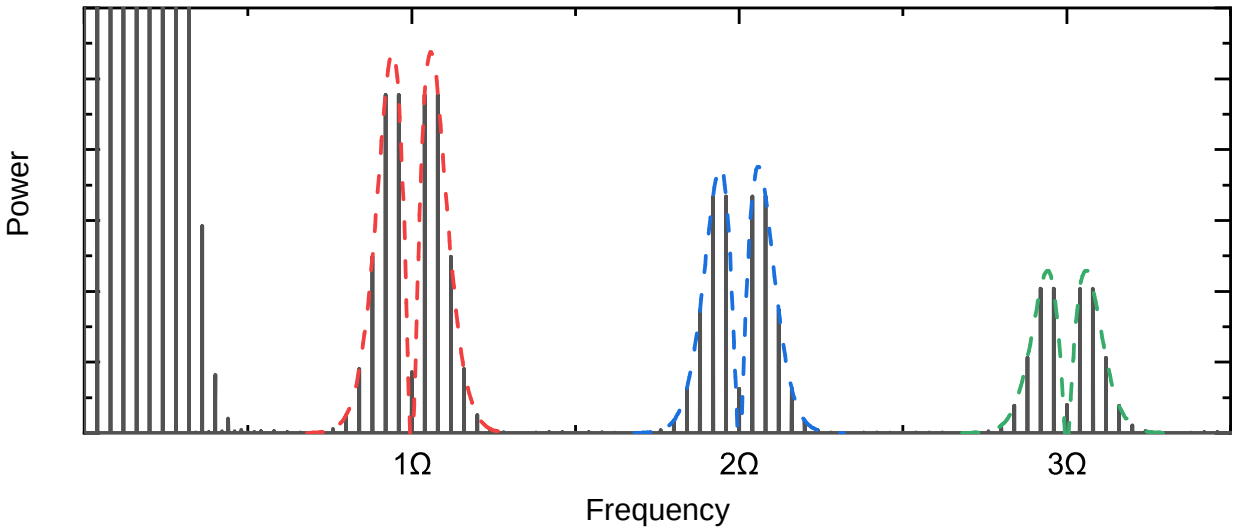

Figure 2.5: Power spectrum as expected at the detector output after pseudo-heterodyne detection. Equally spaced sidebands mM surround the harmonics nΩ of the cantilever modulation. Dashed lines highlight the amplitude distribution according to the Bessel function of first kind. Here a modulation depth of $\gamma = 2.63$ has been chosen, which leads to equal amplitudes for the first and second sidebands.

the signals given by Eq. 2.23

$$\sqrt{u_{n,1}^2 + u_{n,2}^2} = 2\kappa E_{R,0} J_{1,2}(2.63) E_{\text{scat},n} \qquad \propto E_{\text{scat},n} \tag{2.24a}$$

$$\arctan\left(\frac{u_{n,1}}{u_{n,2}}\right) = \arctan\left(\frac{\sin(\phi_{\text{scat,n}} - \psi_R)}{\cos(\phi_{\text{scat,n}} - \psi_R)}\right) \qquad = \phi_{\text{scat,n}} - \psi_R \tag{2.24b}$$

2.3.3 Description of setup

The experimental setup of the s-SNOM for taking near-field measurements is presented in the following. Fig. 2.6 shows a schematic of the layout set-up for this thesis.

The top-central square block contains the AFM setup. The probe tip and cantilever are attached to a holder that uses a piezoelectric actuator to vibrate the tip at frequency Ω. The vibration amplitude is controlled by observing the position of a laser beam that is deflected off the cantilever top surface on a position sensitive diode (PSD, not shown). Based on this feedback signal, the sample is kept at a constant distance to the tip using a piezoelectric tripod powered by a three channel high voltage amplifier (V45BL, Anfatec). The sample, depicted as a periodic gold metasurface, is scanned underneath the tip using a two-axes translation stage (P-517.3CL, Physik Instrumente) with a closed-loop range of $100 \times 100\,\mu\text{m}^2$.

The optical laser light used for performing s-SNOM measurements can be supplied by different laser sources: Toptica DL100 DFB ($\lambda = 855\,\text{nm}$), Sacher Cheetah TEC 50 ($\lambda = 784\,\text{nm}$) or Spectra Physics Excelsior ($\lambda = 532\,\text{nm}$).

The light is fed through a single-mode fibre (P3-780A-FC-2, Thorlabs) and Transversal Magnetic (TM)-polarized by a $\lambda/2$-plate before entering the interferometer. The first beam-splitter (BS1) splits the light into signal (transmission) and reference (reflection) beam.

The signal beam is reflected by a mirror, transmitted through the second beam-splitter (BS2) and reaches the parabolic mirror (top of figure). The parabolic mirror has a focal length of 10 mm; it can be aligned by a three-axes closed-loop piezo stage (NanoCube, Physik Instrumente) with a range of $(100\,\mu\text{m})^3$. The light is focussed onto the tip apex,

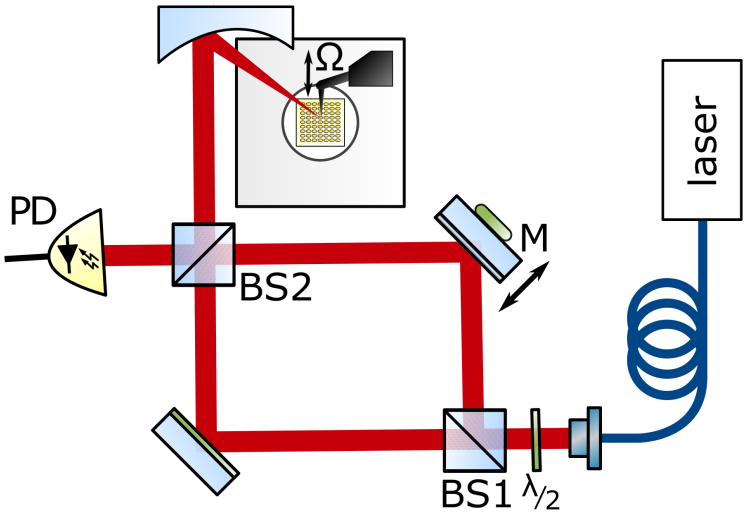

Figure 2.6: Experimental s-SNOM setup for pseudo-heterodyne detection. The laser beam transmits the beamsplitters (BS1, BS2) and is focussed onto the oscillating (Ω) AFM tip apex. The scattered light is collected by the parabolic mirror and reflected by BS2 onto the detector. It interferes with the reference light which is phase-modulated by being reflected off the modulated mirror M.

as explained in Sect. 2.3.1. The scattered light is collimated by the parabolic mirror and reflected at beam-splitter BS2.

At the detector (DET100A, Thorlabs), the signal is heterodyned with the reference beam, which was split off at beam-splitter BS1. It is reflected off the oscillating mirror (M $\approx 800\,\mathrm{Hz}$, A $\approx 250\,\mathrm{nm}$), which is responsible for the phase modulation of the wave explained in Sect. 2.3.2. Both beams impinge on the power-law detector (PD) and the characteristic pseudo-heterodyne beating can be analysed by the lock-in amplifier (not shown).

2.4 Conductive-AFM

Another mode of operation based on the AFM is the Conductive Atomic Force Microscope (c-AFM). Specifically, c-AFM delivers high-resolution current maps and local (nanoscale) Current-Voltage (I-V) characterization. These capabilities have proven useful for the evaluation of nanoscale electrical properties of ultrathin gate dielectrics and integrated circuit failure analysis [88]. Moreover, it is the method of choice for investigating current injection into 2D materials [89], lateral conductivity of graphene and TMDCs [90, 91] and vertical (transversal) current flow across dielectric thin films, 2D insulators [92] and van-der-Waals semiconductors [93].

c-AFM operates in contact mode, i.e. in the repulsive force regime, and uses a metallic probe tip which scans the sample surface. c-AFM measures the topography like AFM, with the feedback based on the tip-sample van-der-Waals forces, and thus independently of the current flow. This is in contrast to Scanning Tunneling Microscopy (STM), where the distance control is based on measuring the tunnel current flow. Consequently, c-AFM application is not limited to conducting samples. The system simultaneously measures the topography of the sample and the current flow. Metallic tip and the substrate each act as an electrode between which a DC bias is applied. The current varies with the conductivity of the sample. Usually, a transimpedance amplifier is necessary to amplify the small currents.

For the system presented here, a low noise current amplifier (DLPCA-100, Femto) with

variable low noise gain between 10^3 - 10^9 V/A and high speed gain up to 10^{11} was used. Its most important specifications are presented in Table 2.1.

Gain setting (low noise) (V/A)	10^6	10^7	10^8	10^9
Upper cut-off frequency -3 dB	200 kHz	50 kHz	7 kHz	1.1 kHz
Current noise density ($/\sqrt{\text{Hz}}$)	130 fA	43 fA	13 fA	4.3 fA
measured at	1 kHz	1 kHz	100 Hz	100 Hz
Integr. noise current (rms)	130 pA	41 pA	5.8 pA	0.8 pA
Max. input current (±)	10 µA	1 µA	0.1 µA	10 nA

Table 2.1: Selected performance data of DLPCA-100 depending on Gain setting [94].

For an I-V measurement, the probing tip is kept in contact with the sample at a fixed position while the DC voltage is swept and the current is recorded. Analysing local I-V characteristics is especially interesting on semiconducting samples, including semiconducting 2D van-der-Waals materials, that may only have very limited lateral dimensions altogether. In particular, mechanically exfoliated TMDC flakes often appear in the form of terraced layers, and individual layers slightly protrude from underneath each other. Accessing these features at the nano- to microscale requires a high-resolution. A more detailed treatment of this topic follows in Chapter 5.

2.4.1 Tip choice

Another experimental key topic is the choice of an appropriate probing tip. c-AFM tips commonly suffer from considerable mechanical wear. Firstly, this is due to friction from operating in contact mode and secondly, due to current flow and heating effects. A good overview covering common issues associated with different tips related to coating material, contact force and current is presented by Krause [95].

Table 2.2 summarizes the cantilevers that were tested for the c-AFM measurements presented in Chapter 5. The first choice, a Silicon tip with 23 nm PtIr coating with low force constant, was tested for scanning. Metal-coated tips usually have small tip radii and offer excellent conductivity. However, they suffer from mechanical wear and their conductivity quickly degrades. Even though PtIr5 is about twice as hard as pure platinum, the experiments confirmed that these cantilevers became unreliable and eventually non-conductive after several scans. The scans were performed with typical contact forces between 25 - 500 nN. With a DC bias of 20 mV, electrical contact between tip and gold sample could be established with minimum forces ranging from 50 - 150 nN.

Cantilever	Tip material	Tip radius	k	f_{res}
Arrow-ContPt10	coated PtIr5	< 25 nm	0.2 N/m	14 kHz
RMN-25PT300B	solid Pt	< 20 nm	18 N/m	20 kHz
RMN-12PT400B	solid Pt	< 20 nm	0.3 N/m	4.5 kHz

Table 2.2: Parameters of three different cantilever types that were tested within this work.

An alternative are fully metallic tips, which are more expensive than metal-coated tips. The second cantilever is such a solid platinum tip with high force constant. As stated above, pure platinum is softer than its alloy. However, even though a fully metallic tip may lose resolution upon degradation, it retains its electrical conductivity. In fact, the effective contact area may even increase with increasing tip wear leading to higher current flow.

Figure 2.7 shows a typical approach curve of deflection (measured as voltage difference, T-B, between top and bottom half of the PSD) and current flow at DC bias of 20 mV over distance d for cantilever RMN-25PT300B. The hysteresis due to the adhesion force upon retract is apparent. Another aspect to note is the deflection of $V_{\text{contact}} = 0.7\,\text{mV}$ upon current onset during approach. Assuming a linear relationship between deflection and distance during contact, one can perform the calibration

$$\frac{\text{force}}{\text{deflection}} = \frac{k}{\frac{\text{deflection}}{\text{distance}}} = \frac{18\,\text{N/m}}{231\,\frac{\text{mV}}{\mu\text{m}}} = 77\,\text{nN/mV} \tag{2.25}$$

and obtain the minimum contact force $F_{\text{contact}} = 54\,\text{nN}$. The deflection prior to approach has a standard deviation noise of 0.4 mV or ±30 nN, which is very large and creates a disadvantage due to the high spring constant that is hardly suitable for contact-mode AFM measurements.

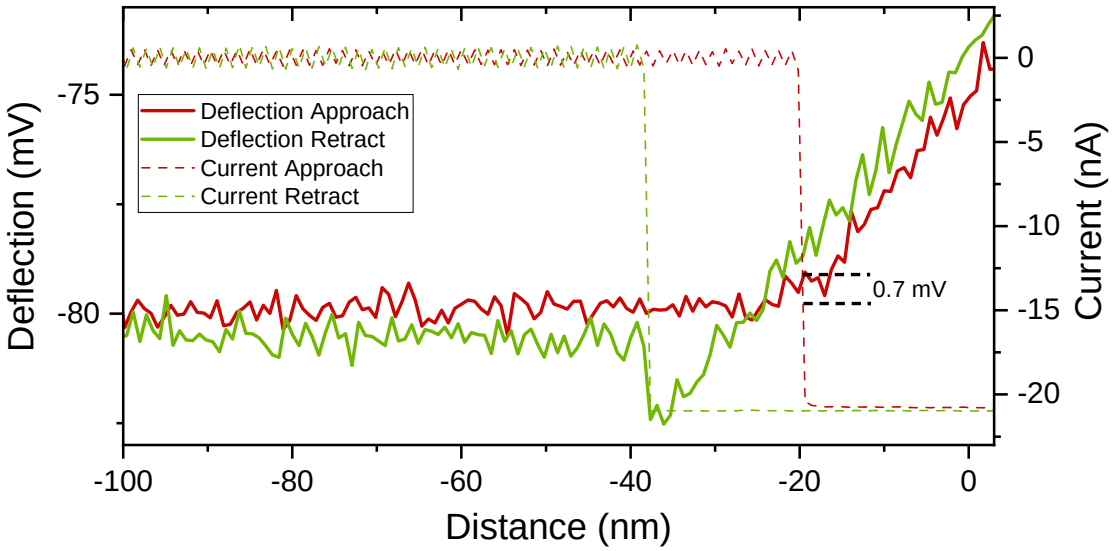

Figure 2.7: Approach curve for cantilever RMN-25PT300B showing deflection and current at bias of 20 mV over tip-sample distance. The measurement allows the calibration of the PSD Deflection Voltage and the contact force. The insufficient force resolution for a cantilever with high spring constant is apparent.

The third cantilever, with a solid platinum tip and low spring constant, is an adequate choice for c-AFM as it does not degrade quickly and offers well-controlled contact force setting. The platinum tip offers good conductivity and resolution. Fig. 2.8 shows the approach curve of the cantilever, which allows the calibration

$$\frac{\text{force}}{\text{deflection}} = \frac{0.3\text{N/m}}{295\frac{\text{mV}}{\mu\text{m}}} = 1\,\text{nN/mV} \tag{2.26}$$

The softer cantilever thus provides a much lower force noise of ±0.4 nN.

Typical DC bias voltages range between ±3 V. The associated currents range from 10 pA to 10 nA when measuring on TMDC van-der-Waals flakes, but can occasionally exceed 10 µA when the tip is short-circuited on the metallic substrate or a metal contact. These currents can lead to extremely high current densities considering the small tip-sample contact area in the range of 10^{-3} to $10^{-2}\,\mu\text{m}^2$. Severe heating, tip degradation, melting and even fusing of the tip apex can occur [95]. High current densities can also damage the sample, an effect that is further discussed in Chapter 5.

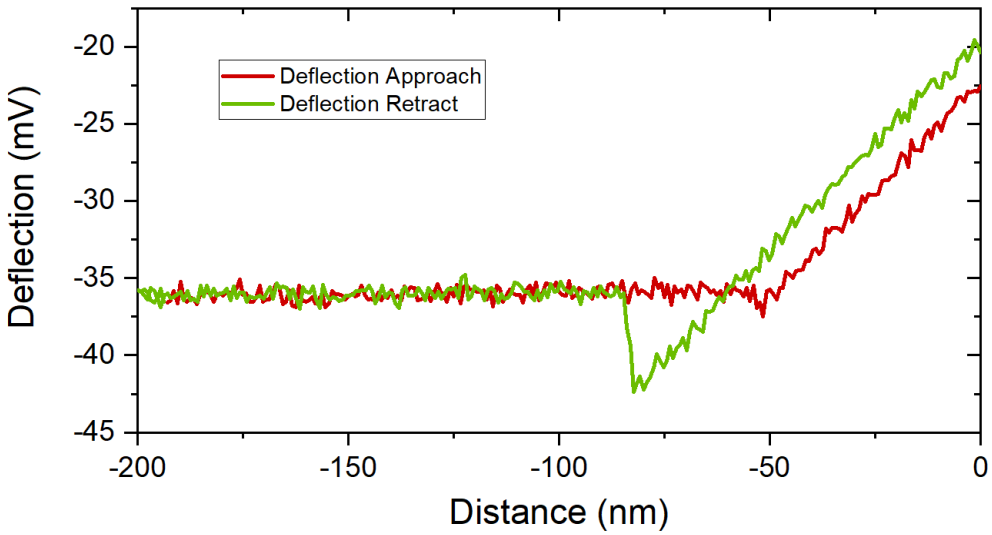

Figure 2.8: Approach curve for cantilever RMN-12PT400B showing deflection over tip-sample distance for a soft spring constant.

2.4.2 Effective contact area

Determining the electrical contact area is critical when analysing the current density across the tip. Furthermore, it is a crucial parameter in the calculation of (tunnel) current densities from the measurement of current flow. However, the electrical contact is not simply equal to the physical probe tip apex area, but scales as a function of contact force and tip radius. In fact, the effective electrical contact area is considerably smaller than πR_{tip}^2 would let one assume due to the paraboloidal shape of the tip [96]. A common approach is to model the contact area between a deformable sphere (the platinum tip) and the deformable sample surface (e.g. WS_2) [97]. The effective electrical contact area between tip and sample is then given by

$$A_{\text{eff}} = \pi r_c^2 = \pi \left(K^{-1} F_{\text{ts}} R_{\text{tip}} \right)^{\frac{2}{3}} \tag{2.27}$$

where F_{ts} is the tip-sample force, R_{tip} is the tip radius and K is the reduced elastic modulus of the tip sample system [98]:

$$\frac{1}{K} = \frac{3}{4} \left(\frac{1 - \nu_{\text{tip}}^2}{E_{\text{tip}}} + \frac{1 - \nu_{\text{sample}}^2}{E_{\text{sample}}} \right) \tag{2.28}$$

with Young's moduli E_i and Poisson's ratio ν_i of tip and sample, as exemplified in Table 2.3.

Material	$E_{i,2D}$	$E_{i,3D}$	ν_i
WS_2	142 Nm^{-1}	237 GPa	0.21
WSe_2	114 Nm^{-1}	163 GPa	0.19
Graphene	339 Nm^{-1}	1000 GPa	0.18
Platinum	-	140 GPa	0.39
Gold	-	70 GPa	0.42

Table 2.3: Young's moduli and Poisson ratios for different materials. [99–101]

The 2D Young's modulus is suitable to characterize 2D materials. For a viable comparison to 3D materials, the parameter can be converted by dividing through the thickness of

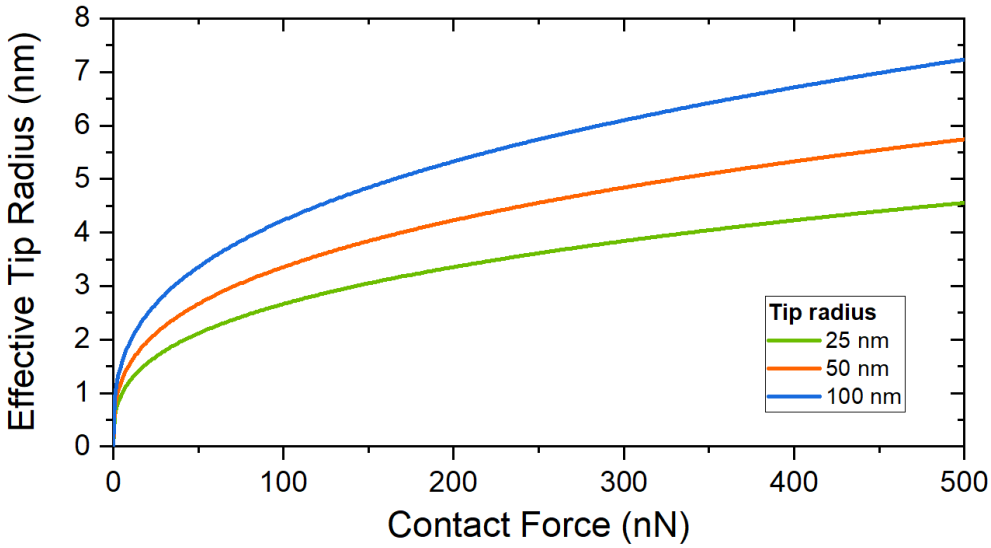

Figure 2.9: Calculated effective tip radius depending on contact force for a platinum tip, considering three different radii, on WS_2 sample.

the 2D material (e.g. 6 Å for WS_2 monolayer) [102]. For a platinum tip with $R_{\text{tip}} = 25\,\text{nm}$ on WS_2, using a contact force of 150 nN, this results in an effective contact area of $29\,\text{nm}^2$ or an effective tip radius of only 3 nm. An effective tip radius exceeding 10 nm can hardly be achieved even with higher contact force, as illustrated in Fig. 2.9.

Chapter 3

Guided mode resonances on metasurfaces

3.1 Introduction

Surface Plasmon Polaritons (SPPs) propagate on two-dimensional interfaces between metallic and dielectric half-spaces. Apart from a simple metallic half-space, a thin metallic layer also supports the propagation of SPPs. In this case, two interfaces above and below the metal exist. The situation is depicted in Fig. 3.2. Furthermore, if the metallic layer is chosen to be very thin, the SPPs *feel* each other - each mode is affected by the two interfaces simultaneously. This is the case when the boundary conditions for the evanescent tails into the metal cannot be considered independently, or if the evanescent electric fields reach the opposite side of the metal film. Then, the modes experience strong coupling and splitting of respective energies and wavevectors is observed [103]. The critical thickness for coupling of opposite interface modes is the penetration depth. It thus depends on material, its structure and the wavelength of the surface waves.

For symmetric dielectric environments on either side of the metal layer, the resulting modes can be labelled as Short-Range and Long-Range Surface Plasmon Polariton (LRSPP). The latter is characterized by significantly lower attenuation and weaker confinement compared to SPPs at a half-space interface, making it interesting for applications [104–106]. On the other hand, in material systems with asymmetric dielectric environments around the metallic layer, i.e. with different refractive indices, the two individual modes also interact. However, their coupling cannot always be classified as strictly into short- and long-range modes due to a phase mismatch of the modes at the interfaces. In this case, LRSPP are affected by additional damping and applications may be initially limited [107].

Under certain conditions, however, these asymmetric structures support so-called guided-mode resonances. This type of mode is characterized by a full vertical confinement on one of the two interfaces, specifically towards the dielectric with low refractive index. However, coupling across the metallic layer leads to radiative losses into the high-index dielectric. This characteristic is observable as leakage into the dielectric cladding or high-index substrate. Guided-mode resonances have found applications in the literature as tunable band-pass filters or sensitive phase detectors [22, 23, 25–27, 108, 109]. The phenomenon appears with different nomenclature that is used interchangeably such as leaky-mode resonances, quasi-guided modes or leaky surface plasmon-polaritons.

Most of the results presented in this chapter were published in condensed form by Walla et al. as “Near-Field Observation of Guided-Mode Resonances on a Metasurface via Dielectric Nanosphere Excitation” [Wal6] and were presented at METANANO 2018 - International

Conference on Metamaterials and Nanophotonics [Wal15].

3.2 Theory

3.2.1 Drude formalism

It is truism to state that SPPs only exist at interfaces between metallic and dielectric media. These categories, however, are not absolute as they appear and should be understood as a descriptive statement of the material response to electromagnetic radiation at a given frequency. This property is expressed by the (dispersive) permittivity ϵ of a material. Being a complex quantity, it reflects both the strength of the polarisation and the phase of the material response. The permittivity is affected by material-specific charge carrier densities, rotational or vibrational resonances, intra- and inter-band transitions. Furthermore, the sub-wavelength (surface) structure of a material may also affect the electromagnetic response and can be represented by an effective permittivity. In the following, the Drude formalism shall be introduced as an instructive model to understand the different regimes that govern the existence and propagation of surface wave.

The Drude(-Lorentz) formalism assumes that free (and bound) electrons perform harmonic oscillations in a lattice of positive ion cores when accelerated by an external field. The details of the lattice potential are reflected by the effective mass m of the electron, which differs from its free mass. The differential equation describing the motion $\vec{r}$ of an electron responding to an applied electromagnetic field $\vec{E}(\vec{r},t)$ is [110]

$$m\ddot{\vec{r}} + m\Gamma\dot{\vec{r}} + m\omega_0^2\vec{r} = -q\vec{E}(\vec{r},t) \tag{3.1}$$

where damping factor Γ, resonance frequency ω_0 and electron charge q have been introduced.

A solution is found for a harmonic driving field $\vec{E}(t) = \vec{E}_0 e^{-i\omega t}$. When responding to the field, the oscillating electrons $\vec{r}(t)$ cause a macroscopic polarization $\vec{P} = -nq\vec{r}$ of the carrier density n, resulting in dielectric displacement $\vec{D} = \epsilon_0\vec{E} + \vec{P}$. The effective relation between field and displacement $\vec{D} = \epsilon_0\epsilon(\omega)\vec{E}$ is then given by the Drude-Lorentz formula

$$\epsilon(\omega) = \epsilon_{\text{vac}} + \epsilon_{\text{free}} + \epsilon_{\text{bound}} \tag{3.2a}$$

$$= 1 - \frac{\omega_p^2}{\omega^2 + i\Gamma\omega} + \sum_j \left[\frac{f_j}{(\omega_{0j}^2 - \omega^2) - i\Gamma_j\omega}\right] \tag{3.2b}$$

where $\omega_p^2 = \frac{nq^2}{\epsilon_0 m}$ is the plasma frequency; $f_j, \omega_{0j}, \Gamma_j$ are oscillator strength, resonance frequency and damping factor of the bound electron resonances j, respectively [110, 111].

When considering only free carriers moving as an electron gas, a reasonable assumption for metals at most frequencies, the third terms of Eqs. 3.1 (restoring force) and 3.2 (bound electrons) vanish. The resulting expression for the permittivity is the Drude formula. In this case, the ansatz of Eq. 3.1 can also be expressed in momentum space, substituting $m\dot{\vec{r}} = \hbar\vec{k}$ to yield

$$\dot{\vec{k}} = -\frac{q}{\hbar}\vec{E}(t) - \vec{k}\Gamma \tag{3.3}$$

which will be applied to positive hole charge carriers in Chapter 6, to identify the origin of higher harmonic Terahertz frequencies generated in a doped Silicon crystal by an intense Terahertz pulse.

The simple assumptions made by Drude of modelling the motion of electrons under an external field like an ideal gas provide good results across a wide range of frequencies. In

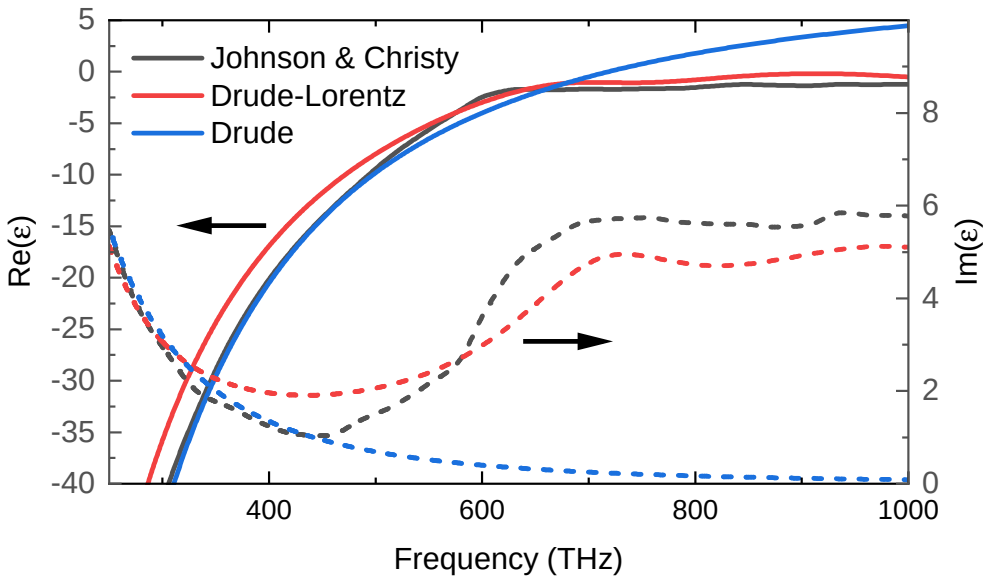

Figure 3.1: Real and imaginary part of the dielectric function of gold according to experimental data [112], Drude-Lorentz' and Drude's model.

noble metals the model diverges from reality when interband transitions set in at higher optical and ultra-violet frequencies [110, 113]. This is shown for gold in Fig. 3.1, where real and imaginary permittivity are compared between Drude[1], Drude-Lorentz [114] and experimental data by Johnson and Christy [112]. At the nanoscale, the permittivity values remain accurate down to dimensions of about 2 nm [115] before non-local effects cause damping and blue shift of the resonances [116, p. 369].

3.2.2 Effective medium approximation

The polarizability α of a spherical particle was introduced in Sect. 2.3 in order to model the effect of the s-SNOM tip as a spherical dipole interacting with the surface

$$\alpha = 4\pi\epsilon_0 a^3 \left(\frac{\epsilon_m - \epsilon_d}{\epsilon_m + 2\epsilon_d}\right) \tag{3.4}$$

In order to approximate the macroscopic permittivity of a metamaterial ϵ_{eff}, one can apply the Clausius-Mossotti relation. It assumes that the permittivity of a bulk material can be modelled by summing over a uniform array of polarizable inclusions (spheres), i.e from its atomic, molecular or meta-atomic unit cells. Clausius-Mossotti states that [117, 118]

$$\frac{\epsilon_{\text{eff}} - \epsilon_d}{\epsilon_{\text{eff}} + 2\epsilon_d} = \sum_j \frac{N_j \alpha_j}{3\epsilon_0} \tag{3.5}$$

where N_j is the number of particles per unit volume, and ϵ_d is the permittivity of the surrounding medium. For a metasurfaces which can be described as a periodic lattice of polarizable spheres, the sum over all polarizabilities results in the Maxwell Garnett equation

$$\left(\frac{\epsilon_{\text{eff}} - \epsilon_d}{\epsilon_{\text{eff}} + 2\epsilon_d}\right) = f\left(\frac{\epsilon_m - \epsilon_d}{\epsilon_m + 2\epsilon_d}\right) \tag{3.6}$$

[1]To account for the residual ϵ of the ion lattice, $\epsilon_\infty = 9.23$ is substituted for ϵ_{vac}.

where f is the volume fraction of the inclusions. This can be solved for the effective permittivity

$$\epsilon_{\text{eff}} = \epsilon_d \frac{2\epsilon_d + \epsilon_m + 2f(\epsilon_m - \epsilon_d)}{2\epsilon_d + \epsilon_m - f(\epsilon_m - \epsilon_d)} \tag{3.7}$$

An extension of the model broadens the scope to include not only spherical inclusions in a dielectric matrix, but also spheroidal particles. Here, merely the result for the anisotropic Maxwell-Garnett homogenization theory is given [116, p.141ff.]

$$\epsilon_{\text{eff}} = \epsilon_d \frac{\epsilon_d + [v_p(1-f)+f](\epsilon_m - \epsilon_d)}{\epsilon_d + v_p(1-f)(\epsilon_m - \epsilon_d)} \tag{3.8a}$$

$$\overset{v_0 \to 0}{=} f\epsilon_m + (1-f)\epsilon_d \tag{3.8b}$$

where v_p is the depolarization factor, with $p \in \{x, y, z\}$. For oblate spheroids resembling thin pancakes, $v_x, v_y \to 0$, and $v_z \to 1$ [117]. Eq. 3.8b thus describes the lateral permittivity for two-dimensional metasurfaces made of elliptical thin disks. Here, the filling factor f is given by $f = \frac{a_s b_s}{a_0 b_0}$. a_s, b_s are the radii of the elliptical disc and a_0, b_0 are the half-lengths of the unit cell [119–121].

To conclude, we can see from Eq. 3.8b that it can be reasonable to approximate the permittivity for a metasurface by taking a weighted average of the permittivities filling the unit cell. However, in general the validity is only given for low filling factors f, as long as spacing between neighbouring unit cells is large and strong interaction between metaatoms can be neglected. Furthermore, in the presence of resonances, the Maxwell Garnett theory is not a reliable homogenization approach.

3.2.3 SPPs at thin metallic layers

The properties of SPPs can be derived by solving Maxwell's equations and choosing appropriate boundary conditions for surface waves propagating in a multi-interface system [122]

$$\vec{\nabla} \times \vec{E} = -\frac{\delta \vec{B}}{\delta t} \qquad \vec{\nabla} \cdot \vec{D} = \rho_{\text{free}} \tag{3.9a}$$

$$\vec{\nabla} \times \vec{H} = \vec{J} + \frac{\delta \vec{D}}{\delta t} \qquad \vec{\nabla} \cdot \vec{B} = 0 \tag{3.9b}$$

The structure of interest here is an IMI multilayer. A thin metallic film of thickness $h = 2a$ is sandwiched at $-a < z < a$ between two dielectrics ϵ_1 and ϵ_3. The field components for a TM-polarized waves are above the metal film $z > a$ (left column) and below the metal film $z < -a$ (right column) [111, p. 30]

$$H_y = Ae^{i\beta x}e^{-k_1 z} \qquad H_y = Be^{i\beta x}e^{k_3 z} \tag{3.10a}$$

$$E_x = iA\frac{1}{\omega\epsilon_0\epsilon_1}k_1 e^{i\beta x}e^{-k_1 z} \qquad E_x = -iB\frac{1}{\omega\epsilon_0\epsilon_3}k_3 e^{i\beta x}e^{k_3 z} \tag{3.10b}$$

$$E_z = -A\frac{\beta}{\omega\epsilon_0\epsilon_1}e^{i\beta x}e^{-k_1 z} \qquad E_z = -B\frac{\beta}{\omega\epsilon_0\epsilon_3}e^{i\beta x}e^{k_3 z} \tag{3.10c}$$

where $\beta = k_x$ is the propagation wavevector, and $k_i \equiv k_{z,i}$ is the wavevector component perpendicular to the interfaces.

For a single interface, the surface mode will exponentially decay into both the dielectric and the metal. However, for a thin interface the modes inside the metallic film $-a < z < a$,

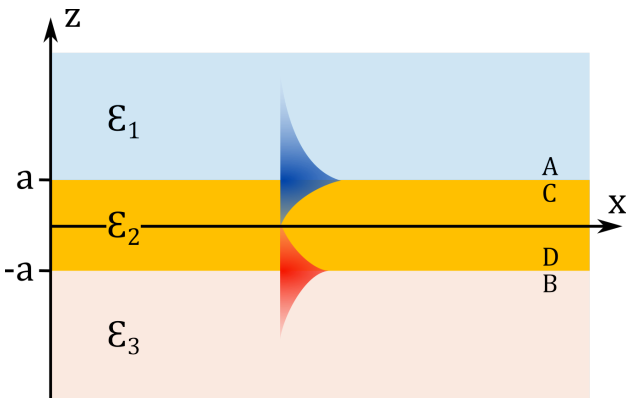

Figure 3.2: Sketch of a three-layer Insulator-Metal-Insulator (IMI) structure with two bound surface modes. The SPPs are localized at the two interfaces between the dielectrics and the thin metal film. Letters A,B,C,D point to the interfaces considered in the derivation.

localized at the top and bottom, will be affected by both interfaces and thus couple

$$H_y = Ce^{i\beta x}e^{k_2 z} + De^{i\beta x}e^{-k_2 z} \tag{3.11a}$$

$$E_x = -iC\frac{1}{\omega\epsilon_0\epsilon_2}k_2 e^{i\beta x}e^{k_2 z} + iD\frac{1}{\omega\epsilon_0\epsilon_2}k_2 e^{i\beta x}e^{-k_2 z} \tag{3.11b}$$

$$E_z = C\frac{\beta}{\omega\epsilon_0\epsilon_2}e^{i\beta x}e^{k_2 z} + D\frac{\beta}{\omega\epsilon_0\epsilon_2}e^{i\beta x}e^{-k_2 a} \tag{3.11c}$$

The system of equations can be solved by imposing continuity at the interfaces $z = \pm a$ of H_y and E_x

$$Ae^{-k_1 a} = Ce^{k_2 a} + De^{-k_2 a} \qquad \frac{A}{\epsilon_1}k_1 e^{-k_1 a} = -\frac{C}{\epsilon_2}k_2 e^{k_2 a} + \frac{D}{\epsilon_2}k_2 e^{-k_2 a} \tag{3.12a}$$

$$Be^{-k_3 a} = Ce^{-k_2 a} + De^{k_2 a} \qquad -\frac{B}{\epsilon_3}k_3 e^{-k_3 a} = -\frac{C}{\epsilon_2}k_2 e^{-k_2 a} + \frac{D}{\epsilon_2}k_2 e^{k_2 a} \tag{3.12b}$$

The linear system of coupled equations can be solved to obtain an implicit expression for the dispersion relation, i.e. a relationship between β and ω, which is dependent on the thickness h. Using the notation $\kappa_i = k_i/\epsilon_i$, this yields[2]

$$\tanh(k_2 h) = \frac{\kappa_1\kappa_2 + \kappa_2\kappa_3}{\kappa_2\kappa_2 + \kappa_1\kappa_3} \tag{3.13}$$

where the following relationship must be fulfilled

$$k_i{}^2 = \beta^2 - \epsilon_i k_0{}^2 \tag{3.14}$$

It is noted that for $\beta_i > \sqrt{\epsilon_i}k_0$, the wavevector of the SPP is larger than that of the dielectric light line, then $k_i > 0$ and the modes are bound or non-radiative. If $\beta_i < \sqrt{\epsilon_i}k_0$, it follows that $k_i{}^2 < 0$ and k_i is imaginary. This solution describes a plane wave solution radiating off of the metal interface.

Two generally discussed limiting cases following from Eq. 3.13 are:

1. The symmetric cladding, $\epsilon_1 = \epsilon_3$, where the expression splits into a pair of odd and even modes [111]

$$\tanh(k_2 a) = -\frac{\kappa_1}{\kappa_2} \qquad \tanh(k_2 a) = -\frac{\kappa_2}{\kappa_1} \tag{3.15}$$

[2]The equivalence of expression Eq. 3.13 and Eq. 2.28 in [111] is shown in Appendix A.1.

The terms odd or even relate to the symmetry or antisymmetry, respectively, of $E_x(z)$. Symmetric (odd) modes do not have a zero crossing inside the metal film. This terminology can be confusing, since E_x and E_z behave oppositely with regards to symmetry.

2. The thick metal layer, i.e. $\lim_{h\to\infty} \tanh(k_2 h) = 1$, i.e. decoupled SPPs at independent interfaces

$$\kappa_1 = \kappa_2 \qquad\qquad \kappa_3 = \kappa_2 \tag{3.16}$$

with $\mathrm{Re}(k_i) > 0$, such that the fields are bound, this yields the well-known dispersion relation for SPPs at a half-space interface

$$\beta_i = k_0 \left(\frac{\epsilon_i \epsilon_2}{\epsilon_i + \epsilon_2} \right)^{1/2} \tag{3.17}$$

In the interesting case of a very thin metallic layer ($h \ll \lambda$) with asymmetric cladding ($n_1 \neq n_3$), two surface waves with different wavevector β_i exist at the interfaces. The possible solutions fall into four distinct regimes as is illustrated in Fig. 3.3, showing amplitude-wavefront sketches of the fields.

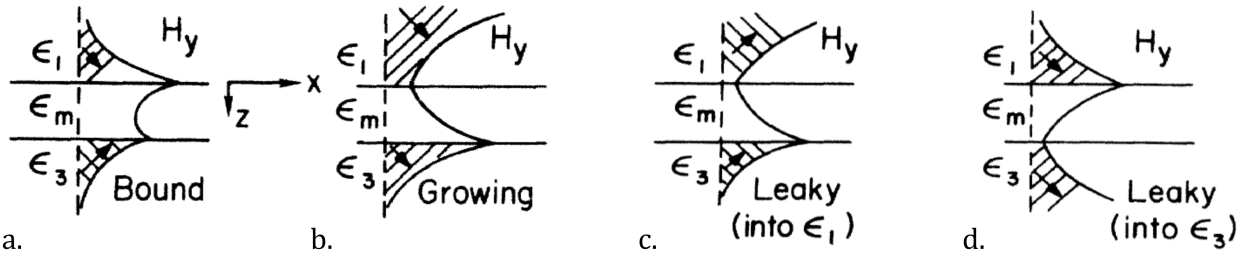

Figure 3.3: Field distributions for bound, leaky and growing modes guided along a thin metal film. The arrows show the energy flow in the dielectrics. Adapted with permission from [104] © The Optical Society.

The common non-radiative case in Fig. 3.3a shows fields decaying away from the film and wave fronts tilted into the metal film. These modes are bound to the surface at both interfaces. Fig. 3.3b shows a growing wave solution into one of the dielectrics. This mode demands an external incident field to constantly supply energy to support the growing character. Fig. 3.3c and Fig. 3.3d show the two cases for leaky solutions into medium 1 and 3, respectively. The wave energy is localized in one dielectric, and the wave front is tilted towards the metal film. In the opposite dielectric, the fields grow exponentially, their wave fronts are tilted away from the metal film and they radiate into the dielectric. [104, 123]

The radiation angle θ for leaky waves which radiate into the dielectric medium is given by considering phase matching at the interface or Snell's law

$$\beta \sin(90°) = n k_0 \sin(\theta) \tag{3.18}$$

Fig. 3.4 shows the numerically calculated dispersion relation for a symmetric IMI multilayer at a gold interface. The metal permittivity is modelled with the Drude model, the dielectric has permittivity $\epsilon_{1,3} = 2.1$. Two straight light lines ($n_0 = 1, n_{1,3} = 1.45$) and the half-space interface SPPs are displayed in long and short dashed lines, respectively. Two two surface modes (blue and red) exist below the light line, shown for three different layer thicknesses $h \in \{20\,\mathrm{nm}, 30\,\mathrm{nm}, 40\,\mathrm{nm}\}$. The characteristic asymptotic behaviour towards

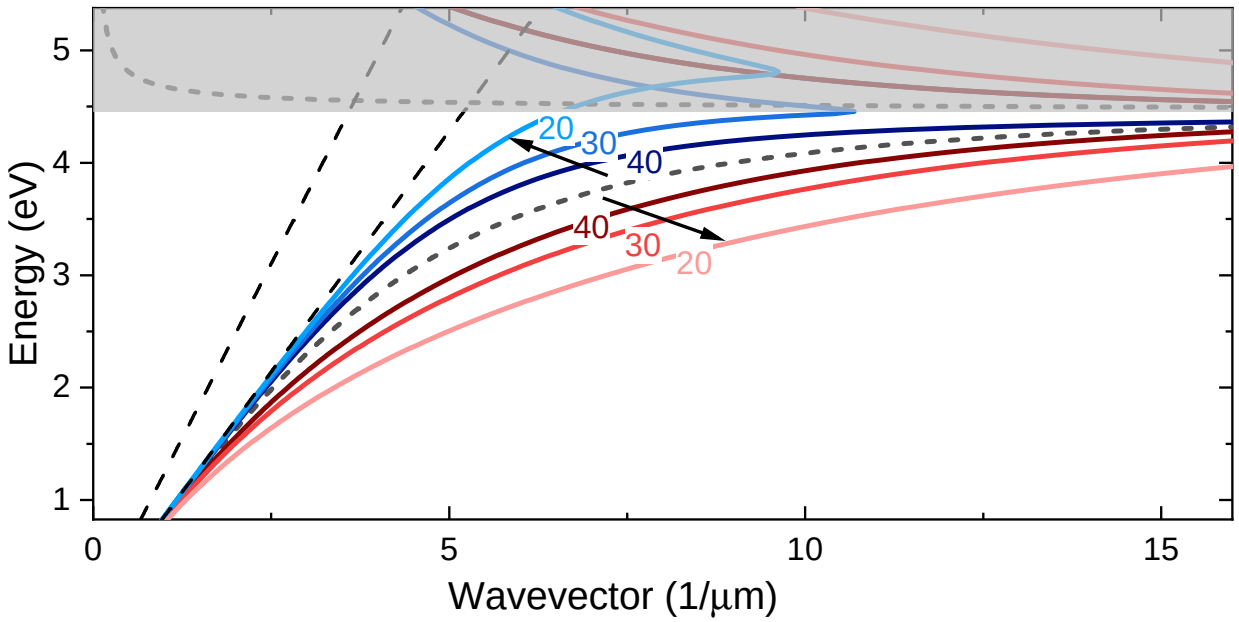

Figure 3.4: Dispersion relation of a (Drude) gold layer sandwiched in a symmetric cladding (n = 1.45). The short-dashed line shows the dispersion for a thick layer. For thin layers (40 nm, 30 nm, 20 nm) two bound modes exist, split into even (red) and odd (blue), shifted towards lower and higher energies, respectively. The grey shading marks the photonic band gap, where the modes are strongly damped.

the surface plasmon resonance $\omega_{\mathrm{sp}} = \omega_p(1 + \epsilon_{1,3})^{-\frac{1}{2}}$ is seen, above which a photonic band gap opens (shaded region). For non-negligible damping, the curve bends through the band gap as a strongly damped evanescent wave. The two surface waves demonstrate energy splitting. Compared to the uncoupled surface wave (short dashed line), they are repelled towards higher and lower energies.

3.2.4 Numerical solution of dispersion relation

The dispersion relation for an IMI three-layer system follows from Eq. 3.13. As shown in Sect. 3.2.3, the solutions to the expression can only be expressed analytically for certain special cases, such as symmetric cladding or thick metal layer. Generally the equation must be solved numerically for the material parameters in question. [105, 124, 125]

Fig. 3.5 shows the numerically calculated dispersion relation for an air-gold-glass multilayer system for varying thickness of the metal layer, h = 10, 20, 40 nm. The permittivity of gold was modelled using the Drude model. The air and substrate ($n_3 = 1.45$) light lines are shown as straight dashed lines. The black dashed bent lines are the dispersion lines for single interface SPP at a air/gold (upper) and gold/substrate (lower) half-space, respectively. For a thin metal layer, these two modes are coupled and they shift towards lower (red) and higher (blue) energies. The corresponding layer thicknesses in nanometers are labelled in the graph with matching colours.

One can observe that the single-interface substrate dispersion line bends back in the photonic band gap above its characteristic surface plasmon resonance at about 4.5 eV. The coupled modes, on the other hand, bend over but turn around to reconnect with their partner. This effect is accompanied by strong damping, as is typical for the evanescent regime [126, p. 298].

Even though each dispersion line describes a mode that is supported by the multilayer

system, the SPP modes are localized primarily at top (blue) or bottom (red) interface, respectively. This is where their electric field energy is propagating and consequently where they may be observed more easily. Still, it is important to note that SPPs stemming from air/metal interface lie above the substrate light line at low frequencies. The field components of this surface mode reaching towards the substrate/metal interface are hence not confined to the surface by momentum conservation. These modes are thus not bound to the interface on both sides and can become radiative/leaky into the substrate.

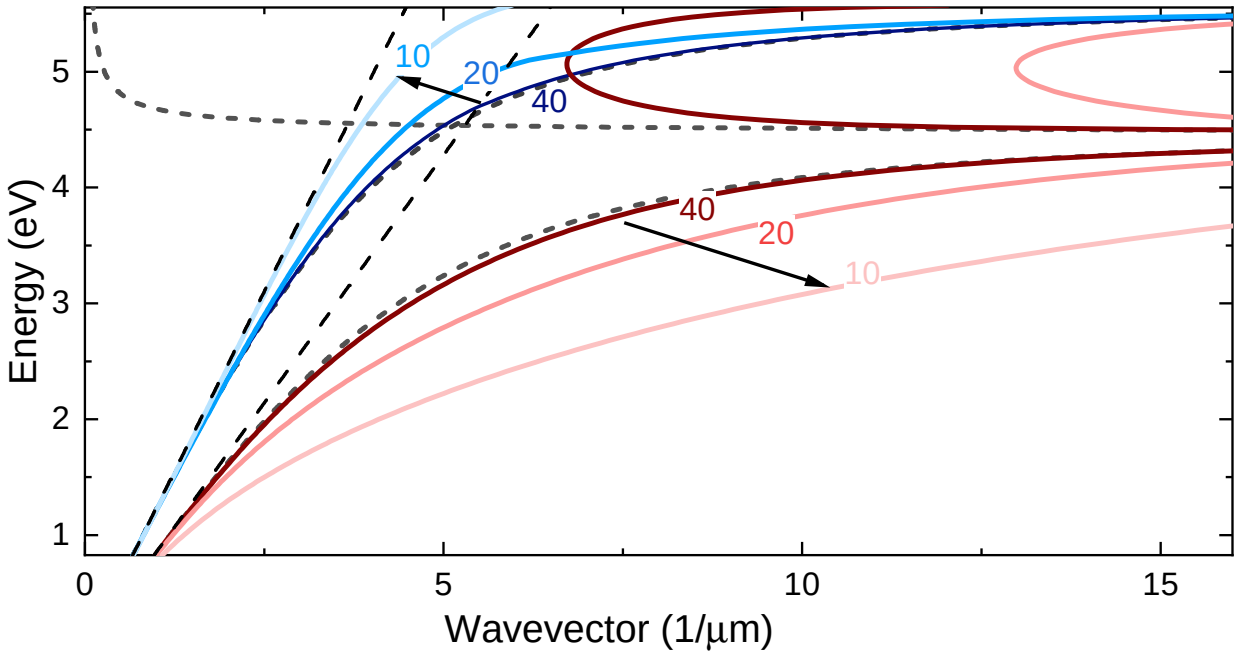

Figure 3.5: Dispersion relation of a (Drude) gold layer sandwiched in an asymmetric cladding ($n_1 = 1, n_3 = 1.45$). The short-dashed lines show the dispersion lines for half-space interfaces of air/gold and air/substrate, respectively. For thin layers (40 nm, 20 nm, 10 nm) two bound modes exist, shifted towards lower (red) and higher (blue) energies, respectively. The odd mode at $h = 40\,\text{nm}$ is barely distinguishable from the uncoupled mode dispersion.

While Fig. 3.5 draws an instructive picture of the situation, the Drude model is in fact not ideal to model the SPP behaviour in this frequency range. Instead, the dispersion relation in Fig. 3.6 was modelled with the Drude-Lorentz permittivity for the gold layer. All other parameters remain the same as before. It becomes apparent how the dispersion is strongly affected by the additional resonances and damping introduced by the interband transitions. Even though $\text{Re}(\epsilon)$ is negative for the whole frequency range depicted, the strong damping contained in $\text{Im}(\epsilon)$ can shift the dispersion line above the light line. This is the case for the single-interface SPP at higher frequencies and, interestingly, also occurs due to very thin layer thickness as can be seen for the blue line at $h = 10\,\text{nm}$.

Another aspect is exemplified at the dashed-dotted horizontal line ($\lambda = 850\,\text{nm}$). The even mode (red) becomes more confined (i.e. higher k-vector) with decreasing layer thickness. More energy propagates inside the metallic layer, the wavelength becomes shorter and absorption losses increase. Meanwhile, the odd line (blue) experiences vanishing confinement. It propagates increasingly in the dielectric, its wavelength approaches that of freely propagating light. Since it is now only weakly guided, absorption losses in the metal fade out. This case is sometimes labelled Long-Range Surface Plasmon Polariton [106, 107, 122] as opposed to its short-range partner [127].

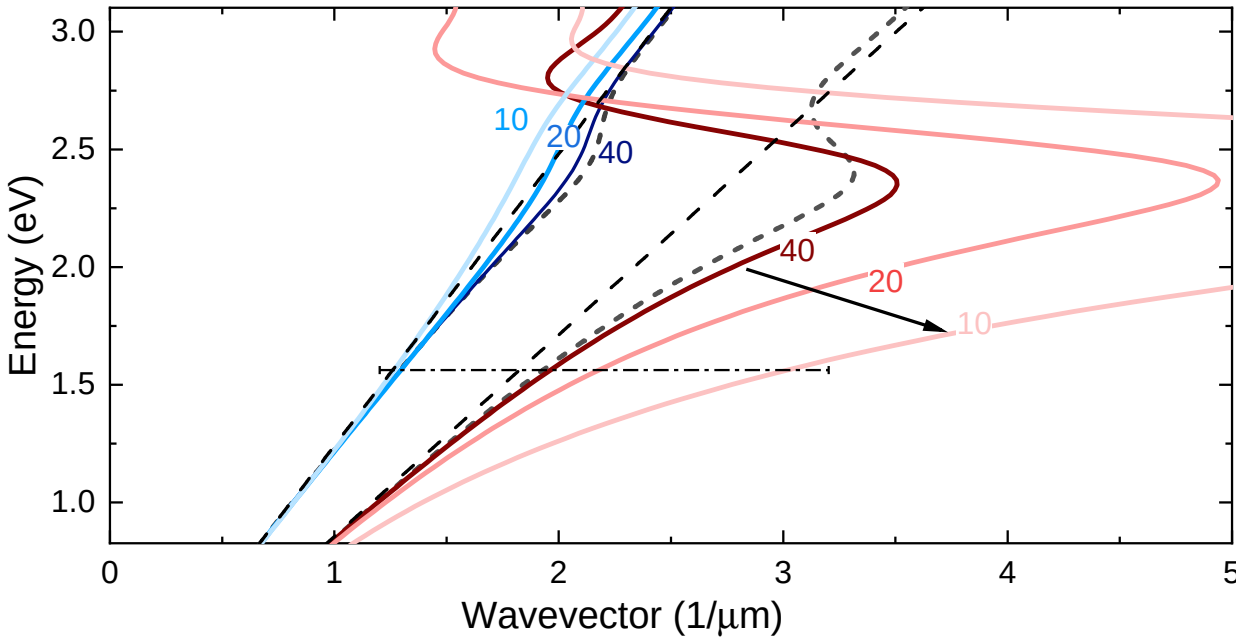

Figure 3.6: Numerically calculated dispersion relation for a Drude-Lorentz gold layer with asymmetric cladding ($n_1 = 1, n_3 = 1.45$). The short-dashed lines show the dispersion lines for half-space interfaces of air/gold and air/substrate, respectively. For thin layers (40 nm, 20 nm, 10 nm) two bound modes exist, shifted towards lower (red) and higher (blue) energies. Strong coupling across ultra-thin layers can shift the odd (blue) mode above the light line.

3.3 Measurements

3.3.1 Overview

s-SNOM is well suited to observe SPPs on plasmonic surfaces with high-resolution. This allows imaging of wavefronts as well as of the polarization fields on the individual metaatoms. [32, 128–130] The measurements presented in this chapter were conducted with the s-SNOM setup detailed in Sect. 2.3.3, at a laser wavelength of $\lambda = 850$ nm. For exciting SPPs on the surface, a dielectric nanosphere was placed on the sample and kept within the focal spot of the laser.

In this section, the metasurface design and the excitation scheme is explained. Then the near-field imaging results are presented for the wavefronts and for the unit cell resonance. The subsequent analysis is based on aforementioned theory surrounding the different surface modes that are theorized and measured on the metasurface. It is concluded that merely one out of three predicted modes is observed in the s-SNOM imaging. The influence of both the excitation channel and the imaging technique is discussed to explain the absence of the remaining two modes from the measurement. Finally, the leaky nature of the observed mode is assessed.

3.3.2 Sample design

The metasurface sample consists of a periodic array of elliptical gold metaatoms on a fused silica substrate. The array is composed of subwavelength gold disks with square unit cell dimensions of 200 nm x 200 nm, as sketched in Fig. 3.7a. The nano-disks have an elliptical base with long and short axes of 175 nm and 140 nm, respectively, and a height of 20 nm.

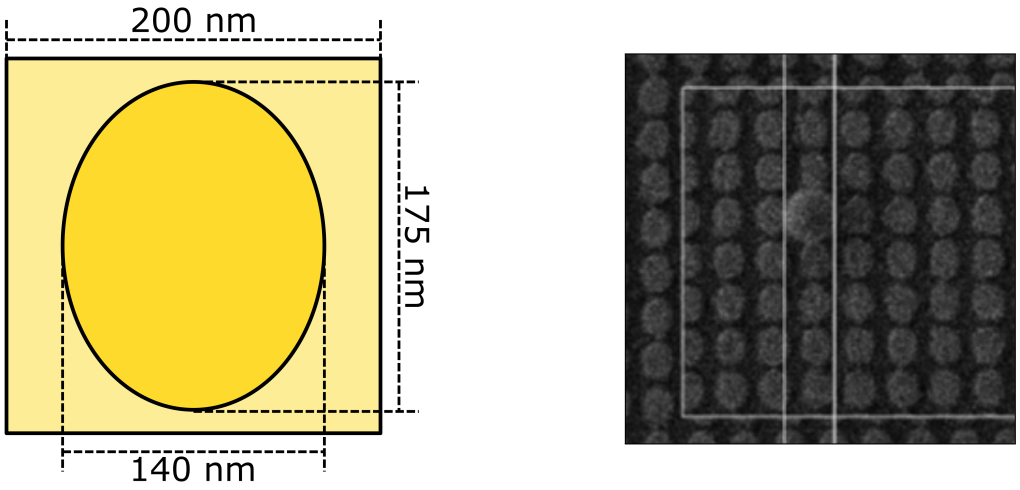

(a) Unit cell design (b) SEM image

Figure 3.7: The metasurface consists of elliptical gold disks of 20 nm thickness in a periodic array on fused silica substrate. (a) The disk and unit cell dimension. (b) SEM image of the metasurface and the Silicon nanosphere used for SPP excitation. Both reprinted with permission from ACS Photonics, **5**, 4238-4243, Ref.[Wal6], Copyright 2018 American Chemical Society.

The sample was fabricated using electron beam lithography[3]. The substrate made of fused silica has a refractive index of $n = 1.45$. The effective permittivity for the gold metasurface is expected to lie below that of a homogeneous gold film, with $\epsilon_{\text{eff}} = -16.5+1.1i$ for gold permittivity of $\epsilon_{\text{Au}} = -28.3 + 1.7i$ at $\lambda = 850\,\text{nm}$ [112], according to Eq. 3.8b.

One can estimate the skin depth or penetration depth L_z (into medium i or into gold) for a single-interface SPPs from Eqs. 3.14 and 3.17 via

$$\frac{1}{L_z} = |\text{Im}(k_z)| = k_0 \text{Im}\left(\frac{\epsilon_{i,2}}{\sqrt{\epsilon_i + \epsilon_2}}\right) \tag{3.19}$$

yielding $L_z = 24.5\,\text{nm}$ under the assumption of a homogenous half-space with the effective permittivity and wavelength as given above. The metasurface thickness of 20 nm lies below the penetration depth. The structure must thus be treated as a multilayer system and modes at the interfaces cannot be treated independently. Furthermore, the different dielectrics air and fused silica around the metallic layer creates an asymmetric IMI environment.

3.3.3 Excitation via nanosphere

Surface modes that are confined to an interface cannot radiate into the space above and below. The reverse is also true: free-space radiation cannot directly couple energy into confined surface modes. This is due to unfulfilled momentum conservation considering the projection of the wavevectors onto the surface for the incoming light and surface wave, respectively, as introduced in Sect. 3.2.3.

The mismatch in momentum or phase of free-space and surface waves has to be bridged by means of an excitation or coupling scheme [111, p. 39ff.]. There are several techniques that facilitate coupling through the use of gratings or prisms (ATR). These techniques can be tuned to efficiently match the momentum difference through appropriate choice of

[3]at the Department of Photonics Engineering, Technical University of Denmark

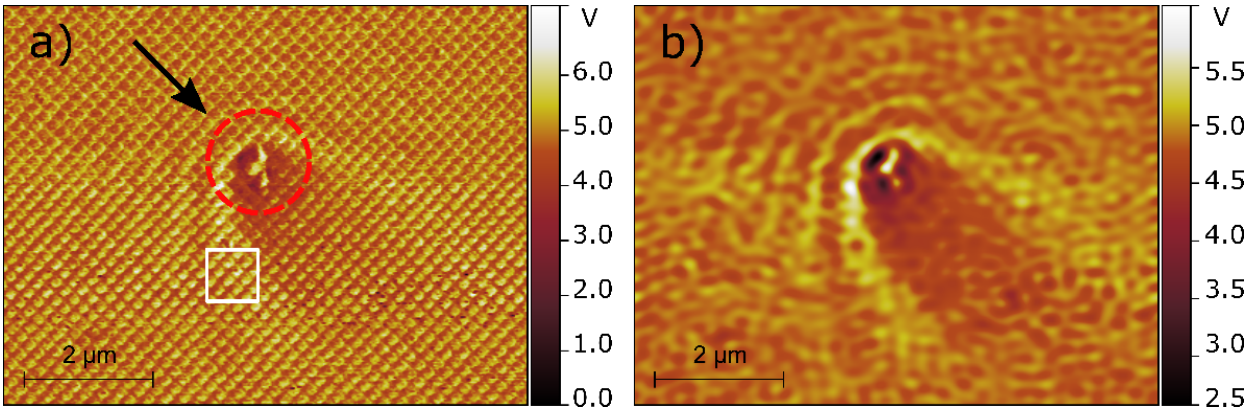

Figure 3.8: s-SNOM 3Ω near-field map of surface waves excited by the silicon nanosphere on the metasurface. (a) The silicon nanosphere is marked by a red circle. The black arrow shows the direction of incident light. The white square is depicted in Fig. 3.9. (b) Fourier-filtering is applied to highlight the interference pattern between SPP and incoming light. Reprinted with permission from ACS Photonics, **5**, 4238-4243, Ref.[Wal6], Copyright 2018 American Chemical Society.

wavelength and angle. Other techniques do not rely on resonant matching conditions, but rather broaden the narrow k-vector of the incoming radiation, such as a highly-focused laser beam [131] or end-fire coupling [123]. Furthermore, an overlap between the k-vectors can also be achieved by using surface defects (grooves or edges) [132], resonant particles or a probing tip. Surface defects break the symmetry of the plane and light that is diffracted leads to the creation of increased (evanescent) wavevector components.

For the experiment presented here, a high-index dielectric nanosphere was fabricated[4] to facilitate coupling into surface modes. Sinev et al. [133, 134] demonstrated that dielectric nanoparticles can provide superior coupling efficiency compared to metallic defects, due to their strong electric *and* magnetic dipole resonances. A Silicon nanosphere with a diameter of 210 nm is used to provide the condition for excitation of surface waves. It can be seen in the SEM image in Fig. 3.7b. The choice of sphere diameter leads to a resonance close to the wavelength of $\lambda = 850$ nm [134]. The Silicon sphere was fabricated by laser printing of amorphous silicon films [135]. Electrostatic pick-and-place nano-manipulation supervised by electron-beam microscopy was used to position the sphere on top of the unit cell [136].

3.3.4 Near-field images of metasurface

The sample was illuminated at $\lambda = 850$ nm, with a power of P ≈ 10 mW and TM-polarization. The scattered signal was detected using pseudo-heterodyne detection with a modulation of the reference mirror at M = 800 Hz and demodulated at the third harmonic 3Ω. The near-field signal imaged on the metasurface is shown in Fig. 3.8a.

The position of the silicon nanosphere is marked by a red circle. A black arrow indicates the incident angle of the laser at polar angle $\Phi = 0°$ relative to the long axis of the gold elliptic discs. The azimuthal angle of the laser beam is $\theta = 70°$ relative to the substrate normal. The feature marked by the white square is further analysed in Fig. 3.9. The periodic features in Fig. 3.8a are a combination by the surface wave pattern and a topography-induced periodic signature of the gold disks. Therefore, a Fourier filter is applied to remove the spatial frequency at the unit cell period of 200 nm. The processed image is shown in

[4]at the Department of Nanophotonics and Metamaterials, ITMO University, Russia

Fig. 3.8b, where the standing wave pattern stemming from the interference of radially propagating surface plasmon polaritons (originating at the nanosphere) and the projection of the exciting light is emphasized [Wal6].

Incidentally, it may appear counter-intuitive to describe the surface plasmon polaritons depicted in Fig. 3.8b as radially propagating. Indeed, this observation demands further analysis as the interference conceals the concentric pattern. Sect. 3.4.2 covers the Fourier analysis performed on the imaging data.

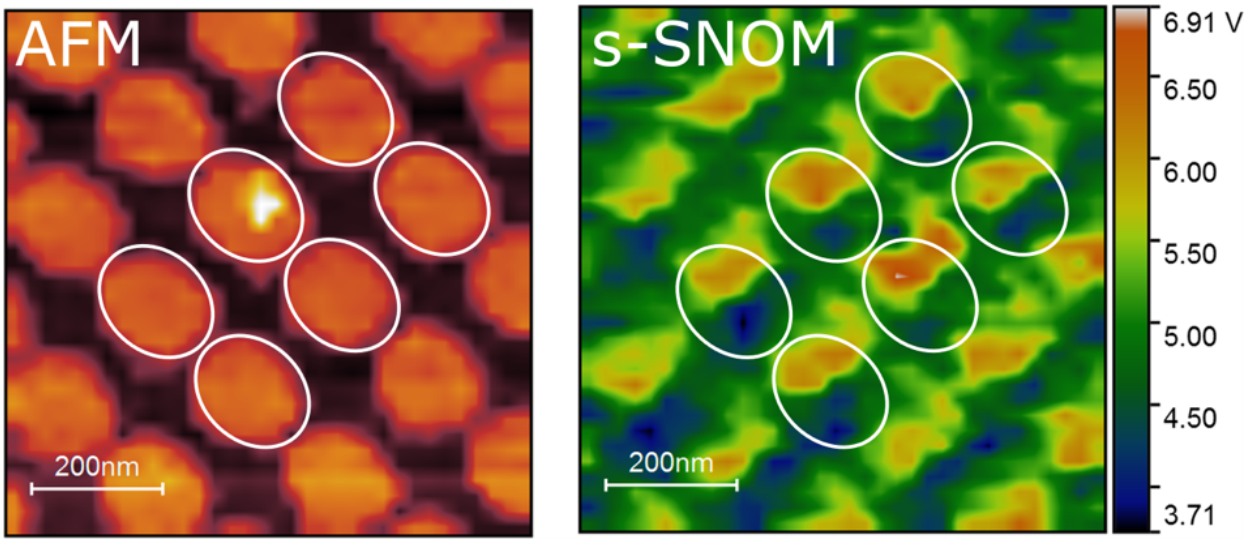

Figure 3.9: AFM image and corresponding s-SNOM map of the area marked in Figure 3a. Individual metaatom dipole modes parallel to the long axis of the gold nanodisks are resolved. Reprinted with permission from ACS Photonics, **5**, 4238-4243, Ref.[Wal6], Copyright 2018 American Chemical Society.

Fig. 3.9 shows the zoomed-in feature marked by a white square in Fig. 3.8a. The AFM topography (left) shows the elliptical gold disks of the sample. White ellipses mark their position, which has been translated into the s-SNOM near-field map (right). Comparing the near-field map with the location of the disks helps in finding the correspondence to the mode excitation within each unit cells. In this case, the near-field distribution resembles a dipole excitation of the structure, which is polarized along the long axis of the disk. The propagating SPP is made up of these individual excitations. Their relative phase lag defines the wavefront and wavevector of the SPP mode. This interpretation is corroborated by simulations depicted in Sect. 3.4.3.

3.4 Analysis

3.4.1 Simulation of dispersion relation

It was shown in Sects. 3.2.3 and 3.2.4 that the dispersion relation for single interfaces and specific multilayer systems can be solved analytically. Generally, homogeneous multilayer systems with coupled interface modes can be solved numerically. For inhomogeneous materials such as metasurfaces, a simple resort is to apply effective medium approximations, as introduced in Sect. 3.2.2. However, it has been noted that this approach suffers in the vicinity of spectral resonances. A more exact approach is to use Finite Difference Time Domain (FDTD) modelling to analyse the dispersion of surface waves. This approach is chosen

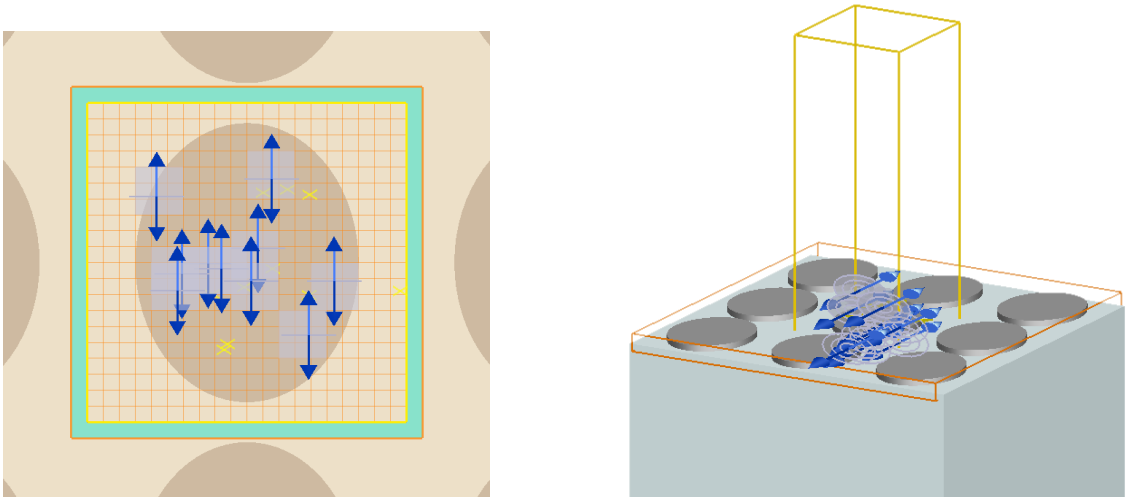

(a) XY view (b) Perspective view

Figure 3.10: Layout of the elliptical disc in the simulation volume (yellow box) as viewed in the Lumerical FDTD software. (a) Top view. (b) Perspective view. Excitation dipoles are marked as blue arrows, here oriented for propagation along the long axis. Time-domain monitors are marked as yellow crosses.

in the following. The dispersion diagrams for the metasurface sample were calculated using the nanophotonic FDTD simulation software Lumerical FDTD.

The simulation is defined as a single unit cell with periodic Bloch boundary conditions, as depicted in Fig. 3.10. The vertical boundary condition (z) is a perfectly matched layer (PML) with distance to the surface large enough to contain the evanescent tails. Specifically, 2 µm and 1 µm above and below the metasurface are defined, respectively. The simulation area is marked as a green square and a yellow box in Figs. 3.10a and 3.10b, respectively.

To excite the structure, ten oriented electric field dipole sources (blue arrows) are placed at randomized locations in the unit cell. They are used to each excite a short pulses with pulselength T = 3.6 fs and a broad frequency spectrum between 200 - 550 THz (about 545 - 1500 nm). The excited pulse passes through the space domain. At the lateral boundaries (x,y) periodic Bloch boundary conditions are employed. These are defined, with a_x being the length of the unit cell, as

$$\vec{E}_{x_{min}} = e^{-ia_x\vec{k}_{\text{bloch}}}\vec{E}_{x_{max}} \tag{3.20a}$$

$$\vec{E}_{x_{max}} = e^{-ia_x\vec{k}_{\text{bloch}}}\vec{E}_{x_{min}} \tag{3.20b}$$

Bloch boundary conditions are similar to periodic boundary conditions, albeit with a non-zero phase shift between opposite boundaries. A single simulation is performed with a broadband pulse for a fixed Bloch phase shift. The critical question that is answered is whether the imposed phase shift will create constructive or destructive interference with the mode excited in the unit cell. By repeating the simulation with increasing values of $\vec{k}_{\text{bloch}}$, different k-vectors are probed for the structure.

Ten monitor points (yellow crosses) are placed at randomized locations at a defined height. The electric field propagating through the simulation volume due to the excitation pulse is recorded by these monitors over an integration time of 150 fs. For each recorded time trace, the resulting signal trace is windowed, effectively blocking out the excitation pulse, and then Fourier-transformed. Since the boundary condition imposes fixed phase shifts, most waves add up destructively. Only waves that match the system's E-k dispersion add

up constructively. These modes make up the eigenmodes of the structure and are observable as a peak in the Fourier spectrum. By iterating this procedure over all boundary vectors $\vec{k}_{\mathrm{bloch}}$, the frequency spectra form a bright contrast in the final plot of E vs. k.

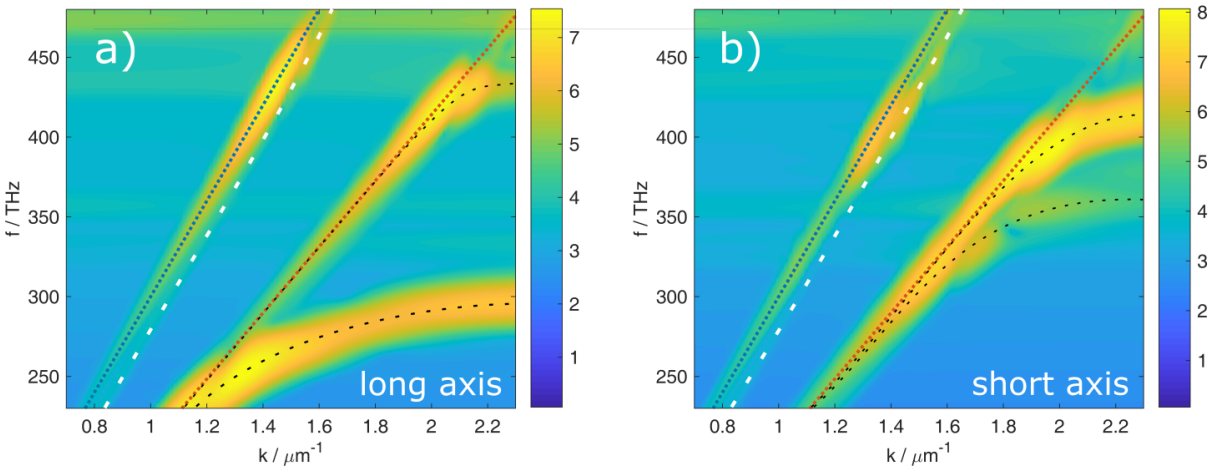

Figure 3.11: Dispersion diagrams for anisotropic metasurface modelled using Lumerical FDTD (a) along the long axis of the metastructure and (b) along the short axis of the metastructure. Reprinted with permission from ACS Photonics, **5**, 4238-4243, Ref.[Wal6], Copyright 2018 American Chemical Society.

Fig. 3.11 shows the resulting dispersion relation for two orientations of the metasurface along long and short axis of the elliptical disks, respectively. Several lines have been added as guides for the eye to help with the interpretation of the graph. Light lines in the dielectrics (air and fused silica), have been marked as blue and red dotted straight lines. Three surface modes are marked with black and white lines.

Both black dotted lines identify surface modes, which bend to the right away from the light line with increasing frequency. A larger wavevector is related to a shrinking wavelength and can be understood as increasing confinement to the surface. Comparison of the two orientations reveals a strong anisotropic behaviour. Moreover, upper and lower branch can be assigned to TM- and Transversal Electric (TE)-polarized SPPs, respectively, as detailed in [26]. It is noted that the prediction of a TE-polarized SPP would be forbidden under the assumption of a homogenized layer. It is bound to the existence of metaatoms. With regards to the theory presented in Sect. 3.2.4, the TM-polarized SPP behaves analogous to the red-shifted mode expected in a multilayer system.

The white dotted line marks another surface mode which is located just underneath the air light line. This indicates that the mode is confined to the upper interface towards air rather than towards the surface. Its small wavevector suggests weak confinement and large evanescent tails. It is important to note that the dispersion line lies inside the cone defined by both light lines. This means that phase-matching to the high-index dielectric is in fact possible. Since the metallic layer is very thin, the mode is expected to radiate into the substrate. A further observation is that the dispersion of this mode displays negligible anisotropy as seen from the comparison of both graphs.

3.4.2 Fourier analysis of near-field map

For further analysis, the real-space data shown in Fig. 3.8b is Fourier-transformed which allows to distinguish between the different components making up the standing wave wattern. In fact, assessing the radial (a)symmetry of the wave pattern can give insight on the

isotropic behaviour of the leaky mode dispersion (white dotted line in Fig. 3.11) mentioned in Sect. 3.4.1. The Fourier space image is shown in Fig. 3.12a in the interval $\pm 3\,\mu m^{-1}$. The resulting pattern is necessarily point-symmetric and consists of two overlapping rings that are offset from the centre in the direction of the incident laser light (black arrow in Fig. 3.8a). The image can be understood by considering it as the sum of two interfering wavevector contributions. Firstly, there is the angle-independent projection of the incident light onto the surface and, secondly, there is the radially propagating surface plasmon polaritons, visible as a circle in Fourier space.

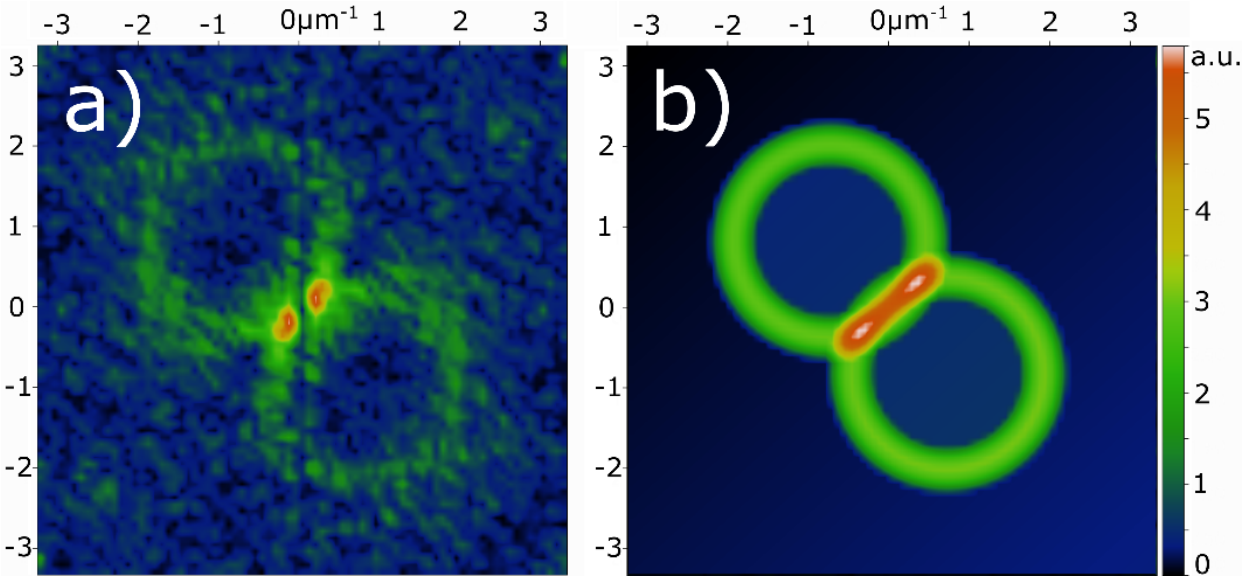

Figure 3.12: (a) 2D Fourier-transform of the near-field measurement in Fig. 3.8b. Interference fringes are visible as a double ring pattern. The radius of the rings corresponds to the wavevector of the surface wave. (b) Fit of two rings on the data in (a) with an offset from the center $k_{off} = 1.09\,\mu m^{-1}$ and radius of $k_{SPP} = 1.20\,\mu m^{-1}$. Reprinted with permission from ACS Photonics, **5**, 4238-4243, Ref.[Wal6], Copyright 2018 American Chemical Society.

To clarify the interpretation, Fig. 3.12b shows a fit of two rings onto the data. The offset from the center k_{offset} can be compared to the expected projection $k_{\text{projection}}$ of the incident wavevector, for an incident azimuthal angle of $\theta = 70°$ relative to the surface normal

$$k_{\text{offset}} = 1.09\,\mu m^{-1} \tag{3.21a}$$

$$k_{\text{projection}} = k_0 \sin(\theta) = 1.10\,\mu m^{-1} \tag{3.21b}$$

The two values show excellent agreement.

Furthermore, the fitted rings have radii of $k_{\text{SPP}} = 1.20\,\mu m^{-1}$, which corresponds to a SPP wavelength of $\lambda_{\text{SPP}} = \frac{2\pi}{k_{\text{SPP}}} = 832\,\text{nm}$. with the excitation wavelength $\lambda_0 = 850\,\text{nm}$, the ratio $\frac{\lambda_{\text{SPP}}}{\lambda_0} = 0.98$ is very close to unity. The weak confinement of the observed wavelength correlates with a weak vertical confinement to the metasurface. Consequently, one would expect a weak coupling between surface and polariton wave. This explains the negligible effect of the anisotropy of the metasurface on the dispersion of this mode.

3.4.3 Dipole resonances of unit cell

Analysing the trends and location of modes in the simulated dispersion relation already yielded several interesting results. However, many interpretations are rather indirect and

it would be advantageous to visualize the modes further. Experimentally this has been attempted by imaging the unit cell with high resolution, as shown in Fig. 3.9.

Here, the software Lumerical FTDT has been used to simulate the unit cell resonance for defined Energy and Bloch-vector. Specifically, Bloch boundary conditions with $k_{\mathrm{bloch,x}} = 0$ and $k_{\mathrm{bloch,y}} = k_{\mathrm{SPP}} = 1.20\,\mu\mathrm{m}^{-1}$ are imposed at an Energy of E = 1.46 eV (correspongding to the excitation at $\lambda = 850\,\mathrm{nm}$) to find the unit cell excitation supporting the leaky mode for a propagation along the long axis of the elliptical disk.

For this simulation, a single electric dipole source is placed in the center of the unit cell. The pulsed excitation and subsequent propagation is analogous to Sect. 3.4.1. A 3D field monitor records the field evolution with time. Then, an apodization window is applied, which excludes effects at the start of the simulation from the Fourier transform of the monitor data. The one-sided apodization window is centered at 250 fs with a width of 50 fs, such that no influence of the excitation is expected and only eigenmodes of the structure are expected to survive.

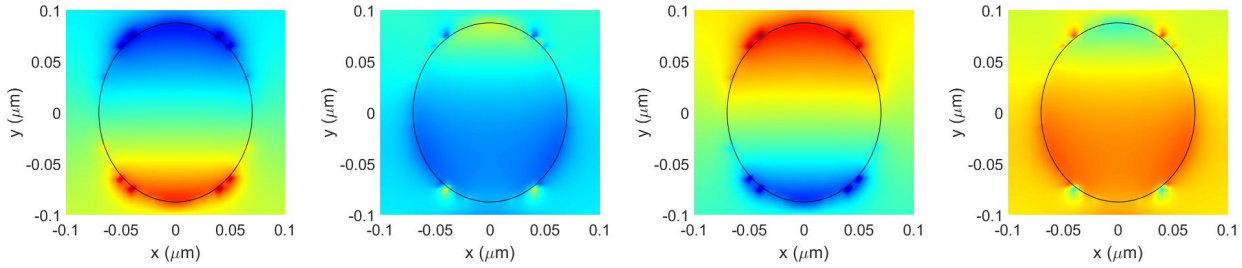

(a) $\phi = 0\pi$ (b) $\phi = \frac{1}{2}\pi$ (c) $\phi = \pi$ (d) $\phi = \frac{3}{2}\pi$

Figure 3.13: Simulated electric field E_z(x,y) at z=10 nm above the metasurface for four different phases. The simulation was performed for E = 1.46 eV ($\lambda = 850\,\mathrm{nm}$) and k = $1.20\,\mu\mathrm{m}^{-1}$.

Fig. 3.13 shows the simulated field E_z of the leaky mode for different phases. The propagation of dipole mode along the long axis of the disk is apparent. As the E_z field component is dominant in an s-SNOM measurement with p-polarized illumination, one should expect a comparable observation in the unit cell's near-field signature shown in Fig. 3.9. The measurement of the individual metaatom shows satisfactory qualitative agreement with Fig. 3.13c.

Changing the perspective, Fig. 3.14 shows cut plane (y,z) through the centre (x=0) of the metasurface along its long axis, i.e. is along the direction of propagation (y). Depicted are the field components E_z (a-d) and E_y (e-h) for different phase evolutions. One can observe that E_z is antisymmetric, while E_y is symmetric. This is the typical signature of the odd (symmetric) mode, as introduced in Sect. 3.2.3. It becomes less bound to the interface with decreasing layer thickness, while its wavevector decreases, as its field distribution is displaced out of the metallic layer. This observation confirms the assumed behaviour that was inferred from the analysis of the dispersion relation.

3.4.4 3D full-wave analysis

From the dispersion relation produced with the Lumerical FDTD simulation, the observed SPP is expected to be a leaky mode due to its location above the substrate light line. In order to further characterize the mode behaviour, and confirm its radiative nature full-wave simulations are performed using CST Microwave Studio.

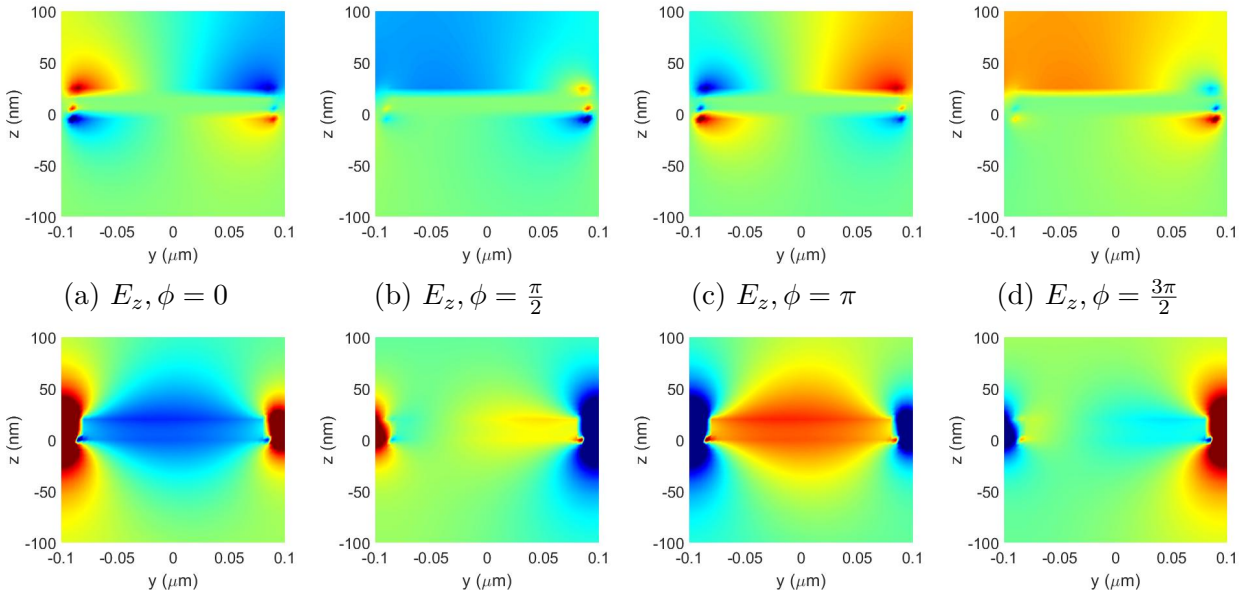

(a) $E_z, \phi = 0$ (b) $E_z, \phi = \frac{\pi}{2}$ (c) $E_z, \phi = \pi$ (d) $E_z, \phi = \frac{3\pi}{2}$

(e) $E_y, \phi = 0$ (f) $E_y, \phi = \frac{\pi}{2}$ (g) $E_y, \phi = \pi$ (h) $E_y, \phi = \frac{3\pi}{2}$

Figure 3.14: Simulated electric field E_z(y,z) (top row) and E_y(y,z) (bottom row), showing a cut through the center of the unit cell ($x = 0$) along the propagation direction. The simulation was performed for E = 1.46 eV ($\lambda = 850\,\text{nm}$) and k = $1.20\,\mu\text{m}^{-1}$.

The full metasurface is modelled for a sample size of $5.8 \times 5.8\,\mu\text{m}^2$ with open boundaries along all three dimensions. The excitation of the surface wave is modelled with a vertical 5 nm long discrete electric dipole (current amplitude of 1 A) located just 20 nm above the metasurface. This almost point-like source represents the nanosphere excitation. However, as the electric dipole does not model the magnetic excitation of the sphere, the TE-polarized surface waves that are expected to couple strongly to the magnetic resonance, will not be excited directly. In this particular case, this is advantageous as it helps to reveal the TM-polarized guided-mode resonance.

Fig. 3.15a shows the E_z electric field for a SPP which is excited at the left edge and propagates to the right. Again, the propagation direction is depicted along the long axis of the metasurface. Two wavelengths can be distinguished from the simulation. At the upper metasurface-air interface, the SPP is only weakly confined and extends quite far out into air. At the lower metasurface-substrate interface, a more strongly confined and short-wavelength SPP is observed.

Fig. 3.15b shows the lateral magnetic field H_y. The homogeneous permeability of the sample allows a clearer comparison of the modes in the dielectrics. Moreover, the figure highlights the leakage radiation which is marked by two black arrows. This radiation is associated with the leaky mode at the upper interface. To calculate the expected radiation angle, one can apply Snell's law, Eq. 3.18, with $\beta = 1.2\,\mu\text{m}^{-1}$. The radiation angle into the substrate yields $\phi = 46°$, which fits well to the simulation results.

A more detailed analysis is facilitated by a plot of horizontal lineouts of the electric field component E_z, shown in Fig. 3.15c. Three positions above the substrate are shown: 20 nm, 30 nm and 40 nm. One can find signatures of the two TM-polarized modes in the interference pattern: a stronger contribution from the upper SPP and a weaker contribution from the leaky SPP. A superposition of two damped radial sine waves is fitted to the lineouts (dotted lines), resulting in wavelengths of $\lambda_1 = (838 \pm 0.4)\,\text{nm}$ and $\lambda_2 = (553 \pm 0.3)\,\text{nm}$. The wavelength λ_1 and the experimental data $\lambda = 832\,\text{nm}$ show good correspondence. The

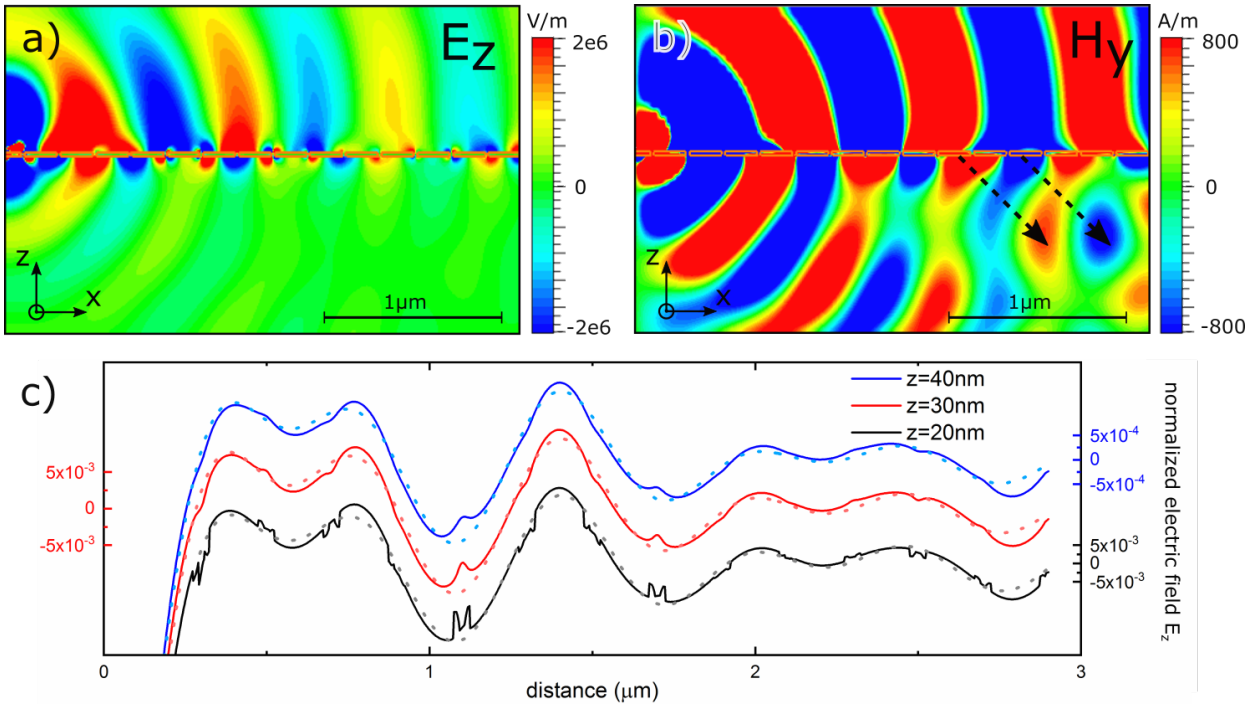

Figure 3.15: (a) E_z field distribution obtained through full-wave simulation of vertical electric dipole above the metasurface consisting of elliptical gold disks shown along the long axis of the metaatoms. Two surface waves are identified at either interface of the metasurface. (b) H_y field distribution reveals the leaky nature of the top interface SPP which is visible as a wave radiating into the substrate marked with black arrows. (c) Lineouts taken from Figure (a) for different heights z above the surface can be fitted with the superposition of two waves that correspond to the surface waves on both interfaces. Reprinted with permission from ACS Photonics, **5**, 4238-4243, Ref.[Wal6], Copyright 2018 American Chemical Society.

decay constants for the fits are summarized in Table 3.1. The much stronger damping of the first mode (λ_1) is a result of its leakage into the substrate.

height z	$A_1(10^{-3})$	α_1 (μm^{-1})	$A_2(10^{-3})$	α_2 (μm^{-1})
40 nm	2.3	0.65	1.4	0.42
30 nm	15.2	0.66	9.7	0.39
20 nm	24.6	0.52	15.3	0.27

Table 3.1: Amplitude and decay fitting parameters from superposition of two damped radial sine waves, shown as dotted lines in Fig. 3.15c.

3.5 Conclusion

This chapter presented near-field measurements of SPPs on an anisotropic metasurface that were excited by means of a silicon nanosphere. Three modes were predicted as eigenmodes of the surface from FDTD simulations. Two of which are expected to show strongly anisotropic dispersion, while the third behaves approximately isotropic and displays leakage into the substrate.

Only the leaky mode (also dubbed guided-mode resonance) was observed in the s-SNOM measurement and could be assigned to the predicted eigenmode. The radiative losses into the substrate were analysed through full-wave simulations, as they are inaccessible by surface scanning. The negligible anisotropic dispersion was explained by the weak confinement to the metallic layer, effectively neglecting the surface structure influence.

The two other anisotropic modes are absent from the near-field measurement. Two reasons are identified for this:

1. The strongly confined modes are localized at the lower metasurface-fused silica interface, with fields penetrating into the metallic layer. This makes it more difficult to access them through s-SNOM measurements of the top surface. Meanwhile, the guided-mode resonance carries most of its energy above the surface, yielding a dominating s-SNOM signal. The signal could potentially overshadow remaining field components of the unobserved modes.

2. The excitation efficiency of the dielectric nanosphere depends on the wavevector matching between the sphere's near-field and the SPPs. The anisotropic modes have much larger wavevectors than the guided-mode resonance and the exciting light. Consequently, the momentum matching between non-resonant coupling channel and SPP is less efficient. It can thus be hypothesized whether the anisotropic modes have been sufficiently excited.

In conclusion, the use of s-SNOM facilitated direct observation of the guided mode resonance. A dielectric nanosphere was well-suited for radial excitation of this mode. However, it was shown that the observation of anisotropic strongly confined modes was not possible under the presented measurement and excitation combination. Whether the dominant challenge is the mode localization underneath the metasurface or the inefficient excitation channel has been discussed.

These findings motivate an adapted experimental approach for future research. Brissinger et al. succeeded in measuring subsurface SPPs through a 55 nm homogenous gold film by s-SNOM using ATR and edge excitation [137]. This approach offers a dual advantage,

as light impinging through ATR already carries an increasing momentum. Moreover, the necessary tuning of the coupling angle to within 2° highlights how a precise matching to the resonance may have to be facilitated. Translated to the silicon sphere excitation, this could be done by preparing differently sized spheres or by wavelength-tuning of the laser source. Another interesting idea is to make use of substrate-enhanced near-field imaging [77]. Based on a multi-reflection model, coincidentally introduced in Sect. 4.2.3, it was shown that the scattered s-SNOM signal from thin layers can be strongly enhanced by choosing am appropriate substrate thickness or refractive index. A more far-fetched idea to visualize buried SPP modes, borrowed from photoemission electron microscopy (PEEM), would be to prepare the interface with "SPP sensitizers", e.g. nanoparticles that exhibit localized surface plasmon resonances [138] or TMDC nanocrystals that induce additional interference patterns on the surface [139].

Finally, it is noted that choosing a longer wavelength is not expected to improve the depth resolution. This may be counter-intuitive due to the different skin depth, but becomes evident from the wavelength-independent lateral resolution predicted by the quasi-static point-dipole model, see Sect. 2.3.1, which equally applies to the vertical dimension. Moreover, subsurface terahertz s-SNOM imaging repeatedly reports depth resolutions not exceeding 50 nm [140–142].

Chapter 4

Photoluminescence enhancement from WS_2

4.1 Introduction

This chapter picks up the idea of light-matter interaction on two-dimensional material systems in the context of TMDC materials, a semiconducting class of van-der-Waals materials which is often compared to graphene with regard to its application potential. Atomically thin TMDCs monolayers have become known for a variety of interesting properties, such as a direct band gap, large exciton binding energy, strong spin-orbit coupling and strong spin valley polarization [143].

This chapter focusses on the photoluminescent nature of one of their representatives: WS_2. In its single layer form, WS_2 has been found to exhibit the strongest light-matter interaction out of the common TMDC candidates: MoS_2, $MoSe_2$, WS_2, WSe_2; all of which show prominent exciton resonances in the visible spectrum [144].

The goal of this research is to enhance the photoluminescence yield which can be obtained from the single layer WS_2. Several ideas have been reported for coupling TMDC layers to achieve this, which can be loosely classified into three different approaches [145]

1. localized surface plasmon resonances, such as plasmonic particles [146], a resonant dielectric Silicon nanosphere [147], metal backed dielectric nanopillars [148], periodic gold nanoantennas [149], or plasmonic metasurfaces [150]

2. photonic structures, such as placing the monolayer onto an integrated photonic crystal cavity [151, 152]

3. modification of the dielectric surroundings in a way that exploits constructive interference effects, such as optimizing the underlying substrate thickness and composition [153, 154]

A central theme is to enhance the light-matter interaction between the active TMDC material and the exciting light. The sample presented here was prepared with the second and third approach in mind, as two types of external microcavities have been integrated into the substrate. To be precise, a single circular Bragg cavity was used, but lateral and vertical interference effects were treated separately to find the desired values for etching of the lateral geometry and vertical depth, respectively.

In order to find the appropriate parameters for substrate material, structure and dimensions, two modelling approaches are discussed in the literature [145]: a multiple reflection model [154] and (transfer) matrix-based analytical models [155]. Both of these approaches

have been applied, one for each of the two cavity orientations, to optimize the structure design.

The structure is designed to enhance both the in-coupling of light at $\lambda_0 = 532\,\text{nm}$ (the laser source) and the out-coupling of light at $\lambda_{\text{PL}} = 615\,\text{nm}$, corresponding to the A exciton resonance at $E = 2.0\,\text{eV}$ [144]. The resonant interaction of the microcavity with the incoming light and with the excitation of the WS_2 monolayer enhances the photoluminescence observed. On one hand, this is due to the expected field enhancement of the incoming light at the centre of the cavity and vertical multi-pass interference which consequently creates an increased absorption cross-section of the atomically thin monolayer. On the other hand, resonant coupling of the microcavity and the exciton resonance can in principle increase the photoluminescence photon yield, tune the spatial emission pattern [156, 157], and modify the spontaneous emission rate.

The sample studied here is a GaP substrate-integrated microcavity covered with few-layer hBN-buffered monolayer WS_2. A reference structure without lateral Bragg-structure, but with vertical circular trench of the same depth, is also covered in the same way. The sample is measured at room temperature using microreflection contrast measurements, microphotoluminescence measurements and s-SNOM.

Sample patterning was done by focused-ion beam milling by a project partner[1]. The design and microscopic optical measurements were performed by another partner[2]. The study was complemented by s-SNOM measurements and data analysis performed by the author of this thesis. The high-resolution data and nano-imaging of the surface electric fields on the microcavity complement the previous measurements and allow an analysis of the structure that would not be accessible with low-resolution microscopy.

This chapter focusses on the near-field optical measurements. The discussion of design and microscopic measurements is restricted to only provide necessary context. For more details on this part of the project, the reader is referred to the joint publication "Near-Field Nano-Imaging of Buried Microcavity for Enhancement of WS2 Monolayer Exciton Photoluminescence" by Mey et al. [Wal13], or the thesis by Schneider [158]. Particularly, the microcavity presented in Sect. 4.2.3 has been designed by F. Wall[2]. The s-SNOM based analysis was presented by the author of this thesis at META 2019 - *Intl. Conf. on Metamaterials, Photonic Crystals and Plasmonics* [Wal13].

4.2 Theory

4.2.1 Transition metal dichalcogenides

TMDC materials are semiconducting crystals which consist of stacked two-dimensional atomic layers which form a bulk to neighbouring layers by van-der-Waals adhesion force. While this makes them similar to graphene, with which heterostacks can be easily formed, TMDCs are neither mono-atomic nor truly flat. They have the chemical composition MX_2, with transition metal M, defined via their partially filled d electron sub-shell, and two chalcogen atoms X, i.e. group 16 of the periodic table. Geometrically, one monolayer consists of three hexagonal atomic planes. The transition metal atom is in the centre and bound to chalcogen atoms in the planes above and below in a zig zag fashion [159]. TMDC materials are receiving a lot of attention due to their intriguing optical and electrical properties, partly caused by their interesting structure.

[1] State Key Laboratory of Modern Optical Instrumentation, Zhejiang University, China
[2] Dept. of Physics and Materials Sciences Center, Philipps-Universität Marburg

Most importantly, the low dimensionality reduces Coulomb screening in these systems and effects that rely on Coulomb force are significantly enhanced. Excitons, i.e. quasiparticles of electron-hole pairs bound by Coulomb interaction, most prominently play a crucial role in optoelectronic properties of TMDCs [160]. For single layers, the indirect bulk band gap transitions into a direct band gap at visible frequencies which leads to strong exciton-binding energies, narrow absorption peaks and high photoluminescence quantum yield at room temperature [161]. For WS_2, an exciton binding energy of 0.71 eV [160] and a record quantum yield among the TMDC candidates of 6% at cryogenic temperatures has been reported [162].

Additionally, monolayer TMDCs have strong intrinsic spin-orbit coupling due to their characteristic d-orbital sub-shells, effectively introducing strong energy-splitting in the valence (and in the conduction) band. Moreover, the two chalcogen planes above and below the transition metal create two degenerate valleys, K and K', in Brillouin space due to broken inversion symmetry, which introduce a valley spin degree of freedom. This means that different energy states can be optically selected by spin, i.e. circularly polarized light, opening an avenue for spintronic and valleytronic applications. [163]

4.2.2 Sample fabrication

The substrate-integrated microcavity and reference have a lateral depth of 70 nm and 105 nm, respectively. The lateral Bragg cavity consists of six rings of nominal widths of $d_{\mathrm{GaP}} = 135\,\mathrm{nm}$ followed by air spacing of $d_{\mathrm{air}} = 110\,\mathrm{nm}$ and a central circle of radius d_{air}. The theoretical radius of both the microcavity and the reference hole consequently is r = 1.58 µm. An AFM image of the Bragg cavity can be seen in Fig. 4.7. The fabrication was performed in GaP substrate using Gallium Focussed Ion Beam (FIB) milling (Auriga Dual Beam SEM-FIB, Zeiss), with an ion beam of 30 kV and 500 pA.

On top of the microstructures, large hBN flakes and mechanically exfoliated WS_2 monolayers were transferred in sequential steps by dry-stamping with a gel film [Wal13, Supp. Info.]. During preparation of the sample, it was shown that a hBN buffer was necessary to avoid photoluminescence quenching due to direct contact with the GaP substrate. Subsequent AFM measurements evaluated the buffer thickness to be 13 nm and 20 nm for microcavity and reference structure, respectively.

Fig. 4.1 shows an optical microscopy image of the sample. Six positions of microcavities or references are highlighted by coloured circles, which are referred to in Table 4.1. The objective cross-hairs with the central circle should not be confused with the sample positions. The hBN flakes are visible across the sample. The large transparent area on the right is due to a large gold sheet obstructing access to the surface by s-SNOM. The square pattern around the yellow cavity is a typical feature which appears due to SEM imaging.

Color	Pattern	Cover	Notes
green	Reference	cover	trapped dust particle
pink	-	-	no information recorded
orange	Reference	-	obstructed by gold particle
purple	Bragg cavity	cover	used for measurements
yellow	Bragg cavity	open	used for measurements
red	Bragg cavity	-	obstructed by gold particle

Table 4.1: Sample overview with color codes depicted in Fig. 4.1. Covered samples have a heterolayer of hBN/WS_2 placed over the structured substrate.

Figure 4.1: Optical microscope impression of the sample gives an overview of the different samples. Circular holes are labelled 'reference' and circular Bragg gratings are labelled 'cavity'. The structures have a diameter of 3.2 µm. The colour codes are summarized in Table 4.1.

4.2.3 Microcavity design

In order to enhance the photoluminescence yield for the monolayer, both the in-coupling of light and photoluminescence out-coupling should be tuned. With this goal in mind, the vertical and lateral structure of the substrate are patterned in a way that creates constructive interference at the two wavelengths $\lambda_0 = 532\,\mathrm{nm}$ and $\lambda_{\mathrm{PL}} = 615\,\mathrm{nm}$.

Both resonators benefit from a high refractive index substrate due to its high amplitude reflectivity r_{ij} according to Fresnel's laws assuming perpendicular incidence

$$r_{ij} = \frac{n_i - n_j}{n_i + n_j} \qquad t_{ij} = \frac{2n_i}{n_i + n_j} \tag{4.1}$$

GaP has been chosen as a substrate due to its high refractive index ($n_{532\,\mathrm{nm}} = 3.474 + 0.002i, n_{615\,\mathrm{nm}} = 3.334, n_{850\,\mathrm{nm}} = 3.178$) for the corresponding wavelengths [164].

For the design along the vertical and lateral orientation, a multiple reflection model [154] and a (transfer) matrix-based analytical model [155] is used, respectively.

Transfer Matrix Method

For the design of the circular Bragg-cavity, the radial symmetry of the structure is exploited by applying a one-dimensional model transfer matrix method rendering all reflections and transmission perpendicular. Within the transfer matrix method, the electromagnetic wave is modelled by calculating the the transfer (or interface) matrix T_{ij}, using Eqs. 4.1, for the propagation across an interface and the phase (or layer) matrix P_i for the phase $\phi_i = n_i k d_i$

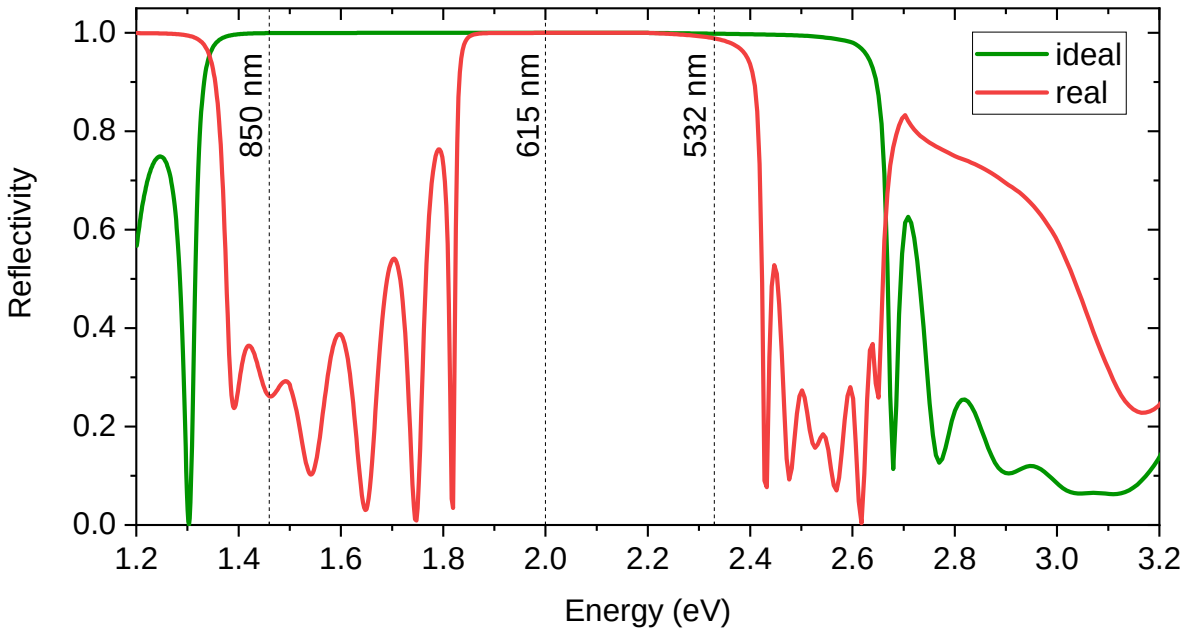

Figure 4.2: Reflectivity of the DBR at different energies shown for the ideal dimensions and the fabricated structure. The real structure is resonant at wavelengths $\lambda_0, \lambda_{\mathrm{PL}}$, and off-resonance at λ_{ref} as indicated with the dashed lines.

associated with propagation through a layer i of width d_i

$$T_{ij} = \frac{1}{t_{ij}} \begin{pmatrix} 1 & r_{ij} \\ r_{ij} & 1 \end{pmatrix} \qquad P_i = \begin{pmatrix} e^{-i\phi_i} & 0 \\ 0 & e^{i\phi_i} \end{pmatrix} \tag{4.2}$$

The electromagnetic field at each position z is expressed in term of its forward and backward travelling waves [161, 165]

$$\vec{E}(z) = \begin{pmatrix} E_i^+(z) \\ E_i^-(z) \end{pmatrix} \tag{4.3}$$

The complete cavity matrix is then modelled my multiplying the transfer and phase matrices alternating air layer by GaP layer

$$S_{\mathrm{cavity}} = P_1 T_{12} P_2 T_{23} \ \ldots \ P_{n-1} T_{(n-1)n} \tag{4.4}$$

$$= \left(P_1 T_{12} P_2 T_{21}\right)^N \cdot P_1 T_{12} \tag{4.5}$$

where $N = 6$ is the number of rings, and the multiplication is simplified using the identical layer and interface matrices (air = 1; GaP = 2).

Finally, the cavity's reflectivity for an emitter in the centre, given by the ratio of the matrix elements s of S_{cavity} [165, Supp. Info.],

$$R_{0n} = \left| \frac{E_0^-}{E_0^+} \right|^2 = \left| \frac{s_{21}}{s_{11}} \right|^2 \tag{4.6}$$

has to be maximized. The resulting ideal air and GaP layer widths for the lateral (in-plane) Distributed Bragg Reflector (DBR) are $d_{\mathrm{air}} = 154\,\mathrm{nm}$ and $d_{\mathrm{GaP}} = 46\,\mathrm{nm}$, respectively. The characteristic relationship of distributed Bragg reflectors $n_{\mathrm{air}} d_{\mathrm{air}} = \frac{\lambda_{\mathrm{PL}}}{4}$ and $n_{\mathrm{GaP}} d_{\mathrm{GaP}} = \frac{\lambda_{\mathrm{PL}}}{4}$ is fulfilled.

However, the structure fabricated by FIB has the alternative parameters for air and GaP layers $d_{\text{air}} = 110\,\text{nm}$ and $d_{\text{GaP}} = 135\,\text{nm}$, as these dimensions were more easily fabricated. Fig. 4.2 shows the reflectivity graph for the ideal (green) and real (red) microcavity, with relevant wavelengths highlighted. Obviously, the alternative parameters define an equally applicable stopband for the wavelengths of in-coupling and out-coupling radiation. Furthermore, using the alternative parameters, a reference wavelength at $\lambda_{\text{ref}} = 850\,\text{nm}$ can be used to test the structure at off-resonance.

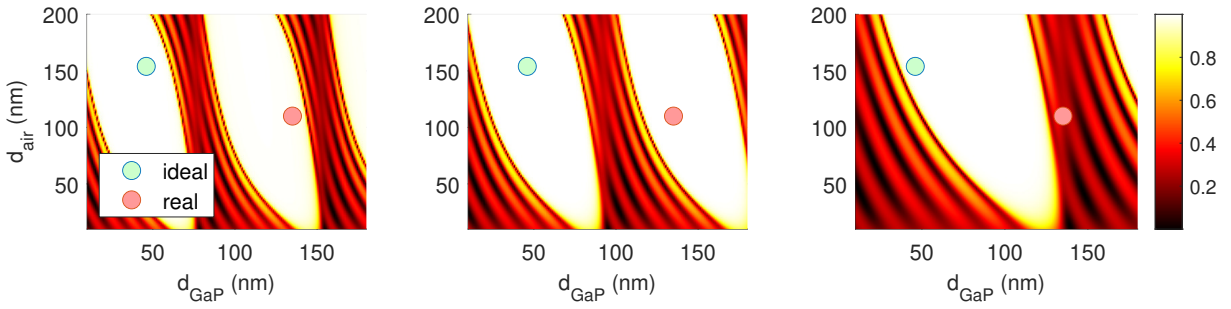

(a) $\lambda_0 = 532\,\text{nm}$ (b) $\lambda_{\text{PL}} = 615\,\text{nm}$ (c) $\lambda_{\text{ref}} = 850\,\text{nm}$

Figure 4.3: Reflectivity maps at different wavelengths for a radial DBR of six GaP rings for different layer thicknesses d_{air} and d_{GaP}. The colorbar shows the reflectivity. The green and red dot show the location of ideal and fabricated microcavity, highlighting the resonance for λ_0, λ_{PL} and off-resonance for λ_{ref} for the real structure.

To account for the tolerance in fabrication, reflectivity maps for swept combinations of layer widths are considered, displayed in Fig. 4.3. The location of ideal and real cavity dimensions are marked by green and red dots for all wavelengths, respectively. The dimensions of the fabricated structure lie safely in the reflectivity maximum for λ_0 and λ_{PL}, wheras the reflectivity is low at λ_{ref} as expected.

Multi-reflection model

For the design of the FIB etching depth, the goal is to maximize the electric field amplitude through constructive interference at the monolayer for λ_0 and λ_{PL}. This is achieved by considering a multi-reflection model for the fabricated structure of three thin layers as depicted in Fig. 4.4. This model is an extension of the reflection by a transparent thin film to a system of multiple layers by Rouard's treatment [166, 167, p. 63ff].

The definitions for Fresnel's laws Eqs. 4.1 and phase $\phi_i = n_i k d_i$ assuming perpendicular incidence are used again. Using the multiple reflection model, one can obtain two enhancement factors for light reaching the monolayer F_{in}, and for light emitted from the monolayer F_{emit}. Both factors contain a dependence on z, the origin of photoluminescence inside the WS_2 monolayer of $d_{WS_2} = 6.18\,\text{Å}$. The derivations are based on adding all electric field reflections and corresponding phase shifts at the different layer interfaces, generating an infinite geometric series which converges into a neat expression. Neighbouring layers are treated by introducing effective reflection coefficients r^*_{ij} and solving recursively from the substrate up to the monolayer. The derivation is omitted here for brevity and the interested reader is referred to the descriptions by Heavens [167, p. 63ff] or Zhang et al. [154, Suppl. Info.].

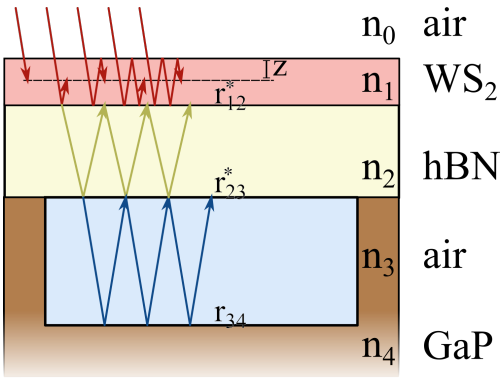

Figure 4.4: Multi-reflection model for optimizing the vertical etching deptch for the multilayer: WS_2 monolayer (6.18 Å), hBN flake (13 − 20 nm), air trench, GaP substrate. The microcavity features are indicated by the vertical GaP pillars.

One obtains the enhancement factors F_{in} for in-coupling

$$F_{\text{in}} = \sum_{n=0}^{\infty} t_{01}(e^{-i\phi_z} + r_{12}^* e^{-i(2\phi_1-\phi_z)})(r_{12}^* r_{10} e^{-2i\phi_1})^n \tag{4.7a}$$

$$= t_{01} e^{-i\phi_z} \frac{1 + r_{12}^* e^{-2i\phi_1}}{1 + r_{12}^* r_{10} e^{-i2\phi_1}} \tag{4.7b}$$

and $F_{\text{emit}} = \frac{t_{10}}{t_{01}} F_{\text{in}}$ for out-coupling. The effective reflection coefficients r_{ij}^* for the hBN and air layer are[3]

$$r_{ij}^* = \frac{r_{ij} + r_{j(j+1)}^* e^{-2i\phi_j}}{1 + r_{ij} r_{j(j+1)}^* e^{-2i\phi_j}} \tag{4.8}$$

Assuming that excitons are homogeneously distributed throughout the WS_2 monolayer, one then integrates over z in the final equation to find the total enhancement factor G given by the product of in-coupling and out-coupling, here normalized to a reference interface [154]

$$G = \frac{1}{N} \int_0^{d_{\text{WS}_2}} |F_{\text{in}}(z) \cdot F_{\text{emit}}(z)|^2 \, dz \tag{4.9}$$

The model was applied to find the optimum etching depth for different hBN flake thicknesses $d_{\text{hBN}_1} = 10$ nm and $d_{\text{hBN}_2} = 30$ nm. Depending on the hBN buffer layer, which is measured only after its final placement on the structure, the theoretical optimum was calculated to lie between $d_{\text{air}} = 104$ nm and $d_{\text{air}} = 54$ nm, respectively. The resulting enhancement factor plots can be found in Fig. SI.3 in [Wal13, Supp. Info.].

The microcavity structure was finally fabricated with an effective trench of $d_{\text{air}} = 70$ nm. The hBN cover thickness was later measured to $d_{\text{hBN}} = 13$ nm. The reference structure without integrated microcavity has an effective trench of $d_{\text{ref,air}} = 105$ nm, and a buffer of $d_{\text{ref,hBN}} = 20$ nm; representative of the expected tolerances due to FIB fabrication and bending of the suspended layers into the structure.

During the preparation of this thesis, the model was applied again to adapt the data to the finally fabricated hBN thickness. Fig. 4.5 shows the wavelength and air layer thickness parameter space for the enhancement factor at two different thicknesses of the hBN layer $d_{\text{hBN}} = 30$ nm and $d_{\text{hBN}} = 13$ nm. The data differs slightly from Fig. SI.3 in [Wal13, Supp. Info.] due to different refractive index data [164, 168, 169]. The optimized air layer

[3]Indices i,j are layer indices; while the imaginary i appears in the exponential term.

thickness at $\lambda_0 = 532\,\text{nm}$ is marked by a green circle and yields $d_{\text{air}} = 89\,\text{nm}$ and $d_{\text{air}} = 61\,\text{nm}$, respectively.

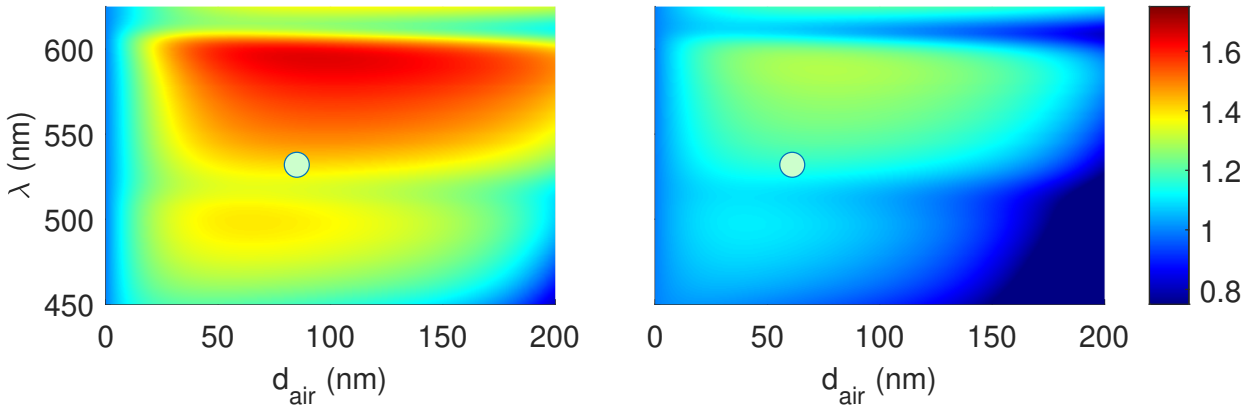

(a) $d_{\text{hBN}} = 13\,\text{nm}$. (b) $d_{\text{hBN}} = 30\,\text{nm}$.

Figure 4.5: Enhancement factor G shown for different wavelengths and air layer thicknesses at two different thicknesses of the hBN layer (a) $d_{\text{hBN}} = 30\,\text{nm}$ and (b) $d_{\text{hBN}} = 13\,\text{nm}$. A green circle marks the optimized thickness at $\lambda_0 = 532\,\text{nm}$ and yields (a) $d_{\text{air}} = 89\,\text{nm}$ and (b) $d_{\text{air}} = 61\,\text{nm}$. Wavelength axis and colorbar apply to both graphs.

4.3 Measurements

The sample was pre-characterized by the project partners using an inverted optical microscope (IX73, Olympus) to excite the sample at $\lambda_0 = 532\,\text{nm}$ and obtain time-integrated photoluminescence images. Fig. 4.6a shows one of these measurements of the circular microcavity covered by 13 nm hBN and monolayer WS_2. The structure displays obvious photoluminescence enhancement and the radial profiles across the structure, see Fig. 4.6b, depict a spatial dependence with a resolution of about 0.4 µm.

Additionally, s-SNOM measurements were performed to optically characterize the structure with a resolution of 20 nm. s-SNOM is sensitive to local surface electric fields as well as beneath the surface in the vicinity of the interface [79, 170]. By scanning the near-field of the hBN/WS_2-covered microcavity, it is thus possible to directly image the excitation of the resonant structure, even through the van-der-Waals stack. A comparison is made between the covered and the open structure at the excitation wavelength of $\lambda_0 = 532\,\text{nm}$ and at the off-resonant reference wavelength of $\lambda_{\text{ref}} = 850\,\text{nm}$.

The experimental setup used for these measurements is outlined in Sect. 2.3.3. However, the detection was performed in non-interferometric mode with reference mirror M blocked. Near-field images at higher harmonics of second and third order, 2Ω and 3Ω, were acquired. AFM images were acquired simultaneously.

Fig. 4.7 shows the measurements for the two samples: hBN/WS_2-covered microcavity (a-c) and open microcavity (d-f). The samples are marked by purple and yellow colour codes from Table 4.1. The three measurements from left to right show the topography measured by AFM, the near-field signal at 3Ω at $\lambda_0 = 532\,\text{nm}$ (green colour scale), and the near-field signal at 3Ω at $\lambda_{\text{ref}} = 850\,\text{nm}$ (red colour scale).

Due to the hBN/WS_2-cover on the sample in Fig. 4.7a, the Bragg cavity is not visible in the topography image. Instead, one can see the indentation of the covering layer bending into hole. However, the data in Figs. 4.7b and 4.7c confirms that the electric field enhancement of the cavity is indeed captured through the van-der-Waals stack of about 13 nm thickness.

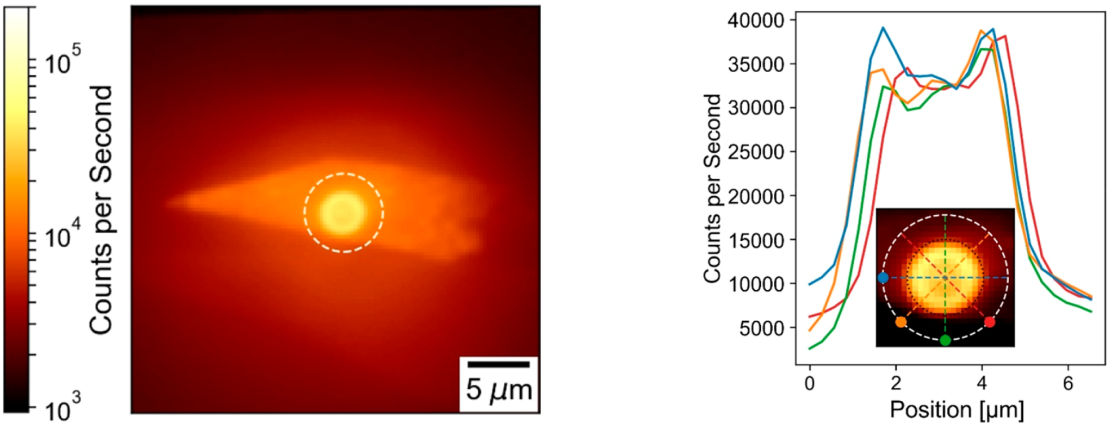

(a) Micro-photoluminescence image.

(b) Corresponding radial profiles.

Figure 4.6: Photoluminescence enhancement from a hBN/WS_2-covered microcavity measured by time-integrated optical photoluminescence microscopy, with 60x magnifying objective. (a) False-color CCD image showing the glowing WS_2 monolayer and the circular enhanced area on top of the structure. (b) Corresponding background-subtracted (5000 counts) cross-sectional intensity traces. Adapted with permission from ACS Nano, 13, 5, 5259-5267, Ref.[Wal13], Copyright 2019 American Chemical Society.

4.4 Analysis

A common observation for the covered and open cavities is that, at the in-coupling wavelength of $\lambda_0 = 532\,\text{nm}$, the near-field shows maximum enhancement at the centre of the Bragg cavity, see Figs. 4.7b and 4.7e, and a minimum for excitation at $\lambda_{\text{ref}} = 850\,\text{nm}$, see Figs. 4.7c and 4.7f. The fact that covered structure and reference structure both display the central enhancement suggests that it can be assigned to the lateral Bragg grating, rather than the vertical interference.

To allow a better comparison between the measurements, Fig. 4.8 shows horizontal profiles through the cavity centre for the six measurements shown in Fig. 4.7. Edges and centre of the circular structure are marked by dashed lines. The profiles corresponding to the resonant wavelength λ_0 are shown in green, the off-resonant profiles corresponding to λ_{ref} are shown in red. Three main observations can be taken away from the comparison:

1. Comparing the signal strengths at the cavity centre, for both covered and open structure the field enhancement is a strong maximum at λ_0 and (almost) minimal at λ_{ref}. This speaks in favour of a strong influence of the lateral DBR design. A difference between covered and open cavity is however not observed here.

2. Considering only the resonant cavity at λ_0, the relative strength of the central maximum to the outer maxima is slightly stronger for the covered cavity compared to the open cavity.

3. Comparing the periods of the topography to the near-field profiles, one can observe a half-period "phase shift" between the two wavelengths. The near-field signal at λ_0 shows field-enhancement in the Bragg grating's gaps. For the off-resonance case, however, the field maxima fall onto the GaP rings. Again, no difference is observed between covered and open cavity with respect to this effect.

The latter observation may be explained by considering the contributions making up the s-SNOM signal [171]. Firstly, the scattering cross-section of the tip apex is sensitive to

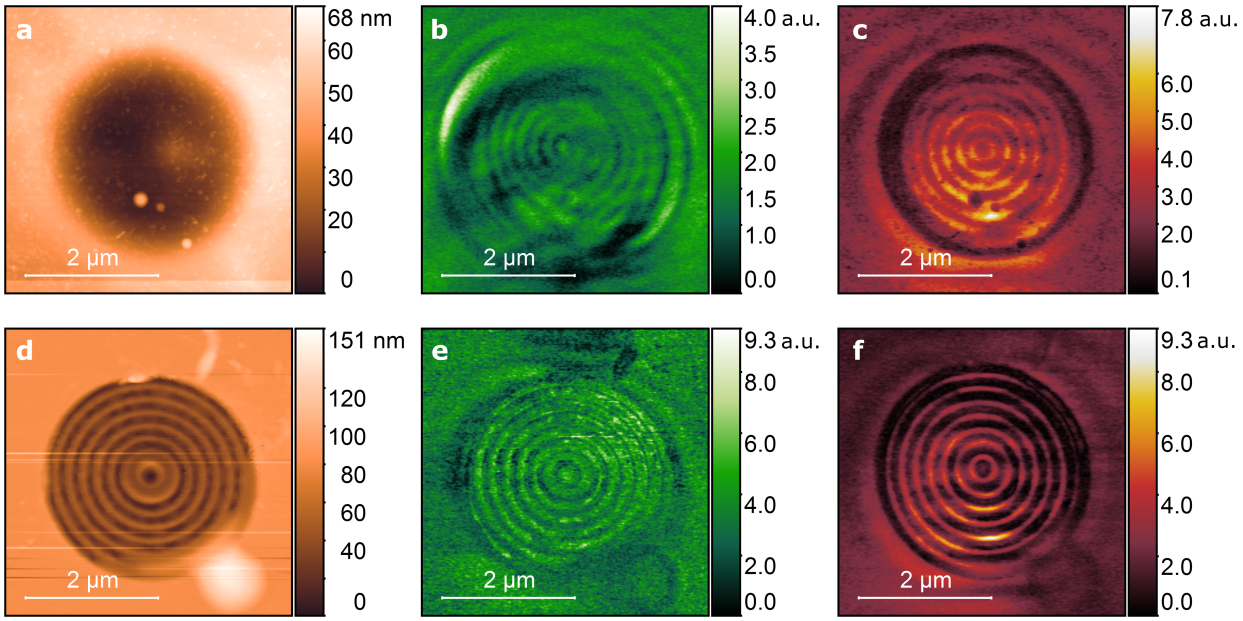

Figure 4.7: Topography and near-field measurements of monolayer-covered and open microcavity structure. (a) Topography of WS2-hBN covered cavity. (b) Near-field map of covered cavity at 532 nm. (c) Near-field map of covered cavity at 850 nm. (d) Topography of open microcavity. (e) Near-field map of open cavity at 532 nm. (f) Near-field map of open cavity at 850 nm. Reprinted with permission from ACS Nano, 13, 5, 5259-5267, Ref.[Wal13], Copyright 2019 American Chemical Society.

the material's permittivity, as outlined in Sect. 2.3.1. Secondly, the near-field interaction is strongly dependent on the tip-sample distance, which is usually kept constant by means of the AFM feedback, see Sect. 2.2.2. However, in the case of scanning buried structures, the assumption of constant distance may not be fulfilled since the depth of the microcavity below the hBN/WS_2 varies. Thirdly, surface electric fields by plasmonic modes and electric field enhancement (hot spots) are scattered by the s-SNOM tip and strongly affect the near-field signal response. Consequently, the near-field image at $\lambda_{\mathrm{ref}} = 850\,\mathrm{nm}$ contains a dominant spectroscopic topography contribution effectively mapping out the permittivities of GaP and air. On the other hand, at $\lambda_0 = 532\,\mathrm{nm}$ the response is dominantly made up of the field enhancement of the resonant cavity, most prominently in its centre. This effect causes the observed reversal of the near-field and explains the radial "phase shift" between the two wavelengths.

Further near-field images taken in parallel at the second harmonic signal 2Ω are shown in Fig. A.1 of Appendix A.2. It is well known that demodulation at the second harmonic is often insufficient to effectively suppress the background contribution, as detailed in Sect. 2.3.2. Indeed, the second harmonic data shows obvious horizontal interference fringes and artifacts that seem to appear due to scattering by the topography. Interestingly though, the comparison between the measurements of the open cavity at the resonant wavelength at 2Ω, Fig. A.1 of Appendix A.2, and 3Ω, Fig. 4.7e, shows a signal reversal across the whole cavity. The latter near-field image clearly traces the topographical structure while suppressing this effect at the third harmonic brings out the reverse field enhancement.

Near-field measurement were also performed on the reference sample, corresponding to the green color code according to Table 4.1. This structure is a hBN/WS_2-covered circular etched hole, but without Bragg cavity. Fig. 4.9 shows the measurements of AFM and s-SNOM on the sample. Unfortunately, a dust particle was trapped on the structure as

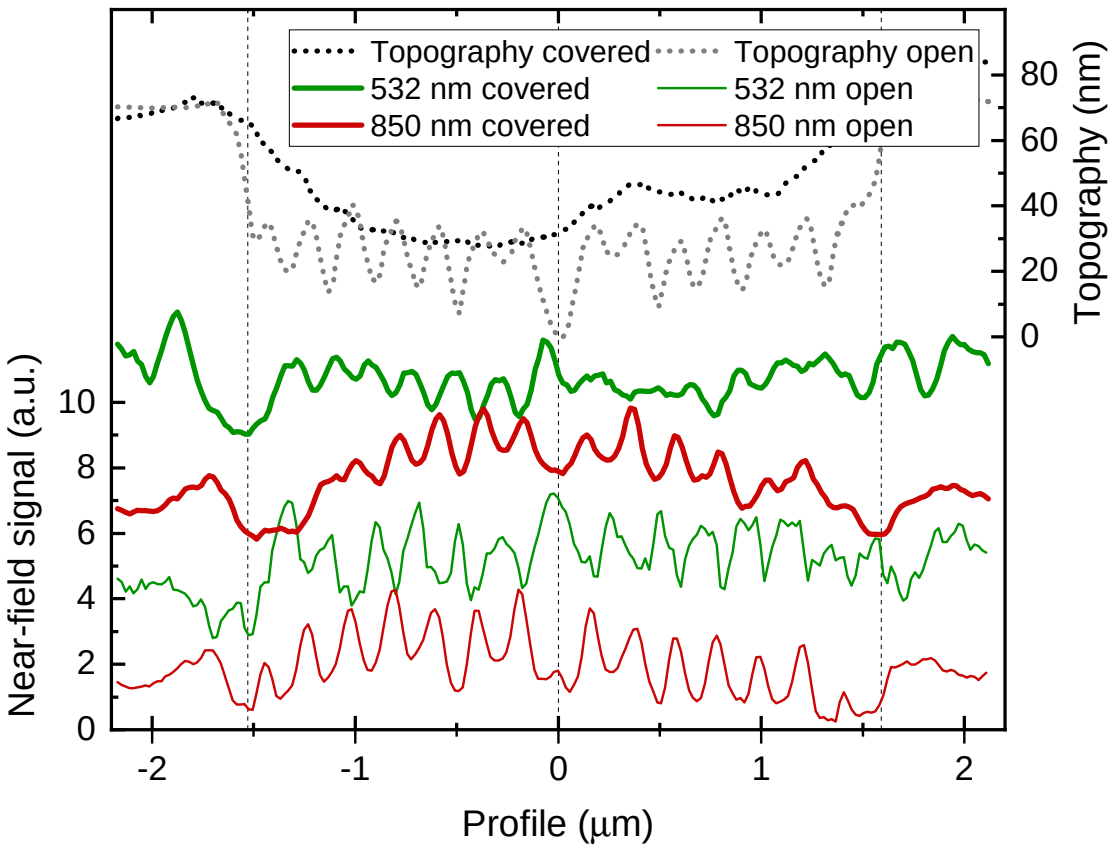

Figure 4.8: Horizontal line-outs taken from the AFM and s-SNOM measurement in Fig. 4.7. Vertical lines mark the edges and centre of the microcavity structure. While the field maxima at 850 nm coincide with the topographical maxima of the Bragg cavity, the field distribution at 532 nm shows a complimentary behaviour. Most strikingly, one can observe a clear field maximum in the centre of the cavity for both measurements taken at 532 nm. Adapted with permission from ACS Nano, 13, 5, 5259-5267, Ref.[Wal13], Copyright 2019 American Chemical Society.

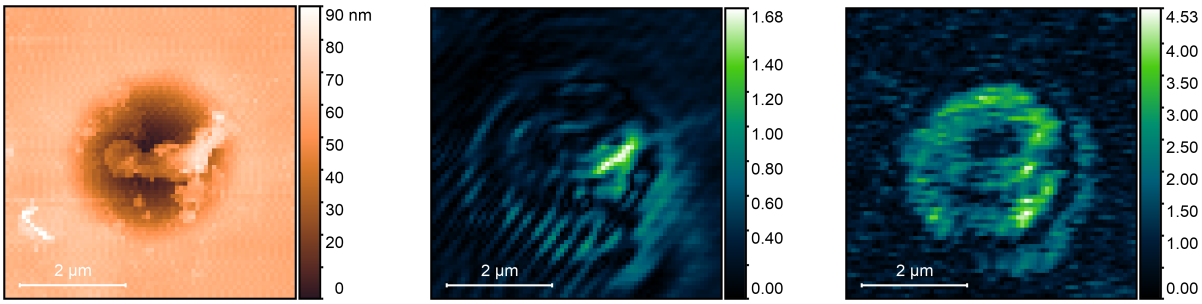

(a) Topography. (b) Near-field at 2Ω. (c) Near-field at 3Ω.

Figure 4.9: Topography and near-field measurements of the reference structure: a hBN/WS_2-covered circular hole without Bragg grating. A dust particle trapped in the structure complicates the analysis. The colourbars of (b) and (c) are in arbitrary units.

apparent from the topography image in Fig. 4.9a. Nonetheless, from the measurement at the third harmonic, Fig. 4.9c, one can deduce an enhancement of the field at the perimeter of the structure. Although mostly obstructed by the dust particle, no spatial pattern or enhancement comparable to the Bragg structure samples can be observed in the central area of the structure.

4.5 Conclusion

In conclusion, structural patterning of the substrate by FIB etching was a viable way to enhance the exciton photoluminescence yield of the WS_2 monolayer (a factor of 10 is reported in [Wal13]). To achieve this, two approaches are combined. Firstly, a lateral DBR microcavity was optimized by transfer matrix method to maximize the reflectivity into its centre. Secondly, the vertical air gap between the substrate and the suspended hBN/WS_2 stack was modelled by a multi-reflection method to optimize for constructive interference of the exciting light at the monolayer. Additionally to optical characterization by photoluminescence microscopy, high-resolution s-SNOM measurements were recorded to support the claim that specifically the in-coupling of radiation at $\lambda_0 = 532\,\mathrm{nm}$ is enhanced by the microcavity. This question could be answered with the presented data.

A strong influence of the lateral DBR patterning was identified through near-field measurement of different structures (open and covered DBR, and reference hole) and at different wavelengths (resonant and off-resonant). A maximum field enhancement was found in the centre of the circular cavity and locally enhanced rings were observed between the circular GaP rings of the Bragg cavity exclusively for resonant illumination. In contrast, no strong dependence on the vertical structuring (open vs covered DBR) could be observed by s-SNOM. However, a clear field enhancement was present also for the reference structure (without Bragg grating) at the perimeter of the hole, demonstrating the generally enhancing effect of the trench by suspending the monolayer. Still, the dominant effect is the lateral Bragg structure, at least with regard to the in-coupling enhancement.

To further disentangle the near-field signal response due to material contrast and surface field enhancement, which is complicating the analysis, one could excite the s-SNOM tip and the structure using s-polarized light, which reduces the material permittivity response [172, 173]. However, in turn one expects a generally reduced signal intensity.

Another idea for further measurements is the direct detection of photoluminescence by means of Tip-Enhanced Photoluminescence [174]. Similarly to Su et al. [175], who demonstrate nanoscale mapping of excitons and trions in monolayer MoS_2, a 20 nm tip could be used to detect and enhance the photoluminescence yield. However, as shown by these authors, a metallized tip in contact with the semiconducting monolayer may affect the sample and the cavity. In fact, a tip or nanoantenna in the proximity of the quantum emitter may tune both the excitation and the emission efficiency [176]. Depending on size and resonance of the tip, this can cause enhancement, resonance shift and even full quenching of the photoluminescence [177]. Thus, the tip's influence has to be factored in when assessing the microcavity enhancement on the photoluminescence out-coupling.

Chapter 5

Vertical tunneling through TMDC layers

5.1 Introduction

Transition Metal Dichalcogenides (TMDCs) are considered excellent candidates for a great number of electro-optical applications due to their occurrence in atomic layers, their direct band gap and strong light-matter interaction in the visible regime, and interesting properties applicable to spin- and valleytronics. The emerging photoluminescence, which arises due to a characteristic transition from indirect to direct band gap for TMDC multilayers when thinned down to single layers, was discussed and studied in Chapter 4. In this context, a brief overview of several defining characteristics was presented in Sect. 4.2.1.

This chapter follows a different perspective and centers their semiconducting properties. Particularly the direct band gap in the visible spectrum has motivated a variety of applications, such as transistors [54, 178] or photovoltaic cells [179]. Furthermore, the possibility to easily fabricate heterostructures by stacking different van-der-Waals layers has become a lively playground for research [180]. One of the central themes is vertical current transport through TMDC single- and multilayers, and heterostructures [159, 181]. Generally, current transport across a thin semiconducting barrier can be classified into field emission, thermionic field emission and thermionic emission. The former conceptualizes two effects known as direct and Fowler-Nordheim tunneling. Thus, four basic transport processes are obtained, which play a role in thin metal-semiconductor-metal contacts. They are illustrated in Fig. 5.1.

Thermionic emission is the dominant process in thick semiconducting layers. One such example is vertical field-effect transistors, which are assembled from stacked TMDC multilayers. These are based on the modulation of the Schottky barrier height, analogous to changing the gate bias in Metal Oxide Semiconductor Field-Effect Transistors (MOSFETs). Some notable examples use heterostructures consisting of graphene/MoS_2/metal [179] or graphene/WS_2/graphene [54].

Field emission, on the other hand, becomes the dominant process in few-layer TMDC barriers and the current dependence on barrier height and voltage bias changes. Graphene is a common contact due to its strongly tunable Fermi level [182], however it does not function as a tunnel barrier due to its zero band gap; in contrast to other van-der-Waals materials, such as isolating hBN ($E_g = 6\,eV$) or semiconducting TMDCs ($E_g \approx 1.0$ - $2.5\,eV$) [183]. Using hBN in the context of tunnelling [55, 182, 184] has led to the successful implementation of vertical Tunnel Field-Effect Transistors, e.g. by sandwiching 4 - 7 layers of hBN between graphene contacts [17]. Notable examples for studies on TMDCs and their use for TFETs

are based on graphene and WS_2 [185], MoSe2 [186], and MoS_2 [187].

Furthermore, a range of properties of TMDCs, as discussed in Sect. 4.2.1, can be merged with mere tunnelling application into exciting research branches. As TMDC materials are photoactive in the visible, the tunnelling current can be tuned by light [188, 189]. Spin-dependent tunnelling has been predicted in vertical tunnelling through MoS_2, due its magnetic properties [190]. Resonant tunnelling and Negative Differential Resistance (NDR) can occur in heterostructures with clean interfaces at room temperature, making promises for vertical quantum electronics [92, 191, 192].

Tunneling effects in TMDC monolayers and its heterostructures evidently show a vast potential. Some authors even highlight the role of TFETs in beyond-Si electronics [159], owing to their excellent shot noise properties suggested to beat MOSFETs' subthreshold swing limit of 60 mV/dec [193, 194] and excel at low power consumption, ranking them as potential successors to silicon transistors once they exhaust their fundamental quantum limits [195].

This chapter introduces some theoretical aspects that are key to understanding tunnelling in TMDC heterostructures. Experimental I-V measurements obtained with c-AFM are demonstrated. The results are discussed with regard to the current transport observed. Experimental challenges related to the measurement technique and sample preparation are then discussed. The chapter covers preliminary studies that were useful to characterize the c-AFM setup. Consequently, a focus is put on some experimental challenges, suggested solutions and propositions for continued studies on the topic.

5.2 Theoretical background

Current transport across a potential barrier can mostly be described by one or a combination of four basic mechanisms, which are illustrated as arrows 1 to 4 in Figs. 5.1b and 5.1c. Direct tunneling (1) and Fowler-Nordheim tunneling (2) are different regimes of field emission. Both tunneling processes refer to tunnelling of carriers from the conduction band through the barrier. The transition from direct tunneling to Fowler-Nordheim tunneling occurs at higher bias voltages once the barrier width becomes dependent on voltage bias. This is indicated by a dotted vertical line to the right of arrow 2 in 5.1c. The processes are explained in detail in Sect. 5.2.1.

Thermionic field emission (3) refers to tunneling of thermally excited carriers through a reduced barrier width at the elevated energy and can be seen as a transition region between field emission and thermionic emission [196, 197], it will not be discussed further in this chapter. Thermionic emission (4) describes current flow of carriers with sufficient energy to overcome the potential barrier. In this case the current depends on the barrier height, but it is independent of barrier shape. The process is discussed in Sect. 5.2.2.

5.2.1 Field emission

Tunneling is a quantum-mechanical effect. According to classical mechanics, carriers can either pass over a potential barrier - which would refer to thermionic emission as mentioned above - or they are completely reflected by it. However, according to quantum mechanics the carrier is represented by a probability wavefunction ψ. The wavefunction of the carrier hitting a potential wall does not immediately decrease to zero, instead a finite probability remains that it penetrates into and eventually through the barrier. Consequently, there is a finite probability that the electron will tunnel through a barrier of given height and width [197, p. 46f].

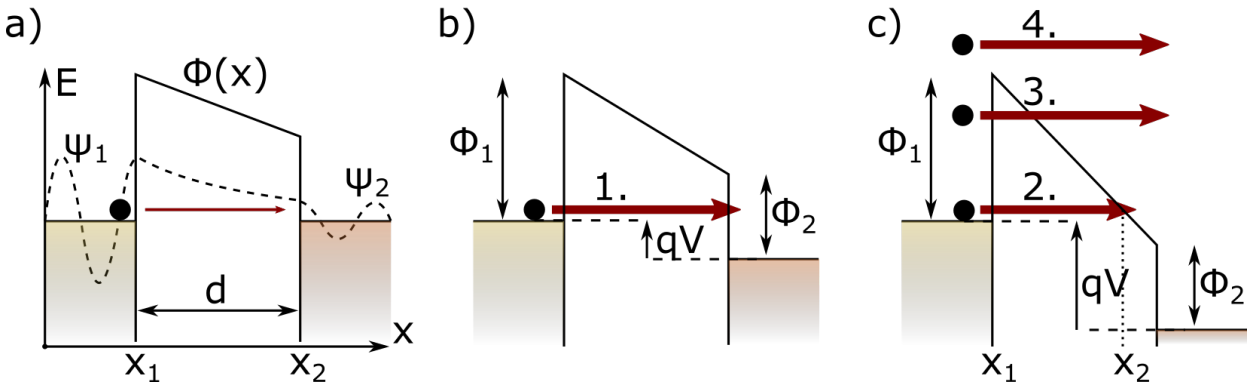

Figure 5.1: Carrier transport between two metal electrodes across a Schottky barrier. a) Wavefunction showing tunneling through a trapezoidal barrier without bias. Net current is zero. b,c) Processes under bias referred to in the main text: (1) Direct tunneling, (2) Fowler-Nordheim tunneling, (3) thermionic field emission, (4) thermionic emission.

Interestingly, the mathematical description is a wave exhibiting exponential decay into the potential barrier, which continues its propagation on the other side. This is analogous to evanescent waves that leak through a very thin metasurface, as described in Sect. 3.2.3. Other analogous examples from the optical realm include ATR and evanescent surface fields that are picked up by a tip, as in photon scanning tunneling microscopy [198, 199]. The effect in this case is known as optical tunneling.

To find the tunneling probability for the carrier, one considers Schrödinger's equation for a particle with effective mass m^* moving through a potential $V(x)$ as sketched in Fig. 5.1a.

$$\frac{d^2\psi}{dx^2} + k(x)^2\psi = 0 \tag{5.1a}$$

$$k(x)^2 = \frac{2m^*}{\hbar^2}\left(E - \Phi(x)\right) \tag{5.1b}$$

with k(x) being imaginary when tunneling through a barrier ($\Phi(x) > E$).

For a constant potential $\Phi_0(x)$ of width d, the tunneling probability T_t can be calculated as the ratio of probability densities between transmitted $|\psi_2|^2$ and reflected $|\psi_1|^2$ wave [197, p. 48]

$$T_t = \frac{|\psi_2|^2}{|\psi_1|^2} \approx \frac{16E(\Phi_0 - E)}{\Phi_0^2}\exp\left(2ikd\right) \tag{5.2}$$

For slowly varying potentials, i.e. when the particle's de Broglie wavelength is much smaller than the variation length scales of $\Phi(x)$, the solution to the Schrödinger equation can be found using the famous Wentzel-Kramers-Brillouin (WKB) approximation. The tunneling probability then becomes [197, p. 48]

$$T_t = \frac{|\psi_2|^2}{\psi_1|^2} \approx \exp\left(2i\int_{x_1}^{x_2} k(x)dx\right) \tag{5.3}$$

The tunneling current density j_t per unit energy dE and unit area can then be calculated as the product of number of available carriers on one side of the barrier, unoccupied

corresponding states on the other side and the respective tunneling probability. Integrating over all energies results in the total current density J_t per unit area given by the Tsu-Esaki formula [200, 201]

$$J_t = \frac{qm^*}{2\pi^2\hbar^3} \int T_t(E, qV) \cdot N(E, qV) dE \tag{5.4}$$

$N(E)$ is the supply function, which is the difference between the Fermi-Dirac distributions in region 1 and region 2, considered only for the longitudinal energies. It is calculated through a separation of the Fermi-Dirac distribution into longitudinal and transversal energy, that is integrated over its transversal energy variable in radial coordinates [200]

$$N(E) = k_B T \ln \left(\frac{1 + \exp\left(-\frac{E-E_f}{k_B T}\right)}{1 + \exp\left(-\frac{E-qV-Ef}{k_B T}\right)} \right) \tag{5.5}$$

Here, the variable E refers to the longitudinal energy over which the integration has to be performed, E_f is the Fermi energy, $k_B T$ is the dependence on Boltzmann constant and temperature.

It is noted that the supply function differs from the one typically assumed in STM, which is simply the difference of Fermi-Dirac distributions of the two regions. This simpler approach, neglecting the uni-directional tunneling, has also been applied in the context of TMDC heterostructures [202].

Direct tunneling and Fowler-Nordheim tunneling

Field emission refers to tunneling of electrons from the conduction band through the potential barrier. In most cases, the potential barrier can be modelled as a trapezoidal potential, as illustrated in Fig. 5.1, with barrier heights Φ_i left and right, respectively. The difference between direct tunneling and Fowler-Nordheim tunneling becomes clear, when considering the location of the turning point x_2. For the low-voltage bias regime, $qV < \Phi_i$, the electron has to pass the whole width of the barrier in order to reach the opposite side. The turning point x_2 is independent of voltage and one speaks of direct tunneling. For the high-voltage regime, $qV > \Phi_i$, the electron tunnels through the triangular part of the barrier. In this case, the turning point x_2 (and hence the tunneling width d) are bias dependent, as the effective barrier width shrinks with increasing bias. This is called Fowler-Nordheim tunneling. [203, 204]

For a generalized description, we can write the trapezoidal potential barrier as

$$\Phi(x) = \begin{cases} 0, & \text{if } x < x_1 \\ \frac{(\Phi_2 - qV) - \Phi_1}{d} x + \Phi_1, & \text{if } x_1 \leq x \leq x_2 \\ -qV, & \text{if } x > x_2 \end{cases} \tag{5.6}$$

and the voltage-dependent turning point x_2, assuming $x_1 = 0$ and positive bias, is

$$x_2 \quad = \quad \begin{cases} d, & \text{if } E < \Phi_2 - qV \\ \frac{(E-\Phi_1)d}{\Phi_2 - qV - \Phi_1}, & \text{if } \Phi_2 - qV \leq E \leq \Phi_1 \\ 0, & \text{if } \Phi_1 < E \end{cases} \tag{5.7}$$

With the potential barrier plugged into Eq. 5.3 for the tunneling probability, and the turning points as the integration boundary, one can calculate the current density using

Eq. 5.4. For an asymmetric trapezoidal barrier, the expression can be solved with a simple numerical integration [205]. Arbitrary barrier shapes require a more nuanced meshing approach [206].

For fitting experimental studies, a common approach [189, 207–209] is to apply approximations suggested by Simmons [203, 210]. It is assumed that the potential barrier $\Phi(x)$ can be expressed by a mean barrier height $\bar{\Phi}$ leading to the expression [207, 210]

$$I = \frac{qA}{4\pi^2\hbar(\beta d)^2}\left\{\left(\bar{\Phi} - qV\right)\exp\left(-\alpha\sqrt{\bar{\Phi} - qV}\right) - \bar{\Phi}\exp\left(-\alpha\sqrt{\bar{\Phi}}\right)\right\} \tag{5.8}$$

where $\alpha = 2\beta(x_2 - x_1)\sqrt{2m^*}/\hbar$, and β is a correction factor of $\frac{23}{24}$. The low and high voltage regimes, respectively, result from the assumptions of the following parameters

$$(x_2 - x_1) = d \qquad \bar{\Phi} = (\Phi_1 + \Phi_2)/2 \qquad \text{low voltage} \tag{5.9a}$$

$$(x_2 - x_1) = \frac{\Phi_i d}{qV} \qquad \bar{\Phi} = \Phi_i/2 \qquad \text{high voltage} \tag{5.9b}$$

where the former leads to direct tunneling and the latter (with i=1 for forward bias) leads to the Fowler-Nordheim tunneling equations. The resulting tunneling current I is expressed by the following equations [203, 209]

$$I = \begin{cases} \frac{Aq^2\sqrt{m^*(\Phi_1+\Phi_2)}}{h^2 d}V\exp\left(-\frac{2d\sqrt{m^*(\Phi_1+\Phi_2)}}{\hbar}\right) & \text{direct tunneling} \\ \frac{Aq^2 m_0}{4\hbar\Phi_i d^2 m^*}V^2\exp\left(-\frac{4d\sqrt{2m^*\Phi_i^3}}{3\hbar eV}\right) & \text{FN tunneling} \end{cases} \tag{5.10}$$

where A is the cross-sectional area, and the transition voltage between the two regimes is given by $qV = \Phi_i$.

One advantage of such an analytical expression is that a "Fowler-Nordheim plot" of $\ln\left(\frac{I}{V^2}\right)$ over $\frac{1}{V}$ can be used to extract the Schottky barrier height $\bar{\Phi}$, since for Fowler-Nordheim tunneling

$$\ln\left(\frac{I}{V^2}\right) \propto -\frac{1}{V}\left(\frac{4d\sqrt{2m^*\Phi^3}}{3\hbar q}\right) \tag{5.11}$$

Fig. 5.2 displays a typical tunneling I-V plot showcasing the transition between direct and Fowler-Nordheim regime. Modelled are direct and Fowler-Nordheim approximations, Eqs. 5.10, the generalized Simmons approximation, Eq. 5.8, and the Tsu-Esaki formula, Eq. 5.4. The graph shows the tunneling current for a rectangular potential barrier of height $\Phi_0 = 1\,\text{eV}$ and width $d_0 = 3\,\text{nm}$, circular contact area $A = 10\,\text{nm}$ radius. The Tsu-Esaki equation was solved by numerical integration over the barrier width $(x_2 - x_1)$ and the longitudinal energies dE. Fig. 5.2a shows that the Fowler-Nordheim approximation is a good fit to the generalized Simmons equation for the high voltage regime. The fact that the WKB approximation in the form of the generalized Simmons approximation overestimates Tsu Esaki's result is confirmed in the literature [211]. Fig. 5.2b shows how the logarithmic plot proposed in Eq. 5.11 exposes the Fowler-Nordheim tunneling regime as a straight line with a slope that depends on barrier height and width. The bend at $1\,\text{V}^{-1}$ shows the transition from direct tunneling to field emission at the transition voltage of $\text{qV} = \Phi_0$ [207].

The example depicts the situation for a rectangular barrier. The approximations for a trapezoidal barrier were stated in Eq. 5.9a. For direct tunneling, the mean barrier height can suffice, or a more complex analytical model for a tilted potential can be applied [212]. For Fowler-Nordheim tunneling, the potential barrier height is chosen which the electrons must initially tunnel through and it thus depends on bias polarity, i.e. Φ_1 for $V > 0$ and Φ_2 for $V < 0$ [213].

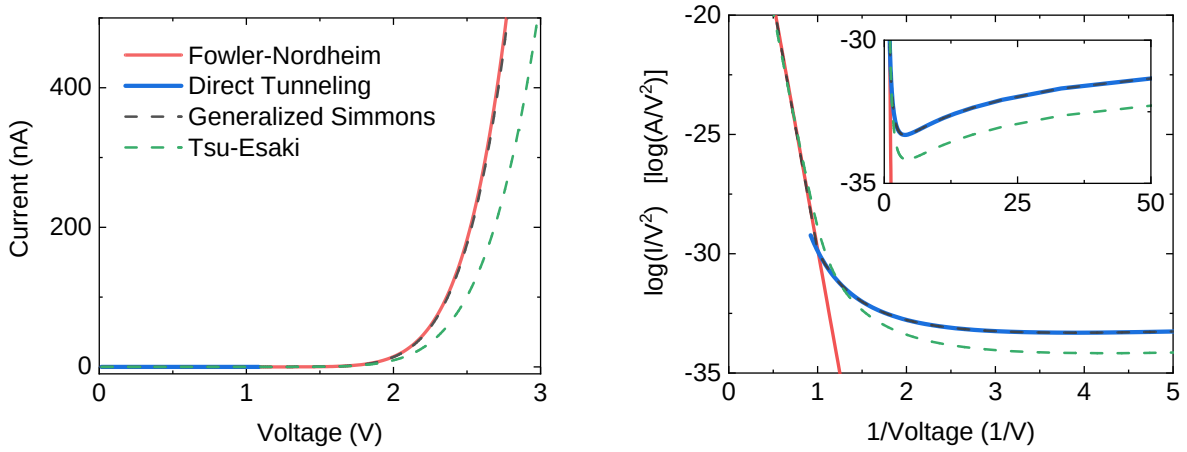

(a) Linear plot.

(b) Fowler-Nordheim plot.

Figure 5.2: Different models and approximations to calculate the tunneling current. Shown for $\Phi = 1\,\mathrm{eV}$, $d_0 = 3\,\mathrm{nm}$. (a) shows a linear plot and (b) a Fowler-Nordheim plot with the characteristic linear slope and an inset showing a larger scale.

5.2.2 Thermionic emission

Thermionic emission or Schottky emission is a conduction process that occurs when electron overcome the Schottky barrier due to thermal activation energy. Contrary to tunneling effects, thermionic emission is strongly temperature dependent and, for a single barrier, can be described by

$$J_{\mathrm{te}} = A^* T^2 \exp\left(-\frac{q\Phi_i}{\nu k_B T}\right)\left[\exp\left(\frac{qV}{k_B T}\right) - 1\right] \tag{5.12}$$

where $A^* = 4\pi q m^* {k_B}^2 h^{-3}$ is the effective Richardson constant of $120\,\mathrm{Acm^{-2}K^{-2}}$ for free electrons [197, p. 157]. The barrier height Φ_i in this case is subject to image force lowering, as described in Sect. 5.2.3. ν is the ideality factor of 1 (ideal) to 1.2 [214].

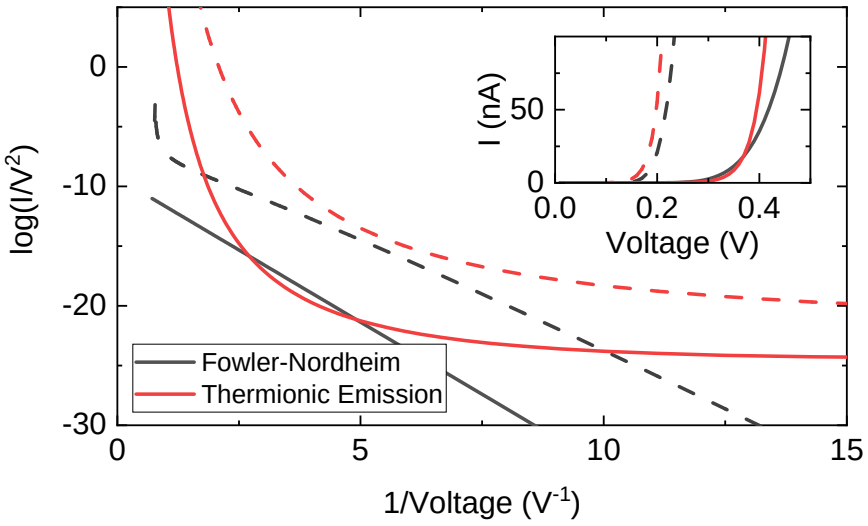

Figure 5.3: Comparison between thermionic emission and Fowler-Nordheim tunneling without (solid lines) and with (dashed lines) image force barrier lowering. The model assumes a Schottky barrier height Φ_i=0.5 eV, barrier width d=1 nm, contact area A=30 $\mathrm{nm^2}$. Different proportionalities are obvious from a $\ln(\mathrm{I/V^2})$ plot.

Several publications report thermionic emission to be the dominant current transport

process in thick vertically stacked TMDC heterostructures [187, 209], e.g. larger than three layers for MoS_2 at room temperature [185]. Occasionally, thermionic emission models have been applied even to single layers [215], though not without valid scepticisms. Moreover, the I-V curve for thermionic emission across a sandwiched TMDC flake can be modelled as two back-to-back Schottky diodes. Depending on bias polarity, one of the contacts is reverse-biased and an asymmetric response is obtained for different contact metals. The total current in this case is given by [214, 215]

$$J = \frac{\hat{J}_1 \hat{J}_2 \sinh\left(\frac{qV}{2k_BT}\right)}{\hat{J}_1 \exp\left(\frac{qV}{2k_BT}\right) + \hat{J}_2 \exp\left(\frac{-qV}{2k_BT}\right)} \tag{5.13}$$

where $\hat{J}_i = A^* T^2 \exp\left(\frac{q\Phi_i}{k_BT}\right)$.

Fig. 5.3 shows that while in a linear plot the distinction between thermionic emission and field emission may not be immediately obvious, the typical plot of $\ln(I/V^2)$ over $1/V$ only generates the characteristic linear slope for Fowler-Nordheim tunneling. Here, the comparison is made between Eqs. 5.12 and 5.10, parameters are noted in the figure caption.

5.2.3 Image force lowering

Electrons that approach the potential barrier induce a positive charge that acts like an image charge inside the potential barrier. The potential of this image charge reduces the effective potential barrier height. The image force lowering tends to be small in comparison to the barrier height. Nevertheless, the effect rounds of the steep edges of the potential barrier. It thus has an effect on the tunnel current density. The image potential in the interval $0 \leq x \leq d$ is calculated using image force methods and is approximately [203, eq. 33]

$$\Phi_{\text{image}}(x) = -\frac{1.15 \ln(2) q^2}{8\pi\epsilon_0\epsilon_r x(1 - \frac{x}{d})} \tag{5.14}$$

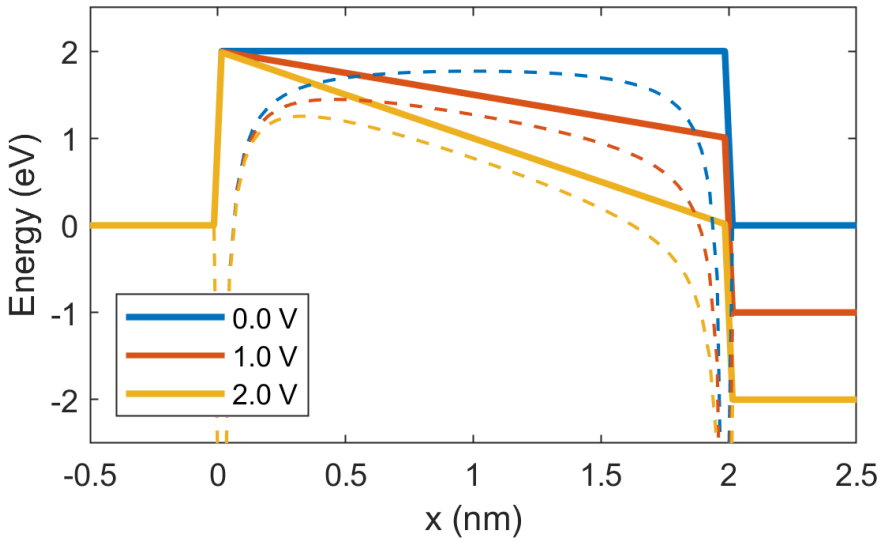

Figure 5.4: Image force lowering in a rectangular tunnel barrier of $\Phi = 4\,\text{eV}$, $d = 2\,\text{nm}$ and $\epsilon_r = 16$ with (dashed) and without (solid) image force lowering at different bias voltages.

Figure 5.4 shows a comparison for a rectangular tunnel barrier of $\Phi = 4\,\text{eV}$, $d = 2\,\text{nm}$ and $\epsilon_r = 16$ with and without image force lowering at different bias voltages. Obviously,

image force lowering affects both the height and the width of the potential barrier. The modified potential barrier can be roughly approximated by subtracting the image force lowering correction [197, p. 146]

$$\Delta\Phi = \sqrt{\frac{qV}{4\pi\epsilon_0\epsilon_r d}} \tag{5.15}$$

from Φ_i to use the effective Schottky barrier height in Eq. 5.10.

5.3 WS_2 on graphene

5.3.1 Sample characterization

These first measurements presented here were performed on a WS_2 flake positioned on top of a graphene flake. Both van-der-Waals materials were mechanically exfoliated (RAPGARD TDS F6F, Nitto) [158, Appendix A1] and transferred onto SiO_2 substrate using dry viscoelastic stamping (PF-20/17-X4, Gel-Pak) by a project partner[1] [216–218]. Preparation of the samples was performed under ambient conditions. The sample was then further processed in Frankfurt by lift-off photolithography and deposition of 100 nm gold on 3 nm chromium to facilitate electrical contacting of the graphene flake.

Fig. 5.5 shows two optical microscopy images and corresponding AFM scans of the sample. Figs. 5.5a and 5.5b show an overview of the sample after the lithographic processing, where the gold contacts can be clearly seen. Fig. 5.5c is a zoomed in image of the same sample, taken before the lithography was performed. One can clearly distinguish between the blue color of the WS_2 flake and the shaded graphene flake underneath. Fig. 5.5d is the corresponding AFM image which shows the step height between the flakes and the substrate. A horizontal imaging artifact is visible in the lower part of the image. Across the step between graphene and WS_2 a profile indicates the data shown in the graph of Fig. 5.6.

I-V measurements were taken with the c-AFM setup as described in Sect. 2.4. The cantilever used in conjunction with this sample was of type RMN-25PT300B with a spring constant of k = 18 N/m, see Table 2.2. The measurements reflect that this cantilever is too stiff for obtaining I-V measurements with well-controlled contact force, and a high contact force of about 1.5 µN was used. The transimpedance amplifier was set to an amplification of 10^6 V/A, see Table 2.1, to be able to measure currents up to 0.5 µA versus a DC bias voltage applied between the PtIr5 tip and the graphene flake (contacted via the gold electrode).

While usually one would expect to observe a transition between direct tunneling to Fowler-Nordheim tunneling regime with increasing bias voltage, the experimental setup here includes a series resistance of 1 MΩ meant to limit the maximum current flow across tip and TMDC flake. This leads to an expected I-V slope

$$\frac{dI}{dU} = \frac{1}{R_0} = \frac{1}{R_{\text{tunnel}} + R_{\text{series}}} \overset{R_{\text{tunnel}}\to 0}{\approxeq} \frac{1}{1\text{M}\Omega} \tag{5.16}$$

and is indeed observed as an experimental linear slope of 1/1.2 MΩ for high voltages, as shown in Sect. 5.3.2.

The potential barrier heights Φ_i at the two heterojunctions PtIr/WS_2 and WS_2/graphene are approximated with the Schottky-Mott rule by calculating the difference between the metal work function Φ_{metal} and the semiconductor's electron affinity χ

$$\Phi_i = \Phi_{\text{metal}} - \chi \tag{5.17}$$

[1] Dept. of Physics and Materials Sciences Center, Philipps-Universität Marburg

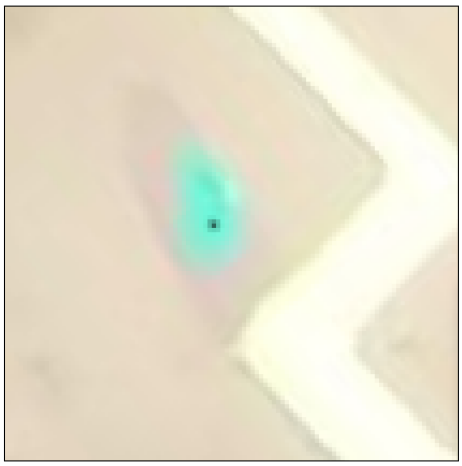

(a) Optical microscopy, 50x.

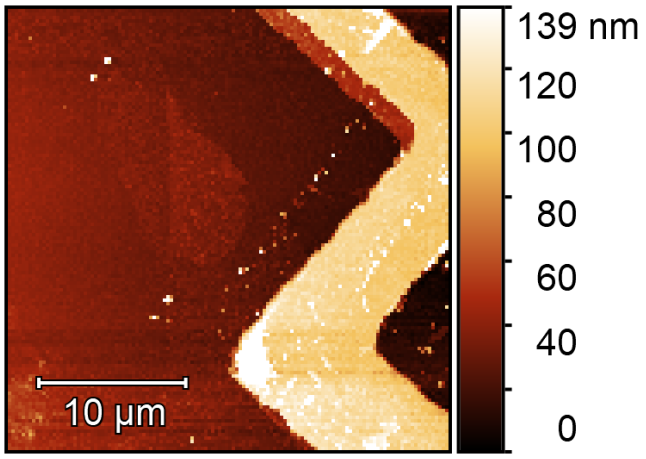

(b) AFM topography.

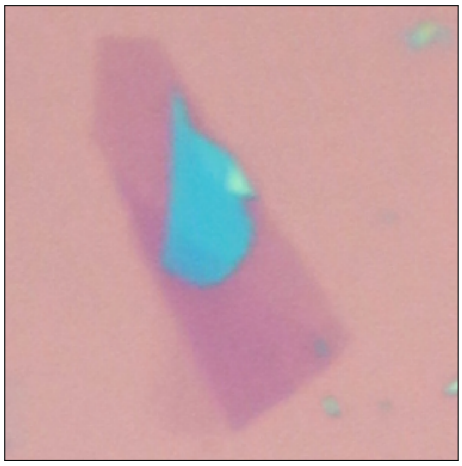

(c) Optical microscopy image, 50x.

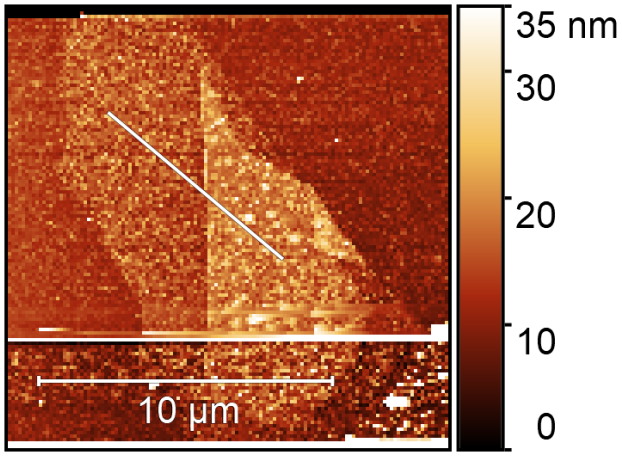

(d) AFM topography.

Figure 5.5: Visualization of the 2D-material heterostructure sample. (a) Image of WS_2 flake (blue) on top of graphene flake. The contact leads were placed using photolithography and gold deposition. (b) WS_2 flake (blue) on top of Graphene flake, before contacting. The orientation can be compared to the AFM scanned images. (c) Gold-contacted graphene flake with WS_2 flake placed on top. (d) WS_2 flake on top of graphene flake. Horizontal white lines are due to scanning artifacts. The lineout is discussed below.

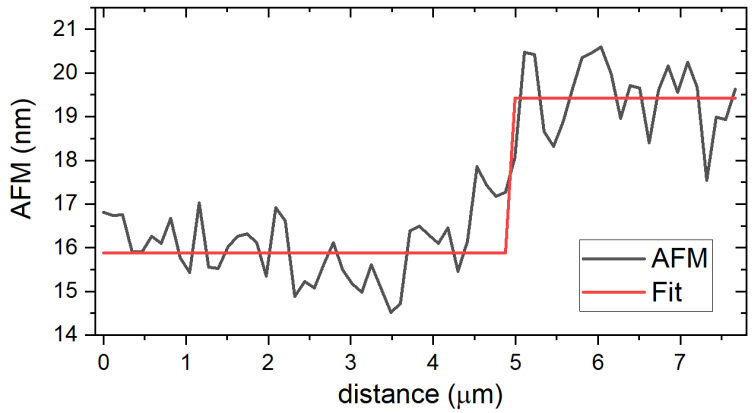

Figure 5.6: Topography profile from Fig. 5.5d. The data is averaged over a linewidth of 20 px and fitted with an edge of step height (3.5 ± 1.0) nm.

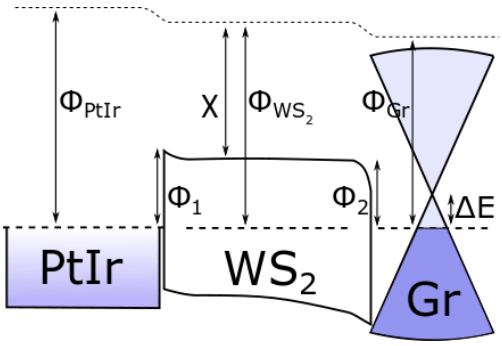

Figure 5.7: Energy-band diagram illustrating the formation of a potential barrier at the heterojunctions of WS_2 sandwiched between PtIr and graphene (Gr). The arrows highlight the magnitudes of the work functions Φ, electron affinities χ and barrier heights Φ_i towards the vacuum level (dotted line). ΔE indicates the difference between graphene's Fermi level and Dirac point.

Work function and electron affinity are defined as the energy required to remove an electron from the Fermi level E_F and from the the conduction band E_C, respectively, to the vacuum level [197, p. 135]. Fig. 5.7 illustrates the formation of the barrier at the heterojunctions. The tunable Fermi level of graphene is indicated by ΔE and can play a crucial role in the design of TFETs [17].

	WS_2	WSe_2	Gr	Pt	PtIr	Au
Work function Φ (eV)	4.73	4.21	4.6	6.35	4.85	5.1
Band gap E_g (eV)	1.54	1.32	0	-	-	-
Electron affinity χ (eV)	3.95	3.7	4.6	-	-	-

Table 5.1: Work function Φ, band gap E_g and electron affinity χ for several materials: WS_2, WSe_2, Graphene (Gr), Pt, PtIr and Gold [219–223].

Table 5.1 states general values for Φ, band gap E_g and χ for some materials relevant to this chapter. According to these parameters one would expect with Eq. 5.17 the ideal barrier heights $\Phi_1 = 0.9\,\text{eV}$ and $\Phi_2 = 0.65\,\text{eV}$. The most important deviations of experimental barrier heights from the ideal values are due to interface layers, chargeable interface (surface) states, and image-force lowering, see Sect. 5.2.3 [197, p. 135].

5.3.2 Tunnel current analysis

Fig. 5.8 shows a I-V measurement on the WS_2 flake in linear and Fowler-Nordheim plot, demonstrating the characteristic linear slope. The data shows both up and down sweep for the I-V measurement. The linear data interval is manually selected (orange and yellow circles) and fitted with the Fowler-Nordheim model, Eq. 5.10. The two asymmetric polarities were fitted simultaneously to find the potential barrier heights Φ_1 and Φ_2. The remaining parameters were assumed, i.e. a contact area of $A = 29\,\text{nm}^2$ (see Sect. 2.4.2), an effective mass in WS_2 of $m^* = 0.34m_0$ [224] and a barrier width of $d = 3.5\,\text{nm}$ (see AFM measurement in Fig. 5.6). It is noted that the programmatic fit emphasizes the high voltage data points, due to their increased density in the 1/V plot. The slight hysteresis is neglected for this analysis.

The least squares fit is plotted as solid lines in both the linear and Fowler-Nordheim plot of Fig. 5.8 and yields barrier heights $\Phi_1 = 0.54\,\text{eV}$ and $\Phi_2 = 0.44\,\text{eV}$. The results are

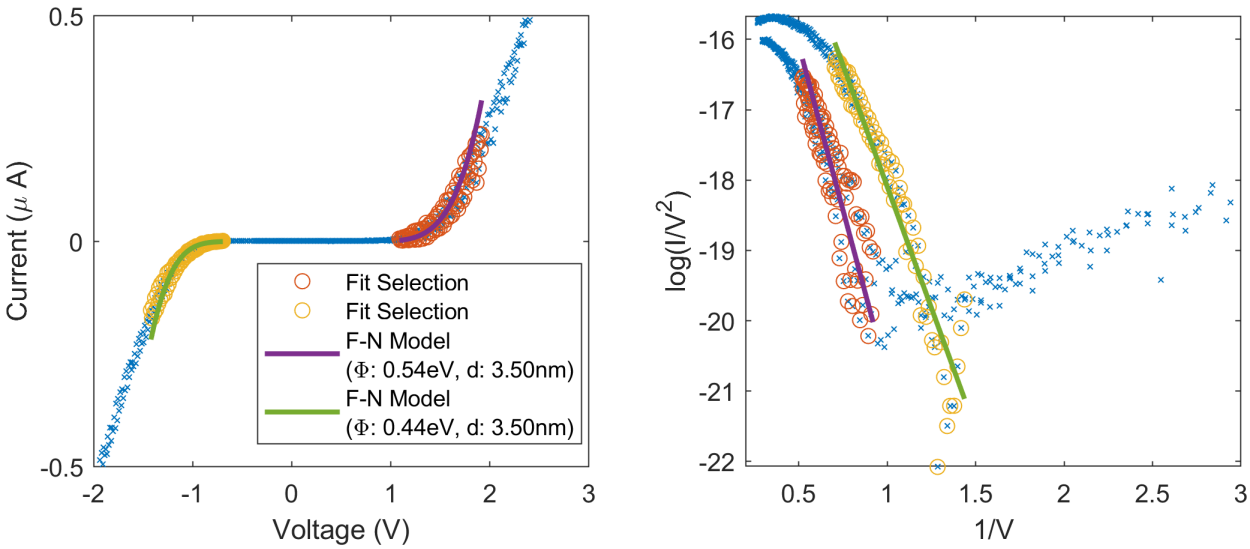

Figure 5.8: I-V measurement on the WS_2/Gr flake, shown in linear scale and as Fowler-Nordheim plot. The data range used to fit the Fowler-Nordheim model is marked with orange and yellow circles. Solid lines indicate the fit result with the parameters given in the legend.

summarized in Table 5.2 together with results for two alternative estimations of the barrier width d.

Assuming ideal barriers, one would expect theoretical barrier heights $\Phi_1 = 0.90\,\text{eV}$ and $\Phi_2 = 0.65\,\text{eV}$, see Sect. 5.3.1. The fitting result thus deviates considerably from the theoretical prediction. Moreover, Table 5.2 clearly shows that the fitting routine is very sensitive to the tunnel width. An accurate determination of the true tunnel barrier width or the number of TMDC layers is thus crucial for obtaining a reliable fitting result.

	d (nm)	Φ_1 (eV)	Φ_2 (eV)
experimental	1.8	0.90	0.73
	3.5	0.54	0.44
	4.8	0.42	0.34
theoretical	-	0.90	0.65

Table 5.2: Fitting parameter d and fitting results Φ_i for the Fowler-Nordheim model and data shown in Fig. 5.8. Other parameters are given in the text.

Two main reasons are likely responsible for the deviation between experimental and theoretical values of the barrier heights. Firstly, an incorrect prediction of the theoretically ideal barrier height. This may be on the one hand due to neglecting the image force lowering, as suggested in Sect. 5.2.3, and on the other hand due to the influence of graphene's tunable density of states. The strong influence of graphene's tunable Fermi level and consequently available states on the tunneling current density [225] is not considered in the above model. Since the density of states of graphene is electrostatically tunable, it is effectively a function of bias voltage. The interface dipole across the graphene-metal interface creates a potential drop ΔV, which causes an energy shift ΔE of its work function. It can be expressed in analytical form for $T \to 0$ as [226]

$$\Delta E = \pm \frac{\sqrt{1 + 4\alpha q\,|V - V_D|} - 1}{2\alpha} \tag{5.18}$$

where $\alpha = \frac{2q^2(d-d_0)}{\epsilon\pi\hbar^2\nu_f^2}$, with $(d - d_0)$ being the effective distance between the charge sheets of graphene and the opposite metal electrode and $\nu_f \approx c/300$ being the Fermi velocity. d_0 is the equilibrium distance of $\approx 2 - 3$Å [227, 228]. For a bias voltage of $\pm 2\,\mathrm{V}$ this creates a Fermi shift of up to 0.16 eV for an assumed layer thickness of 1.8 nm.

Secondly, a systematic error (and noise) in the tunnel width determination by AFM would lead to an ill determination of the barrier heights Φ_i. Recently, inconsistencies in AFM topography measurements on TMDC materials, specifically WS_2, have been reported on [229]. Though analysed in the context of non-contact AFM measurements, the anomalies attributed to water adsorbates and resulting capillary effects in the order of $\pm 6\,\mathrm{nm}$ could well be transferred to the case of contact-mode AFM. The suggested remedies are using increased contact forces to push through the capillary potential and annealing the sample prior to topography measurements [230]. An additional artifact occurring in contact-mode AFM imaging of two-dimensional materials is associated with anisotropic friction coefficients that depend on scan direction, and can lead to height variations of up to 5 times [231].

Lastly, experimental challenges with regards to the current measurement, that could affect the I-V data, are considered at the end of this chapter.

5.4 WS_2 on gold

5.4.1 Sample characterization

Further measurements were performed on a mechanically exfoliated WS_2 flake that was placed directly on a gold substrate which had been prepared by evaporation of 100 nm gold on 3 nm chromium. The transfer of the TMDC flake was again performed in Marburg via dry viscoelastic stamping onto the substrate prepared in Frankfurt by thermal evaporation deposition. The gold substrate was electrically connected to serve as the bottom electrode. Photolithography processing was not necessary. The layered structure of the WS_2 flake is best seen in the optical microscopy images, shown in Figs. 5.9a and 5.9d, due to their different transparencies. We can distinguish three terraces of different heights.

Fig. 5.9c shows a photoluminescence microscopy image, taken with the setup mentioned in Sect. 4.3. Here, the excitation light at 532 nm is filtered out and the red photoluminescence at 615 nm becomes visible. Photoluminescence is verification for monolayer presence, since it requires a direct band gap that is only present for the single layer structure. One can observe that the photoluminescence only appears on the upper part of the monolayer terrace and is quenched below the apparent fracture that passes through the flake, as is visible in both the optical and the AFM image, Figs. 5.9d and 5.9e. A possible explanation could be a different contact between monolayer and substrate for these two regions, where the lower region allows for charge transfer and subsequent recombination at the gold interface [202, 232, 233]. An uneven contact between flake and substrate could be given for the whole flake. This introduces some uncertainty concerning the true thickness of the flake, considering inclusions of air or water.

The AFM topography images shown in Figs. 5.9b and 5.9e show the same detail visible in the corresponding optical microscopy images. However, the AFM scans allow to determine the height of the WS_2 flake and highlight the size of surface features such as holes, particles, dust and surface defects. A profile of 1 px width spanning across the WS_2 terraces is indicated as a black line in Fig. 5.9e and extracted into the plot given in Fig. 5.10. The three layers were fitted with two steps of equal height, resulting in a step height of Δh = 1.3 nm. Given the thickness of a single WS_2 layer of 6 Å, a step appears to consist of an increase of two layers. Even though the monolayer terrace can be cleary made out in

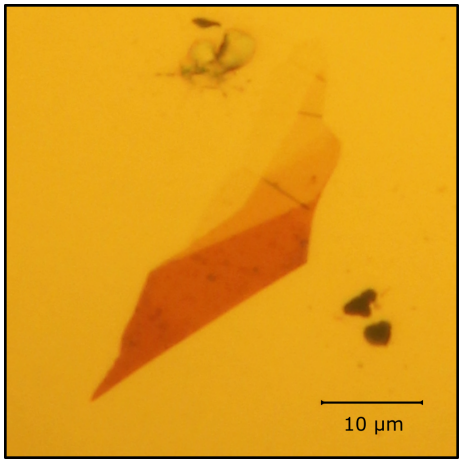

(a) Optical microscopy (50x)

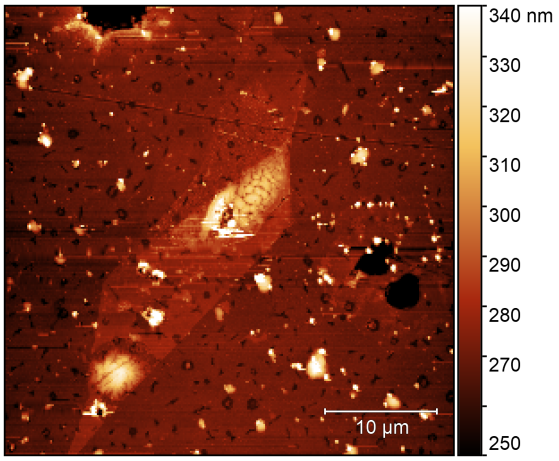

(b) AFM topography

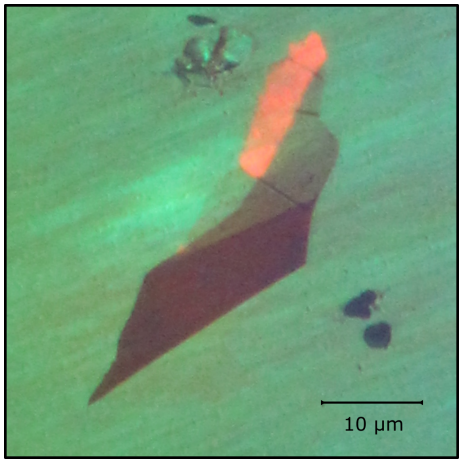

(c) Micro-photoluminescence (50x)

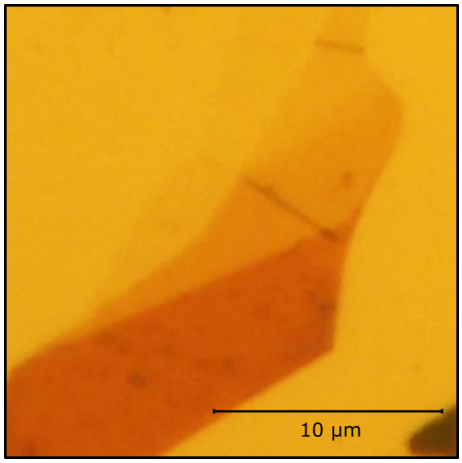

(d) Optical microscopy (50x)

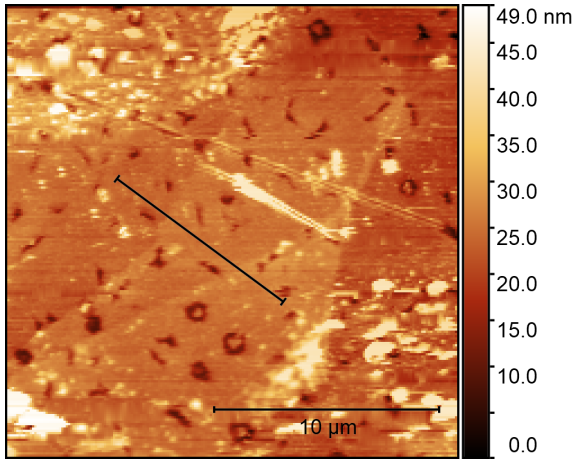

(e) AFM topography

Figure 5.9: Optical microscopy and AFM topography of WS_2 flake on gold substrate. (a,b) The overview shows several larger defects and surface contaminations of the sample. (c) The monolayer can be verified via its photoluminescence. (d,e) The terraces have different layer thicknesses, the profile in (e) is shown in Fig. 5.10.

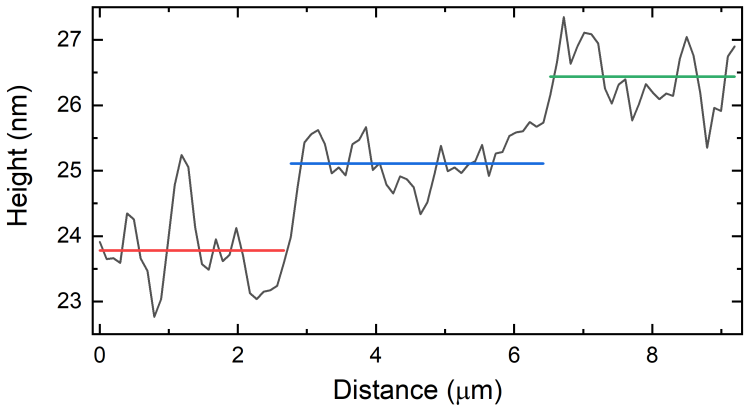

Figure 5.10: Topography lineout from figure 5.9e. The lineout has width of 1 px and passes through two indentation. The three terraces are highlighted by horizontal lines of height spacing $\Delta h = 1.3\,\mathrm{nm}$.

the optical microscopy image and is confirmed by photoluminescence microscopy, the AFM does not resolve the topography contrast. The insufficient AFM heigh resolution may be caused by the use of open-loop height piezos and possibly capillary forces from water films introducing topographical artifacts [229].

For I-V measurements on this sample, cantilever type RMN-12PT400B was used (see Table 2.2) and a contact force of about 100 nN was applied.

5.4.2 Tunnel current analysis

I-V measurements were performed on the three terraces of the WS_2 flake shown in Fig. 5.10. An analysis of the data collected on the two upper terraces (thicker tunneling width) is presented here. No useable I-V measurements were possible on the first terrace. This may be due to the monolayer thickness and thus steep onset and high current flows through the single layer, which could not be resolved.

Figs. 5.11 and 5.12 show the data for the middle and top terrace, respectively. The Fowler-Nordheim model, Eq. 5.11, was fit to the manually selected linear regime of the Fowler-Nordheim plot (right). The data used for fitting is marked by circles; only one sweep direction was considered. For these fits, the three parameters for tunnel barrier heights Φ_1, Φ_2 and a common barrier width d were simultaneously determined with a least squares fit. A contact area of $A = 29\,\mathrm{nm}^2$ and an effective mass $m^* = 0.39 m_0$ for WS_2 were assumed, as with the previous sample. The results are shown by solid lines in both figures with parameters given in the legends and summarized in Table 5.3 for middle and top terrace.

	d (nm)	Φ_1 (eV)	Φ_2 (eV)
middle terrace	4.88	0.91	1.06
top terrace	5.97	0.76	1.02

Table 5.3: Fitting results for Schottky barrier height and tunneling width for the two data sets shown in figures 5.11 and 5.12.

From Schottky-Mott's rule, Eq. 5.17, and Table 5.1, the theoretical ideal tunnel barrier heights are calculated to be

$$\Phi_1 = \Phi_{\mathrm{PtIr}} - \chi = 0.90\,\mathrm{eV} \tag{5.19a}$$

$$\Phi_2 = \Phi_{\mathrm{Au}} - \chi = 1.15\,\mathrm{eV} \tag{5.19b}$$

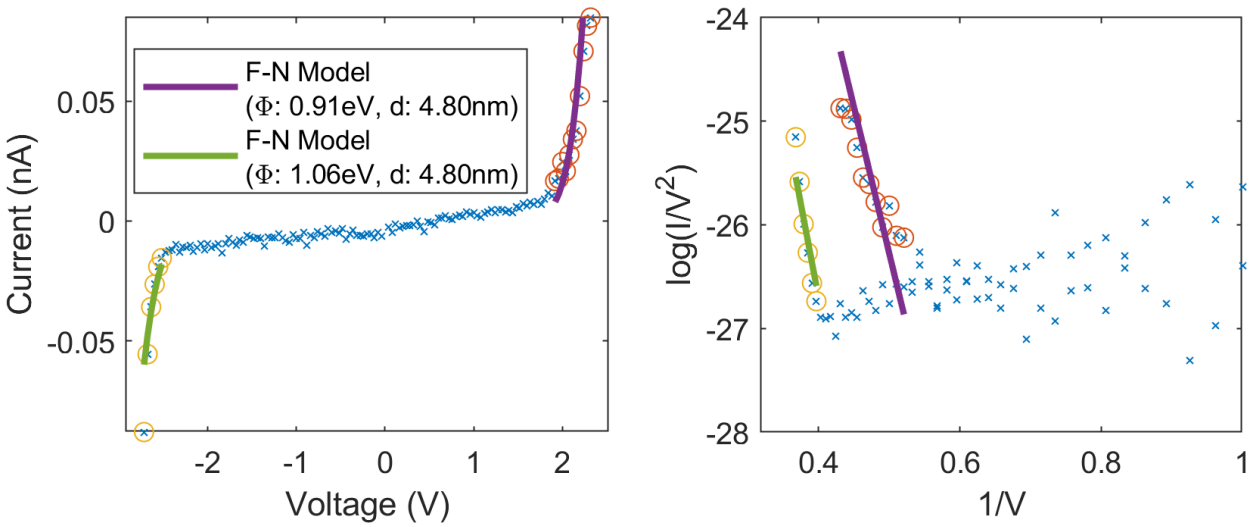

Figure 5.11: I-V measurement on the middle terrace of the WS_2 flake, shown in linear scale and as Fowler-Nordheim plot. The data range used to fit the Fowler-Nordheim model is marked with orange and yellow circles. Solid lines show the fitting result with the parameters as shown in the legend.

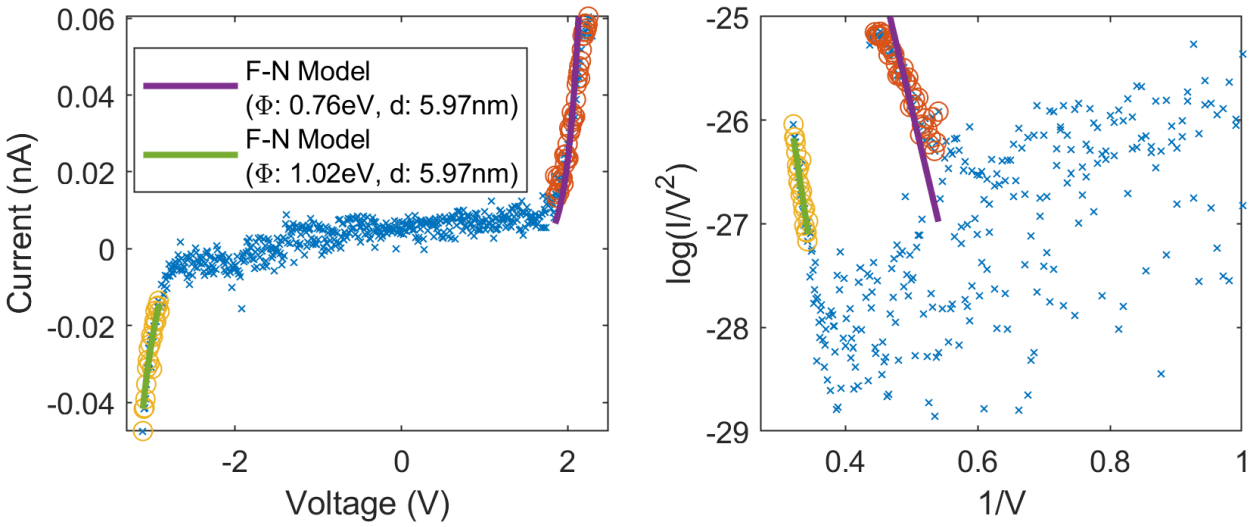

Figure 5.12: I-V measurement on the top terrace of the WS_2 flake. The data range for the Fowler-Nordheim fit is marked with orange and yellow circles. The fit result is shown by solid lines for the parameters in the legend.

and the tunnel widths, as determined from Fig. 5.10, are $d_{\mathrm{middle}} = 3a$ and $d_{\mathrm{top}} = 5a$, where $a = 6\,\text{Å}$ is the single layer thickness of WS_2.

The resulting values for the Schottky barrier heights are comparable in size for the middle and upper terrace and lie close to the theoretical values. Moreover, additional image force lowering further lowers the expected values. The difference in tunneling widths $\Delta d = 1.09\,\mathrm{nm}$ is equal to $1.8a$, i.e. about two layers. The relative thicknesses between middle and top terrace thus matches the expected step height from the AFM measurement. However, the absolute tunneling thicknesses of $\approx 8a$ and $\approx 10a$ (where $a = 6$ Å) is twice the value expected from the AFM profile, Fig. 5.10.

Several reasons could lead to these deviations. Firstly, as with the WS_2 on graphene sample described Sect. 5.3.1, systematic AFM measurement errors could occur, e.g. due to water adsorption [229] . Unfortunately, the monolayer thickness could not be resolved in the measurement, which would allow to reference the AFM topography to the known monolayer thickness (identified through photoluminescence microscopy). Secondly, water adsorbents also affect the current flow between tip and sample as the electrical contact may not be well-controlled. Thirdly, the contact between TMDC flake and gold substrate was assumed to be ideal. However, roughness of the surface may easily lead to on inhomogeneous contact that would factor into the heterojunction formation as well as directly into the current flow. As these issues are prone to affect all c-AFM measurements presented here, they are considered more detailed in Sect. 5.5.

Indeed, repeated measurements at identical and different locations on the WS_2 terraces showed weak reproducibility of the I-V data, which may be due to variances of the contact formation between substrate, sample and probing tip. An impression of the variation in measurement results is given by several additional I-V graphs and Fowler-Nordheim analysis in Appendix A.3.

5.5 Experimental challenges

5.5.1 Water adsorption in ambient atmosphere

From the comparison of measurements and theoretical predictions for the two samples analysed in this chapter, it was suggested that the contact between TMDC flake and c-AFM tip may not behave ideally. Firstly, a systematic topographical offset was suspected to distort the experimental determination of the van-der-Waals flakes' thicknesses. Secondly, a non-ideal electrical contact between surface and tip would affect the I-V characterization of the tunnel barrier.

Indeed, several authors point out experimental challenges with c-AFM and AFM measurements on two-dimensional materials. A possible reasons for systematic AFM topography offsets was proposed by Gupta et al. to be due to a different tip-sample attraction force on different materials, e.g. explaining an offset of 0.3 nm when measuring on graphene and SiO_2 [234]. This however can hardly explain the offset of about 3 nm obtained in Sect. 5.4.2. Additionally, the height resolution of the setup used here is only about 1 nm and thus unable to resolve the offset stated by Gupta et al. Contrary to the lateral translational stage, the z axis piezoelectric actuators of the AFM used here run in open-loop (only the AFM feedback applies) which may slightly affect quantitative topography readings.

Protrusions of 0.3 nm height have also been described by Ando et al. and could be assigned to surface contamination with water adsorbates [235]. Furthermore, the authors compare c-AFM measurement in ambient (60% humidity) to vacuum atmosphere and conclude that "current measurement in the existence of adsorbed water is not suitable for

quantitative analysis" [235] of Fowler-Nordheim plots.

Furthermore, Sumaiya et al. report that "electrical contact resistance measurements performed via c-AFM suffer from poor reliability and reproducibility ... due to ... sample roughness, contamination via adsorbates, changes in ... humidity and temperature, as well as deformation of the tip apex caused by contact pressures and/or Joule heating" [236]. Switching from ambient to dry nitrogen atmosphere is suggested to resolve most issues; additionally annealing and a higher contact force ($> 30\,\mathrm{nN}$) also improve the reliability.

The references strongly suggest that the measurements presented in this chapter may be affected by water adsorption, as they were also performed under ambient conditions. Water adsorption appears to be a general issue in c-AFM measurements, dry or vacuum atmosphere should be used to verify this hypothesis in future measurements.

5.5.2 Substrate roughness

Another source for reliability and reproducibility issues stated by Sumaiya et al. is sample roughness [236]. The use of an evaporated gold film on a chromium adhesion layer as a substrate for the WS_2 flake in the second sample was meant to render the photolithography processing unnecessary, due to issues detailed in Sect. 5.5.3. However, the gold surface may introduce additional surface roughness compared to the use of graphene on SiO_2 for the first sample.

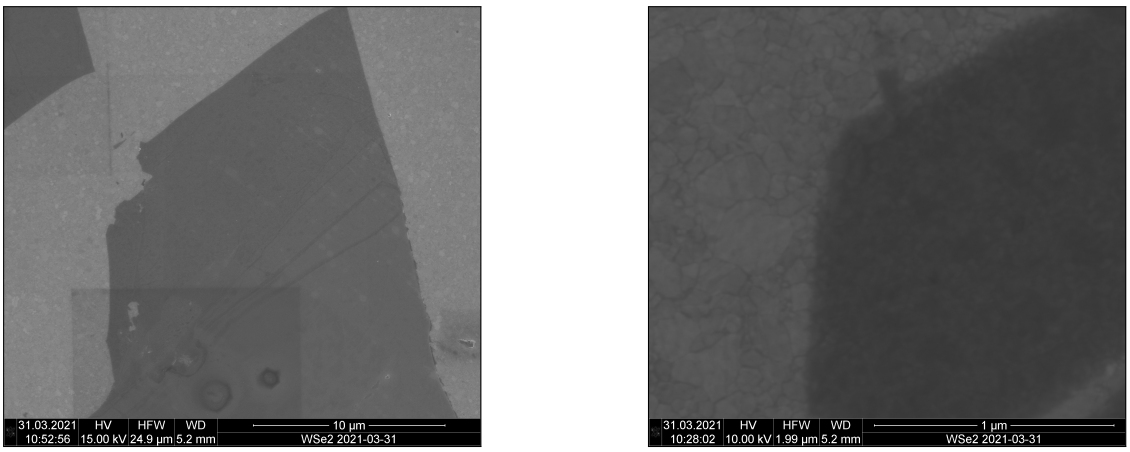

(a) Overview of WSe_2 on gold. (b) Zoom on gold surface and WSe_2 edge.

Figure 5.13: SEM images of a WSe_2 flake on an evaporated gold film. The high-resolution allows to evaluate the surface roughness of the surface. (a) Overview with a scale bar of $10\,\mu\mathrm{m}$. (b) Magnified view of flake edge to amplify the surface roughness (light grey area) with a scale bar of $1\,\mu\mathrm{m}$.

Fig. 5.13 shows SEM images of a TMDC flake on a comparable gold substrate. Surface structure and roughness of the evaporated film are better resolved than in the AFM images. While the TMDC flake is smooth, a rough gold surface is apparent from Fig. 5.13b. The gold appears in islands of very roughly $100\,\mathrm{nm}$ diameter. The gold film was deposited at a rate of about $1.5\,\mathrm{Å/s}$ onto unheated SiO_2 substrate. These parameters are similar to the evaluation of Figs. 1a and 5a by Liu et al. [237] and correlate with a surface roughness of about $5\,\mathrm{nm}$. The metal-WS_2 interface partially inherits the roughness from the substrate, since the layer doesn't conformally follow the rough surface. It has been suggested that a roughness $>2\,\mathrm{nm}$ causes variations in the metal-TMDC distance leading to local band bending and formation of trap states [238].

Evidently, the gold surface may give rise to an ill-defined heterojunction or tunnel barrier variations and additionally permit water or air inclusions below the exfoliated WS_2 flake. Another viable method for clean transfer of van-der-Waals crystals to noble metal surfaces is to thermally evaporate the metal onto bulk TMDC crystals [239] or onto TMDC monolayers [240]. Alternatively, it may be more feasible to return to using graphene as a bottom electrode. This was done for the sample presented in Sect. 5.3, and gold deposition was only needed to create an electrical contact to the larger smooth graphene flake.

5.5.3 Choice of photoresist

It was pointed out that using graphene as a bottom electrode placed directly onto SiO_2 substrate has advantages over using a fully gold coated substrate. It is well-known that one of the key advantages of working with two-dimensional materials is that they can be readily stacked into van-der-Waals heterostructures [180].

For the sample fabrication gold contacts were created as electrical contacts by photolithography, gold-evaporation and lift-off. It was discovered during the preparation of several samples used within thesis that the standard image reversal photoresist AR-U 4040 (Allresist) is not appropriate when TMDC flakes are already present on the substrate, since heavy bubble formation after the first UV-exposure in the photoresist prevents further processing. The exposure was tried for varying exposure times from -1 s to +10 s deviation from the standard process. Fig. 5.14 shows the typical state of the photoresist imaged with an optical microscope. The pads and leads (5 µm width) meant to define the gold electrical leads can be seen at the right and centre of the image.

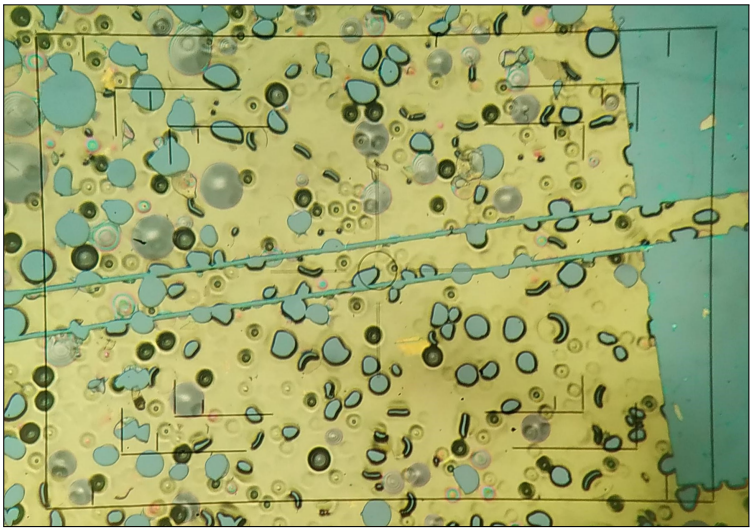

Figure 5.14: Typical state of a structure when bubbles are formed during the UV exposure. The slanted parallel lines each have a width of 5 µm. The bubble formation occurs solely on substrates that had been prepared with TMDCs flakes.

The established process used regularly on clean SiO_2 substrates is tempering the photoresist to room temperature, spin-coating it onto the substrate (15 s at 2000 rpm and 60 s at 6000 rpm), tempering (5 min at 85°C) and image-wise UV exposure (2.6 s at 4.7 mW cm^{-2}). It is noted that the irradiance given by the optical energy controller of the mask aligner MA 45 (SUSS) at channel 1 (i.e. 4.7 mW cm^{-2}) is probed at 365 nm. The photoresist AR-U 4040 is photosensitive at 365 nm, 405 nm and 436 nm. These spectral lines of the mercury-vapor lamp can be assumed to be roughly of the same intensity. The crosslinking bake (5 min at

103°C) and flood exposure (29 s at 4.7 mW cm^{-2}) were not performed when bubbles formation occured. Annealing the sample at 160° (5 min) could not solve the bubble formation issue. Complete removal of the TMDC flakes by hydrofluoric acid (1 min) however did.

Bubble formation during the exposure is often due to out-gassing of nitrogen gas in (typically positive but also reversal) photoresists on diazonaphthoquinone (DNQ) basis. Ideally, nitrogen diffuses rapidly from the resist film. However, if nitrogen cannot escape quickly, bubbles, blisters or cracks can form. Typically, this is the case for thick resist layers, high exposure intensity or insufficient soft-bake tempering prior to exposure. For the TMDC sample here, nitrogen gas may be trapped on the sample due to adhesion on TMDC flakes or residuals. Using a negative resist without out-gassing components may also solve the issue. [241]

Switching to the negative resist AR-N 4340 (Allresist) indeed solved the issue. Appropriate process parameters were found close to the data sheet with spin-coating (60 s at 4000 rpm), soft-bake (1 min at 90°C), UV exposure (6.4 s at 4.5 mW cm^{-2}), crosslink bake (2 min at 95°C) and development (60 s in AR 300-35, Allresist).

5.5.4 Sample defects due to current flow

Lastly, it was observed that applying a voltage bias and measuring current flow across the TMDC flake can permanently damage the sample. Fig. 5.15a shows one of these characteristic defects with a diameter of about 3 µm. The sample shown is the WSe_2 on gold substrate, which was depicted in the SEM images of Sect. 5.5.2. A white line marks the profile extracted into Fig. 5.15d, showing the terraced multilayer structure. All defects visible in the AFM images are also seen at the bottom of Fig. 5.13a.

In order to inspect the defect formation further, two I-V scan were performed at locations next to the existing defect. Firstly, a sequence of five scans with contact force of 50 nN and maximum current of 1 nA was applied. Fig. 5.15b shows the protrusion, which occurred due to these scans. The main protrusion has a diameter of about 1 µm, however a total diameter of 3 µm is observed for the defect. Another I-V sequence of three scans with maximum current of 1 nA led to the formation of the triangular defect shown in Fig. 5.15c, which lies at the edge of the layered flakes. Again, the diameter is about 3 µm.

The protrusions in Figs. 5.15a and 5.15b have heights of 50 - 60 nm. One hypothesis for the formation of these nano summits is that the metallic tip welds itself to the van-der-Waals layer due to heating from the current flow and then pulls the layer up when retracting after the I-V measurement. Furthermore, the formation of a tip-attached water nanomeniscus could increase the tip-sample adhesion force even further [242]. From Fig. 2.8 one can read the adhesive force of the contact-mode tip on gold of to be 6 nN, which translates into a cohesion energy of about 2.5 J m^{-2} for a tip area of 29 nm^2 [242, Methods]. Assuming an interlayer adhesion force of 0.5 J m^{-2} as for MoS_2/MoS_2 [242], hoisting the WSe_2 layer with the nanotip appears a plausible explanation.

Fig. 5.16 shows the general conditions of a sample images prior to performing I-V measurements, Fig. 5.16a, and after having performed many measurements, Fig. 5.16b. The strong degradation and formation of protrusions is apparent and most definitely affects both reproducibility and reliability of the c-AFM measurements.

5.6 Conclusion

The nanoscopic measurement technique c-AFM was introduced in this chapter to measure vertical currents on two WS_2 flakes placed on graphene and on gold, respectively. The

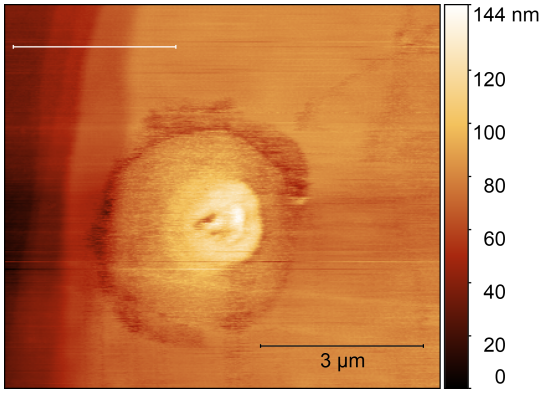

(a) Single defect prior to sequential scans.

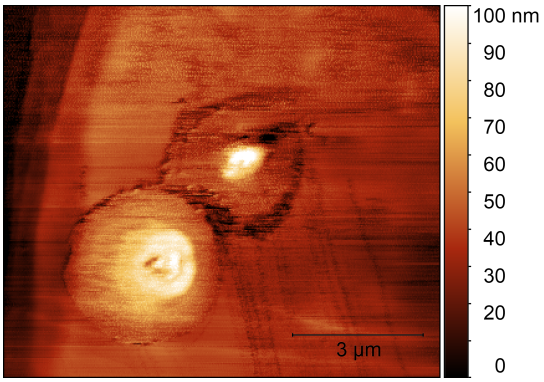

(b) Second defect to the right of (a).

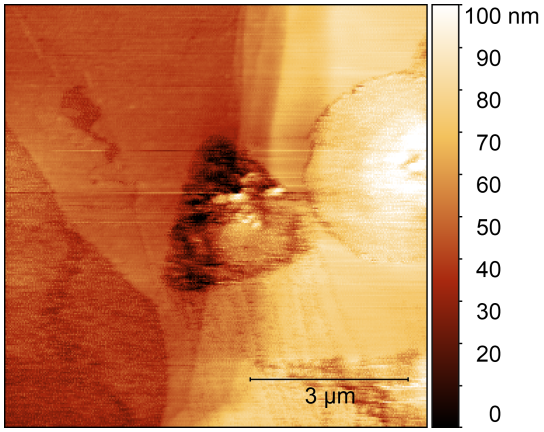

(c) Third defect to the left of (a).

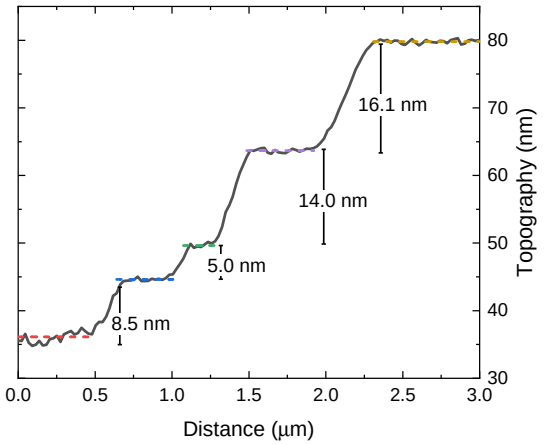

(d) Profile extracted from (a).

Figure 5.15: Different surface defects on a terraced WSe_2 sample that appeared after c-AFM measurements at the respective locations stated in the captions of (a-c). (d) shows the step profile marked in (a) as a white horizontal line.

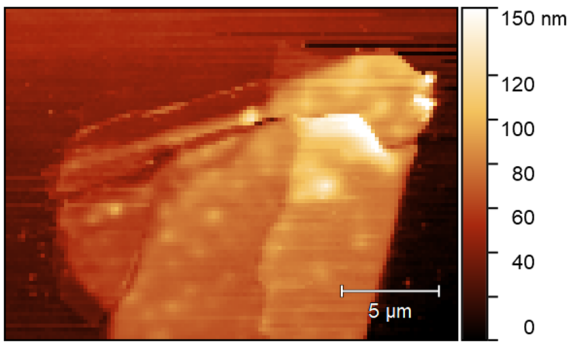

(a) WS_2 flake prior to I-V measurements.

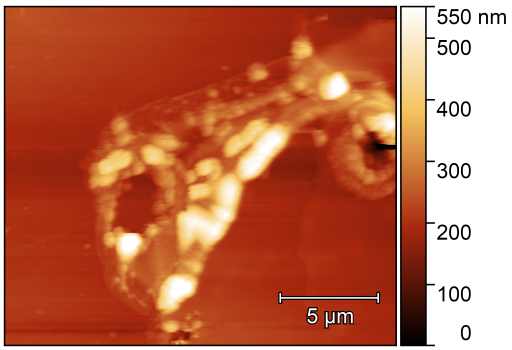

(b) WS_2 after many I-V measurements.

Figure 5.16: Comparison of the condition of a WS_2 flake (a) before and (b) after many c-AFM measurements primarily on the terraces of different layer thicknesses. The sample is heavily deteriorated which complicates topography and I-V measurements.

measured currents through the TMDC flake were identified as due to Fowler-Nordheim tunneling. By fitting a Fowler-Nordheim model to the experimental data, the Schottky barrier height of WS_2 to the bottom material and to the platinum tip, and in one case the barrier width, were extracted and compared to expected ideal values.

It was found, however, that the AFM shows systematic measurement artifacts and the c-AFM measurements suffer from weak reproducibility. Several experimental challenges are summarized and referenced to relevant literature. The take-away messages for future experiments are as follows:

1. The nanoscopic c-AFM measurements in ambient conditions are influenced by uncontrolled water adsorption on the sample surface and the probing tip, and the use of dry atmosphere is recommended.

2. High roughness of the metal substrate cause an ill-defined contact and Schottky barrier between WS_2 and the substrate. The use of graphene as a bottom electrode circumvents the fabrication issues connected to the evaporated thin film.

3. Photo-resists with nitrogen out-gassing components are not well-suited for samples that are prepared with TMDC flakes. This is probably due to gas adhesion on vander-Waals crystals or fabrication residuals. An alternative negative photo-resist is suggested.

4. Strong deterioration of the TMDC flake even after single I-V measurements are observed. Tip heating and water menisci are suggested as main origins causing an excessive adhesion between tip and sample, which may generates protrusions of the sample upon retraction of the tip.

Further c-AFM measurements on TMDC, obviously considering these observations, seem promising as the preliminary studies could already clearly identify Fowler-Nordheim tunneling, withstanding the above-mentioned issues which challenge a faithful quantitative interpretation. Prospectively, more complex two-dimensional heterostructures can be fabricated with relative ease, allowing for vertical tunneling (transistors) with multiple barriers [185–187] and eventually resonant tunneling [92, 243, 244].

Chapter 6

Terahertz higher harmonics from p-doped silicon

6.1 Introduction

The preceding chapters have focussed on the physics of two-dimensional systems, their interaction with light and prospective application in nanoscale devices. Two-dimensional materials are even heralded as a promising platform for tailored nano-electronics and photonics at terahertz frequencies [245]. Viti and Vitiello make out the major disruptive branches in the field: THz detection, modulation, non-linear light–matter interaction and THz nanoscience [245]. With respect to non-linear optics, graphene has already fuelled relevant research on saturable absorption [246, 247] and higher harmonic generation [248, 249] owing to its unique bandstructure [250]. Recently, higher harmonics up to the ninth order could be demonstrated from graphene coupled to a gold-grating metasurface from a fundamental of 0.7 THz and field strength of $\sim$30 kV cm^{-1} [251].

While the non-linear response of two-dimensional materials is drawing increasing attention, many aspects of optical harmonic generation in bulk crystals are still subject to avid research [252–255]. In fact, the first observation of high-order harmonics in bulk crystalline solid was only made in 2010 by using mid-infrared few-cycle laser pulses [256]. Still, the differences of the microscopic mechanisms that govern higher harmonic generation from solids as opposed to atomic gases remain a topic of intense debate [257, 258]. Furthermore, a clear understanding of the microscopic processes, their relationship to the bandstructure and macroscopic propagation effects is still lacking [259]. An exciting research direction is the use of higher harmonic spectra for all-optical reconstruction of the bandstructure [260–262]. This is achieved by exploiting the coherent motion of carriers driven by intense laser pulses. Using long-wavelength (below-the-bandgap) pulses, the spectra reflect the ultrafast dynamics and non-linearities of carrier wave packets in conduction and valence band of the bulk crystal [263].

In this chapter, these ideas are drawn upon to study higher harmonic generation from p-doped silicon. In contrast to the non-linearity from electrons in n-doped silicon, the mechanisms for holes in the valence band are not yet equally well understood [264–266]. Here, the relative importance of the microscopic mechanisms underlying the non-linear response is analysed with respect to the light and heavy hole band dynamics in two silicon crystals at cryogenic and room temperature, respectively.

For the case of electrons, it is usually assumed that higher harmonics originate from a combination of bandstructure non-parabolicity or the energy dependence of the momentum scattering rate. The first scenario considers that carriers are driven in their band by the

pulse electric field. For high intensities, carriers are driven with a large amplitude and the parabolic band approximation fails. Hence, non-linear frequency components are generated. In the second scenario, the accelerated carries experience energy-dependent momentum scattering mechanisms. Since the carriers energy oscillates with the momentum according to the band relation E(k), this introduces a non-linear damping term and thus higher harmonics. The relevant scattering mechanisms are scattering by ionized impurities, acoustic and optical phonons.

These mechanisms are disentangled by modelling the higher harmonics spectra using a one-dimensional single particle time domain simulation, which allows to inspect the relative strengths of the two contributions. These simulations are motivated by measurements performed by co-researches at the FELBE[1] and TELBE[2] research facilities. Spectra from two boron-doped silicon crystals were acquired by using short terahertz pulses of high intensity at cryogenic and room temperature, respectively.

The chapter covers the theoretical background on the bandstructure model, the scattering mechanisms and the influence of the density of states. Then, the single particle time domain model is explained and the results from the numerical solution of the differential equation are presented. Finally, the results are compared to the experimental data and a conclusion with respect to the origin of the higher harmonics from p-doped silicon is discussed.

6.2 Theory

6.2.1 Silicon bandstructure model

Silicon has a diamond cubic crystal structure and a lattice parameter of 0.543 nm. Its Brillouin zone is depicted in Fig. 6.1. The high symmetry points and their connecting paths are marked with red circles and lines, respectively.

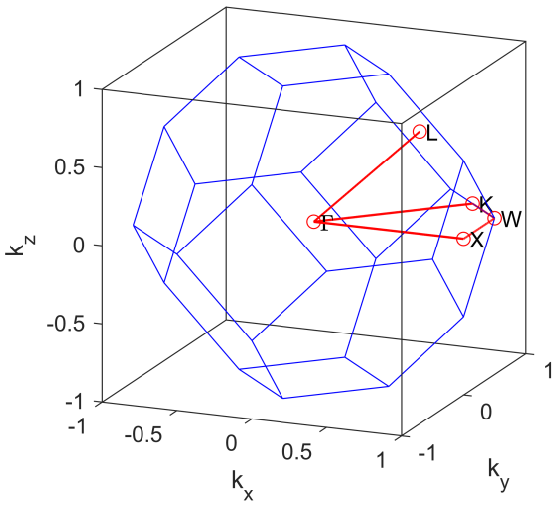

Figure 6.1: Face-centered cubib unit cell of Silicon. The paths between the high-symmetry points represented in the bandstructure diagram are shown in red.

[1]Free Electron Laser at ELBE (Electron Linear accelerator with high Brilliance and low Emittance), Helmholtz-Zentrum Dresden-Rossendorf

[2]High-Field High-Repetition-Rate Terahertz facility at ELBE, Helmholtz-Zentrum Dresden-Rossendorf

The bandstructure relates the momentum position of a carrier in the Brillouin zone to an energy. Fig. 6.2 shows a two-dimensional representation of the bandstructure, where the path along the high-symmetry points is mapped onto the x-axis in units $|k|$. This depictions is somewhat uncommon for the non-radial paths (X-W-K), as they are not represented along the path and thus appear rather short, but helps to give a more intuitive idea of the curvature/slope of E(k). While some parts of the bandstructure can be approximated with a parabolic energy band approximation, e.g. around Γ as depicted in the insets of Fig. 6.2, in general numerical models are employed to gain a full representation of the bandstructure for larger k-values and across the whole Brillouin zone. Fig. 6.2 shows the result for the tight-binding model including spin-orbit coupling (solid line) [267] and a Non-Local Empirical Pseudo Potential Method (EPM) including spin-orbit coupling (dashed line) [268, 269] for the valence bands in two parts of the Brillouin zone (Γ-X and Γ-K). The fact that heavy and light hole valence band both converge at the Γ point means that carriers in both bands contribute to the higher harmonic generation.

Obviously the exact shape of the bandstructure differs for the two approaches, even in the vicinity of Γ, see insets. The EPM is expected to be more exact, and the calculations in this chapter are based on numerical data based on this model[3] This is possible since the carrier dynamics along Γ-X, or ⟨100⟩, are the focus of this chapter. The tight-binding model is only utilized to allow a comparison of the three-dimensional density of states for which the whole Brillouin zone must be discretized. The comparison of curvatures along Γ-X and Γ-K shows obvious differences pointing towards different effective masses along those two directions. To verify that this is indeed plausible, these values are compared to a warped energy surface approximation [270, p. 12ff].

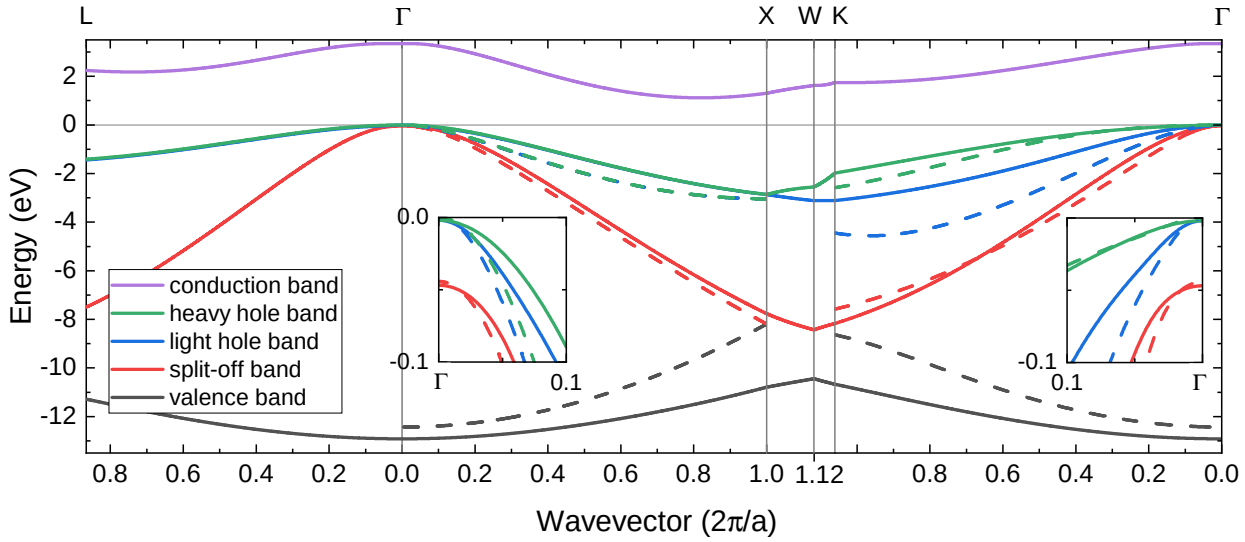

Figure 6.2: Silicon bandstructure calculated with tight binding (solid) and for selected orientations and bands with EPM (dashed). The insets show a zoom onto the vicinity of Γ, pointing out the different curvatures of heavy and light hole band and the splitting of the split-off band as well as different curvatures along the directions Γ-X and Γ-K.

Warped energy surface approximation

Using the warped energy surfaces model [270, p. 12ff, 271, p. 55], the effective masses of heavy and light hole bands in Silicon can be approximated. The band parameters of common

[3] calculated by C. Jungemann, Institut für Theoretische Elektrotechnik, RWTH Aachen.

cubic semiconductors are given in Table 1.1 and Eq. 1.44 of Lundstrom [270, p. 14f] as A = 4.22, B = 0.78, C = 4.80, giving the parameters

$$a = \frac{\hbar^2 A}{2m_0}, \qquad b = \frac{B}{A}, \qquad c = \frac{C}{A} \tag{6.1}$$

The warping function g is [270, Eq. 1.43]

$$g = \left(b^2 + c^2\left(\sin^4(\theta)\cos^2(\phi)\sin^2(\phi) + \sin^2(\theta)\cos^2(\theta)\right)\right)^{1/2} \tag{6.2}$$

from which the effective mass for heavy and light holes, respectively, is calculated

$$m^* = -\frac{\hbar^2}{2a\left(1 \pm g(\theta,\phi)\right)}; \tag{6.3}$$

Table 6.1 demonstrates that the magnitude of the difference in effective masses between heavy and light hole in fact depends strongly on the crystal orientation, as is consistently predicted by the warped energy surface approximation and the EPM. However, the tight binding model displays severe discrepancies with regard to the effective mass. For reference, the average heavy and light effective masses (averaged over all directions) are $0.467\,\mathrm{m_0}$ and $0.159\,\mathrm{m_0}$, respectively [272, p. 94].

	Γ-X (θ=$\frac{\pi}{2}$, ϕ=0)		Γ-K (θ=$\frac{\pi}{2}$, ϕ=$\frac{\pi}{4}$)	
	heavy hole	light hole	heavy hole	light hole
WARP	$0.291\,\mathrm{m_0}$	$0.200\,\mathrm{m_0}$	$0.589\,\mathrm{m_0}$	$0.148\,\mathrm{m_0}$
EPM	$0.273\,\mathrm{m_0}$	$0.199\,\mathrm{m_0}$	$0.551\,\mathrm{m_0}$	$0.146\,\mathrm{m_0}$
TB	$0.564\,\mathrm{m_0}$	$0.303\,\mathrm{m_0}$	$0.943\,\mathrm{m_0}$	$0.249\,\mathrm{m_0}$

Table 6.1: Comparison of effective masses for heavy and light hole along to crystal orientation calculated using three different models: warped energy surface (WARP), EPM and tight binding (TB).

6.2.2 Scattering mechanisms

In the semi-classical view on carrier transport, the wave packet is described in the particle picture. Several assumptions allow this simplification. Momentum and energy are assumed to be known with low uncertainty. The position is assumed to be well known in comparison to length scales over which the potential may vary. In this case, carrier motion and velocity can be described in classic terms with the well-known relation between force and (crystal) momentum $F = \hbar\dot{k}$. For Silicon, this means that the potential must vary more slowly than the hole's thermal de Broglie wavelength of about 6 nm at room temperature. Smaller scales only become critical in ultra-small devices, quantum wells or nanowires. However, a quantum-mechanical treatment is required to describe scattering events, since they involve varying potentials on small scales. [270, p. 40f]

In the particle picture, carriers (in the form of Bloch waves) move through the crystal undisturbed until they encounter a (weak) perturbation which causes a scattering event and changes its momentum k_0 to k_0'. The transition rate $S(k_0, k_0')$ depends on the perturbing potential $U_s(z,t)$ of the scattering type via the matrix element $H^{a,e}_{k_0'k_0}$ for absorption $E' = E + \hbar\omega$ and emission $E' = E - \hbar\omega$.

$$S(k_0, k_0') = \frac{2\pi}{\hbar}\left|H^{a,e}_{k_0'k_0}\right|^2 \delta(E' - E \pm \hbar\omega) \tag{6.4}$$

This is *Fermi's Golden Rule*, a central equation to determine the scattering in semiconductors from the matrix element H_{k_0',k_0} of the scattering potential

$$H_{k_0',k_0} \equiv \int \psi_{k_0'}(z) U_s(z,t) \psi_{k_0}(z) dz \tag{6.5a}$$

$$\simeq \frac{1}{L} \int_{-L/2}^{+L/2} e^{-ik'z} U_s(z,t) e^{ikz} dz \tag{6.5b}$$

The approximation Eq. 6.5b assumes that the overlap integral approaches unity, which is the case for parabolic bands. The electron is then expressed in a plane wave expansion rather than in Bloch waves [270, p. 45]. The perturbing potential can be similar to a δ-like center (defect or impurity) or periodic (phonon), depending on the type of scattering experienced by the carrier [271, p. 55ff, 273, Table 2].

Momentum and energy scattering

In order to find the transition rates, one needs to identify the perturbation potentials for the applicable scattering events. In the following, scattering by ionized impurities, acoustic and optical phonons is discussed.

According to the previous description, the *scattering rate* $\Gamma = \frac{1}{\tau(\vec{p}_0)}$ is given by the average time between collisions

$$\frac{1}{\tau(\vec{p}_0)} = \sum_{p',\uparrow} S(\vec{p}_0, \vec{p}') \tag{6.6}$$

However, two other measures must be introduced that are critical for distinguishing different scattering mechanisms: momentum relaxation and energy relaxation.

Several scattering mechanisms mainly deflect by small angles. The carriers are thus not scattered isotropically and even after several scattering events, the original momentum may only be fractionally affected. The *momentum relaxation rate* is a measure of the mean time (and thus number of scattering events) necessary until a carrier loses its original direction. It is defined via the polar angle α between the momenta $\vec{p}_0$ before and $\vec{p}'$ after a scattering event. The average time to scatter the carrier into any direction is thus increased.

$$\frac{1}{\tau_m(\vec{p}_0)} = \sum_{p',\uparrow} S(\vec{p}_0, \vec{p}') \left[1 - \frac{p'}{p_0} \cos(\alpha)\right] \tag{6.7}$$

The *energy relaxation rate*, on the other hand, is the scattering rate weighted by the fractional energy change. One example where it would differ from the momentum relaxation rate is a scattering event that merely changes the direction of a particle while its energy remains constant (elastic collisions).

$$\frac{1}{\tau_E(\vec{p}_0)} = \sum_{p',\uparrow} S(\vec{p}_0, \vec{p}') \left[1 - \frac{E(\vec{p}')}{E(\vec{p}_0)}\right] \tag{6.8}$$

These three quantities are related to how often, in what direction and at what energy loss carriers are scattered when moving through a crystal.

Perturbing potentials

The scattering potential of an ionized impurity can be described via the Coulomb potential with an additional term accounting for screening by mobile carriers n_0

$$U_s(r) = \frac{q^2}{4\pi\epsilon_r\epsilon_0 r} e^{-r/L_d} \qquad \text{ionized impurities} \tag{6.9}$$

where $L_d = \sqrt{\epsilon_r\epsilon_0 k_B T/(q^2 n_0)}$ is the Debye length, a measure of the screening distance. For low mobile carrier densities, the exponential screening term can be neglected.

Scattering by phonons occurs because vibrations in the crystal lattice deform the band-structure and create a periodic grating that scatters the carriers. Acoustic phonons are waves where oscillating neighbouring atoms are in phase and the lattice spacing is affected by the strain $\frac{\delta u}{\delta x}$ instead of directly by the atom displacement $u(x,t)$. On the other hand, optical phonons displace neighbouring atoms with a half-cycle phase-shift and the lattice spacing is directly affected by the atom displacement $u(x,t)$. The corresponding perturbing potentials are defined via their respective deformation potential constants D_A and D_O [270, p. 61]

$$U_{AP}(x,t) = D_A \frac{\delta u}{\delta x} \qquad \text{acoustic phonons} \tag{6.10a}$$

$$U_{OP}(x,t) = D_O u(x,t) \qquad \text{optical phonons} \tag{6.10b}$$

Both acoustic and optical phonon scattering are relevant processes for hole scattering in silicon. The constants D_A and D_O (with different units) for silicon are given in Table 6.2. For electrons, on the other hand, optical phonon scattering is limited by symmetry conditions and forbidden along $\langle 100 \rangle$.

From the perturbation potentials given above, one can now go on to calculate the scattering times for the different scattering processes. Finally, the scattering rates can be added together to yield the total scattering time, according to *Matthiessen's rule* [270, p. 167], see Sect. 6.2.2.

Ionized Impurity Scattering

Having determined the perturbing potential of an ionized impurity, Eq. 6.9, one can calculate the Hamiltonian using Eq. 6.5b using spherical coordinates.

$$H_{\vec{p}',\vec{p}_0} = \frac{1}{\Omega} \int e^{-i\vec{p}'\vec{r}/\hbar} U_s(r) e^{i\vec{p}\vec{r}/\hbar} d^3r \tag{6.11a}$$

$$= \frac{1}{\Omega} \left(\frac{q^2}{4\pi\epsilon_r\epsilon_0} \right) \int e^{-i\vec{p}'\vec{r}/\hbar} \left(r^{-1} e^{-r/L_d} \right) e^{i\vec{p}\vec{r}/\hbar} d^3r \tag{6.11b}$$

$$= \frac{1}{\Omega} \left(\frac{q^2}{4\pi\epsilon_r\epsilon_0} \right) \int_0^{2\pi} d\phi \int_{\theta_{\min}}^{\theta_{\max}} \int_0^{\infty} e^{-r/L_d} e^{i(\vec{p}-\vec{p}')\cdot\vec{r}/\hbar} r dr \sin\theta d\theta \tag{6.11c}$$

One can use the fact, that impurity scattering is elastic and energy is conserved as well as $\hbar\vec{\beta} = \vec{p}' - \vec{p}$ and $|\hbar\beta| = 2p\sin(\frac{\alpha}{2})$ as illustrated in the inset of Fig. 6.3. This allows to formulate [270, p. 67f]

$$H_{\vec{p}',\vec{p}} = \frac{1}{\Omega} \left(\frac{q^2}{4\pi\epsilon_r\epsilon_0} \right) \int_0^{\infty} \int_0^{2\pi} \int_{-1}^{+1} e^{r/L_d} e^{-i\beta r\cos\theta} d(\cos\theta) d\phi dr \tag{6.12a}$$

$$= \frac{q^2}{\Omega\epsilon_r\epsilon_0} \frac{1}{\beta^2 + 1/L_d} \tag{6.12b}$$

The scattering rate for a single impurity per volume Ω then follows from Fermi's Golden Rule, Eq. 6.4. For the total scattering rate, one multiplies by the number of impurities in that volume $N\Omega$.

$$S(\vec{p},\vec{p}') = \frac{2\pi N q^4}{\hbar \epsilon_r^2 \epsilon_0^2 \Omega} \frac{\delta(E'-E)}{\left[4\left(\frac{p}{\hbar}\right)^2 \sin^2\left(\frac{\alpha}{2}\right) + L_d^{-2}\right]^2} \tag{6.13}$$

This approach, which is based on a screened Coulomb potential, is known as Brooks-Herring's approach [270]. Continuing to calculate the momentum scattering rate as described by Eq. 6.7 leads to an expression which correctly describes the decreasing influence of ionized impurity scattering for high energy carriers, because fast-moving carriers spend less time interacting with the perturbing potential. However, for carrier energies approaching zero the momentum scattering rate diverges. This means that once carriers are described by $E = 0$, they will be unable to gain kinetic energy since they experience infinite scattering. This is shown in Fig. 6.3.

The alternative Conwell-Weisskopf approach offers a solution [274]. Screening is neglected altogether ($L_d \to \infty$). Instead, scattering by the Coulomb potential of a single impurity is limited to a distance $b_{\max} = \frac{1}{2}N^{-1/3}$ equal to half the distance between neighbouring impurities. Since carriers passing by an impurity at a distance greater than $b_{\max}$ will not be deflected, this creates a minimum deflection angle $\theta_{\min} = 2\cot^{-1}(b_{max}\frac{2E}{Zq^2})$. For calculating the momentum scattering rate, from Eqs. 6.13 and 6.7 in a spherical coordinate system, the deflection angle α simply equals the azimuthal angle θ; it is integrated over the possible scattering angles within $\theta_{\min} < \alpha < \pi$. The result gives as an expression for the momentum scattering rate after Conwell-Weisskopf that is applicable for low doping and low energy carriers [270, p. 70ff]

$$\Gamma_m(E) = \frac{\pi q^4}{(4\pi\epsilon_0\epsilon_r)^2\sqrt{2m^*}} N E^{-\frac{3}{2}} \ln\left(1 + \left(\frac{E}{E_0}\right)^2\right) \tag{6.14}$$

where $E_0 = \frac{N^{\frac{1}{3}}q^2}{4\pi\epsilon_0\epsilon_r}$. Fig. 6.3 demonstrates how Eq. 6.14 does not diverge for small energies, e.g. for holes passing through the Γ point of silicon's bandstructure.

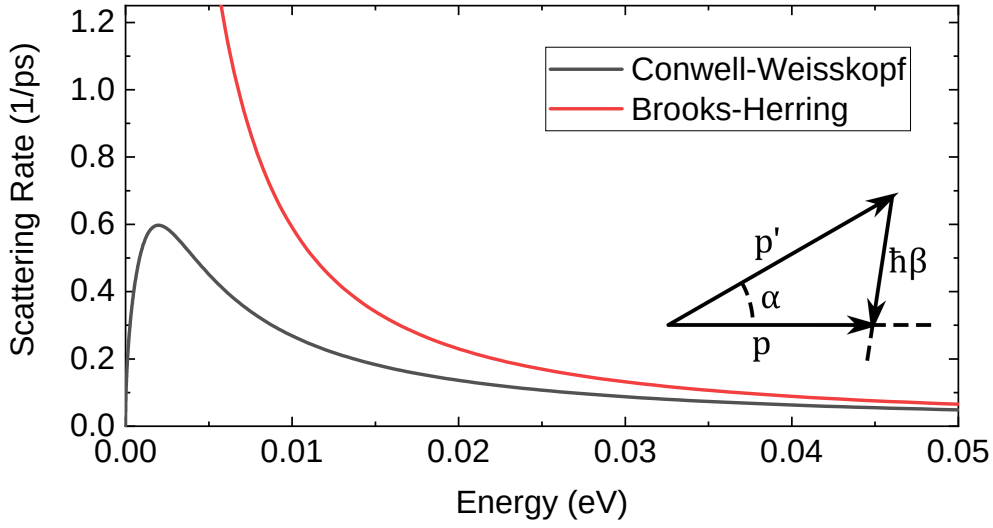

Figure 6.3: Comparison of momentum scattering rate according to Conwell-Weisskopf and Brooks-Herring for silicon with doping density N=5.7 $\times$ 10^{15} cm^{-3} at room temperature. The inset depicts a carrier scattered in an elastic collision by an angle α from $\vec{p}$ to $\vec{p}'$.

Acoustic Phonon Scattering

Using the perturbing potential for acoustic phonons, Eq. 6.10a, and an elastic phonon wave

$$u(x,t) = A_\beta e^{+i(\beta x - \omega t)} + A_\beta^* e^{-i(\beta x - \omega t)} \tag{6.15}$$

one can evaluate the squared matrix element to yield [270, Eq. 2.60]

$$|H_{k_0',k_0}|^2 = |D_A\beta|^2 |A_\beta|^2 \delta_{\vec{p}',\vec{p}\pm\hbar\beta} \tag{6.16}$$

Now, using Fermi's Golden Rule, Eq. 6.4, and unifying momentum and energy conservation into a single expression by assuming parabolic bands, the transition rate yields [270, p. 77]

$$S(k_0,k_0') = \frac{2\pi}{\hbar}|D_A\beta|^2|A_\beta|^2 \frac{1}{\hbar v\beta}\delta\left(\pm\cos(\theta) + \frac{\hbar\beta}{2p} \mp \frac{\omega_\beta}{v\beta}\right) \tag{6.17}$$

The total phonon energy $|A_\beta|^2$ must account for quantized phonon absorption and emission and hence is [270, p. 78]

$$|A_\beta|^2 = \frac{\hbar}{2\rho\Omega\omega_\beta}\left(N_{\omega_\beta} + \frac{1}{2} \mp \frac{1}{2}\right) \tag{6.18}$$

Finally, one needs to integrate the transition rate Eq. 6.17 over all possible transitions according to Eq. 6.7 to find the momentum relaxation rate. Here, conservation of energy and momentum dictates that

$$\hbar\beta = 2p\left[\mp\cos(\theta) \pm \frac{\omega}{v(p)\beta}\right] \tag{6.19}$$

via the polar angle θ between p and β, where $v(p) \approx 10^7\,\mathrm{cm\,s^{-1}}$ is the carrier velocity. The limits of $\cos(\theta)$ of ±1 determine the range of phonon wave vectors β, that are involved in these scattering events and thus define the integration limits $\hbar\beta \in [0, 2m^*v(p)]$. For intravalley scattering, only phonons near the Brillouin zone centre can participate in the scattering processes. In this regime, their dispersion relation is approximately linear and given by the sound velocity $v_s = \omega/\beta$.

The final expression for the momentum relaxation rate due to acoustic optical phonon scattering yields [270, Eq. 2.84]

$$\Gamma_m(E) = \frac{\pi D_A^2 k_B T}{\hbar c_l} g(E) \tag{6.20}$$

where $c_l = v_s^2\rho$ is the elasticity constant given by the sound velocity and the mass density. The values are given in Table 6.2. g(E) is the density of states.

Parameter	Symbol	Value in Si
Mass density	ρ	2.329 g/cm^3
Lattice constant	a	5.43Å
Longitudinal acoustic velocity	v_s	9.04·10^5 cm/s
Hole acoustic deformation potential	D_A	5.00 eV
Hole optical deformation potential[4]	D_O	6.00·10^8 eV/cm
Longitudinal optical phonon energy	E_O	0.063 eV

Table 6.2: Transport parameters for silicon. [270, p. 114f]

[4]Incorrectly tabulated in [270]. Here corrected with missing factor 10^8.

Optical Phonon Scattering

The scattering potential for optical phonons scattering Eq.. 6.10b resembles that of acoustic phonons up to a factor of β^2 in the squared matrix element

$$|H_{k_0',k_0}|^2 = |D_A A_\beta|^2 \delta_{\vec{p}',\vec{p}\pm\hbar\beta} \tag{6.21}$$

Furthermore, since the dispersion relation of optical phonons (nearly constant) differs from that of acoustic phononcs ($\beta = \omega/v_s$), the condition for phonons that can be part of a scattering event changes

$$\hbar\beta = p\left[\mp\cos(\theta) \pm \sqrt{\cos^2(\theta) \pm \frac{\hbar\omega}{E(p)}}\right] \tag{6.22}$$

As above, the term $\cos^2(\theta) \leq 1$ limits the maximum wave vector of the optical phonons. Again, only optical phonons near the Brillouin zone centre are relevant in intravalley scattering. Moreover, scattering with optical phonon cannot be assumed to be elastic as their energy is comparable to thermalized carriers at room temperature.

Using the limitation on phonon wavevectors β as boundaries for the integration over transition rates, one obtains the momentum relaxation rate [270, Eq. 2.86]

$$\Gamma_m(E) = \frac{\pi\hbar D_O^2}{2\rho E_O}\left\{(N_O + 1/2 \mp 1/2)g(E \pm E_O)\right\} \tag{6.23a}$$

$$\equiv \frac{\pi\hbar D_O^2}{2\rho E_O}\left\{N_O g(E + E_O) + (N_O + 1)g(E - E_O)\cdot u(E - E_O)\right\} \tag{6.23b}$$

where $u(E - E_O)$ is the Heaviside step function that takes into account the fact that the emission of an optical phonon is limited to phonons that exceed the optical phonon energy E_O, given by Table 6.2, and

$$N_O = \left(e^{\frac{E_O}{k_B T}} - 1\right)^{-1} \tag{6.24}$$

Matthiessen's rule

Matthiessen's rule states that one can assume the different scattering contributions to be independent of each other and obtain the total scattering time by computing the sum of the individual scattering rates [270, p. 167]. Fig. 6.4 shows a graph with the total and individual scattering times for the two different temperatures ans doping densities considered in this chapter.

Furthermore, as the single particle is expected to represent the average momentum of an ensemble of thermally distributed carriers, the total energy-dependent momentum scattering rate $\Gamma_m(E)$ is convolved by a normalized Gaussian function with a standard deviation $\sigma = 2\mathrm{k_B T}$

$$G(E) = \frac{1}{\sqrt{2\pi\sigma^2}} e^{-\frac{E^2}{2\sigma^2}} \tag{6.25}$$

resulting in a smoothed scattering rate in general and an increased scattering rate at the centre of the Brillouin zone k = 0 and E = 0 eV. The normalized Gaussian is shown in Fig. 6.4 (dotted yellow line).

The convolved momentum scattering times at k = 0 from Fig. 6.4 result in 33.3 ps and 0.2 ps for the temperatures 10 K and 300 K (and corresponding carrier densities), respectively. These values are compared to literature mobilities $\mu = 1 \times 10^5\,\mathrm{cm^2\,V^{-1}\,s}$ and $\mu = 5 \times 10^2\,\mathrm{cm^2\,V^{-1}\,s}$ [275, 276] summarized in [277, p. 123] which yield scattering times of 33.5 ps and 0.2 ps, respectively, substantiating the plausibility of the scattering rate model assumptions.

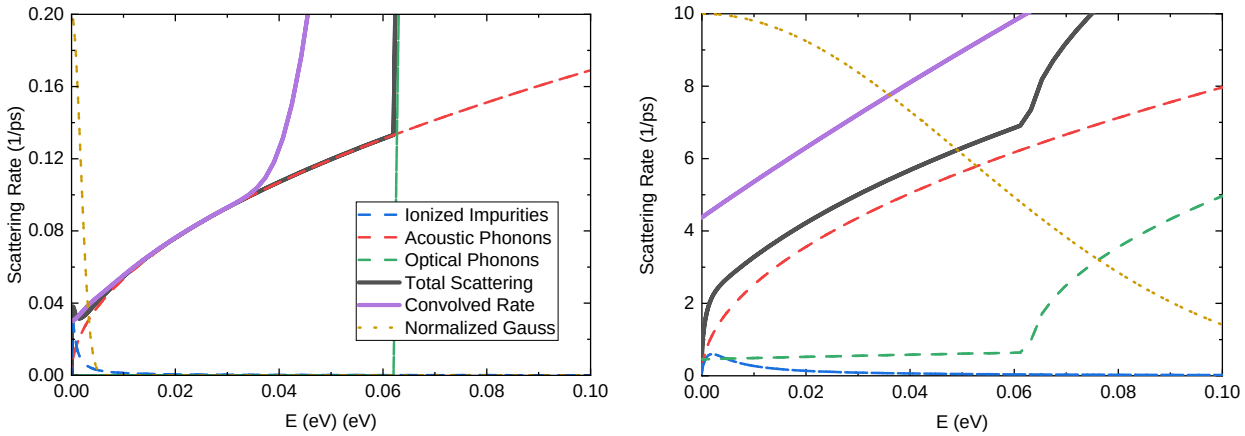

(a) T = 10 K, n = 10^{13} cm^{-3} (b) T = 300 K, n = 5.75×10^{15} cm^{-3}

Figure 6.4: Scattering rate contributions from ionized impurities, acoustic and optical phonons (dashed lines). The sum makes up the total scattering (black). Assuming an initial thermal energy distribution, the total scattering rate is smoothed with a Gaussian ($\sigma = k_B T$, yellow dotted line) to obtain the convolved momentum scattering rate (purple).

6.2.3 Density of states

It has become clear that the phonon scattering rates due to acoustic and optical phonons, Eqs. 6.20 and 6.23b, depend directly on the available density of states for the carriers to scatter into. In Fig. 6.2, the bandstructure appears to be a continuous distribution mapping k-vector to energy. In reality, in a semiconductor of finite size only a finite number of k states may exist, due to the finite number of atoms with finite number of energy levels (bands). In k-space, these states are uniformly distributed across the Brillouin zone. The density of states (per volume in k-space) thus is a constant

$$g_k = \frac{1}{(2\pi)^d} \tag{6.26}$$

where d is the dimensionality of the system (equal to 3 for the bulk crystal considered here), and a factor of 2 is neglected which would account for the spin degeneracy of charge carriers. [270, p. 26]

With a uniform distribution in k-space, the density of states in energy space necessarily cannot be uniform for a non-linear bandstructure. It is instead given by counting the number of states $\Omega(E)$ per interval $[E, E + dE]$.

$$g(E) = \frac{1}{V} \sum_{\mathrm{BZ}} \delta(E - E_i(\vec{k'})) \tag{6.27}$$

for the i-th band.

The sum was calculated numerically for the bands according to the tight binding model, since data for the full Brillouin zone is available. For the crystal structure of silicon, only a wedge of only $\frac{1}{48}$th of the Brillouin zone needs to be considered when exploiting all symmetries, as seen from Fig. 6.1 [270, p. 21]. For the integration, a cubic k-space mesh of resolution $2\pi/N$ with N = 150 was used and an energy resolution of ± 0.05 eV. The density of states in units of eV^{-1} m^{-3} is obtained by considering the volume of a single state $V = (N\frac{a}{2\pi})^3$. Fig. 6.5 visualizes the k states associated with a given energy for the heavy hole band of silicon that are summed to obtain the density of states. An analogous depiction for the light hole band is given in Appendix A.4. Both bands are strongly warped, i.e. anisotropic, for larger energies.

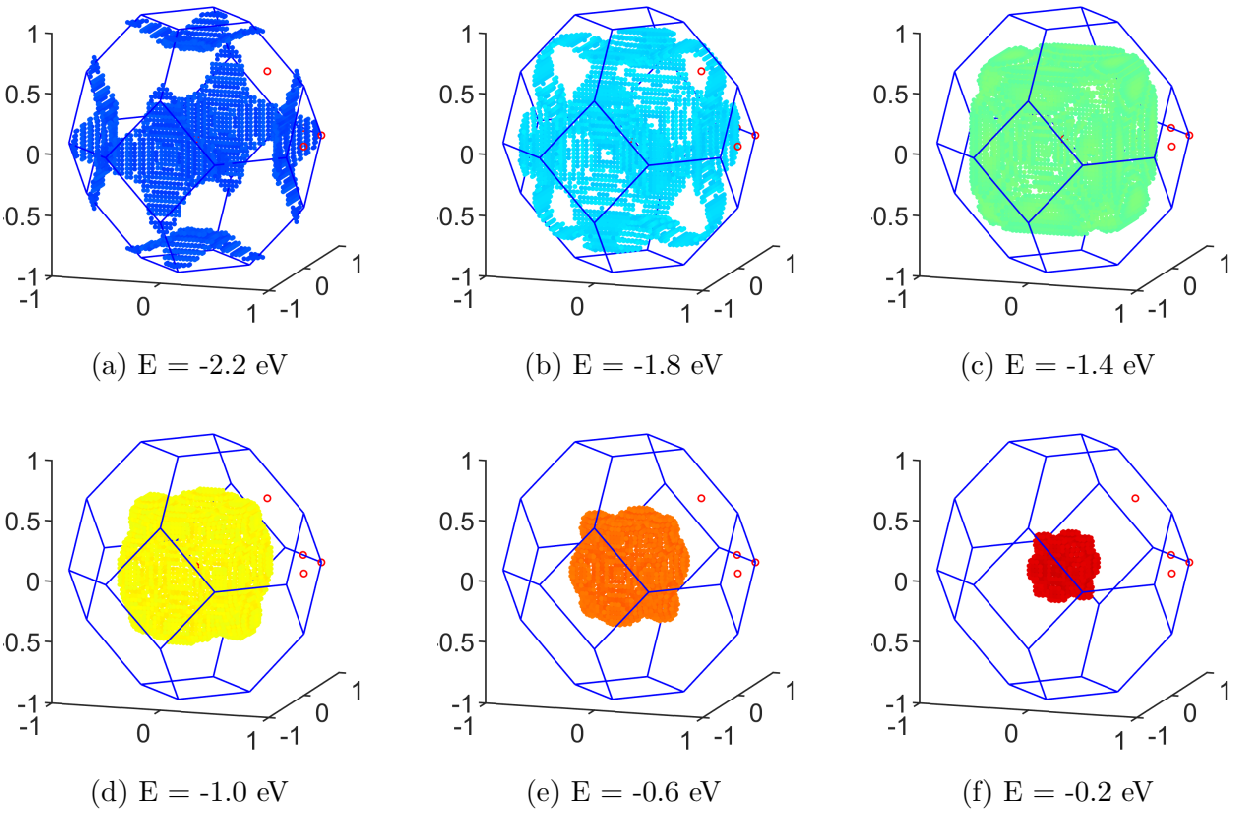

(a) E = -2.2 eV (b) E = -1.8 eV (c) E = -1.4 eV

(d) E = -1.0 eV (e) E = -0.6 eV (f) E = -0.2 eV

Figure 6.5: k-states associated with different energies (ΔE $\pm$ 0.05 eV) for the heavy hole band. The density of states is given by adding the number of k states per energy bin. The high symmetry points are marked by red circles. The axes are in units of $k = 2\pi/a$.

Fig. 6.6 shows the density of states for the heavy hole band of silicon with crosses indicating the energy bins ΔE $\pm$ 0.05 eV with colors relating to the selected visualization in Fig. 6.5. The peak at -1.5 eV is due to the end of the Brillouin zone at the L-point as seen in Fig 6.2.

The density of states can be obtained more easily for a monotonic and spherically symmetric dispersion relation, e.g. an isotropic parabolic bandstructure. In this case (or in these regimes) the density of states is directly given by the change in occupied volume fraction $\Omega(E)$ of the Brillouin zone, sketched in Fig. 6.5, such that

$$g(E) = \frac{d\Omega(E(k))}{dE} = \frac{d\Omega(k)}{dk}\frac{dk}{dE} = \frac{4\pi k^2}{V}\frac{dk}{dE} \tag{6.28}$$

which is given here in three dimensions. An additional factor of 2 needs to be added to account for spin degeneracy.

Applying Eq. 6.28 to a parabolic band $E = \frac{(\hbar k)^2}{2m^*}$, the general three-dimensional density of states is obtained

$$g(E) = 2 \cdot \frac{4\pi k^2}{(2\pi)^3}\frac{dk}{dE} \tag{6.29a}$$

$$= \frac{(2m^*)^{3/2}}{2\pi^2\hbar^3}\sqrt{E} \tag{6.29b}$$

It is noted that for the case of anisotropic bands, different effective masses are usually averaged. Due to the different dependencies on the effective mass the averaging method

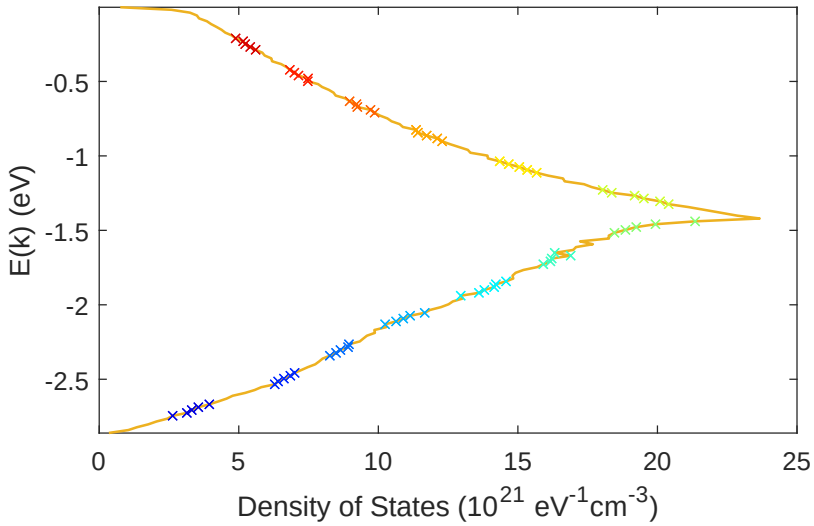

Figure 6.6: Density of states of the heavy hole band numerically calculated from a tight binding bandstructure model. Colored crosses mark the energy bins of equal size ΔE and relate to Fig. 6.5.

depends on the purpose. To average the longitudinal and transversal components of the conduction band, for example, the geometric mean is applied for the density of states effective mass and the harmonic mean is applied for the conductivity effective mass. For the approximately spherical but degenerate valence bands, the generalized mean is used. The split-off band ($m^* = 0.29\,m_0$) is additionally weighted by the split-off energy $\Delta = 43\,\mathrm{meV}$. [278, 279]

$$m^*_{\mathrm{dos}} = \left({m_{\mathrm{hh}}}^{3/2} + {m_{\mathrm{lh}}}^{3/2} + (m_{\mathrm{so}} e^{-\frac{\Delta}{k_B T}})^{3/2} \right)^{2/3} \tag{6.30}$$

The calculated total m^*_{dos} yields $0.527\,m_0$ at $0\,\mathrm{K}$ and $0.539\,m_0$ at $300\,\mathrm{K}$. However, at elevated temperatures the approximated calculation is not very reliable and a density of states effective mass of $0.59\,m_0$ at $4\,\mathrm{K}$ and $0.81\,m_0$ at $300\,\mathrm{K}$ should be used instead mainly due to the influence of light hole non-parabolicity and additional split-off states [277, 280].

6.2.4 Equation of motion

In the semi-classical picture of charge transport, one can use a ballistic assumption for the movement of electrons and apply a damping or scattering term to account for the combined scattering events. In this case, the equation of motion already introduced in Eq. 3.3 can be applied, where here we use the notation $\vec{\mathcal{E}}(t)$ for the electric field and E for the carrier energy to describe the motion of the hole carriers $\vec{k}(t)$ in momentum space

$$\frac{d\vec{k}(t)}{dt} = -\frac{q}{\hbar}\vec{\mathcal{E}}(t) - \vec{k}(t)\Gamma_m(E) \tag{6.31}$$

where the momentum scattering rate $\Gamma_m(E)$ is given as the sum of scattering rates due to ionized impurities, acoustic and optical phonons. The energy of a carrier is related to its momentum k by the dispersion relation given by the bandstructure.

For the experiments modelled here, an intense short Terahertz pulse was used to accelerate the hole carriers in the silicon crystal. The electric field $\vec{\mathcal{E}}(t)$ is given by a Gaussian

pulse defined via the maximum electric field $\vec{\mathcal{E}}_0$, pulse width T, frequency ω and phase shift φ_0

$$\vec{\mathcal{E}}(t) = \vec{\mathcal{E}}_0 e^{-2\log(2)\left(\frac{t}{T}\right)^2} e^{i\omega t+\varphi_0} \tag{6.32}$$

Solving the differential equation of motion numerically yields the response of the hole carriers to the driving force exerted by the Terahertz pulse - an oscillatory movement through the bandstructure parallel to the field polarization.

To find the carrier group velocity, the relationship between position $\vec{k}$ in momentum space and associated velocity $\vec{v}(\vec{k})$ can be used, as given by the derivative of the bandstructure [281]

$$\vec{v}(\vec{k}) = \frac{1}{\hbar}\nabla_{\vec{k}} E(\vec{k}) \tag{6.33}$$

By solving the differential equation of motion for $k(t)$ and applying the relationship $v(k)$, one can thus obtain the time-dependent group velocity $v(t)$.

It is noted that the effective mass m^* can also be calculated by evaluating the second derivative of the bandstructure at the Γ point. In one dimension it is given by

$$\frac{1}{m^*} = \hbar^{-1}\frac{dv}{dk} = \hbar^{-2}\frac{d^2E}{dk^2} \tag{6.34}$$

6.2.5 Terahertz emission

The coherently emitted field $\mathcal{E}_{em}$ is proportional to the current density [281, 282]

$$j(t) = -qnv(t) = -2\mathcal{E}_{\text{emit}}(t)/(Z_0 d) \tag{6.35}$$

where n is the hole density, $Z_0 = \mu_0 c$ is the impedance of free space and d is the thickness of the sample. If the thickness d is much smaller than the wavelength λ, all carriers are driven by the same electric field $\mathcal{E}(t)$, otherwise corrections have to be considered.

Initially, a proportionality between current density $j(t)$ and emitted field $\mathcal{E}_{em}(t)$ may seem counter-intuitive. Usually, the electromagnetic field's power radiated by a single charged particle is proportional to its acceleration $\dot{v}(t)$ rather than its velocity $v(t)$ according to Larmor's formula [84, p. 665]

$$P = \frac{2}{3}\frac{q^2}{c^3}|\dot{\vec{v}}|^2 \tag{6.36}$$

However, rather than treating the charge as a single moving particle, one assumes an "extended sheet of simultaneously moving particles" [282]. The interference within the sheet current between the individual contributions yields an electric field at the sample $\mathcal{E}$ that is proportional to the current density $j(t) \propto v(t)$ rather than to the charge acceleration [283, Eq. 3.7]

$$\mathcal{E} = -\frac{Z_0}{1+\sqrt{\epsilon_r}} j(t) \tag{6.37}$$

The emitted THz radiation $\mathcal{E}_{\text{emit}}$ will be in the form of plane waves. Now, the specific geometry of the experimental setup, as shown in Fig. 6.7, is important for the detection. By imaging the silicon crystal onto the detector via two mirrors, one obtains the emitted electric field $\mathcal{E}_{\text{emit}} = -\mathcal{E}_{\text{detector}}$ [281].

It is thus justified to equate the detected electric field to the emitted electric and assume proportionality to the group velocity. Rearranging Eq. 6.35 yields

$$\mathcal{E}_{\text{emit}}(t) = -0.5 Z_0 d \cdot qnv(t) \tag{6.38}$$

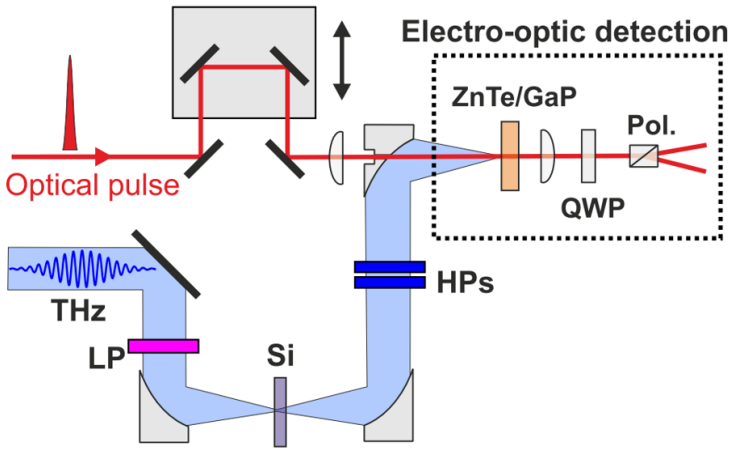

Figure 6.7: The silicon crystal is excited by the Terahertz pulse which is focused by a paraboloidal mirror. The emitted radiation is collimated and then refocussed for electro-optic detection. The 35-fs optical pulse from a Ti:sapphire sampling laser probes a small area in the centre of the focussed Terahertz beam. Reprinted from [Wal11].

6.3 Simulation of 1D single particle current

If the holes accelerated by the Terahertz pulse respond non-linearly, higher harmonics appear in the emitted electric field. For frequencies in the microwave and far-infrared, two possible mechanisms lead to this anharmonic response [264]. Firstly, carriers moving in a non-parabolic band E(k) are subject to a non-linear velocity-momentum relation which induces mixed frequency components when they oscillate due to an applied electromagnetic field [284]. Secondly, the carrier motion is damped by an energy-dependent (and thus momentum-dependent) momentum scattering rate $\Gamma_m\left(E(k)\right)$, which introduces additional non-linearities [285, 286]. Since the latter origin for non-linear effects exists also for semiconductors with parabolic bands, it presents a simple method for isolating the two effects, as noted by Kaw [285].

As shown in Eqs. 6.28 and 6.34, the density of states and the effective mass both are related to the derivative of the bandstructure. Since the density of states strongly influences the scattering rate and the effective mass is a measure of the parabolicity of the bandstructure, experimentally the two mechanisms, band non-parabolicity and energy-dependent momentum scattering rate, cannot simply be separated. However, if one models the scattering rate as being unaffected by changes made to the bandstructure, it is possible to switch the band parabolicity on or off and thus obtain a measure of its influence on the generation of higher harmonics.

Fig. 6.8 shows the bandstructure, group velocity and effective mass of light (lh) and heavy (hh) holes in silicon for the direction Γ-X. The solid lines depict the dispersion according to the EPM. The dashed line, on the other hand, depicts the band with switched-off non-parabolicity. As a result, it is characterized by a constant effective mass, equal to $m^*_{\mathrm{EPM}}(\Gamma)$, and linear group velocity.

Assuming that the density of states and hence the momentum scattering rate remains the same for the bandstructure with and without non-parabolicity, the solution for $k(t)$ of the differential equation of motion, Eq. 6.31, is independent of the bandstructure. However, the velocity-momentum relation $v(k)$ obviously differs significantly. By introducing this separation of the two non-linear mechanisms, one can thus break down the contributions to the higher harmonic generation and obtain a band-dependent carrier motion $v(t)$.

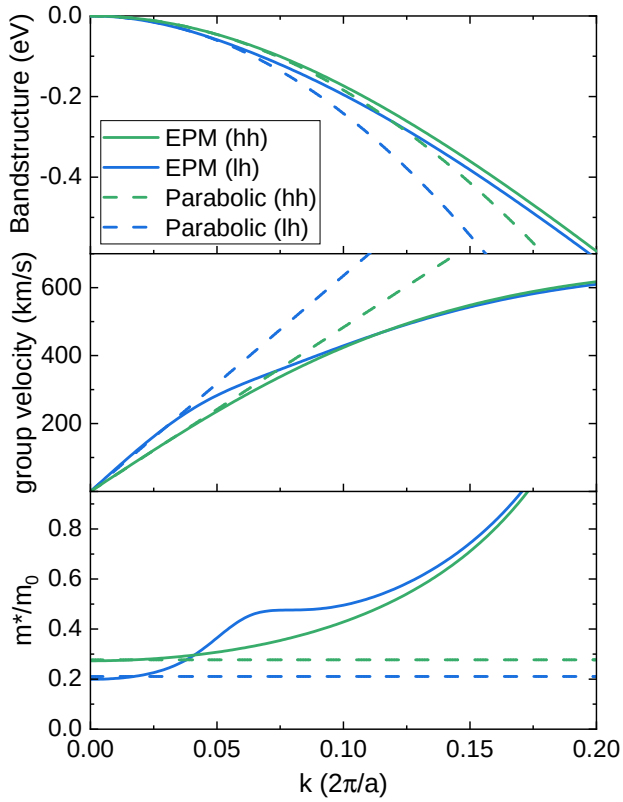

Figure 6.8: Valence bandstructure (top panel) of heavy (hh) and light (lh) hole along the Γ-X direction for the realistic EPM and parabolic approximation (Parabolic). Group velocity (centre panel) and effective mass (bottom panel) correspond to the respective bandstructures.

The emitted field is easily obtained from the proportional relationship given by Eq. 6.38. Finally, the harmonic spectrum is given by the Fourier transform

$$\mathcal{E}_{\text{emit}}(\omega) = F \int_{-\infty}^{\infty} \mathcal{E}_{\text{emit}}(t) e^{-i\omega t} dt \tag{6.39}$$

which is calculated using the fast Fourier transform and scaled by a factor

$$F = 2 \times \sqrt{\frac{2\log(2)}{\pi \tau_{\text{fdhm}}^2}} \times T \tag{6.40}$$

The factor 2 accounts for the double-sided spectrum, the root term accounts for the Gaussian pulse envelope with pulse duration τ_{fdhm} (full duration at half maximum) and the last term scales by the Fourier transform sampling period T.

The following sections present simulation results corresponding to two different experiments with intense Terahertz pulses at low temperature and at room temperature. Table 6.3 summarizes the different parameters used in the simulation to model the different experiments. The numerical solution to the equation of motion Eq. 6.31 was calculated with a time discretization of $dt = 10^{-3}\frac{2\pi}{\omega}$ and a time window of $T = 16\tau_{\text{fdhm}}$.

[5] Extrapolated from [272, Fig. 2.35] and used instead of the (frozen out) doping density at 10 K.

[6] A common thickness d = 100 µm was assumed for both simulation, as no absolute emitted electric field, Eq. 6.38, was calculated.

	sample 1 low temperature	sample 2 room temperature
Temperature T	10 K	293 K
Boron doping density N	$5 \times 10^{16}\,\mathrm{cm}^{-3}$	$5.75 \times 10^{15}\,\mathrm{cm}^{-3}$
Residual free carrier density[5]	$1 \times 10^{13}\,\mathrm{cm}^{-3}$	-
Avg. effective mass m^*	$0.59\,m_0$	$0.81\,m_0$
Crystal thickness[6] d	275 µm	900 µm
Frequency $\omega/(2\pi)$	1.29 THz	0.3 THz
Pulse width τ_{fdhw}	17 ps	22 ps
Peak electric field $\mathcal{E}_0$	$24\,\mathrm{kV\,cm}^{-1}$	$70\,\mathrm{kV\,cm}^{-1}$

Table 6.3: Overview of the key parameters used to model the two measurements on the different boron-doped silicon crystals at different temperatures.

6.3.1 Silicon at low temperature (10 K)

This section presents the simulation results pertaining to low-temperature measurements at 10 K on a boron-doped silicon crystal ($\epsilon_r \approx 12$). The boron density is given in Table 6.3, however at this low temperature most hole carriers are frozen out and a residual free carrier density at 10 K of $1 \times 10^{13}\,\mathrm{cm}^{-1}$ is extrapolated from [272, Fig. 2.35]. At this temperature, the averaged density of states is $m^* = 0.59\,m_0$, see Sect. 6.2.3. Other parameters used for the calculation of the momentum scattering rate are listed in Table 6.2. The sample is excited by a 17 ps Terahertz pulse at 1.29 THz with high peak electric field of up to $\mathcal{E}_0 = 24\,\mathrm{kV\,cm}^{-1}$ (scaled to field value in silicon).

As heavy and light hole band dynamics are treated separately, the spectra generated by a single hole carrier in these bands are extracted independently as shown in Figs. 6.9a and 6.9b, respectively. Each graph shows the emitted field intensity of the first, third and fifth harmonic modelled using the realistic EPM (green and blue) and the respective parabolic band approximation (red). The insets show the third and fifth harmonics on a linear scale to highlight the relative strengths of harmonic generation with and without non-parabolicity.

There are two main observations from the comparison between the bands and between the models. Firstly, the intensities of the higher harmonics are much stronger for the light hole than for the heavy hole, specifically factor 31 for the third and factor 65 for the fifth harmonic. Secondly, the intensities of all the harmonics decrease significantly when the non-parabolicity of the band is switched off (i.e. using the parabolic band approximation). This is most dominant for the third harmonics with a drop to 1% and 0.1% for heavy and light hole, respectively, and for the light hole fifth harmonic generation where the intensity drops to 1%. The least reduction is observed for the fifth harmonic of the heavy hole band (23%), since the realistic band harmonic generation is already relatively weak to begin with.

From the data one can conclude that the effect of band non-parabolicity for the generation of higher harmonics is dominant over the effect of energy-dependent scattering. The strong non-linearity of the light holes can be traced back to the notable curvature most noticeable in the effective mass m^* of Fig. 6.8.

Next, a brief inspection of the first harmonic of both bands is presented in Fig. 6.10 verifying the plausibility of the comparison. The ratio between the emitted electric fields of the linear components is given directly by the ratio of the effective masses of heavy and light hole band at the Γ point $\frac{0.237\,\mathrm{m_0}}{0.199\,\mathrm{m_0}} = 1.37$, as given in Table 6.1. Moreover, no difference is expected between the realistic bandstructure and the parabolic approximation for the first harmonic component.

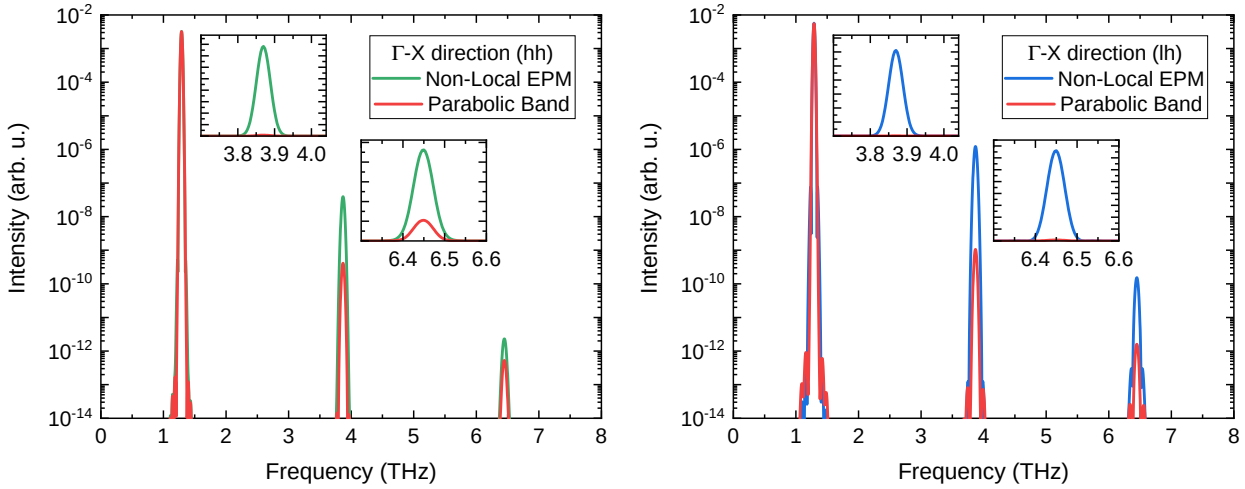

(a) Heavy holes (b) Light holes

Figure 6.9: First, third and fifth harmonics generated by a single (a) heavy and (b) light hole carrier according to EPM (green and blue) and the parabolic approximation (red) at 10 K. The insets have a linear scale and magnify the relative intensities.

From above analysis, one could conclude the relatively stronger impact of a single light hole carrier as compared to a single heavy hole carrier. However, heavy and light holes have significantly different effective masses, which are directly related to their three-dimensional densities of states $g(E) \propto (m^*)^{3/2}$ via Eq. 6.29b. This yields a population ratio of 83:17 for the averaged effective masses for heavy and light hole of $0.467\,\mathrm{m}_0$ and $0.159\,\mathrm{m}_0$, respectively [272, p. 94]. Considering the intensity of the coherent emission $I \propto |\mathcal{E}_{\mathrm{emit}}|^2$, the ratio of effective masses must be cubed, which yields a contribution to the intensity of 96:4.

Fig. 6.11 shows a plot of the weighted total intensity $I \propto |\mathcal{E}_{\mathrm{hh}} + \mathcal{E}_{\mathrm{lh}}|^2$ as well as the single band contributions (dashed) multiplied with their respective weighting factor. Additionally, the total weighted power is shown for the parabolic band simulation (red). For the third harmonic, the total contributions from heavy and light hole bands are about equal, since the strongly non-linear light hole contribution is weighted with a much lower population fraction. For the fifth harmonic, the light hole contribution is still about 2.5 times more dominant than the heavy hole contribution even after accounting for the low population. Again, the strong non-parabolicity of the bandstructure, see Fig. 6.8, is responsible for this. However, in this case the total power is lower than the light hole contribution, which points towards a destructive phase relationship between the emitted electric fields of heavy and light hole.

With respect to the relative contributions of non-parabolic bandstructure and momentum scattering rate, the plot of the total emitted field Fig. 6.11 confirms that simulating the harmonic generation with a parabolic band strongly suppresses the non-linear effects. Even for the fifth harmonic, where the suppression is less severe, the anharmonic bandstructure mechanism still makes up more than 80% of the total non-linearity.

Returning again to the phase relationship between the emitted fields from heavy and light hole band, it is interesting to consider the coherent sum of the two intensities. Fig. 6.12 considers three different scenarios. The coherent sum of the two electric fields $I \propto |\mathcal{E}_{\mathrm{hh}} + \mathcal{E}_{\mathrm{lh}}|^2$ (Total) respecting the simulated phase is shown in yellow. The fully incoherent sum with an effective phase lag of $\pi/2$ between the fields $I_{\mathrm{incoh.}} \propto |\mathcal{E}_{\mathrm{hh}}|^2 + |\mathcal{E}_{\mathrm{lh}}|^2$ (Incoh.) is shown in purple. The fully coherent sum where the fields are assumed to be completely in phase $I_{\mathrm{coh.}} \propto (|\mathcal{E}_{\mathrm{hh}}| + |\mathcal{E}_{\mathrm{lh}}|)^2$ (Coh.) is shown in yellow.

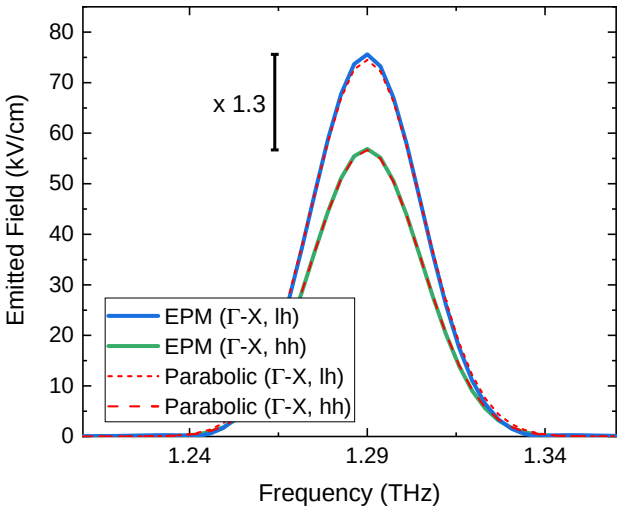

Figure 6.10: Emitted field at the first harmonic for a single heavy and light hole carrier according to EPM (green and blue) and the parabolic approximation (red). The ratio 1.3 of the intensities is equal to the effective mass ratio.

It is apparent that the emitted fields are completely in phase for the first and third harmonic. However, the fifth harmonic displays a different phase relationship. Here the contributions of heavy and light hole band interfere destructively and effectively reduce the total emitted power.

6.3.2 Silicon at room temperature (293 K)

The simulations presented in this section model room-temperature measurements at 293 K on a different boron-doped silicon crystal with doping density of $5.75 \times 10^{15}\,\mathrm{cm}^{-3}$. The averaged valence band density of states is $m^* = 0.81\,m_0$ and the same parameters listed in Table 6.2 apply for the momentum scattering rate. The sample is excited by a 22 ps Terahertz pulse, at 0.3 THz with high peak electric field of up to about $50\,\mathrm{kV\,cm}^{-1}$ (scaled to field value in silicon). The results of this simulation are structured analogously to the low temperature results in Sect. 6.3.1. Figs. 6.13a and 6.13b show the emitted field intensity of the first, third and fifth harmonic from the realistic EPM (green and blue) and the respective parabolic band approximations (red).

The observations in this case differ considerably from the low temperature simulation. Firstly, although the light hole higher harmonics still outperform the heavy holes for the third and fifth harmonic, the ratios are only about 2.2 and 2.5 times, respectively. This means that the contributions by a single hole are much more balanced. Secondly, switching off the non-parabolicity does not have such a drastic impact on the harmonic generation. The non-linearity due to band non-parabolicity accounts for about 7% for the heavy hole (about equal for third and fifth harmonic) and accounts for about 28% for the light hole (again about equal for third and fifth harmonic). These findings can be seen in the respective insets of Fig. 6.13. One can conclude that the non-linearity results mostly from the energy-dependent momentum scattering. This is especially true for the heavy hole band, while for the light hole band momentum scattering is the dominant effect but band anharmonicity still contributes significantly. These conclusions equally apply to the seventh and ninth higher harmonics as depicted in Appendix A.5.

Fig. 6.13 shows the contributions per single hole carrier in each individual band. In order to obtain the total emitted power it is necessary to weigh each band by the popu-

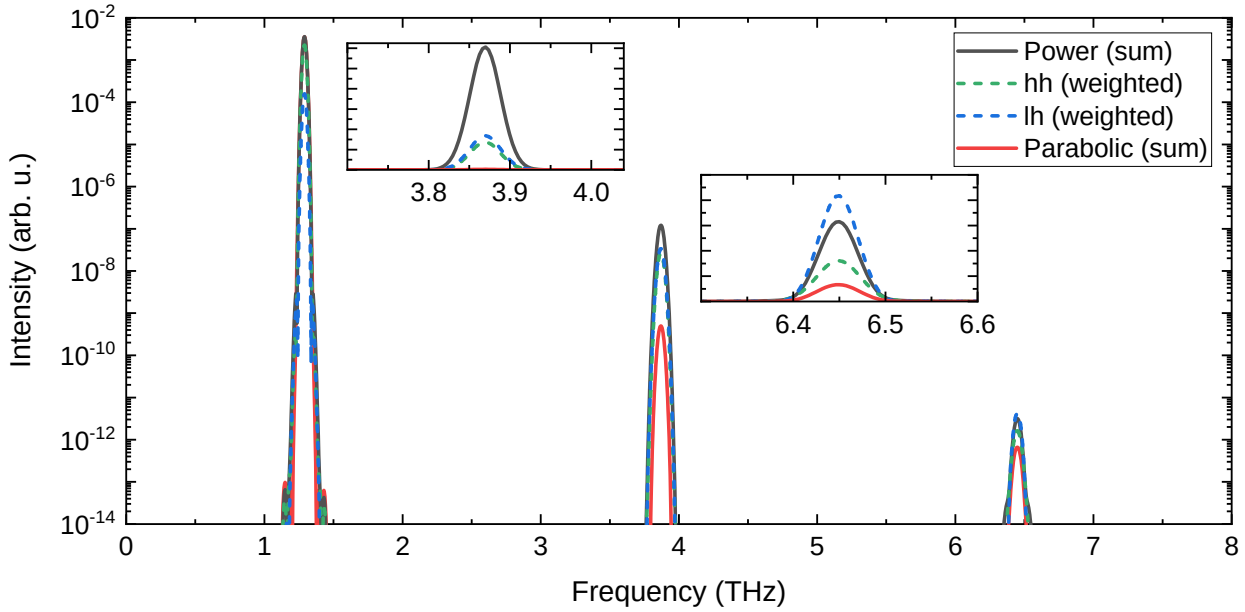

Figure 6.11: Weighted and coherently summed intensity of the first, third and fifth harmonics for EPM (black) and the parabolic approximation (red). The dashed line visualize the individual weighted intensities (96:4) of heavy and light hole. The insets have a linear scale and magnify the relative intensities.

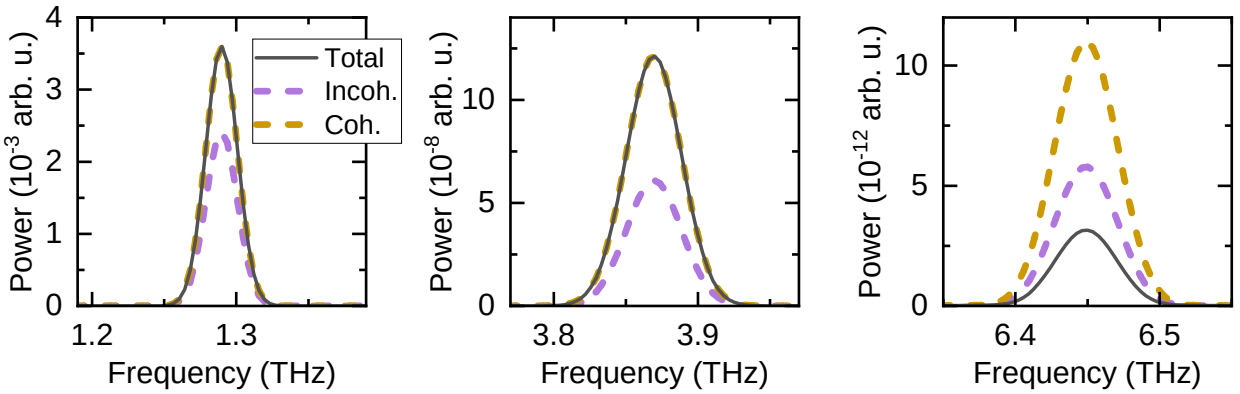

Figure 6.12: Coherently weighted total intensity of light and heavy hole (black) compared to fully coherent (Coh., $\Delta\phi = 0$) and fully incoherent (Incoh., $\Delta\phi = \pi/2$) intensities. For first and third harmonic, the coherent sum coincides with the fully coherent assumption. However, for the fifth harmonic the coherent sum of heavy and light hole shows destructive interference leading to a lower than anticipated emitted intensity.

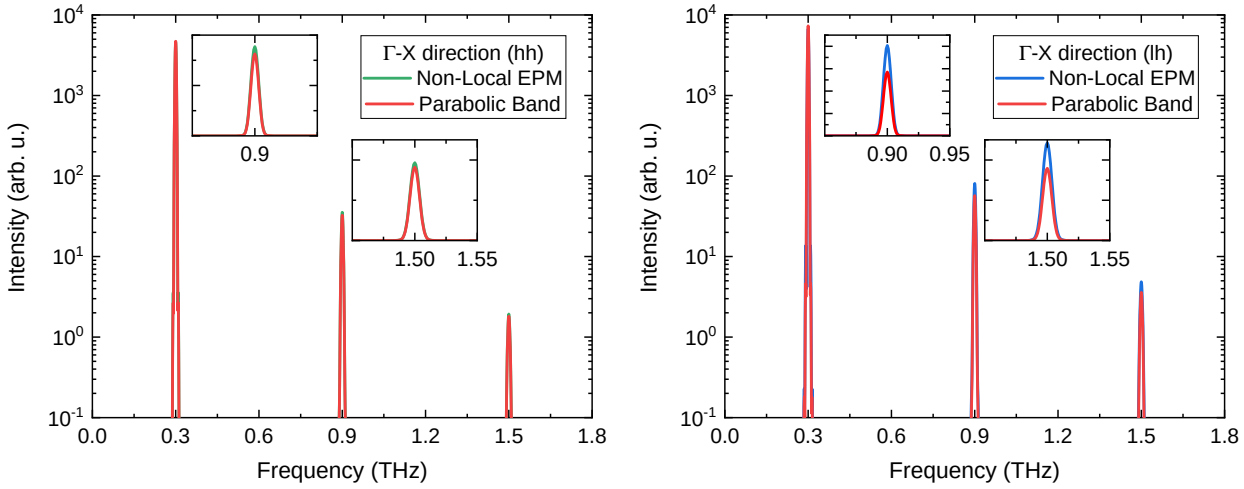

(a) Heavy holes (b) Light holes

Figure 6.13: First, third and fifth harmonics generated by a single (a) heavy and (b) light hole carrier according to EPM (green and blue) and the parabolic approximation (red) at 293 K. The insets have a linear scale and magnify the relative intensities.

lation ratio 83:17 (hh:lh) or by 96:4 (hh:lh) for the intensity contribution as explained in Sect. 6.3.1. The weighted total intensity $I \propto |\mathcal{E}_{\mathrm{hh}} + \mathcal{E}_{\mathrm{lh}}|^2$ is shown in Fig. 6.14 compared with the weighted individual band contributions (dashed). The weighted total intensity with the parabolic band (red) was simulated analogously. Firstly, the additional population weighting decreases the influence of the light hole band to a degree that allows to almost completely neglect its contribution to the higher harmonic generation. This is in stark contrast to the low temperature simulation. Secondly, the dominance of the heavy hole band further highlights the total contribution of energy-dependent momentum scattering to the generation of higher harmonics at room temperature. The contribution due to band non-parabolicity only accounts for 13% and 10% of the total non-linearity for third and fifth harmonic, respectively.

A detailed comparison of the phase relationship between heavy and light hole emitted fields is omitted here since the minor contribution of the light hole band allows to neglect it from the total power. An analysis analogous to Fig. 6.12 confirmed that the sum of the complex fields (Total) equals the fully coherent sum (Coh.) for the room temperature simulation.

6.4 Measurements

6.4.1 Silicon at low temperature (10 K)

The corresponding measurements on boron-doped silicon at low temperature were performed by co-researchers at the FELBE facility with sample and beam parameters as stated in Table 6.3. The spectral analysis of the data was facilitated by Fourier transform infrared spectroscopy. A detailed description of the experimental setup is given in ref. [266]. Results discussing the higher harmonics spectra at different pump pulse electric fields and the origin of the residual free carrier density are currently under review and expected to be published as “Fifth-Harmonic Generation in Si” [Wal11]. A key observation of the experiment is the generation of the fifth harmonic signal by free holes in the valence band of the boron-doped silicon crystal. The paper also summarizes the findings detailed in Sect. 6.3.1 differentiating

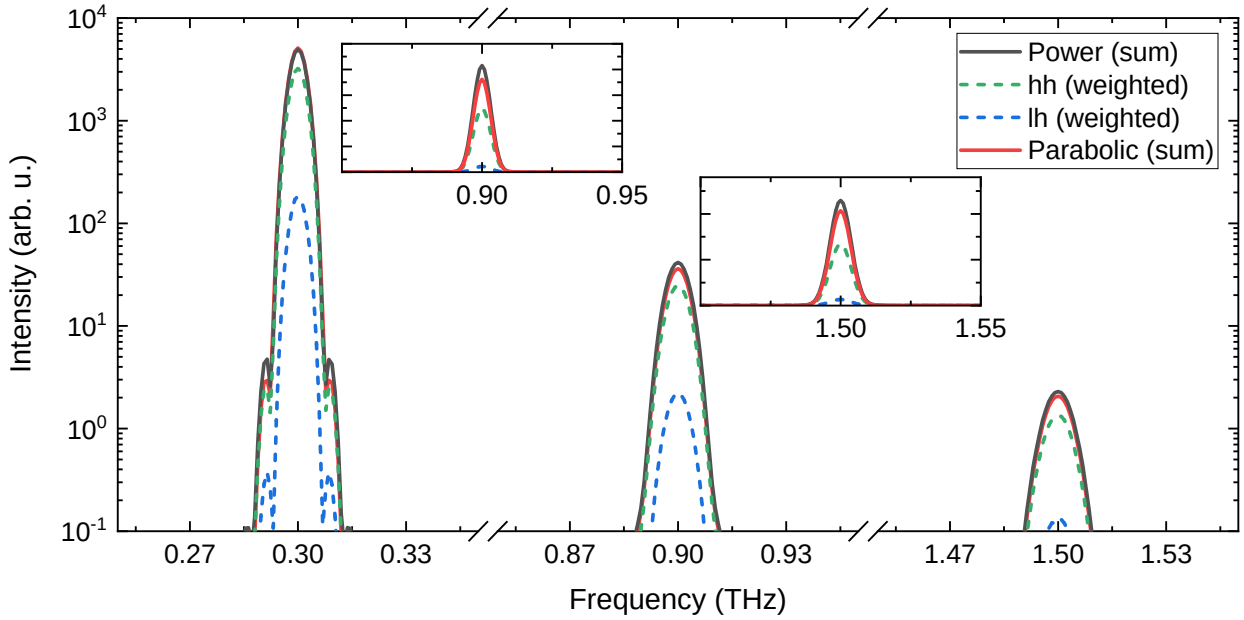

Figure 6.14: Coherently summed weighted intensity of the first, third and fifth harmonics for EPM (black) and the parabolic approximation (red). The dashed lines visualize the individual weighted intensities (96:4) of heavy and light hole. The insets have a linear scale and magnify the relative intensities. Note the broken frequency axis.

between the different non-linear mechanisms, which have been contributed by the author of this thesis.

6.4.2 Silicon at room temperature (293 K)

Room-temperature measurements on a different boron-doped silicon crystal at room temperature were performed at TELBE. The relevant sample and beam parameters are again given in Table 6.3.

Fig. 6.15 shows the measured emitted fields at the different harmonics for increasing pump electric fields. Naïvely assuming that the optical susceptibility χ is constant, one would expect a dependence $\propto \mathcal{E}^n$ for the electric field strength of the nth harmonic, according to

$$P(t) = \epsilon_0 \left[\chi^{(1)}\tilde{\mathcal{E}}(t) + \chi^{(3)}\tilde{\mathcal{E}}^3(t) + \chi^{(5)}\tilde{\mathcal{E}}^5(t) + \dots\right] \tag{6.41a}$$

$$\equiv P^{(1)}(t) + P^{(3)}(t) + P^{(5)}(t) + \dots \tag{6.41b}$$

where even terms of the non-linear polarization series are suppressed for centrosymmetric crystals, such as silicon [287]. Fig. 6.15 indeed shows linear slopes in the log-log plot for experiment and simulation for lower electric fields. Linear fits (dashed) highlight the slope, which for the simulated data was fit for electric fields $\mathcal{E}_0 < 12\,\mathrm{kV\,cm^{-1}}$. The experimental as well as simulated slopes are lower than the expected value n for the nth harmonic, as shown in Table 6.4.

This suggests an additional field-dependence of the susceptibility $\chi(\mathcal{E})$ itself. Typically, this may be due to ionization-induced high-order non-linear susceptibility [288], though ionization processes have not been considered in the simulation. Still, there is general agreement between the experimental and simulated field-dependence on the pump electric field which suggests that the reduced slope is (also) affected by the bandstructure landscape or cross-terms between lower and higher-order susceptibilities.

Harmonic:	3rd	5th	7th	9th
Experiment	2.6	3.3	4.1	5.7
Simulation	2.4	3.9	5.5	6.3

Table 6.4: Comparison of low-field exponents n of $\mathcal{E}_0{}^n$ representing the linear fits in Fig. 6.15 for experimental data and simulation.

Furthermore, experiment and simulation both show an onset of saturation of the susceptibility at electric fields of $\sim$50 kV cm^{-1} and $\sim$20 kV cm^{-1}, respectively. It is noted that the comparison is obviously complicated by the non-absolute scale of the simulated data. Still, it is noticeable that the saturation onset is shifted and, moreover, the relative strengths of the third harmonic deviates considerably between the experiment and simulation.

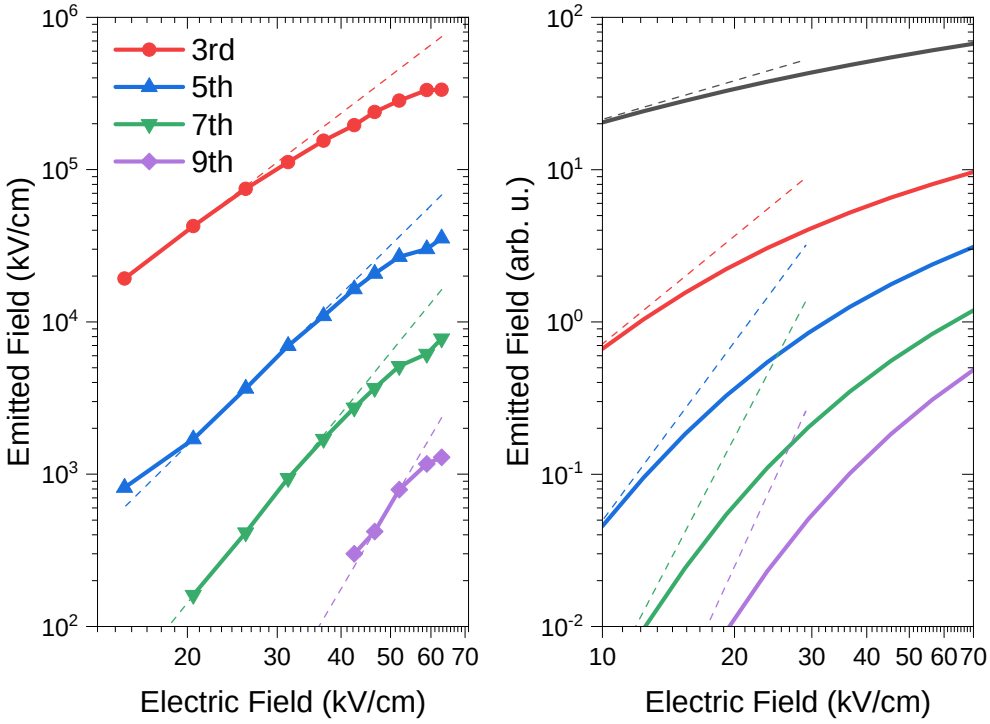

Figure 6.15: Emitted electric field for different higher harmonics determined from measurements at TELBE (left) compared to simulated higher harmonics (right). The qualitative comparison shows a saturation of the emitted field for high pump electric fields for both graphs.

Fig. 6.16 compares the phase evolution with electric field for third, fifth and seventh harmonic in the experiment to the simulation. The experimental phases were extracted by considering the bandwidth filtered higher harmonic time domain pulses and fitting a Gaussian pulses with relative phase shifts and envelopes fixed in time. One obtains an increasing phase lag for the emitted higher harmonic pulses with higher pulse electric field for both measurement and simulation. The results all qualitatively show a linear slope, though the simulation predicts a much lower slope of only about 1/4.

Overall, the simple time domain one-dimensional single particle simulation is able to capture the general trend of the higher harmonic generation and its saturation quite well. However, its strengths remains with supplying a conceptual understanding of the different non-linear mechanisms at play. Further influences such as impact ionization, interband scattering and propagation of the pulse through the 900 µm bulk crystal should further

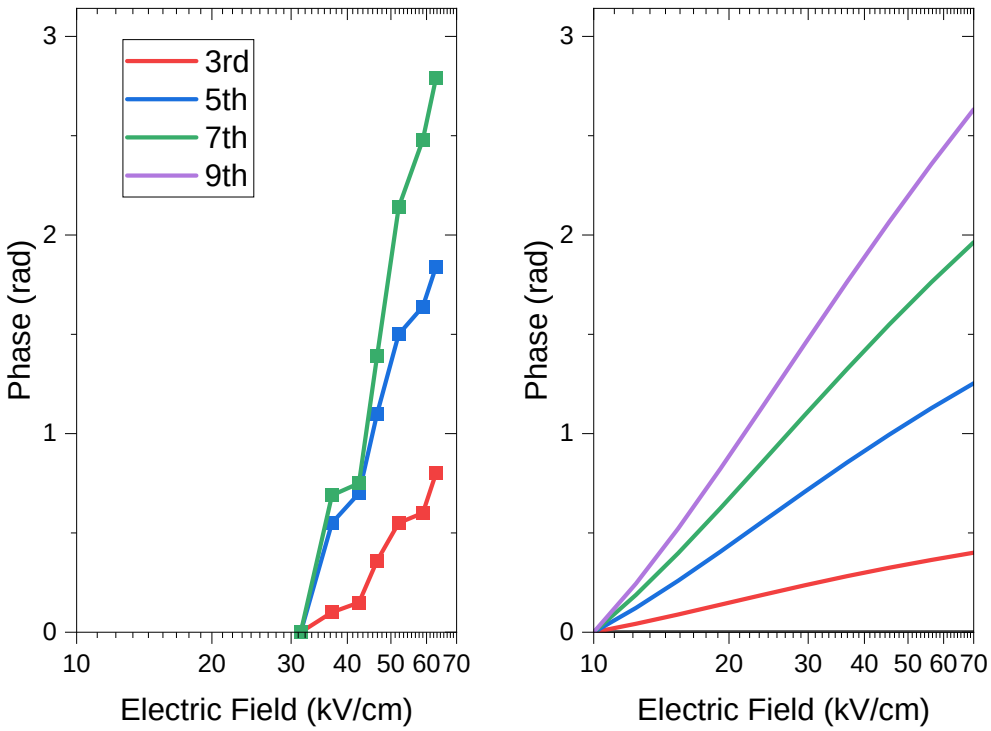

Figure 6.16: Phase comparison of emitted electric field for higher harmonics from measurements at TELBE (left) and simulation (right). The data has been referenced to the lowest available pump power and is relative to the phase of the fundamental. The simulation qualitatively shows an increae in phase with increasing electric field, albeit with a much lower slope of only about 1/4.

improve the agreement between measurement and simulation.

6.5 Conclusion

To summarize, the non-linear dynamics of holes in silicon's light and heavy valence bands due to excitation by intense Terahertz pulses were modelled based on a one-dimensional single particle time domain approach. Based on previously conducted measurements, two scenarios were considered.

Firstly, at cryogenic temperatures the carrier density is strongly reduced due to freeze-out, the density of states is low and the scattering rate is relatively weak. Experimentally, signals at the third and fifth harmonic were observed with a fundamental at 1.29 THz and 24 kV/cm maximum electric field. The harmonics were reproduced qualitatively in the simulation allowing an assessment of their microscopic origin by switching on and off the non-parabolicity of the bands. It was found that heavy and light hole both contribute equally to the emission of the third harmonic and significantly to the fifth harmonic. This is despite the lower density of states of the light hole band which is compensated by its strong band non-parabolicity. Furthermore, the third harmonic generation is almost exclusively due to band non-parabolicity, as deduced from the vanishing signals when switching to the parabolic band approximation. The fifth harmonic is also dominated by band non-parabolicity, however with a significant contribution by energy-dependent momentum scattering from the heavy hole band. Lastly, the phase relationship between heavy and light hole contribution at the fifth harmonic appears to be destructive. This may be due to the different contributing mechanisms in the two band and motivates further investigation since experimental time

domain data was not available to verify the plausibility of this finding.

Secondly, at room temperature a weakly-doped crystal was used, in which case the density of states and the scattering rate are higher. Experimentally, harmonics up to the ninth order are observed at low fundamental frequency of 0.3 THz and high intensity pulse excitation up to 70 kV/cm. The spectra and power dependence was reproduced qualitatively in the simulation. It was found that the heavy hole band dominates the higher harmonic generation with only a negligible contribution by the light hole band. This is in agreement with the finding that contrary to the low temperature case, energy-dependent momentum scattering is almost exclusively responsible for the generation of higher harmonics at room temperature. Therefore, the light hole's low density of states is not counterbalanced by its non-parabolicity - which still contributes, but is the secondary mechanisms even considered the light hole band individually. A qualitative comparison of the power dependence of higher harmonic generation shows a saturation towards higher electric fields for experiment and simulation. While initially saturation seems to set in at slightly higher fields for the experimental data, the nth harmonic power dependencies from experiment and simulation all fall below the expected power low exponents of n. This suggests that the data already describes the non-perturbative non-linear regime, and saturation effects must be considered even for low electric field for both experiment and simulation.

In conclusion, modelling the higher harmonic generation in p-doped silicon semiclassically by a one-dimensional single particle in the time domain allows to switch off the non-linear effect of the non-parabolic bandstructure and consider the isolated effect of energy-dependent momentum scattering. By applying this approach and qualitatively comparing the generated spectra to experimental results, the origin of the higher harmonic generation could be assigned to one or the other microscopic mechanisms, which turned out to differ with temperature. The simulation could thus give valuable insight even though several effects were neglected, most importantly: propagation of the pulse through the crystal causing absorption and phase delay, the wave (or statistical) nature of the hole (particle) ensemble, the field-dependent carrier density due to impact ionization and explicit interband scattering.

These effects can be taken into account by applying a full-band Monte Carlo simulations as performed by Jungemann et al. [269, 289] to model the full traversal of the pulse through the bulk silicon crystal. This approach has been followed through a collaboration with C. Jungemann and a comparison to the results presented in Sects. 6.3.2 and 6.4.2 is meant to supplement a future manuscript.

Chapter 7

Summary

To summarize, this thesis aimed at presenting the experimental work surrounding nanoscale measurements on metasurfaces and TMDC materials. Two experimental setups were implemented by the author of this thesis to conduct the measurements: an s-SNOM and a c-AFM. The theoretical aspects explained the necessity for optical near-field imaging techniques and the experimental setup are detailed in Chapter 2.

The central work on a metallic metasurface made up of elliptical gold disk unit cells is presented in Chapter 3. The corresponding theory section introduces the concept of Surface Plasmon Polaritons, which is essential for the field of plasmonics in general. Different methods for calculating the dispersion relation of these surface modes at single and multi-layer interfaces are applied to the studied metasurface sample. The model predicts three different modes, weakly and strong confined, that are expected to propagate at the interface. A silicon nanosphere placed on the sample is used as a radial excitation source. The comparison to near-field images obtained through s-SNOM measurements, analysed by spatial Fourier analysis reveals that only the weakly-confined guided mode resonance was sufficiently excited to be detectable by s-SNOM imaging. Observation of the remaining strongly-confined anisotropic buried modes would demand an improved depth sensitive resolution of the system, which should in principle be feasible for layer thicknesses of 20 nm. Moreover, the observation puts into question whether the excitation efficiency given by the momentum and mode volume matching of the nanosphere create sufficient excitation cross section to generate detectable buried SPP modes. Several ideas for follow-up measurements conclude Chapter 3.

Chapter 4 continues with the idea of visualizing buried electrical fields using s-SNOM. Here, it is applied to the study of WS_2, a two-dimensional TMDC layer exhibiting photoluminescence. By patterning the substrate underneath the suspended monolayer, supported by a thin layer of hBN, the photoluminescence yield is enhanced by a factor of 10. This is achieved by designing a lateral DBR microcavity with additionally optimized vertical depth which was etched into the substrate. High-resolution imaging of the electric field distribution in the resonator was facilitated by employing s-SNOM in order to assess the in-coupling enhancement due to the two these two approaches. It could be concluded that the lateral structure contributes dominantly to the strong photoluminescence yield, while for the in-coupling no obvious enhancement could be attributed to the vertical patterning.

The two-dimensional material WS_2 is studied again in Chapter 5 by employing c-AFM. Thin flakes were prepared on graphene and gold to serve as tunnel barriers for vertical currents. The nanoscopic tip was used in contact mode to image the topography of the sample and access the microscopic terraces of different thicknesses for obtaining I-V measurements. The data could be fitted with a Fowler-Nordheim model with parameters for the

tunnel width and Schottky barrier heights of the two interfaces. However, the measurements showed weak reproducibility which warranted a more detailed summary of the relevant error source. The conclusion of the chapter suggests several key aspects to be taken into account for future measurements. Critically, c-AFM is very sensitive to water film adsorption to the sample surface, which WS_2 surfaces suffer from under ambient conditions. Unreliable c-AFM measurements as well as surface deterioration based on strong tip-sample adhesion are associated to the formation of water menisci. Additionally, the use of two-dimensional materials, e.g. graphene, as substrate electrodes is suggested to ensure a well-defined interface. These remarks on the preliminary measurements are expected to enable further studies on vertical currents through two-dimensional heterostructures, paving the way for more complex layered material systems, as suggested in the conclusion of Chapter 5.

Chapter 6 delves into the description of higher harmonic terahertz generation from bulk silicon. This presents a digression from the theme of nanoscale surface measurements and is partly motivated by the exciting experimental data of high harmonics from silicon up to the ninth harmonic that were being analysed at the time. Further links to two-dimensional materials are suggested in the introduction of Chapter 6, where current research on generation of higher harmonics in two-dimensional materials is touched upon. The chapter outlines a one-dimensional single particle time domain model, which was applied to simulate the oscillating motion of hole carriers due to the excitation by an intense terahertz pulse. From the two non-linear effects expected to contribute to the generation of higher-harmonics in p-doped silicon, the non-parabolic bandstructure and energy-dependent momentum scattering, each was found to dominate in either of the two measurement conducted at different temperatures of 10 K and room temperature, respectively. The result qualitatively describes the experimental data and offers a contribution to the ongoing discussion on the origin of non-linearity in higher harmonic generation from solid crystals. Concluding the chapter, several additional parameters are discussed that are neglected in the treatment and can be included in ongoing quantitative analysis of the data.

In conclusion, the presented topics form contributions to the experimental research based on near-infrared s-SNOM and the setup variation c-AFM. The tip-based nanoscopic raster-scanning measurement techniques were applied to study the surface - and to an extend shallow volumes - of a plasmonic metasurface and mono- and multilayer TMDC materials. In this context, near-field imaging provided evidence for surface wave dispersion of a guided mode resonance excited via a dielectric nanosphere. Moreover, it facilitated a high-resolution field imaging of a buried substrate-integrated photoluminescence-enhancing microcavity and substantiated its enhancing effect on the in-coupled radiation. An endeavour to utilize the AFM in contact mode with a conductive tip to measure quantum tunnel currents through thin WS_2 flakes showed preliminary results and was concluded with a report on how to proceed with future studies. Lastly, additional work concerning the debate on the origin of higher harmonics generation from the valence band of doped silicon completes the thesis. Though not studied within the scope of two-dimensional surfaces, the relevance as a substantiating contribution to current experimental results from two high intensity terahertz facilities merit its inclusion in this thesis.

Appendix

A.1 Thin-layer SPP dispersion relation

The dispersion relation for thin-layer SPPs and an overview over different mode types at a thin three-layer IMI system is presented in Sect. 3.2.3. For the general expression of the dispersion relation two different presentations are prevailing in the literature. The equivalence of the form of Eq. 3.13 and Eq. 2.28 in [211] is confirmed in the following.

Beginning with Eq. 2.28 in [211, p. 31], where the labelling of the layer numbering here refers to the reference such that $k_1 \widehat{=} k_3$ (top layer), $k_2 \widehat{=} k_1$ (metal layer), $k_3 \widehat{=} k_2$ (bottom layer).

$$\exp(-4k_2a) = \frac{k_2/\epsilon_2 + k_3/\epsilon_3}{k_2/\epsilon_2 - k_3/\epsilon_3}\frac{k_2/\epsilon_2 + k_1/\epsilon_1}{k_2/\epsilon_2 - k_1/\epsilon_1} \tag{1}$$

By substituting $2a = h$, and $\kappa_i = k/\epsilon_i$

$$\exp(-2k_2h) = \frac{\kappa_2 + \kappa_3}{\kappa_2 - \kappa_3}\frac{\kappa_2 + \kappa_1}{\kappa_2 - \kappa_1} \tag{2a}$$

$$= \frac{\kappa_2\kappa_2 + \kappa_1\kappa_2 + \kappa_2\kappa_3 + \kappa_1\kappa_3}{\kappa_2\kappa_2 - \kappa_1\kappa_2 - \kappa_2\kappa_3 + \kappa_1\kappa_3} \tag{2b}$$

$$\exp(2k_2h) = \frac{\kappa_2\kappa_2 - \kappa_1\kappa_2 - \kappa_2\kappa_3 + \kappa_1\kappa_3}{\kappa_2\kappa_2 + \kappa_1\kappa_2 + \kappa_2\kappa_3 + \kappa_1\kappa_3} \tag{2c}$$

$$= \frac{2\kappa_2\kappa_2 + 2\kappa_1\kappa_3 - (\kappa_2\kappa_2 + \kappa_1\kappa_2 + \kappa_2\kappa_3 + \kappa_1\kappa_3)}{\kappa_2\kappa_2 + \kappa_1\kappa_2 + \kappa_2\kappa_3 + \kappa_1\kappa_3} \tag{2d}$$

$$= \frac{2(\kappa_2\kappa_2 + \kappa_1\kappa_3)}{\kappa_2\kappa_2 + \kappa_1\kappa_3 + \kappa_2\kappa_3 + \kappa_1\kappa_2} - 1 \tag{2e}$$

$$= \frac{2}{\frac{\kappa_2\kappa_2+\kappa_1\kappa_3}{(\kappa_2\kappa_2+\kappa_1\kappa_3)} + \frac{\kappa_2\kappa_3+\kappa_1\kappa_2}{(\kappa_2\kappa_2+\kappa_1\kappa_3)}} - 1 \tag{2f}$$

$$= \frac{2}{1+K} - 1 \qquad \text{, with } K = \frac{\kappa_2\kappa_3 + \kappa_1\kappa_2}{\kappa_2\kappa_2 + \kappa_1\kappa_3} \tag{2g}$$

$$\frac{2}{\exp(2k_2h)+1} = 1 + K \tag{2h}$$

$$1 - \frac{2}{\exp(2k_2h)+1} = K \tag{2i}$$

Now one can apply the identity $\tanh(x) = 1 - \frac{2}{\exp(2x)+1}$

$$\tanh(k_2h) = \frac{\kappa_2\kappa_3 + \kappa_1\kappa_2}{\kappa_2\kappa_2 + \kappa_1\kappa_3} \tag{3a}$$

$$\tanh(-k_2h) = \frac{\kappa_2\kappa_3 + \kappa_1\kappa_2}{\kappa_2\kappa_2 - \kappa_1\kappa_3} \tag{3b}$$

A.2 Second harmonic s-SNOM data of microcacity

Fig. 4.7 of Sect. 4.2.1 shows AFM and s-SNOM measurements demodulated at the third harmonic 3Ω of the hBN/WS_2-covered microcavity and an open microcavity for reference. Fig. A.1 shown here supplements the s-SNOM images by imaging data demodulated at the second harmonic signal 2Ω. The ordering corresponds to the measurements shown in Fig. 4.7, with covered cavity in the top row and open cavity in the bottom row. The colorscales used relate to the excitation wavelengths $\lambda_0 = 532\,\text{nm}$ (green) and $\lambda_{\text{ref}} = 850\,\text{nm}$ (red).

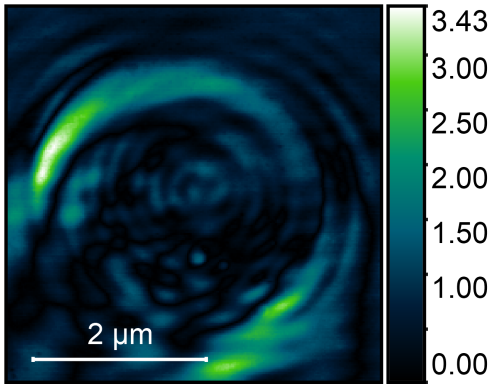

(a) Covered cavity at λ_0.

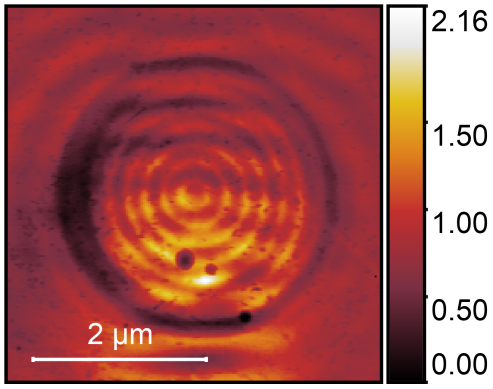

(b) Covered cavity at λ_{ref}.

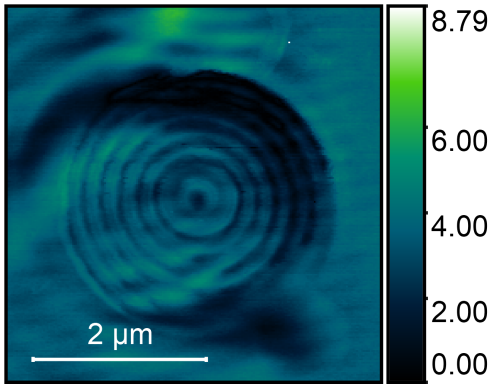

(c) Open cavity at λ_0.

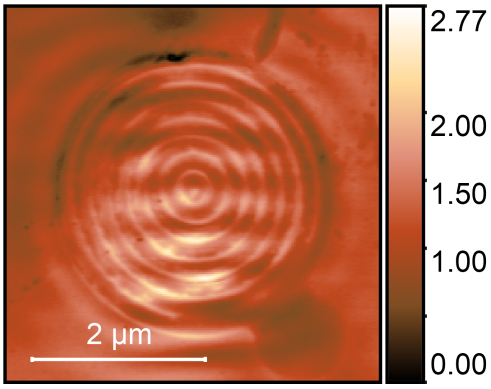

(d) Open cavity at λ_{ref}.

Figure A.1: s-SNOM images at the second harmonic 2Ω, taken simultaneously to the data shown in Fig. 4.7 of Chapter 4. The colorbars show the s-SNOM signal intensity in arbitrary units.

A.3 Supplementary c-AFM data on WS_2/Au

Sect. 5.4.2 presents tunnel I-V measurements on two terraces of a WS_2 flake. The c-AFM data's weak reproducibility is exemplified in this section by supplementary measurements on the same sample. Figs. A.2 to A.7 refer to the top terrace and Figs. A.8 and A.9 refer to the middle terrace. Table 1 summarizes the fitting results displayed in the graphs. Reasons for the high variance of the data are discussed in the main chapter.

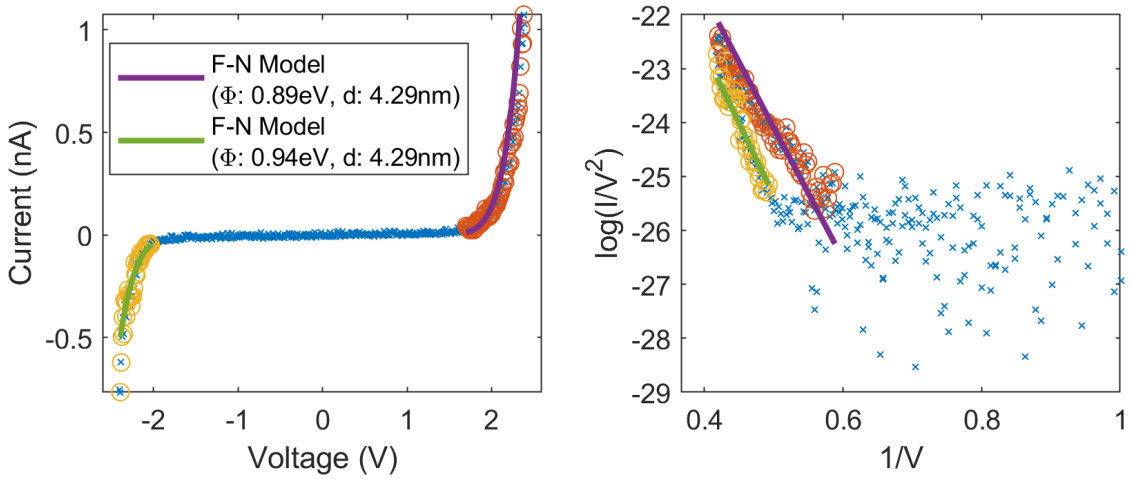

Figure A.2: WS_2Au (top terrace) tunnel current analysis.

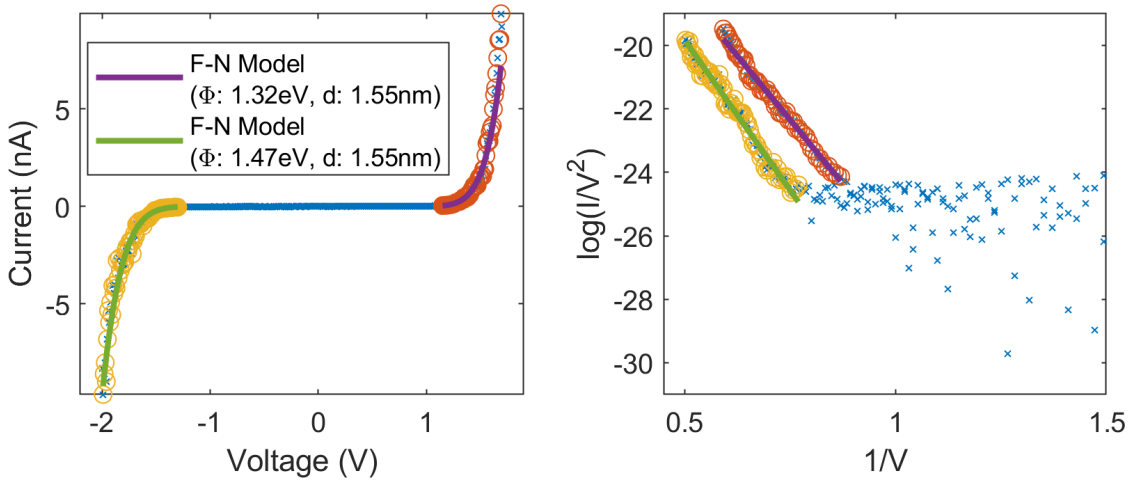

Figure A.3: WS_2Au (top terrace) tunnel current analysis.

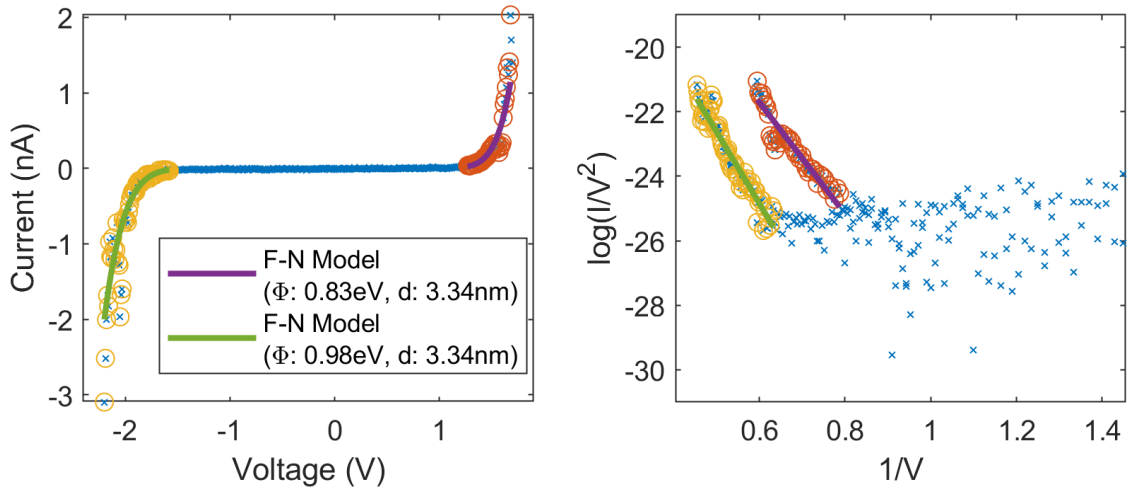

Figure A.4: WS_2Au (top terrace) tunnel current analysis.

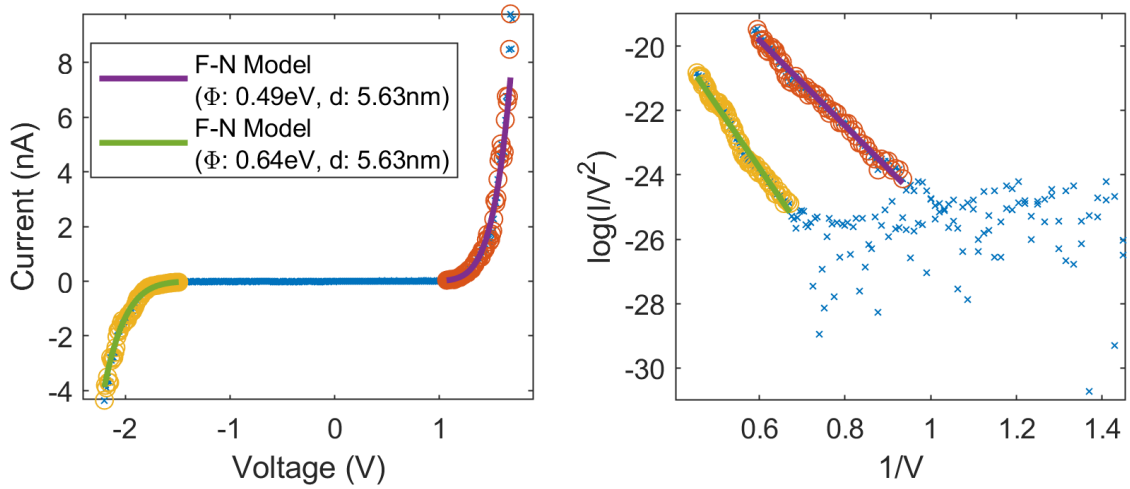

Figure A.5: WS_2Au (top terrace) tunnel current analysis.

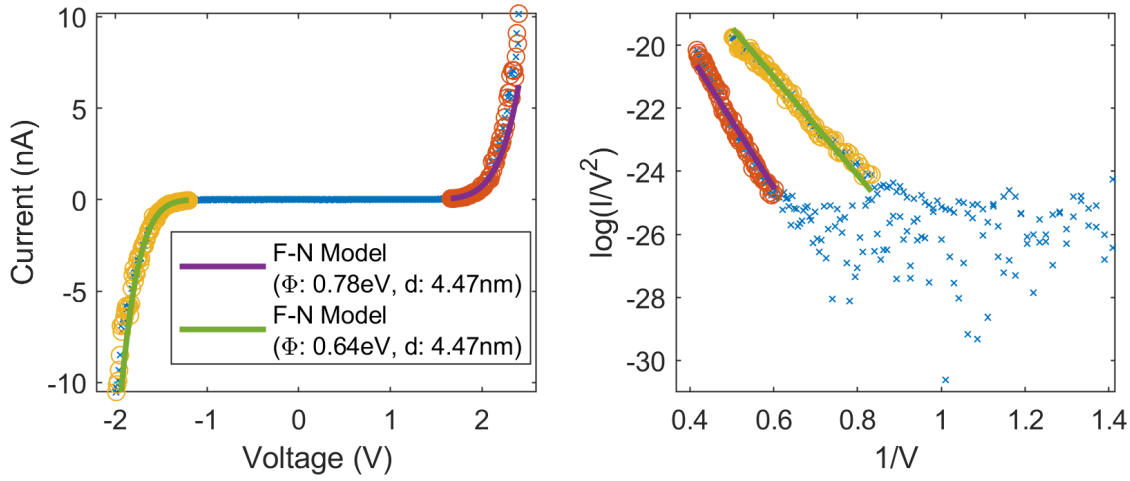

Figure A.6: WS_2Au (top terrace) tunnel current analysis.

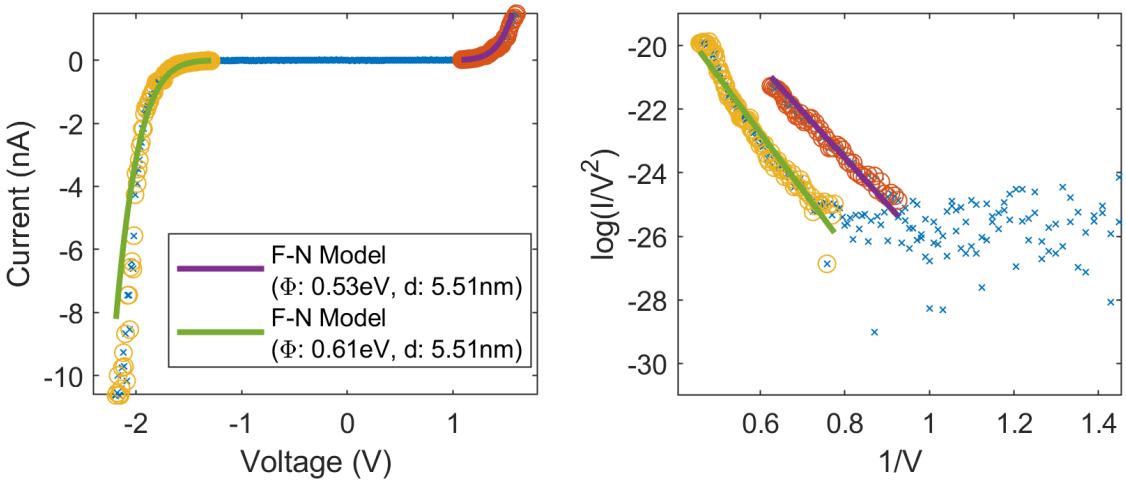

Figure A.7: WS_2Au (top terrace) tunnel current analysis.

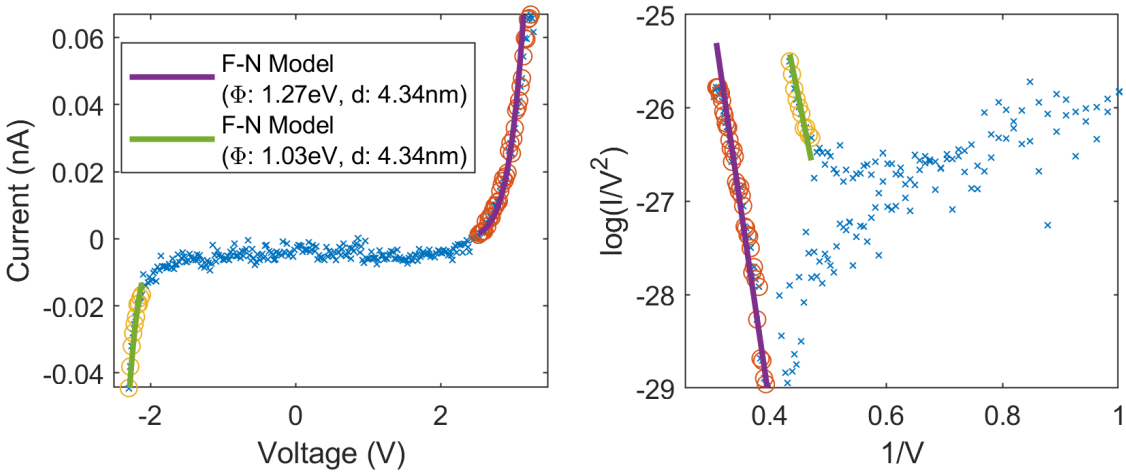

Figure A.8: WS_2Au (middle terrace) tunnel current analysis.

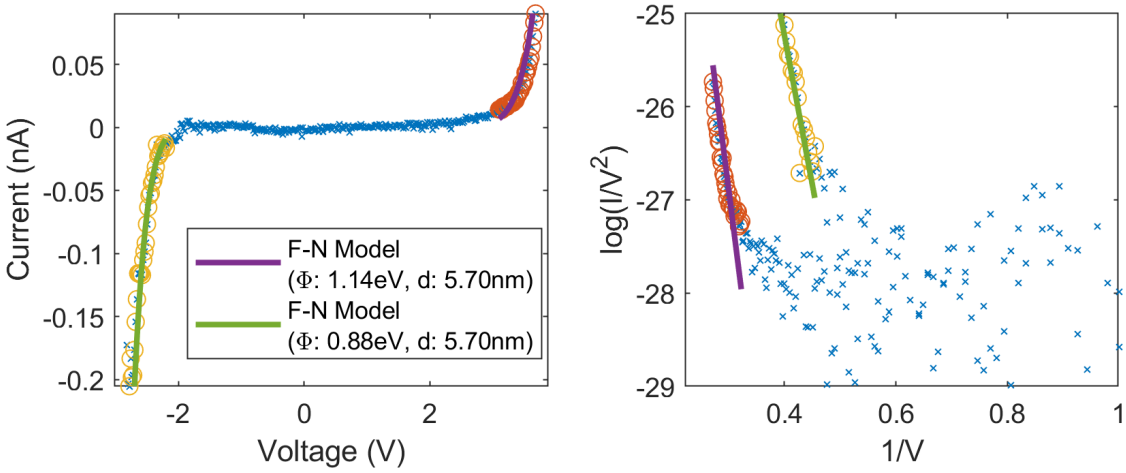

Figure A.9: WS_2Au (middle terrace) tunnel current analysis.

	d (nm)	Φ_1 (eV)	Φ_2 (eV)	Figure
top terrace	5.97	0.76	1.02	Fig. 5.12
	2.29	0.89	0.94	Fig. A.2
	1.55	1.32	1.47	Fig. A.3
	3.34	0.83	0.98	Fig. A.4
	5.63	0.49	0.64	Fig. A.5
	4.47	0.78	0.64	Fig. A.6
	5.51	0.53	0.61	Fig. A.7
mean ± std.	4.11 ± 1.74	0.80 ± 0.27	0.90 ± 0.31	
middle terrace	4.88	0.91	1.06	Fig. 5.11
	4.34	1.03	1.27	Fig. A.8
	5.70	0.88	1.14	Fig. A.9
mean ± std.	4.97 ± 0.69	0.94 ± 0.08	1.16 ± 0.11	

Table 1: Fitting results for Schottky barrier height and tunneling width for supplementary data shown here and in Sect. 5.4.2.

A.4 Iso-energy surfaces of light hole band

Fig. A.10 visualizes the iso-energy surfaces in k-space of the light hole band with the respective Energy levels stated in the captions for an interval of $\Delta E \pm 0.05\,eV$. The k states associated with a given energy are summed to obtain the density of states, as explained for the heavy hole band in Sect. 6.2.3. This is shown in Fig. A.11 in units of $eV^{-1}\,cm^3$. As for the heavy hole band, Fig. A.10 shows the strong warping of the band especially for larger energies.

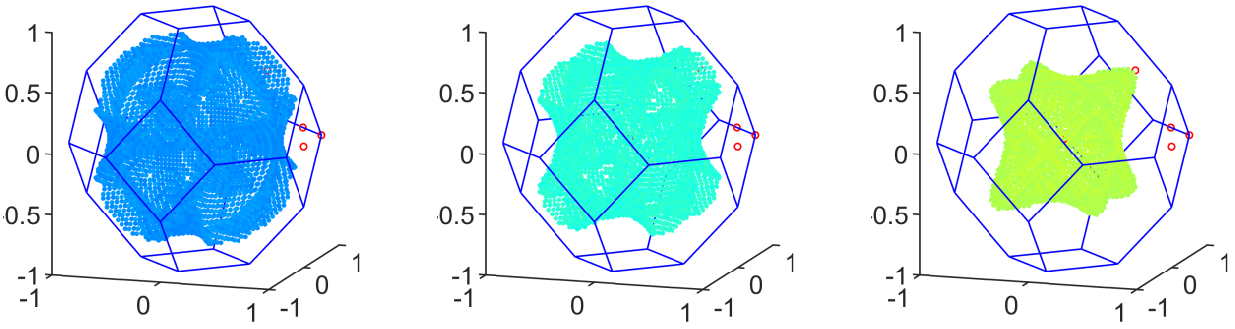

(a) E = -2.2 eV (b) E = -1.8 eV (c) E = -1.4 eV

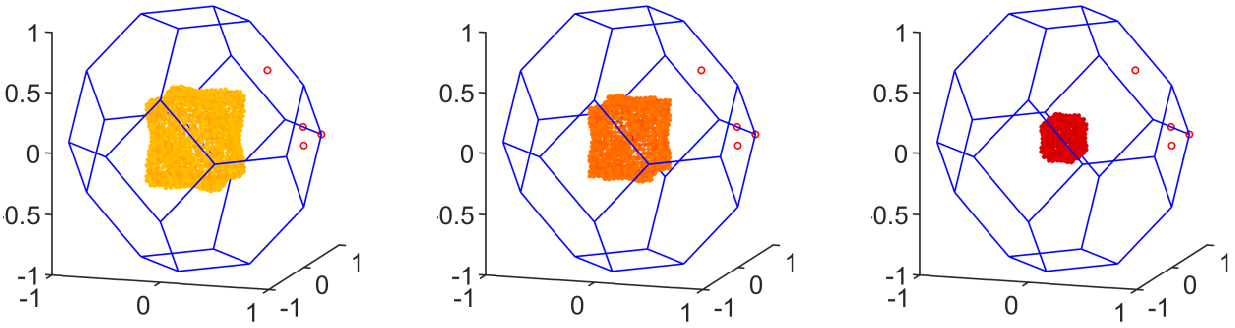

(d) E = -1.0 eV (e) E = -0.6 eV (f) E = -0.2 eV

Figure A.10: k-states associated with different energies ($\Delta E \pm 0.05\,eV$) for the light hole band. The density of states is given by adding the number of k states per energy bin. The high symmetry points are marked by red circles.

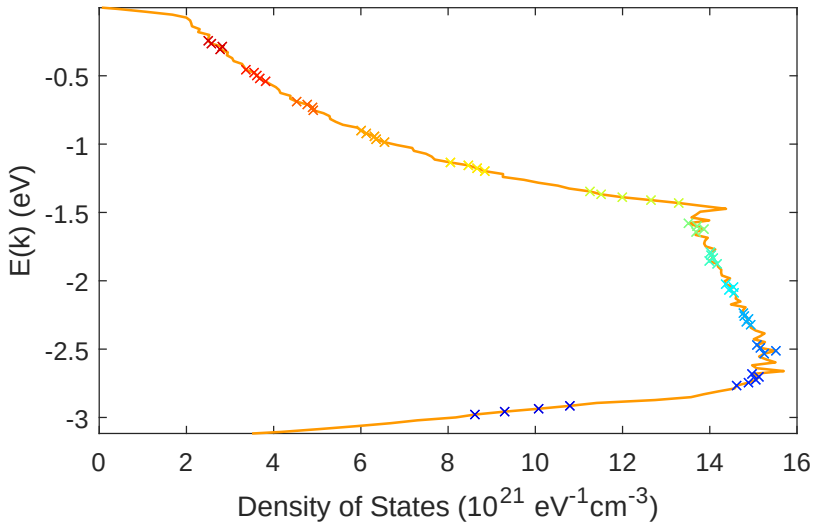

Figure A.11: Density of states of the light hole band. Colors relate to Fig. A.10.

A.5 7th and 9th harmonic simulation at 293 K

This section extends the higher harmonics analysis at room temperature from Sect. 6.3.2 to the 7th and 9th harmonic. Figs. A.12a and A.12b show the spectrum centred around the respective frequencies in linear intensity scale. Plotted are the simulation results for the realistic non-local empirical pseudo potential (green and blue) and the parabolic band approximation (red). The relative strength between band non-parabolicity and energy-dependent momentum scattering as non-linear mechanisms is the same as for the 3rd and 5th harmonic, discussed in Sect. 6.3.2.

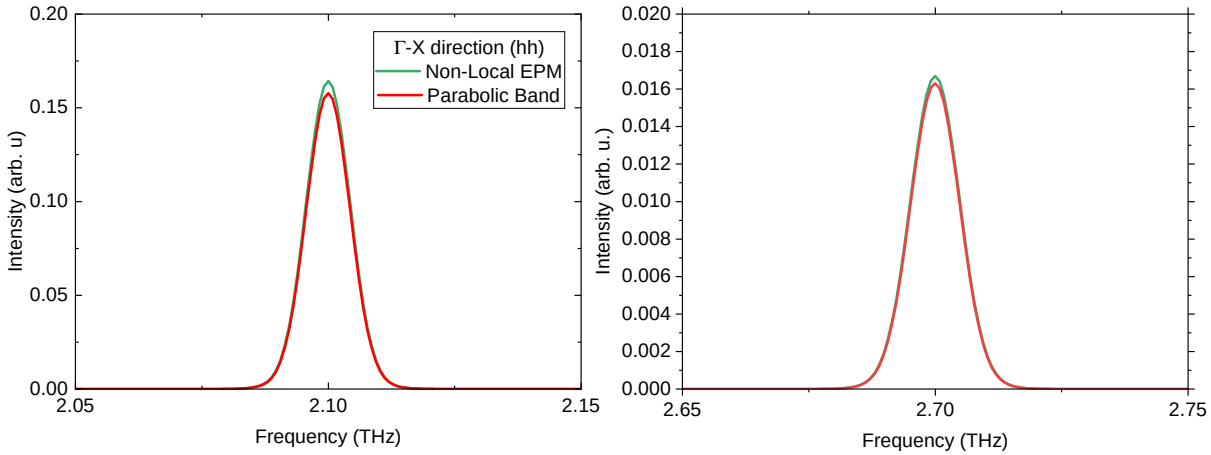

(a) Heavy holes

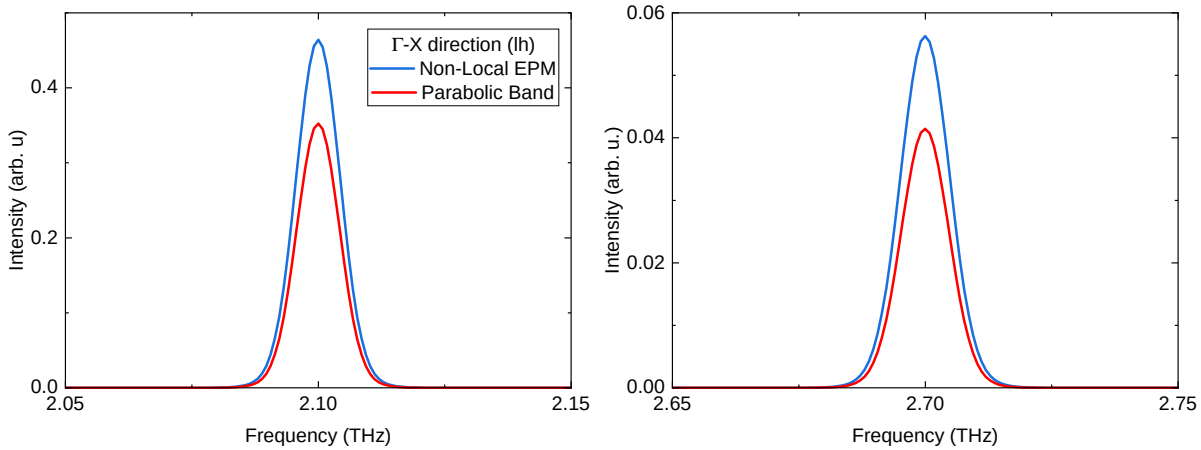

(b) Light holes

Figure A.12: Seventh (left) and ninth (right) harmonics generated by a (a) heavy and (b) light hole carrier according to EPM and the parabolic approximation. The conclusion about relative strengths from Sect. 6.3.2 can be extended to these frequencies.

List of own publications

Journal articles

[Wal1] F. Meng, F. Walla, Q. ul-Islam, A. Pashkin, H. Schneider, C. Jungemann, M. D. Thomson, and H. G. Roskos. "Importance of Valence-Band Anharmonicity and Contribution of Light Holes for Higher-Harmonic Generation in Si:B Pumped with Intense Terahertz Pulses". In: *Physical Review B* (2021).

[Wal2] A. Soltani, F. Kuschewski, M. Bonmann, A. Generalov, A. Vorobiev, F. Ludwig, M. M. Wiecha, D. Čibiraitė, F. Walla, S. Winnerl, S. C. Kehr, L. M. Eng, J. Stake, and H. G. Roskos. "Direct Nanoscopic Observation of Plasma Waves in the Channel of a Graphene Field-Effect Transistor". In: *Light Sci Appl* 9.1 (2020).

[Wal3] B. Jerez, F. Walla, A. Betancur, P. Martín-Mateos, C. de Dios, and P. Acedo. "Electro-Optic THz Dual-Comb Architecture for High-Resolution, Absolute Spectroscopy". In: *Opt. Lett., OL* 44.2 (2019).

[Wal4] O. Mey, F. Wall, L. M. Schneider, D. Günder, F. Walla, A. Soltani, H. Roskos, N. Yao, P. Qing, W. Fang, and A. Rahimi-Iman. "Enhancement of the Monolayer Tungsten Disulfide Exciton Photoluminescence with a Two-Dimensional Material/Air/Gallium Phosphide In-Plane Microcavity". In: *ACS Nano* 13.5 (2019).

[Wal5] B. Jerez, P. Martín-Mateos, F. Walla, C. de Dios, and P. Acedo. "Flexible Electro-Optic, Single-Crystal Difference Frequency Generation Architecture for Ultrafast Mid-Infrared Dual-Comb Spectroscopy". In: *ACS Photonics* 5.6 (2018).

[Wal6] F. Walla, F. Bürkle, I. Sinev, M. M. Wiecha, N. Mecklenbeck, K. Ladutenko, R. Malureanu, F. Komissarenko, A. Lavrinenko, A. Bogdanov, A. Soltani, and H. G. Roskos. "Near-Field Observation of Guided-Mode Resonances on a Metasurface via Dielectric Nanosphere Excitation". In: *ACS Photonics* 5.11 (2018).

[Wal7] F. Walla, M. M. Wiecha, N. Mecklenbeck, S. Beldi, F. Keilmann, M. D. Thomson, and H. G. Roskos. "Anisotropic Excitation of Surface Plasmon Polaritons on a Metal Film by a Scattering-Type Scanning near-Field Microscope with a Non-Rotationally-Symmetric Probe Tip". In: *Nanophotonics* 7.1 (2018).

[Wal8] B. Jerez, F. Walla, C. de Dios, P. Martin-Mateos, and P. Acedo. "Fully Frequency-Locked Multiheterodyne Architecture for Remote Optical Frequency Comb Rapid Detection". In: *J. Lightwave Technol.* 35.19 (2017).

Conference proceedings

[Wal9] F. Meng, F. Walla, Q. ul-Islam, M. D. Thomson, S. Kovalev, J.-C. Deinert, I. Ilyakov, M. Chen, A. Ponomaryov, S. G. Pavlov, H.-W. Hübers, N. V. Abrosimov, C. Jungemann, and H. G. Roskos. "High-Harmonic Generation from Weakly

p-Doped Si Pumped with Intense THz Pulses". In: *2021 46th International Conference on Infrared, Millimeter and Terahertz Waves (IRMMW-THz)*. 2021 46th International Conference on Infrared, Millimeter and Terahertz Waves (IRMMW-THz). 2021.

[Wal10] F. Meng, F. Walla, Q. ul-Islam, M. D. Thomson, S. Kovalev, J.-C. Deinert, I. Ilyakov, M. Chen, A. Ponomaryov, S. G. Pavlov, H.-W. Hübers, N. V. Abrosimov, and H. G. Roskos. "High-Harmonic Generation from Doped Si Pumped with Intense THz Pulses". In: *2021 Conference on Lasers and Electro-Optics Europe European Quantum Electronics Conference (CLEO/Europe-EQEC)*. 2021 Conference on Lasers and Electro-Optics Europe European Quantum Electronics Conference (CLEO/Europe-EQEC). 2021.

[Wal11] F. Meng, F. Walla, Q. ul-Islam, M. D. Thomson, A. Pashkin, H. Schneider, and H. G. Roskos. "Fifth-Harmonic Generation in Si:B Pumped with Intense Terahertz Pulses". In: *2021 46th International Conference on Infrared, Millimeter and Terahertz Waves (IRMMW-THz)*. 2021 46th International Conference on Infrared, Millimeter and Terahertz Waves (IRMMW-THz). 2021.

[Wal12] F. Kuschewski, A. Soltani, M. Bonmann, A. Generalov, A. Vorobiev, F. Ludwig, D. Čibiraitė, F. Walla, S. C. Kehr, L. M. Eng, J. Stake, and H. G. Roskos. "Direct Proof of the Dyakonov-Shur Postulate – Nanoscopic Observation of Charge Density Waves in the Channel of a Graphene Field-Effect Transistor". In: French-German Terahertz Conference (FRTC-2019). Kaiserslautern, Deutschland, 2019.

[Wal13] O. Mey, F. Wall, L. M. Schneider, D. Günder, F. Walla, S. Kehr, L. Eng, J. Stake, and H. Roskos. "Near-Field Nano-Imaging of Buried Microcavity for Enhancement of WS2 Monolayer Exciton Photoluminescence". In: *Proceedings of META 2019, The 10th International Conference on Metamaterials, Photonic Crystals and Plasmonics*. Intl. Conf. on Metamaterials, Photonic Crystals and Plasmonics META. Lisboa, Portugal, 2019.

[Wal14] A. Soltani, F. Kuschewski, M. Bonmann, A. Generalov, A. Vorobiev, F. Ludwig, M. Wiecha, D. Čibiraitė, F. Walla, S. Kehr, L. Eng, J. Stake, and H. Roskos. "Unveiling the Plasma Wave in the Channel of Graphene Field-Effect Transistor". In: *2019 44th International Conference on Infrared, Millimeter, and Terahertz Waves (IRMMW-THz)*. 2019 44th International Conference on Infrared, Millimeter, and Terahertz Waves (IRMMW-THz). 2019.

[Wal15] F. Walla, F. Bürkle, I. Sinev, A. Bogdanov, F. Komissarenko, A. Soltani, R. Malureanu, A. Lavrinenko, and H. G. Roskos. "Direct Near-Field Mapping of Nano-Sphere-Excited Leaky Surface Modes Atanisotropic Metasurface". In: *Journal of Physics: Conference Series*. Vol. 1092. 2018.

[Wal16] B. Jerez, F. Walla, C. de Dios, P. Martín-Mateos, and P. Acedo. "Fully Remote Rapid Multiheterodyne Spectroscopy Based on the Remote Detection of an Optical Frequency Comb through Optical Injection Locking and Electro-Optic Comb Generation". In: *2017 European Conference on Lasers and Electro-Optics and European Quantum Electronics Conference (2017), Paper ED_P_5*. European Quantum Electronics Conference. Optical Society of America, 2017.

[Wal17] A. Moreno-Oyervides, J. P. López, P. Martín-Mateos, F. Walla, R. Criado, V. Krozer, and P. Acedo. "Use of Functional Principal Components Analysis in CW subTHz Spectroscopy for Hydrocarbon Emulsified Water Assessment". In: *2017 42nd International Conference on Infrared, Millimeter, and Terahertz Waves (IRMMW-THz)*. 2017 42nd International Conference on Infrared, Millimeter, and Terahertz Waves (IRMMW-THz). 2017.

[Wal18] F. Walla, B. Jerez, P. Martín-Mateos, C. de Dios, and P. Acedo. "Absolute-Frequency High-Resolution Real-Time Terahertz Dual-Comb Spectrometer". In: *2017 42nd International Conference on Infrared, Millimeter, and Terahertz Waves (IRMMW-THz)*. 2017 42nd International Conference on Infrared, Millimeter, and Terahertz Waves (IRMMW-THz). 2017.

Bibliography

[1] Y. Fang and M. Sun. "Nanoplasmonic Waveguides: Towards Applications in Integrated Nanophotonic Circuits". In: *Light Sci Appl* 4.6 (2015).

[2] E. Ozbay. "Plasmonics: Merging Photonics and Electronics at Nanoscale Dimensions". In: *Science* 311.5758 (2006).

[3] W. O. F. Carvalho and J. R. Mejía-Salazar. "Plasmonics for Telecommunications Applications". In: *Sensors (Basel)* 20.9 (2020).

[4] O. Hess, J. B. Pendry, S. A. Maier, R. F. Oulton, J. M. Hamm, and K. L. Tsakmakidis. "Active Nanoplasmonic Metamaterials". In: *Nature Mater* 11.7 (2012).

[5] A. Y. Zhu, A. I. Kuznetsov, B. Luk'yanchuk, N. Engheta, and P. Genevet. "Traditional and Emerging Materials for Optical Metasurfaces". In: *Nanophotonics* 6.2 (2017).

[6] C. M. Soukoulis and M. Wegener. "Past Achievements and Future Challenges in the Development of Three-Dimensional Photonic Metamaterials". In: *Nature Photon* 5.9 (2011).

[7] H.-H. Hsiao, C. H. Chu, and D. P. Tsai. "Fundamentals and Applications of Metasurfaces". In: *Small Methods* 1.4 (2017).

[8] F. Capasso. "The Future and Promise of Flat Optics: A Personal Perspective". In: *Nanophotonics* 7.6 (2018).

[9] J. S. Gomez-Diaz and A. Alù. "Flatland Optics with Hyperbolic Metasurfaces". In: *ACS Photonics* 3.12 (2016).

[10] Y. Guo, W. Newman, C. L. Cortes, and Z. Jacob. "Applications of Hyperbolic Metamaterial Substrates". In: *Advances in OptoElectronics* 2012 (2012).

[11] N. Engheta, A. Salandrino, and A. Alù. "Circuit Elements at Optical Frequencies: Nanoinductors, Nanocapacitors, and Nanoresistors". In: *Phys. Rev. Lett.* 95.9 (2005).

[12] N. Engheta. "Circuits with Light at Nanoscales: Optical Nanocircuits Inspired by Metamaterials". In: *Science* 317.5845 (2007).

[13] N. Meinzer, W. L. Barnes, and I. R. Hooper. "Plasmonic Meta-Atoms and Metasurfaces". In: *Nature Photon* 8.12 (2014).

[14] J. Meyer. "It's Still All about Graphene". In: *Nature Mater* 10.1 (2011).

[15] C. Schneider, M. M. Glazov, T. Korn, S. Höfling, and B. Urbaszek. "Two-Dimensional Semiconductors in the Regime of Strong Light-Matter Coupling". In: *Nat Commun* 9.1 (2018).

[16] A. M. Ionescu and H. Riel. "Tunnel Field-Effect Transistors as Energy-Efficient Electronic Switches". In: *Nature* 479.7373 (2011).

[17] L. Britnell, R. V. Gorbachev, R. Jalil, B. D. Belle, F. Schedin, A. Mishchenko, T. Georgiou, M. I. Katsnelson, L. Eaves, S. V. Morozov, N. M. R. Peres, J. Leist, A. K. Geim, K. S. Novoselov, and L. A. Ponomarenko. "Field-Effect Tunneling Transistor Based on Vertical Graphene Heterostructures". In: *Science* 335.6071 (2012).

[18] S. B. Glybovski, S. A. Tretyakov, P. A. Belov, Y. S. Kivshar, and C. R. Simovski. "Metasurfaces: From Microwaves to Visible". In: *Physics Reports* 634 (2016).

[19] H. Lamb. "On the Reflection and Transmission of Electric Waves by a Metallic Grating". In: *Proceedings of the London Mathematical Society* s1-29.1 (1897).

[20] T. Yamaguchi, S. Yoshida, and A. Kinbara. "Effect of Retarded Dipole–Dipole Interactions between Island Particles on the Optical Plasma-Resonance Absorption of a Silver-Island Film". In: *J. Opt. Soc. Am.* 64.11 (1974).

[21] N. Yu and F. Capasso. "Flat Optics with Designer Metasurfaces". In: *Nature Mater* 13.2 (2014).

[22] Y. Liu and X. Zhang. "Metasurfaces for Manipulating Surface Plasmons". In: *Appl. Phys. Lett.* 103.14 (2013).

[23] J. S. Gomez-Diaz, M. Tymchenko, and A. Alù. "Hyperbolic Metasurfaces: Surface Plasmons, Light-Matter Interactions, and Physical Implementation Using Graphene Strips [Invited]". In: *Opt. Mater. Express, OME* 5.10 (2015).

[24] O. Y. Yermakov, A. I. Ovcharenko, M. Song, A. A. Bogdanov, I. V. Iorsh, and Y. S. Kivshar. "Hybrid Waves Localized at Hyperbolic Metasurfaces". In: *Phys. Rev. B* 91.23 (2015).

[25] F. Monticone and A. Alù. "Metamaterial, Plasmonic and Nanophotonic Devices". In: *Rep. Prog. Phys.* 80.3 (2017).

[26] A. Samusev, I. Mukhin, R. Malureanu, O. Takayama, D. V. Permyakov, I. S. Sinev, D. Baranov, O. Yermakov, I. V. Iorsh, A. A. Bogdanov, and A. V. Lavrinenko. "Polarization-Resolved Characterization of Plasmon Waves Supported by an Anisotropic Metasurface". In: *Opt. Express* 25.26 (2017).

[27] G. Bartal. "Bright Future for Hyperbolic Chips". In: *Nature* 522.7555 (2015).

[28] A. A. High, R. C. Devlin, A. Dibos, M. Polking, D. S. Wild, J. Perczel, N. P. de Leon, M. D. Lukin, and H. Park. "Visible-Frequency Hyperbolic Metasurface". In: *Nature* 522.7555 (2015).

[29] L. Salomon, G. Bassou, H. Aourag, J. P. Dufour, F. de Fornel, F. Carcenac, and A. V. Zayats. "Local Excitation of Surface Plasmon Polaritons at Discontinuities of a Metal Film: Theoretical Analysis and Optical near-Field Measurements". In: *Phys. Rev. B* 65.12 (2002).

[30] Y. Li, A. Chernikov, X. Zhang, A. Rigosi, H. M. Hill, A. M. van der Zande, D. A. Chenet, E.-M. Shih, J. Hone, and T. F. Heinz. "Measurement of the Optical Dielectric Function of Monolayer Transition-Metal Dichalcogenides: MoS 2 , Mo S e 2 , WS 2 , and WS e 2". In: *Phys. Rev. B* 90.20 (2014).

[31] A. Klick, S. de la Cruz, C. Lemke, M. Großmann, H. Beyer, J. Fiutowski, H.-G. Rubahn, E. R. Méndez, and M. Bauer. "Amplitude and Phase of Surface Plasmon Polaritons Excited at a Step Edge". In: *Appl. Phys. B* 122.4 (2016).

[32] Z. Fei, A. S. Rodin, G. O. Andreev, W. Bao, A. S. McLeod, M. Wagner, L. M. Zhang, Z. Zhao, M. Thiemens, G. Dominguez, M. M. Fogler, A. H. C. Neto, C. N. Lau, F. Keilmann, and D. N. Basov. "Gate-Tuning of Graphene Plasmons Revealed by Infrared Nano-Imaging". In: *Nature* 487.7405 (2012).

[33] J. Chen, M. Badioli, P. Alonso-González, S. Thongrattanasiri, F. Huth, J. Osmond, M. Spasenović, A. Centeno, A. Pesquera, P. Godignon, A. Zurutuza Elorza, N. Camara, F. J. G. de Abajo, R. Hillenbrand, and F. H. L. Koppens. "Optical Nano-Imaging of Gate-Tunable Graphene Plasmons". In: *Nature* 487.7405 (2012).

[34] A. Woessner, M. B. Lundeberg, Y. Gao, A. Principi, P. Alonso-González, M. Carrega, K. Watanabe, T. Taniguchi, G. Vignale, M. Polini, J. Hone, R. Hillenbrand, and F. H. L. Koppens. "Highly Confined Low-Loss Plasmons in Graphene–Boron Nitride Heterostructures". In: *Nature Mater* 14.4 (2015).

[35] Y. Xu, X. Zhang, Z. Tian, J. Gu, C. Ouyang, Y. Li, J. Han, and W. Zhang. "Mapping the Near-Field Propagation of Surface Plasmons on Terahertz Metasurfaces". In: *Appl. Phys. Lett.* 107.2 (2015).

[36] F. Peragut, L. Cerruti, A. Baranov, J. P. Hugonin, T. Taliercio, Y. De Wilde, and J. J. Greffet. "Hyperbolic Metamaterials and Surface Plasmon Polaritons". In: *Optica* 4.11 (2017).

[37] B. J. Bohn, M. Schnell, M. A. Kats, F. Aieta, R. Hillenbrand, and F. Capasso. "Near-Field Imaging of Phased Array Metasurfaces". In: *Nano Lett.* 15.6 (2015).

[38] M. Schnell, P. Sarriugarte, T. Neuman, A. B. Khanikaev, G. Shvets, J. Aizpurua, and R. Hillenbrand. "Real-Space Mapping of the Chiral Near-Field Distributions in Spiral Antennas and Planar Metasurfaces". In: *Nano Lett.* 16.1 (2016).

[39] A. B. Khanikaev, N. Arju, Z. Fan, D. Purtseladze, F. Lu, J. Lee, P. Sarriugarte, M. Schnell, R. Hillenbrand, M. A. Belkin, and G. Shvets. "Experimental Demonstration of the Microscopic Origin of Circular Dichroism in Two-Dimensional Metamaterials". In: *Nat Commun* 7.1 (2016).

[40] A. Baev, P. N. Prasad, H. Ågren, M. Samoć, and M. Wegener. "Metaphotonics: An Emerging Field with Opportunities and Challenges". In: *Physics Reports* 594 (2015).

[41] G. Spektor, A. David, B. Gjonaj, G. Bartal, and M. Orenstein. "Metafocusing by a Metaspiral Plasmonic Lens". In: *Nano Lett.* 15.9 (2015).

[42] D. Wintz, A. Ambrosio, A. Y. Zhu, P. Genevet, and F. Capasso. "Anisotropic Surface Plasmon Polariton Generation Using Bimodal V-Antenna Based Metastructures". In: *ACS Photonics* 4.1 (2017).

[43] S. Dobmann, A. Kriesch, D. Ploss, and U. Peschel. "Near-Field Analysis of Bright and Dark Modes on Plasmonic Metasurfaces Showing Extraordinary Suppressed Transmission". In: *Advanced Optical Materials* 2.10 (2014).

[44] B. Dagens, M. Février, P. Gogol, S. Blaize, A. Apuzzo, G. Magno, R. Mégy, and G. Lerondel. "Direct Observation of Optical Field Phase Carving in the Vicinity of Plasmonic Metasurfaces". In: *Nano Lett.* 16.7 (2016).

[45] A. Splendiani, L. Sun, Y. Zhang, T. Li, J. Kim, C.-Y. Chim, G. Galli, and F. Wang. "Emerging Photoluminescence in Monolayer MoS2". In: *Nano Lett.* 10.4 (2010).

[46] K. F. Mak, C. Lee, J. Hone, J. Shan, and T. F. Heinz. “Atomically Thin MoS 2 : A New Direct-Gap Semiconductor”. In: *Phys. Rev. Lett.* 105.13 (2010).

[47] P. A. D. Gonçalves, L. P. Bertelsen, S. Xiao, and N. A. Mortensen. “Plasmon-Exciton Polaritons in Two-Dimensional Semiconductor/Metal Interfaces”. In: *Phys. Rev. B* 97.4 (2018).

[48] H. Zhang, B. Abhiraman, Q. Zhang, J. Miao, K. Jo, S. Roccasecca, M. W. Knight, A. R. Davoyan, and D. Jariwala. “Hybrid Exciton-Plasmon-Polaritons in van Der Waals Semiconductor Gratings”. In: *Nat Commun* 11.1 (2020).

[49] M. Nauman, J. Yan, D. de Ceglia, M. Rahmani, K. Zangeneh Kamali, C. De Angelis, A. E. Miroshnichenko, Y. Lu, and D. N. Neshev. “Tunable Unidirectional Nonlinear Emission from Transition-Metal-Dichalcogenide Metasurfaces”. In: *Nat Commun* 12.1 (2021).

[50] S. Manzeli, D. Ovchinnikov, D. Pasquier, O. V. Yazyev, and A. Kis. “2D Transition Metal Dichalcogenides”. In: *Nat Rev Mater* 2.8 (2017).

[51] A. Srivastava, M. Sidler, A. V. Allain, D. S. Lembke, A. Kis, and A. Imamoğlu. “Valley Zeeman Effect in Elementary Optical Excitations of Monolayer WSe2”. In: *Nature Phys* 11.2 (2015).

[52] K. F. Mak and J. Shan. “Photonics and Optoelectronics of 2D Semiconductor Transition Metal Dichalcogenides”. In: *Nature Photon* 10.4 (2016).

[53] B. Radisavljevic, A. Radenovic, J. Brivio, V. Giacometti, and A. Kis. “Single-Layer MoS2 Transistors”. In: *Nature Nanotech* 6.3 (2011).

[54] T. Georgiou, R. Jalil, B. D. Belle, L. Britnell, R. V. Gorbachev, S. V. Morozov, Y.-J. Kim, A. Gholinia, S. J. Haigh, O. Makarovsky, L. Eaves, L. A. Ponomarenko, A. K. Geim, K. S. Novoselov, and A. Mishchenko. “Vertical Field-Effect Transistor Based on Graphene–WS2 Heterostructures for Flexible and Transparent Electronics”. In: *Nature Nanotech* 8.2 (2013).

[55] L. Britnell, R. V. Gorbachev, R. Jalil, B. D. Belle, F. Schedin, M. I. Katsnelson, L. Eaves, S. V. Morozov, A. S. Mayorov, N. M. R. Peres, A. H. Castro Neto, J. Leist, A. K. Geim, L. A. Ponomarenko, and K. S. Novoselov. “Electron Tunneling through Ultrathin Boron Nitride Crystalline Barriers”. In: *Nano Lett.* 12.3 (2012).

[56] L. Novotny and B. Hecht. *Principles of Nano-Optics*. 2nd ed. Cambridge: Cambridge University Press, 2012.

[57] D. G. Voelz. *Computational Fourier Optics: A MATLAB Tutorial*. SPIE, 2011.

[58] A. Zayats, D. Richards, and A. V. Zayats, eds. *Nano-Optics and near-Field Optical Microscopy*. Artech House Nanoscale Science and Engineering. Boston, Mass.: Artech House, 2009.

[59] A. Bitzer, H. Merbold, A. Thoman, T. Feurer, H. Helm, and M. Walther. “Terahertz Near-Field Imaging of Electric and Magnetic Resonances of a Planar Metamaterial”. In: *Opt. Express* 17.5 (2009).

[60] G. Binnig, C. F. Quate, and C. Gerber. “Atomic Force Microscope”. In: *Phys. Rev. Lett.* 56.9 (1986).

[61] L. Gross, F. Mohn, N. Moll, P. Liljeroth, and G. Meyer. “The Chemical Structure of a Molecule Resolved by Atomic Force Microscopy”. In: *Science* 325.5944 (2009).

[62] P. Eaton and P. West. *Atomic Force Microscopy*. First published in paperback. Oxford: Oxford University Press, 2018.

[63] Y. Seo and W. Jhe. "Atomic Force Microscopy and Spectroscopy". In: *Rep. Prog. Phys.* 71.1 (2008).

[64] F. J. Giessibl. "Forces and Frequency Shifts in Atomic-Resolution Dynamic-Force Microscopy". In: *Phys. Rev. B* 56.24 (1997).

[65] H. Hölscher, U. D. Schwarz, and R. Wiesendanger. "Calculation of the Frequency Shift in Dynamic Force Microscopy". In: *Applied Surface Science* 140.3 (1999).

[66] N. Chan, C. Lin, T. Jacobs, R. W. Carpick, and P. Egberts. "Quantitative Determination of the Interaction Potential between Two Surfaces Using Frequency-Modulated Atomic Force Microscopy". In: *Beilstein J. Nanotechnol.* 11 (2020).

[67] J. E. Sader, I. Larson, P. Mulvaney, and L. R. White. "Method for the Calibration of Atomic Force Microscope Cantilevers". In: *Review of Scientific Instruments* 66.7 (1995).

[68] S. Belikov, J. Alexander, C. Wall, I. Yermolenko, S. Magonov, and I. Malovichko. "Thermal Tune Method for AFM Oscillatory Resonant Imaging in Air and Liquid". In: *2014 American Control Conference*. 2014 American Control Conference - ACC 2014. Portland, OR, USA: IEEE, 2014.

[69] L. Jiang, J. Weber, F. M. Puglisi, P. Pavan, L. Larcher, W. Frammelsberger, G. Benstetter, and M. Lanza. "Understanding Current Instabilities in Conductive Atomic Force Microscopy". In: *Materials* 12.3 (2019).

[70] E. A. Ash and G. Nicholls. "Super-Resolution Aperture Scanning Microscope". In: *Nature* 237.5357 (1972).

[71] D. W. Pohl, W. Denk, and M. Lanz. "Optical Stethoscopy: Image Recording with Resolution $\lambda/20$". In: *Appl. Phys. Lett.* 44.7 (1984).

[72] A. Lewis, M. Isaacson, A. Harootunian, and A. Muray. "Development of a 500 Å Spatial Resolution Light Microscope". In: *Ultramicroscopy* 13.3 (1984).

[73] A. Cvitkovic, N. Ocelic, and R. Hillenbrand. "Analytical Model for Quantitative Prediction of Material Contrasts in Scattering-Type near-Field Optical Microscopy". In: *Opt. Express* 15.14 (2007).

[74] Y. Li, S. Popov, A. T. Friberg, and S. Sergeyev. "Rigorous Modeling and Physical Interpretation of Terahertz Near-Field Imaging". In: *JEOS:RP* 4 (2009).

[75] B. Knoll and F. Keilmann. "Near-Field Probing of Vibrational Absorption for Chemical Microscopy". In: *Letters to Nature* 399 (1999).

[76] J. A. Porto, P. Johansson, S. P. Apell, and T. López-Ríos. "Resonance Shift Effects in Apertureless Scanning Near-Field Optical Microscopy". In: *Phys. Rev. B* 67.8 (2003).

[77] J. Aizpurua, T. Taubner, F. J. G. de Abajo, M. Brehm, and R. Hillenbrand. "Substrate-Enhanced Infrared near-Field Spectroscopy". In: *Opt. Express, OE* 16.3 (2008).

[78] K. Moon, Y. Do, M. Lim, G. Lee, H. Kang, K.-S. Park, and H. Han. "Quantitative Coherent Scattering Spectra in Apertureless Terahertz Pulse Near-Field Microscopes". In: *Appl. Phys. Lett.* 101.1 (2012).

[79] B. Hauer, A. P. Engelhardt, and T. Taubner. “Quasi-Analytical Model for Scattering Infrared near-Field Microscopy on Layered Systems”. In: *Opt. Express* 20.12 (2012).

[80] A. A. Govyadinov, I. Amenabar, F. Huth, P. S. Carney, and R. Hillenbrand. “Quantitative Measurement of Local Infrared Absorption and Dielectric Function with Tip-Enhanced Near-Field Microscopy”. In: *J. Phys. Chem. Lett.* 4.9 (2013).

[81] S. C. Schneider, S. Grafström, and L. M. Eng. “Scattering Near-Field Optical Microscopy of Optically Anisotropic Systems”. In: *Phys. Rev. B* 71.11 (2005).

[82] S. Schneider. “Scattering Scanning Near-Field Optical Microscopy on Anisotropic Dielectrics”. Dresden: Technische Universität Dresden, 2007.

[83] A. S. McLeod, P. Kelly, M. D. Goldflam, Z. Gainsforth, A. J. Westphal, G. Dominguez, M. H. Thiemens, M. M. Fogler, and D. N. Basov. “Model for Quantitative Tip-Enhanced Spectroscopy and the Extraction of Nanoscale-Resolved Optical Constants”. In: *Phys. Rev. B* 90.8 (2014).

[84] J. D. Jackson. *Classical Electrodynamics*. 3rd ed. Hoboken, NY: Wiley, 2009.

[85] H.-G. von Ribbeck. “THz Near-Field Microscopy and Spectroscopy”. Dresden: Technische Universit¨at Dresden, 2014.

[86] N. Ocelic. “Quantitative Near-field Phonon-polariton Spectroscopy”. München: TU München, 2007.

[87] N. Ocelic, A. Huber, and R. Hillenbrand. “Pseudoheterodyne Detection for Background-Free near-Field Spectroscopy”. In: *Appl. Phys. Lett.* 89.10 (2006).

[88] M. Lanza, M. Porti, M. Nafría, X. Aymerich, E. Whittaker, and B. Hamilton. “Note: Electrical Resolution during Conductive Atomic Force Microscopy Measurements under Different Environmental Conditions and Contact Forces”. In: *Review of Scientific Instruments* 81.10 (2010).

[89] P. Bampoulis, R. van Bremen, Q. Yao, B. Poelsema, H. J. W. Zandvliet, and K. Sotthewes. “Defect Dominated Charge Transport and Fermi Level Pinning in MoS2/Metal Contacts”. In: *ACS Appl Mater Interfaces* 9.22 (2017).

[90] F. Giannazzo, I. Deretzis, A. La Magna, F. Roccaforte, and R. Yakimova. “Electronic Transport at Monolayer-Bilayer Junctions in Epitaxial Graphene on SiC”. In: *Phys. Rev. B* 86.23 (2012).

[91] F. Giannazzo, G. Fisichella, A. Piazza, S. Agnello, and F. Roccaforte. “Nanoscale Inhomogeneity of the Schottky Barrier and Resistivity in MoS 2 Multilayers”. In: *Phys. Rev. B* 92.8 (2015).

[92] Y.-C. Lin, R. K. Ghosh, R. Addou, N. Lu, S. M. Eichfeld, H. Zhu, M.-Y. Li, X. Peng, M. J. Kim, L.-J. Li, R. M. Wallace, S. Datta, and J. A. Robinson. “Atomically Thin Resonant Tunnel Diodes Built from Synthetic van Der Waals Heterostructures”. In: *Nat Commun* 6.1 (2015).

[93] F. Giannazzo, E. Schilirò, G. Greco, and F. Roccaforte. “Conductive Atomic Force Microscopy of Semiconducting Transition Metal Dichalcogenides and Heterostructures”. In: *Nanomaterials* 10.4 (2020).

[94] FEMTO. *Variable Gain Low Noise Current Amplifier DLPCA-200*. 2021.

[95] O. Krause. “Fabrication and Reliability of Conductive AFM Probes”. In: *Conductive Atomic Force Microscopy*. Ed. by M. Lanza. Weinheim, Germany: Wiley-VCH Verlag GmbH & Co. KGaA, 2017.

[96] U. Celano, T. Hantschel, G. Giammaria, R. C. Chintala, T. Conard, H. Bender, and W. Vandervorst. “Evaluation of the Electrical Contact Area in Contact-Mode Scanning Probe Microscopy”. In: *Journal of Applied Physics* 117.21 (2015).

[97] D. Sarid. *Exploring Scanning Probe Microscopy with MATHEMATICA*. 1st ed. Wiley, 2006.

[98] N. A. Burnham, O. P. Behrend, F. Oulevey, G. Gremaud, P.-J. Gallo, D. Gourdon, E. Dupas, A. J. Kulik, H. M. Pollock, and G. A. D. Briggs. “How Does a Tip Tap?” In: 8.2 (1997).

[99] F. Zeng, W.-B. Zhang, and B.-Y. Tang. “Electronic Structures and Elastic Properties of Monolayer and Bilayer Transition Metal Dichalcogenides MX_2 (M = Mo, W; X = O, S, Se, Te): A Comparative First-Principles Study”. In: *Chinese Phys. B* 24.9 (2015).

[100] S. Bertolazzi, J. Brivio, and A. Kis. “Stretching and Breaking of Ultrathin MoS_2”. In: *ACS Nano* 5.12 (2011).

[101] M. C. Salvadori, I. G. Brown, A. R. Vaz, L. L. Melo, and M. Cattani. “Measurement of the Elastic Modulus of Nanostructured Gold and Platinum Thin Films”. In: *Phys. Rev. B* 67.15 (2003).

[102] K. Liu and J. Wu. “Mechanical Properties of Two-Dimensional Materials and Heterostructures”. In: *J. Mater. Res.* 31.7 (2016).

[103] D. Gérard, L. Salomon, F. de Fornel, and A. V. Zayats. “Suppression of Radiative Losses of Surface Polaritons on Nanostructured Thin Metal Films”. In: *Opt. Lett.* 30.7 (2005).

[104] J. J. Burke, G. I. Stegeman, and T. Tamir. “Surface-Polariton-like Waves Guided by Thin, Lossy Metal Films”. In: *Phys. Rev. B* 33.8 (1986).

[105] C. M. Baltar, K. Drozdowicz-Tomsia, and E. M. “Propagating Surface Plasmons and Dispersion Relations for Nanoscale Multilayer Metallic-Dielectric Films”. In: *Plasmonics - Principles and Applications*. Ed. by K. Y. Kim. InTech, 2012.

[106] P. Berini. “Long-Range Surface Plasmon Polaritons”. In: *Adv. Opt. Photon.* 1.3 (2009).

[107] Q. Min, C. Chen, P. Berini, and R. Gordon. “Long Range Surface Plasmons on Asymmetric Suspended Thin Film Structures for Biosensing Applications”. In: *Opt. Express* 18.18 (2010).

[108] J. S. Gomez-Diaz, M. Tymchenko, and A. Alù. “Hyperbolic Plasmons and Topological Transitions Over Uniaxial Metasurfaces”. In: *Phys. Rev. Lett.* 114.23 (2015).

[109] R. Magnusson, M. Shokooh-Saremi, K. J. Lee, J. Curzan, D. Wawro, S. Zimmerman, W. Wu, J. Yoon, H. G. Svavarsson, and S. H. Song. “Leaky-Mode Resonance Photonics: An Applications Platform”. In: SPIE NanoScience + Engineering. Ed. by E. A. Dobisz and L. A. Eldada. San Diego, California, USA, 2011.

[110] K. Höflich. “Plasmonische Eigenschaften von metallhaltigen Nanostrukturen”. Halle-Wittenberg, Germany: Martin-Luther-Universität Halle-Wittenberg, 2010.

[111] S. A. Maier. “Surface Plasmon Polaritons at Metal / Insulator Interfaces”. In: *Plasmonics: Fundamentals and Applications*. New York, NY: Springer US, 2007.

[112] P. B. Johnson and R. W. Christy. “Optical Constants of the Noble Metals”. In: *Phys. Rev. B* 6.12 (1972).

[113] A. Pinchuk, G. von Plessen, and U. Kreibig. “Influence of Interband Electronic Transitions on the Optical Absorption in Metallic Nanoparticles”. In: 37.22 (2004).

[114] A. D. Rakić, A. B. Djurišić, J. M. Elazar, and M. L. Majewski. “Optical Properties of Metallic Films for Vertical-Cavity Optoelectronic Devices”. In: *Appl. Opt., AO* 37.22 (1998).

[115] F. J. García de Abajo. “Nonlocal Effects in the Plasmons of Strongly Interacting Nanoparticles, Dimers, and Waveguides”. In: *J. Phys. Chem. C* 112.46 (2008).

[116] C. F. Bohren and D. R. Huffman. *Absorption and Scattering of Light by Small Particles*. Weinheim: Wiley-VCH, 2004.

[117] V. A. Markel. “Introduction to the Maxwell Garnett Approximation: Tutorial”. In: *J. Opt. Soc. Am. A* 33.7 (2016).

[118] V. A. Markel. “Maxwell Garnett Approximation (Advanced Topics): Tutorial”. In: *J. Opt. Soc. Am. A, JOSAA* 33.11 (2016).

[119] X. Zhang and Y. Wu. “Effective Medium Theory for Anisotropic Metamaterials”. In: *Sci Rep* 5.1 (2015).

[120] J. S. T. Smalley, F. Vallini, S. A. Montoya, L. Ferrari, S. Shahin, C. T. Riley, B. Kanté, E. E. Fullerton, Z. Liu, and Y. Fainman. “Luminescent Hyperbolic Metasurfaces”. In: *Nat Commun* 8.1 (2017).

[121] S. M. Rytov. “Electromagnetic Properties of a Finely Stratified Medium”. In: *Soviet Physics JETP* 2.3 (1956).

[122] A. V. Zayats, I. I. Smolyaninov, and A. A. Maradudin. “Nano-Optics of Surface Plasmon Polaritons”. In: *Physics Reports* 408.3-4 (2005).

[123] G. I. Stegeman, R. F. Wallis, and A. A. Maradudin. “Excitation of Surface Polaritons by End-Fire Coupling”. In: *Opt. Lett.* 8.7 (1983).

[124] E. N. Economou. “Surface Plasmons in Thin Films”. In: *Phys. Rev.* 182.2 (1969).

[125] F. Burton and S. Cassidy. “A Complete Description of the Dispersion Relation for Thin Metal Film Plasmon-Polaritons”. In: *J. Lightwave Technol.* 8.12 (1990).

[126] B. E. Sernelius. *Surface Modes in Physics*. 1st ed. Wiley, 2001.

[127] D. Jaisson. “Simple Closed Formulae for the Number of the Short-Range Surface-Plasma Wave Guided by a Thin, Plane Metallic Film, Between Claddings with Unequal Permittivities”. In: *Plasmonics* 13.5 (2018).

[128] T. Taubner, R. Hillenbrand, and F. Keilmann. “Performance of Visible and Mid-Infrared Scattering-Type near-Field Optical Microscopes”. In: *J Microsc* 210.3 (2003).

[129] A. Huber, N. Ocelic, and R. Hillenbrand. “Local Excitation and Interference of Surface Phonon Polaritons Studied by Near-Field Infrared Microscopy”. In: *J Microsc* 229.3 (2008).

[130] F. Keilmann and R. Hillenbrand. “Near-Field Microscopy by Elastic Light Scattering from a Tip”. In: *Philosophical Transactions of the Royal Society of London. Series A: Mathematical, Physical and Engineering Sciences* 362.1817 (2004). Ed. by D. Richards and A. Zayats.

[131] A. Bouhelier, F. Ignatovich, A. Bruyant, C. Huang, G. Colas des Francs, J.-C. Weeber, A. Dereux, G. P. Wiederrecht, and L. Novotny. "Surface Plasmon Interference Excited by Tightly Focused Laser Beams". In: *Opt. Lett.* 32.17 (2007).

[132] G. Gay, O. Alloschery, B. Viaris de Lesegno, C. O'Dwyer, J. Weiner, and H. J. Lezec. "The Optical Response of Nanostructured Surfaces and the Composite Diffracted Evanescent Wave Model". In: *Nature Phys* 2.4 (2006).

[133] I. Sinev, I. Iorsh, A. Bogdanov, D. Permyakov, F. Komissarenko, I. Mukhin, A. Samusev, V. Valuckas, A. I. Kuznetsov, B. S. Luk'yanchuk, A. E. Miroshnichenko, and Y. S. Kivshar. "Polarization Control over Electric and Magnetic Dipole Resonances of Dielectric Nanoparticles on Metallic Films". In: *Laser & Photonics Reviews* 10.5 (2016).

[134] I. S. Sinev, A. A. Bogdanov, F. E. Komissarenko, K. S. Frizyuk, M. I. Petrov, I. S. Mukhin, S. V. Makarov, A. K. Samusev, A. V. Lavrinenko, and I. V. Iorsh. "Chirality Driven by Magnetic Dipole Response for Demultiplexing of Surface Waves: Chirality Driven by Magnetic Dipole Response for Demultiplexing of Surface Waves". In: *Laser & Photonics Reviews* 11.5 (2017).

[135] P. A. Dmitriev, S. V. Makarov, V. A. Milichko, I. S. Mukhin, A. S. Gudovskikh, A. A. Sitnikova, A. K. Samusev, A. E. Krasnok, and P. A. Belov. "Laser Fabrication of Crystalline Silicon Nanoresonators from an Amorphous Film for Low-Loss All-Dielectric Nanophotonics". In: *Nanoscale* 8.9 (2016).

[136] A. I. Denisyuk, F. E. Komissarenko, and I. S. Mukhin. "Electrostatic Pick-and-Place Micro/Nanomanipulation under the Electron Beam". In: *Microelectronic Engineering* 121 (2014).

[137] D. Brissinger, A. L. Lereu, L. Salomon, T. Charvolin, B. Cluzel, C. Dumas, A. Passian, and F. de Fornel. "Discontinuity Induced Angular Distribution of Photon Plasmon Coupling". In: *Opt. Express, OE* 19.18 (2011).

[138] K. Yamagiwa, M. Shibuta, and A. Nakajima. "Visualization of Surface Plasmons Propagating at the Buried Organic/Metal Interface with Silver Nanocluster Sensitizers". In: *ACS Nano* 14.2 (2020).

[139] J. Vogelsang, L. Wittenbecher, D. Pan, J. Sun, S. Mikaelsson, C. L. Arnold, A. L'Huillier, H. Xu, and A. Mikkelsen. "Coherent Excitation and Control of Plasmons on Gold Using Two-Dimensional Transition Metal Dichalcogenides". In: *ACS Photonics* 8.6 (2021).

[140] K. Moon, H. Park, J. Kim, Y. Do, S. Lee, G. Lee, H. Kang, and H. Han. "Subsurface Nanoimaging by Broadband Terahertz Pulse Near-Field Microscopy". In: *Nano Lett.* 15.1 (2015).

[141] L. Mester, A. A. Govyadinov, S. Chen, M. Goikoetxea, and R. Hillenbrand. "Subsurface Chemical Nanoidentification by Nano-FTIR Spectroscopy". In: *Nat Commun* 11.1 (2020).

[142] M. M. Wiecha, A. Soltani, and H. G. Roskos. *Terahertz Nano-Imaging with s-SNOM*. IntechOpen, 2021.

[143] N. M. H. Duong, Z.-Q. Xu, M. Kianinia, R. Su, Z. Liu, S. Kim, C. Bradac, T. T. Tran, Y. Wan, L.-J. Li, A. Solntsev, J. Liu, and I. Aharonovich. "Enhanced Emission from WSe $_2$ Monolayers Coupled to Circular Bragg Gratings". In: *ACS Photonics* 5.10 (2018).

[144] Y. Li, N. Zhou, E. C. Kinzel, X. Ren, and X. Xu. "The Origin of Interferometric Effect Involving Surface Plasmon Polariton in Scattering Near-Field Scanning Optical Microscopy". In: *Opt. Express* 22.3 (2014).

[145] M. Brotons-Gisbert, J. P. Martínez-Pastor, G. C. Ballesteros, B. D. Gerardot, and J. F. Sánchez-Royo. "Engineering Light Emission of Two-Dimensional Materials in Both the Weak and Strong Coupling Regimes". In: *Nanophotonics* 7.1 (2018).

[146] J. Wen, H. Wang, W. Wang, Z. Deng, C. Zhuang, Y. Zhang, F. Liu, J. She, J. Chen, H. Chen, S. Deng, and N. Xu. "Room-Temperature Strong Light–Matter Interaction with Active Control in Single Plasmonic Nanorod Coupled with Two-Dimensional Atomic Crystals". In: *Nano Lett.* 17.8 (2017).

[147] S. Lepeshov, A. Krasnok, and A. Alù. "Enhanced Excitation and Emission from 2D Transition Metal Dichalcogenides with All-Dielectric Nanoantennas". In: *Nanotechnology* 30.25 (2019).

[148] X. Ao, X. Xu, J. Dong, and S. He. "Unidirectional Enhanced Emission from 2D Monolayer Suspended by Dielectric Pillar Array". In: *ACS Appl. Mater. Interfaces* 10.41 (2018).

[149] S. Najmaei, A. Mlayah, A. Arbouet, C. Girard, J. Léotin, and J. Lou. "Plasmonic Pumping of Excitonic Photoluminescence in Hybrid MoS $_2$ –Au Nanostructures". In: *ACS Nano* 8.12 (2014).

[150] Z. Wang, Z. Dong, Y. Gu, Y.-H. Chang, L. Zhang, L.-J. Li, W. Zhao, G. Eda, W. Zhang, G. Grinblat, S. A. Maier, J. K. W. Yang, C.-W. Qiu, and A. T. S. Wee. "Giant Photoluminescence Enhancement in Tungsten-Diselenide–Gold Plasmonic Hybrid Structures". In: *Nat Commun* 7.1 (2016).

[151] S. Wu, S. Buckley, A. M. Jones, J. S. Ross, N. J. Ghimire, J. Yan, D. G. Mandrus, W. Yao, F. Hatami, J. Vučković, A. Majumdar, and X. Xu. "Control of Two-Dimensional Excitonic Light Emission via Photonic Crystal". In: *2D Mater.* 1.1 (2014).

[152] J.-S. Wu, D. N. Basov, and M. M. Fogler. "Topological Insulators Are Tunable Waveguides for Hyperbolic Polaritons". In: *Phys. Rev. B* 92.20 (2015).

[153] D.-H. Lien, J. S. Kang, M. Amani, K. Chen, M. Tosun, H.-P. Wang, T. Roy, M. S. Eggleston, M. C. Wu, M. Dubey, S.-C. Lee, J.-H. He, and A. Javey. "Engineering Light Outcoupling in 2D Materials". In: *Nano Lett.* 15.2 (2015).

[154] H. Zhang, Y. Wan, Y. Ma, W. Wang, Y. Wang, and L. Dai. "Interference Effect on Optical Signals of Monolayer MoS $_2$". In: *Appl. Phys. Lett.* 107.10 (2015).

[155] H. Benisty, R. Stanley, and M. Mayer. "Method of Source Terms for Dipole Emission Modification in Modes of Arbitrary Planar Structures". In: *J. Opt. Soc. Am. A, JOSAA* 15.5 (1998).

[156] F. Prins, D. K. Kim, J. Cui, E. De Leo, L. L. Spiegel, K. M. McPeak, and D. J. Norris. "Direct Patterning of Colloidal Quantum-Dot Thin Films for Enhanced and Spectrally Selective Out-Coupling of Emission". In: *Nano Lett.* 17.3 (2017).

[157] C. Janisch, H. Song, C. Zhou, Z. Lin, A. L. Elías, D. Ji, M. Terrones, Q. Gan, and Z. Liu. "MoS 2 Monolayers on Nanocavities: Enhancement in Light–Matter Interaction". In: 3.2 (2016).

[158] L. M. Schneider. "Optical Properties of TMDC Monolayers and Their Heterostructures". Marburg: Philipps-Universität Marburg, 2020.

[159] M. Shrivastava and V. Ramgopal Rao. “A Roadmap for Disruptive Applications and Heterogeneous Integration Using Two-Dimensional Materials: State-of-the-Art and Technological Challenges”. In: *Nano Lett.* 21.15 (2021).

[160] B. Zhu, X. Chen, and X. Cui. “Exciton Binding Energy of Monolayer WS2”. In: *Sci Rep* 5.1 (2015).

[161] L. C. Flatten, Z. He, D. M. Coles, A. A. P. Trichet, A. W. Powell, R. A. Taylor, J. H. Warner, and J. M. Smith. “Room-Temperature Exciton-Polaritons with Two-Dimensional WS2”. In: *Sci Rep* 6.1 (2016).

[162] Y. Ye, Z. J. Wong, X. Lu, X. Ni, H. Zhu, X. Chen, Y. Wang, and X. Zhang. “Monolayer Excitonic Laser”. In: *Nature Photon* 9.11 (2015).

[163] T. Norden, C. Zhao, P. Zhang, R. Sabirianov, A. Petrou, and H. Zeng. “Giant Valley Splitting in Monolayer WS2 by Magnetic Proximity Effect”. In: *Nat Commun* 10.1 (2019).

[164] D. E. Aspnes and A. A. Studna. “Dielectric Functions and Optical Parameters of Si, Ge, GaP, GaAs, GaSb, InP, InAs, and InSb from 1.5 to 6.0 eV”. In: *Phys. Rev. B* 27.2 (1983).

[165] F. Wall, O. Mey, L. M. Schneider, and A. Rahimi-Iman. “Continuously-Tunable Light–Matter Coupling in Optical Microcavities with 2D Semiconductors”. In: *Sci Rep* 10.1 (2020).

[166] P. Rouard. “Études Des Propriétés Optiques Des Lames Métalliques Très Minces”. In: *Ann. Phys.* 11.7 (1937).

[167] O. S. Heavens. *Optical Properties of Thin Solid Films*. Dover Books on Physics and Chemistry. New York: Dover, 1991.

[168] G.-H. Jung, S. Yoo, and Q.-H. Park. “Measuring the Optical Permittivity of Two-Dimensional Materials without a Priori Knowledge of Electronic Transitions”. In: *Nanophotonics* 8.2 (2018).

[169] S.-Y. Lee, T.-Y. Jeong, S. Jung, and K.-J. Yee. “Refractive Index Dispersion of Hexagonal Boron Nitride in the Visible and Near-Infrared”. In: *Phys. Status Solidi B* 256.6 (2019).

[170] A. P. Engelhardt, B. Hauer, and T. Taubner. “Visibility of Weak Contrasts in Subsurface Scattering Near-Field Microscopy”. In: *Ultramicroscopy* 126 (2013).

[171] A. J. Huber, D. Kazantsev, F. Keilmann, J. Wittborn, and R. Hillenbrand. “Simultaneous IR Material Recognition and Conductivity Mapping by Nanoscale Near-Field Microscopy”. In: *Adv. Mater.* 19.17 (2007).

[172] M. Schnell, A. Garcia-Etxarri, J. Alkorta, J. Aizpurua, and R. Hillenbrand. “Phase-Resolved Mapping of the Near-Field Vector and Polarization State in Nanoscale Antenna Gaps”. In: *Nano Lett.* 10.9 (2010).

[173] T. Neuman, P. Alonso-González, A. Garcia-Etxarri, M. Schnell, R. Hillenbrand, and J. Aizpurua. “Mapping the near Fields of Plasmonic Nanoantennas by Scattering-Type Scanning near-Field Optical Microscopy: Mapping the near Fields of Plasmonic Nanoantennas”. In: *Laser & Photonics Reviews* 9.6 (2015).

[174] H. Lee, D. Y. Lee, M. G. Kang, Y. Koo, T. Kim, and K.-D. Park. “Tip-Enhanced Photoluminescence Nano-Spectroscopy and Nano-Imaging”. In: *Nanophotonics* 9.10 (2020).

[175] W. Su, N. Kumar, S. Mignuzzi, J. Crain, and D. Roy. "Nanoscale Mapping of Excitonic Processes in Single-Layer MoS $_2$ Using Tip-Enhanced Photoluminescence Microscopy". In: *Nanoscale* 8.20 (2016).

[176] M. Thomas, J.-J. Greffet, R. Carminati, and J. R. Arias-Gonzalez. "Single-Molecule Spontaneous Emission Close to Absorbing Nanostructures". In: *Appl. Phys. Lett.* 85.17 (2004).

[177] J. N. Farahani, D. W. Pohl, H.-J. Eisler, and B. Hecht. "Single Quantum Dot Coupled to a Scanning Optical Antenna: A Tunable Superemitter". In: *Phys. Rev. Lett.* 95.1 (2005).

[178] W. J. Yu, Z. Li, H. Zhou, Y. Chen, Y. Wang, Y. Huang, and X. Duan. "Vertically Stacked Multi-Heterostructures of Layered Materials for Logic Transistors and Complementary Inverters". In: *Nature Mater* 12.3 (2013).

[179] W. J. Yu, Y. Liu, H. Zhou, A. Yin, Z. Li, Y. Huang, and X. Duan. "Highly Efficient Gate-Tunable Photocurrent Generation in Vertical Heterostructures of Layered Materials". In: *Nature Nanotech* 8.12 (2013).

[180] K. S. Novoselov, A. Mishchenko, A. Carvalho, and A. H. Castro Neto. "2D Materials and van Der Waals Heterostructures". In: *Science* 353.6298 (2016).

[181] Q. H. Wang, K. Kalantar-Zadeh, A. Kis, J. N. Coleman, and M. S. Strano. "Electronics and Optoelectronics of Two-Dimensional Transition Metal Dichalcogenides". In: *Nature Nanotech* 7.11 (2012).

[182] L. A. Ponomarenko, B. D. Belle, R. Jalil, L. Britnell, R. V. Gorbachev, A. K. Geim, K. S. Novoselov, A. H. Castro Neto, L. Eaves, and M. I. Katsnelson. "Field-Effect Control of Tunneling Barrier Height by Exploiting Graphene's Low Density of States". In: *Journal of Applied Physics* 113.13 (2013).

[183] F. Xia, H. Wang, D. Xiao, M. Dubey, and A. Ramasubramaniam. "Two-Dimensional Material Nanophotonics". In: *Nature Photon* 8.12 (2014).

[184] G.-H. Lee, Y.-J. Yu, C. Lee, C. Dean, K. L. Shepard, P. Kim, and J. Hone. "Electron Tunneling through Atomically Flat and Ultrathin Hexagonal Boron Nitride". In: *Appl. Phys. Lett.* 99.24 (2011).

[185] T. Yamaguchi, R. Moriya, Y. Inoue, S. Morikawa, S. Masubuchi, K. Watanabe, T. Taniguchi, and T. Machida. "Tunneling Transport in a Few Monolayer-Thick WS_2 /Graphene Heterojunction". In: *Appl. Phys. Lett.* 105.22 (2014).

[186] T. S. Ghiasi, J. Quereda, and B. J. van Wees. "Bilayer H-BN Barriers for Tunneling Contacts in Fully-Encapsulated Monolayer MoSe $_2$ Field-Effect Transistors". In: *2D Mater.* 6.1 (2018).

[187] F. Ahmed, M. S. Choi, X. Liu, and W. J. Yoo. "Carrier Transport at the Metal–MoS $_2$ Interface". In: *Nanoscale* 7.20 (2015).

[188] L. Britnell, R. M. Ribeiro, A. Eckmann, R. Jalil, B. D. Belle, A. Mishchenko, Y. J. Kim, R. V. Gorbachev, T. Georgiou, S. V. Morozov, A. N. Grigorenko, A. K. Geim, C. Casiraghi, A. H. C. Neto, and K. S. Novoselov. "Strong Light-Matter Interactions in Heterostructures of Atomically Thin Films". In: *Science* 340.6138 (2013).

[189] F. Li, Z. Lu, Y.-W. Lan, L. Jiao, M. Xu, X. Zhu, X. Zhang, H. Wu, and J. Qi. "Force and Light Tuning Vertical Tunneling Current in the Atomic Layered MoS_2". In: *Nanotechnology* 29.27 (2018).

[190] N. Myoung, K. Seo, S. J. Lee, and G. Ihm. “Large Current Modulation and Spin-Dependent Tunneling of Vertical Graphene/MoS_2 Heterostructures”. In: *ACS Nano* 7.8 (2013).

[191] R. Yan, S. Fathipour, Y. Han, B. Song, S. Xiao, M. Li, N. Ma, V. Protasenko, D. A. Muller, D. Jena, and H. G. Xing. “Esaki Diodes in van Der Waals Heterojunctions with Broken-Gap Energy Band Alignment”. In: *Nano Lett.* 15.9 (2015).

[192] X. Yan, C. Liu, C. Li, W. Bao, S. Ding, D. W. Zhang, and P. Zhou. “Tunable $SnSe_2$ /WSe_2 Heterostructure Tunneling Field Effect Transistor”. In: *Small* 13.34 (2017).

[193] N. Ma and D. Jena. “Interband Tunneling in Two-Dimensional Crystal Semiconductors”. In: *Appl. Phys. Lett.* 102.13 (2013).

[194] P. Zhou, W. J. Hardy, K. Watanabe, T. Taniguchi, and D. Natelson. “Shot Noise Detection in hBN-based Tunnel Junctions”. In: *Appl. Phys. Lett.* 110.13 (2017).

[195] G. Fiori, F. Bonaccorso, G. Iannaccone, T. Palacios, D. Neumaier, A. Seabaugh, S. K. Banerjee, and L. Colombo. “Electronics Based on Two-Dimensional Materials”. In: *Nature Nanotech* 9.10 (2014).

[196] E. L. Murphy and R. H. Good. “Thermionic Emission, Field Emission, and the Transition Region”. In: *Phys. Rev.* 102.6 (1956).

[197] S. M. Sze and K. K. Ng. *Physics of Semiconductor Devices*. 3. ed. Hoboken, NJ: Wiley-Interscience, 2007.

[198] R. C. Reddick, R. J. Warmack, and T. L. Ferrell. “New Form of Scanning Optical Microscopy”. In: *Phys. Rev. B* 39.1 (1989).

[199] J. M. Vigoureux, D. Courjon, and C. Girard. “General Principles of Scanning Tunneling Optical Microscopy”. In: *Opt. Lett.* 14.19 (1989).

[200] R. Tsu and L. Esaki. “Tunneling in a Finite Superlattice”. In: *Appl. Phys. Lett.* 22.11 (1973).

[201] A. Gehring and S. Selberherr. “Modeling of Tunneling Current and Gate Dielectric Reliability for Nonvolatile Memory Devices”. In: *IEEE Trans. Device Mater. Relib.* 4.3 (2004).

[202] H. M. Hill, A. F. Rigosi, K. T. Rim, G. W. Flynn, and T. F. Heinz. “Band Alignment in MoS_2 /WS_2 Transition Metal Dichalcogenide Heterostructures Probed by Scanning Tunneling Microscopy and Spectroscopy”. In: *Nano Lett.* 16.8 (2016).

[203] J. G. Simmons. “Electric Tunnel Effect between Dissimilar Electrodes Separated by a Thin Insulating Film”. In: *Journal of Applied Physics* 34.9 (1963).

[204] P. Gehring and M. Burghard. “Topologische Isolatoren: Leitende Oberflächen mit exotischen Eigenschaften”. In: *Physik in unserer Zeit* 45.6 (2014).

[205] T. E. Hartman. “Tunneling Through Asymmetric Barriers”. In: *Journal of Applied Physics* 35.11 (1964).

[206] T. M. Abdolkader, A. Shaker, and A. N. M. Alahmadi. “Numerical Simulation of Tunneling through Arbitrary Potential Barriers Applied on MIM and MIIM Rectenna Diodes”. In: *Eur. J. Phys.* 39.4 (2018).

[207] J. M. Beebe, B. Kim, J. W. Gadzuk, C. Daniel Frisbie, and J. G. Kushmerick. "Transition from Direct Tunneling to Field Emission in Metal-Molecule-Metal Junctions". In: *Phys. Rev. Lett.* 97.2 (2006).

[208] I. C. Infante, F. Sánchez, V. Laukhin, A. Pérez del Pino, J. Fontcuberta, K. Bouzehouane, S. Fusil, and A. Barthélémy. "Functional Characterization of SrTiO3 Tunnel Barriers by Conducting Atomic Force Microscopy". In: *Appl. Phys. Lett.* 89.17 (2006).

[209] J. R. Durán Retamal, D. Periyanagounder, J.-J. Ke, M.-L. Tsai, and J.-H. He. "Charge Carrier Injection and Transport Engineering in Two-Dimensional Transition Metal Dichalcogenides". In: *Chem. Sci.* 9.40 (2018).

[210] J. G. Simmons. "Generalized Formula for the Electric Tunnel Effect between Similar Electrodes Separated by a Thin Insulating Film". In: *Journal of Applied Physics* 34.6 (1963).

[211] A. Mayer. "Numerical Testing of the Fowler–Nordheim Equation for the Electronic Field Emission from a Flat Metal and Proposition for an Improved Equation". In: *Journal of Vacuum Science & Technology B, Nanotechnology and Microelectronics: Materials, Processing, Measurement, and Phenomena* 28.4 (2010).

[212] N. Tuomisto, A. Zugarramurdi, and M. J. Puska. "Modeling of Electron Tunneling through a Tilted Potential Barrier". In: *Journal of Applied Physics* 121.13 (2017).

[213] D. Pantel and M. Alexe. "Electroresistance Effects in Ferroelectric Tunnel Barriers". In: *Phys. Rev. B* 82.13 (2010).

[214] A. J. Chiquito, C. A. Amorim, O. M. Berengue, L. S. Araujo, E. P. Bernardo, and E. R. Leite. "Back-to-Back Schottky Diodes: The Generalization of the Diode Theory in Analysis and Extraction of Electrical Parameters of Nanodevices". In: *J. Phys.: Condens. Matter* 24.22 (2012).

[215] J. Quereda, J. J. Palacios, N. Agräit, A. Castellanos-Gomez, and G. Rubio-Bollinger. "Strain Engineering of Schottky Barriers in Single- and Few-Layer MoS $_2$ Vertical Devices". In: *2D Mater.* 4.2 (2017).

[216] A. Castellanos-Gomez, M. Buscema, R. Molenaar, V. Singh, L. Janssen, H. S. J. van der Zant, and G. A. Steele. "Deterministic Transfer of Two-Dimensional Materials by All-Dry Viscoelastic Stamping". In: *2D Mater.* 1.1 (2014).

[217] H. Masenda, L. M. Schneider, M. Adel Aly, S. J. Machchhar, A. Usman, K. Meerholz, F. Gebhard, S. D. Baranovskii, and M. Koch. "Energy Scaling of Compositional Disorder in Ternary Transition-Metal Dichalcogenide Monolayers". In: *Adv. Electron. Mater.* 7.8 (2021).

[218] M. A. Aly, M. Shah, L. M. Schneider, K. Kang, M. Koch, E.-H. Yang, and A. Rahimi-Iman. *Radiative Pattern of Intralayer and Interlayer Excitons in Two-Dimensional WS2/WSe2 Heterostructure*. 2021. URL: `http://arxiv.org/abs/2111.06621` (visited on 12/06/2021).

[219] C. Gong, H. Zhang, W. Wang, L. Colombo, R. M. Wallace, and K. Cho. "Band Alignment of Two-Dimensional Transition Metal Dichalcogenides: Application in Tunnel Field Effect Transistors". In: *Appl. Phys. Lett.* 103.5 (2013).

[220] M. Farmanbar and G. Brocks. "Ohmic Contacts to 2D Semiconductors through van Der Waals Bonding". In: *Adv. Electron. Mater.* 2.4 (2016).

[221] B. Bhushan, ed. *Encyclopedia of Nanotechnology*. Dordrecht: Springer Netherlands, 2012.

[222] Y. Lv, J. Cui, Z. M. Jiang, and X. Yang. "Nanoscale Electrical Property Studies of Individual GeSi Quantum Rings by Conductive Scanning Probe Microscopy". In: *Nanoscale Res Lett* 7.1 (2012).

[223] J. Xiao, Y. Zhang, H. Chen, N. Xu, and S. Deng. "Enhanced Performance of a Monolayer MoS2/WSe2 Heterojunction as a Photoelectrochemical Cathode". In: *Nano-Micro Lett.* 10.4 (2018).

[224] H. Tang, B. Shi, Y. Pan, J. Li, X. Zhang, J. Yan, S. Liu, J. Yang, L. Xu, J. Yang, M. Wu, and J. Lu. "Schottky Contact in Monolayer WS $_2$ Field-Effect Transistors". In: *Adv. Theory Simul.* 2.5 (2019).

[225] A. Di Bartolomeo. "Graphene Schottky Diodes: An Experimental Review of the Rectifying Graphene/Semiconductor Heterojunction". In: *Physics Reports* 606 (2016).

[226] F. A. Chaves, D. Jiménez, A. W. Cummings, and S. Roche. "Physical Model of the Contact Resistivity of Metal-Graphene Junctions". In: *Journal of Applied Physics* 115.16 (2014).

[227] P. A. Khomyakov, G. Giovannetti, P. C. Rusu, G. Brocks, J. van den Brink, and P. J. Kelly. "First-Principles Study of the Interaction and Charge Transfer between Graphene and Metals". In: *Phys. Rev. B* 79.19 (2009).

[228] R. M. Feenstra, D. Jena, and G. Gu. "Single-Particle Tunneling in Doped Graphene-Insulator-Graphene Junctions". In: *Journal of Applied Physics* 111.4 (2012).

[229] K. Godin, C. Cupo, and E.-H. Yang. "Reduction in Step Height Variation and Correcting Contrast Inversion in Dynamic AFM of WS2 Monolayers". In: *Sci Rep* 7.1 (2017).

[230] K. Pürckhauer, D. Kirpal, A. J. Weymouth, and F. J. Giessibl. "Analysis of Airborne Contamination on Transition Metal Dichalcogenides with Atomic Force Microscopy Revealing That Sulfur Is the Preferred Chalcogen Atom for Devices Made in Ambient Conditions". In: *ACS Appl. Nano Mater.* 2.5 (2019).

[231] T. F. Fernandes and B. R. A. Neves. "Friction Coefficient Mapping of 2D Materials via Friction-Induced Topographic Artifact in Atomic Force Microscopy". In: *JAN* 1.2 (2016).

[232] U. Bhanu, M. R. Islam, L. Tetard, and S. I. Khondaker. "Photoluminescence Quenching in Gold - MoS2 Hybrid Nanoflakes". In: *Sci Rep* 4.1 (2015).

[233] S. Y. Kim, H. I. Yang, and W. Choi. "Photoluminescence Quenching in Monolayer Transition Metal Dichalcogenides by Al $_2$ O $_3$ Encapsulation". In: *Appl. Phys. Lett.* 113.13 (2018).

[234] A. Gupta, G. Chen, P. Joshi, S. Tadigadapa, and Eklund. "Raman Scattering from High-Frequency Phonons in Supported n -Graphene Layer Films". In: *Nano Lett.* 6.12 (2006).

[235] A. Ando, R. Hasunuma, T. Maeda, K. Sakamoto, K. Miki, Y. Nishioka, and T. Sakamoto. "Conducting Atomic Force Microscopy Studies on Local Electrical Properties of Ultrathin SiO2 Films". In: *Applied Surface Science* 162–163 (2000).

[236] S. A. Sumaiya, A. Martini, and M. Z. Baykara. “Improving the Reliability of Conductive Atomic Force Microscopy-Based Electrical Contact Resistance Measurements”. In: *Nano Express* 1.3 (2020).

[237] Z. H. Liu, N. M. D. Brown, and A. McKinley. “Evaluation of the Growth Behaviour of Gold Film Surfaces Evaporation-Deposited on Mica under Different Conditions”. In: *J. Phys.: Condens. Matter* 9.1 (1997).

[238] R. H. Godiksen, S. Wang, T. V. Raziman, M. H. D. Guimaraes, J. G. Rivas, and A. G. Curto. “Correlated Exciton Fluctuations in a Two-Dimensional Semiconductor on a Metal”. In: *Nano Lett.* 20.7 (2020).

[239] S. B. Desai, S. R. Madhvapathy, M. Amani, D. Kiriya, M. Hettick, M. Tosun, Y. Zhou, M. Dubey, J. W. Ager, D. Chrzan, and A. Javey. “Gold-Mediated Exfoliation of Ultralarge Optoelectronically-Perfect Monolayers”. In: *Adv. Mater.* 28.21 (2016).

[240] A. Krayev, C. S. Bailey, K. Jo, S. Wang, A. Singh, T. Darlington, G.-Y. Liu, S. Gradecak, P. J. Schuck, E. Pop, and D. Jariwala. “Dry Transfer of van Der Waals Crystals to Noble Metal Surfaces To Enable Characterization of Buried Interfaces”. In: *ACS Appl. Mater. Interfaces* 11.41 (2019).

[241] C. Koch and T. J. Rinke. *Photolithography: Basics of Microstructuring*. 1st edition. Ulm, Germany: MicroChemicals GmbH, 2017.

[242] H. Rokni and W. Lu. “Direct Measurements of Interfacial Adhesion in 2D Materials and van Der Waals Heterostructures in Ambient Air”. In: *Nat Commun* 11.1 (2020).

[243] S. Das, A. Prakash, R. Salazar, and J. Appenzeller. “Toward Low-Power Electronics: Tunneling Phenomena in Transition Metal Dichalcogenides”. In: *ACS Nano* 8.2 (2014).

[244] F. Liu, J. Wang, and H. Guo. “Negative Differential Resistance in Monolayer WTe $_2$ Tunneling Transistors”. In: *Nanotechnology* 26.17 (2015).

[245] L. Viti and M. S. Vitiello. “Tailored Nano-Electronics and Photonics with Two-Dimensional Materials at Terahertz Frequencies”. In: *Journal of Applied Physics* 130.17 (2021).

[246] H. Y. Hwang, N. C. Brandt, H. Farhat, A. L. Hsu, J. Kong, and K. A. Nelson. “Nonlinear THz Conductivity Dynamics in P-Type CVD-Grown Graphene”. In: *J. Phys. Chem. B* 117.49 (2013).

[247] P. Bowlan, E. Martinez-Moreno, K. Reimann, T. Elsaesser, and M. Woerner. “Ultrafast Terahertz Response of Multilayer Graphene in the Nonperturbative Regime”. In: *Phys. Rev. B* 89.4 (2014).

[248] N. Yoshikawa, T. Tamaya, and K. Tanaka. “High-Harmonic Generation in Graphene Enhanced by Elliptically Polarized Light Excitation”. In: *Science* 356.6339 (2017).

[249] H. A. Hafez, S. Kovalev, J.-C. Deinert, Z. Mics, B. Green, N. Awari, M. Chen, S. Germanskiy, U. Lehnert, J. Teichert, Z. Wang, K.-J. Tielrooij, Z. Liu, Z. Chen, A. Narita, K. Müllen, M. Bonn, M. Gensch, and D. Turchinovich. “Extremely Efficient Terahertz High-Harmonic Generation in Graphene by Hot Dirac Fermions”. In: *Nature* 561.7724 (2018).

[250] H. A. Hafez, S. Kovalev, K.-J. Tielrooij, M. Bonn, M. Gensch, and D. Turchinovich. "Terahertz Nonlinear Optics of Graphene: From Saturable Absorption to High-Harmonics Generation". In: *Advanced Optical Materials* 8.3 (2020).

[251] J.-C. Deinert, D. Alcaraz Iranzo, R. Pérez, X. Jia, H. A. Hafez, I. Ilyakov, N. Awari, M. Chen, M. Bawatna, A. N. Ponomaryov, S. Germanskiy, M. Bonn, F. H. Koppens, D. Turchinovich, M. Gensch, S. Kovalev, and K.-J. Tielrooij. "Grating-Graphene Metamaterial as a Platform for Terahertz Nonlinear Photonics". In: *ACS Nano* 15.1 (2021).

[252] O. Schubert, M. Hohenleutner, F. Langer, B. Urbanek, C. Lange, U. Huttner, D. Golde, T. Meier, M. Kira, S. W. Koch, and R. Huber. "Sub-Cycle Control of Terahertz High-Harmonic Generation by Dynamical Bloch Oscillations". In: *Nature Photon* 8.2 (2014).

[253] G. Vampa, C. R. McDonald, G. Orlando, P. B. Corkum, and T. Brabec. "Semiclassical Analysis of High Harmonic Generation in Bulk Crystals". In: *Phys. Rev. B* 91.6 (2015).

[254] F. Langer, M. Hohenleutner, C. P. Schmid, C. Poellmann, P. Nagler, T. Korn, C. Schüller, M. S. Sherwin, U. Huttner, J. T. Steiner, S. W. Koch, M. Kira, and R. Huber. "Lightwave-Driven Quasiparticle Collisions on a Subcycle Timescale". In: *Nature* 533.7602 (2016).

[255] G. Vampa, H. Liu, T. F. Heinz, and D. A. Reis. "Disentangling Interface and Bulk Contributions to High-Harmonic Emission from Solids". In: *Optica, OPTICA* 6.5 (2019).

[256] S. Ghimire, A. D. DiChiara, E. Sistrunk, P. Agostini, L. F. DiMauro, and D. A. Reis. "Observation of High-Order Harmonic Generation in a Bulk Crystal". In: *Nature Phys* 7.2 (2011).

[257] G. Vampa, T. J. Hammond, N. Thiré, B. E. Schmidt, F. Légaré, C. R. McDonald, T. Brabec, and P. B. Corkum. "Linking High Harmonics from Gases and Solids". In: *Nature* 522.7557 (2015).

[258] G. Ndabashimiye, S. Ghimire, M. Wu, D. A. Browne, K. J. Schafer, M. B. Gaarde, and D. A. Reis. "Solid-State Harmonics beyond the Atomic Limit". In: *Nature* 534.7608 (2016).

[259] S. Ghimire and D. A. Reis. "High-Harmonic Generation from Solids". In: *Nature Phys* 15.1 (2019).

[260] G. Vampa, T. J. Hammond, N. Thiré, B. E. Schmidt, F. Légaré, C. R. McDonald, T. Brabec, D. D. Klug, and P. B. Corkum. "All-Optical Reconstruction of Crystal Band Structure". In: *Phys. Rev. Lett.* 115.19 (2015).

[261] C.-M. Wang, T.-S. Ho, and S.-I. Chu. "Determination of Band Structure from the Intra-Band Power Spectrum of High Harmonic Generation in Crystal". In: *J. Phys. B: At. Mol. Opt. Phys.* 49.22 (2016).

[262] Y.-T. Zhao, Y.-T. Zhao, S.-y. Ma, S.-C. Jiang, Y.-J. Yang, X. Zhao, X. Zhao, and J.-G. Chen. "All-Optical Reconstruction of k-Dependent Transition Dipole Moment by Solid Harmonic Spectra from Ultrashort Laser Pulses". In: *Opt. Express, OE* 27.23 (2019).

[263] A. A. Lanin, E. A. Stepanov, A. B. Fedotov, and A. M. Zheltikov. "Mapping the Electron Band Structure by Intraband High-Harmonic Generation in Solids". In: *Optica, OPTICA* 4.5 (2017).

[264] A. Mayer and F. Keilmann. "Far-Infrared Nonlinear Optics. II. χ (3) Contributions from the Dynamics of Free Carriers in Semiconductors". In: *Phys. Rev. B* 33.10 (1986).

[265] C. C. Wang and N. W. Ressler. "Nonlinear Optical Effects of Conduction Electrons in Semiconductors". In: *Phys. Rev.* 188.3 (1969).

[266] F. Meng, M. D. Thomson, Q. ul-Islam, B. Klug, A. Pashkin, H. Schneider, and H. G. Roskos. "Intracavity Third-Harmonic Generation in Si:B Pumped by Intense Terahertz Pulses". In: *Phys. Rev. B* 102.7 (2020).

[267] L. Nevou. *Q_band_ZB*. GitHub. 2021. URL: `https://github.com/LaurentNevou/Q_band_ZB` (visited on 12/06/2021).

[268] M. M. Rieger and P. Vogl. "Electronic-Band Parameters in Strained Si 1 - x Ge x Alloys on Si 1 - y Ge y Substrates". In: *Phys. Rev. B* 48.19 (1993).

[269] C. Jungemann, S. Keith, M. Bartels, and B. Meinerzhagen. "Efficient Full-Band Monte Carlo Simulation of Silicon Devices". In: *IEICE Transactions on Electronics* 82 (1999).

[270] M. Lundstrom. *Fundamentals of Carrier Transport*. 2nd ed. Cambridge: Cambridge University Press, 2000.

[271] L. Reggiani, ed. *Hot-Electron Transport in Semiconductors*. Vol. 58. Topics in Applied Physics. Berlin, Heidelberg: Springer Berlin Heidelberg, 1985.

[272] A. Dargys and J. Kundrotas. *Handbook on Physical Properties of Ge, Si, GaAs and InP*. Vilnius: Science and Encyclopedia Publ, 1994.

[273] C. Jacoboni and L. Reggiani. "Bulk Hot-Electron Properties of Cubic Semiconductors". In: *Advances in Physics* 28.4 (1979).

[274] B. K. Ridley. "Reconciliation of the Conwell-Weisskopf and Brooks-Herring Formulae for Charged-Impurity Scattering in Semiconductors: Third-body Interference". In: *J. Phys. C: Solid State Phys.* 10.10 (1977).

[275] F. J. Morin and J. P. Maita. "Electrical Properties of Silicon Containing Arsenic and Boron". In: *Phys. Rev.* 96.1 (1954).

[276] R. A. Logan and A. J. Peters. "Impurity Effects upon Mobility in Silicon". In: *Journal of Applied Physics* 31.1 (1960).

[277] O. Madelung, U. Rössler, and M. Schulz, eds. *Group IV Elements, IV-IV and III-V Compounds. Part b - Electronic, Transport, Optical and Other Properties*. Vol. b. Landolt-Börnstein - Group III Condensed Matter. Berlin/Heidelberg: Springer-Verlag, 2002.

[278] F. L. Madarasz, J. E. Lang, and P. M. Hemeger. "Effective Masses for Nonparabolic Bands in p -type Silicon". In: *Journal of Applied Physics* 52.7 (1981).

[279] M. A. Green. "Intrinsic Concentration, Effective Densities of States, and Effective Mass in Silicon". In: *Journal of Applied Physics* 67.6 (1990).

[280] H. D. Barber. "Effective Mass and Intrinsic Concentration in Silicon". In: *Solid-State Electronics* 10.11 (1967).

[281] W. Kuehn, P. Gaal, K. Reimann, M. Woerner, T. Elsaesser, and R. Hey. "Coherent Ballistic Motion of Electrons in a Periodic Potential". In: *Phys. Rev. Lett.* 104.14 (2010).

[282] W. Kuehn, P. Gaal, K. Reimann, M. Woerner, T. Elsaesser, and R. Hey. "Terahertz-Induced Interband Tunneling of Electrons in GaAs". In: *Phys. Rev. B* 82.7 (2010).

[283] K. Reimann. "Table-Top Sources of Ultrashort THz Pulses". In: *Rep. Prog. Phys.* 70.10 (2007).

[284] P. A. Wolff and G. A. Pearson. "Theory of Optical Mixing by Mobile Carriers in Semiconductors". In: *Phys. Rev. Lett.* 17.19 (1966).

[285] P. Kaw. "Optical Mixing by Mobile Carriers in Semiconductors". In: *Phys. Rev. Lett.* 21.8 (1968).

[286] B. S. Krishnamurthy and V. V. Paranjape. "Note on Optical Mixing by Mobile Carriers in Semiconductors". In: *Phys. Rev.* 181.3 (1969).

[287] R. Boyd. *Nonlinear Optics*. Elsevier, 2020.

[288] M. Nurhuda, A. Suda, and K. Midorikawa. "Saturation of Nonlinear Susceptibility". In: *J. Nonlinear Optic. Phys. Mat.* 13.02 (2004).

[289] C. Jungemann, S. Yamaguchi, and H. Goto. "Efficient Full Band Monte Carlo Hot Carrier Simulation for Silicon Devices". In: *ESSDERC '96: Proceedings of the 26th European Solid State Device Research Conference*. ESSDERC '96: Proceedings of the 26th European Solid State Device Research Conference. 1996.

Zusammenfassung

Nanoplasmonik beschreibt ein Teilgebiet der Nanophotonik, das die Erzeugung, Erkennung und Manipulation von Licht im Nanometerbereich umfasst. Das Forschungsgebiet konzentriert sich auf die Wechselwirkungsprozesse von Licht und Leitungselektronen an metallisch-dielektrischen Grenzflächen oder metallischen Nanostrukturen. Es erforscht optische Nahfelder in Sub-Wellenlängen-Volumina und Wechselwirkungen zwischen räumlich begrenzten elektrischen Feldern und Materie. Die Motivation der Forschung folgt dem Trend in der Nanophotonik, miniaturisierte optische Anwendungen in der Mikroskopie, optischen Kommunikation und Sensorik zu entwickeln, deren Größe die relevante optische Wellenlänge unterschreitet. Dabei liegt die Herausforderung in der Zusammenführung von nanoelektronischen Dimensionen von wenigen Nanometern und optischen Frequenzen bis Hunderte Terahertz.

Der Einschluss von Licht auf nanoskaligen Dimensionen führt zu starken elektromagnetischen Feldern, die die Untersuchung der Licht-Materie-Wechselwirkung in einem breiten Frequenzbereich vom sichtbaren bis zum Terahertzbereich ermöglichen. Diese Wechselwirkung kann durch resonante Strukturen wie metallische Nanopartikel, strukturierte Oberflächen, Metaoberflächen und 2D-Materialien zusätzlich verstärkt werden. Spannende Phänomene die daraus resultieren sind z.B. negative Brechung, Fokussierung im Sub-Wellenlängenbereich und die Oberflächenführung von Licht. Darüber hinaus beruhen viele optoelektronische Anwendungen wie Detektoren, Modulatoren und Schalter sowie die Erzeugung von Frequenzen höherer Harmonischer auf der starken Wechselwirkung zwischen Licht und Materie. [4]

Metaoberflächen sind künstlich hergestellte ultradünne periodische Mikro- oder Nanostrukturen, die auf einfallendes Licht resonant reagieren. Im Gegensatz zu dreidimensionalen Metamaterialien zeigen sie deutlichen geringere optische Verluste und profitieren in der Halbleitertechnologie etablierten Herstellungsverfahren, wie Lithographie und Nanodruck. Zudem lassen sie sich potentiell direkt in photonische Mikro- und Nanochips integrieren [7]. Das Design ihrer Subwellenlängenkomponenten steuert ihre effektiven Materialeigenschaften, wie Permittivität und Permeabilität, in einer Weise, die es ermöglicht, den Brechungsindex und die Wechselwirkung mit Licht auf neue Weise zu gestalten.

2D-Materialien, wie Graphen, hexagonales Bornitrid (hBN) oder Übergangsmetall-Dichalcogenide (TMDCs), sind Kristalle, welche in schwach gebundenen Schichten wachsen, die durch intermolekulare van-der-Waals-Kräfte zusammengehalten werden. Die Schichten können mechanisch von dem Kristall abgelöst oder direkt gewachsen werden. Sie bieten sich somit als ideale zweidimensionale Oberflächen an, um die Kopplung von Licht und Materie, wie Plasmonen, Elektronen, Exzitonen oder Phononen, in Form von Polaritonen zu untersuchen. TMDCs Materialien gewinnen derzeit aufgrund ihrer halbleitenden Eigenschaften, direkten Bandlücke im sichtbaren Spektrum , starken Photolumineszenz und Spin-Orbit-Kopplung als vielversprechendes 2D-Material in Grundlagenforschung und für Anwendungen an Bedeutung.

Die optische Bildgebung von an Oberflächen gebundenen Polaritonen stellt eine beson-

dere Herausforderung dar, da ihre elektrischen Felder senkrecht zur Oberfläche schnell abklingen und generell im Fernfeld nicht aufgelöst werden können. Im Rahmen dieser Arbeit wurde daher ein optisches Rasternahfeldmikroskop (s-SNOM) implementiert, welches elektrische Oberflächenfelder und lokale Materialeigenschaften mit Nanometer-Auflösung auf metallischen Schichten [29–31] und 2D-Materialien [32–34] auflösen kann.

Das Messprinzip beruht auf der Erfassung der schnell abklingenden evaneszenten Komponenten des elektrischen Feldes, die auf die Oberfläche gebunden sind. Durch Abtasten eines Detektors, einer kleinen Blende oder eines Streuers in der Nähe der Oberfläche können die evaneszenten Felder gestreut und in das Fernfeld propagiert werden. Im Gegensatz zur Fernfeldstrahlung enthalten die evaneszenten Wellen hochaufgelöste Detailinformationen über die Probenoberfläche weit unterhalb ihrer Wellenlänge. Beim s-SNOM wird dies dadurch erreicht, dass man eine scharfe Spitze knapp über der Oberfläche oszillieren lässt. Zusätzlich wird ein Laserstrahl auf die Spitze fokussiert, die als optische Antenne für die Einkopplung und Streuung von Licht fungiert. Die Spitze wird durch das elektromagnetische Feld polarisiert, Amplitude und Phase des gestreuten Lichts werden durch die Wechselwirkung mit der Probe beeinflusst. Die Sondenspitze wirkt also als Streuer für das Nahfeld im Subwellenlängenbereich. Sie wandelt evaneszente Wellen in sich ausbreitende Wellen um, die im Fernfeld nachgewiesen werden können. Die enge Beziehung zwischen Streudipol und Streuquerschnitt ermöglicht die entscheidende räumliche Auflösung in der Größenordnung der Messspitze und nicht der Wellenlänge. [58]

Die vorliegende Arbeit präsentiert Forschungsarbeiten basierend auf nanoskopischen Oberflächenmessungen an plasmonischen Metaoberflächen und zweidimensionalen Materialien, insbesondere dem halbleitenden TMDC WS_2. Die Thesis ist in sieben Kapitel untergegliedert. Die Einleitung vermittelt einen Überblick über die treibenden Kräfte hinter der Forschung im Bereich der Nanophotonik an zweidimensionalen Materialsystemen. Die Untersuchung der Licht-Materie-Wechselwirkung an dünnen Materialgrenzflächen zieht sich als roter Faden durch die gesamte Arbeit.

Das zweite Kapitel beschreibt den experimentellen Aufbau, der für die Durchführung der nanoskopischen Messungen in dieser Arbeit implementiert wurde. Es werden theoretische Grundlagen, das Messprinzip und die Implementierung des s-SNOM Aufbaus skizziert. Außerdem wird ein Strom-Spannungs-Rasterkraftmikroskop (c-AFM) im Kontaktmodus genutzt, um elektrische Ströme auf mikroskopischen zweidimensionalen TMDC-Terrassen zu messen. In den folgenden vier Kapiteln werden die Beiträge dieser Arbeit zur Untersuchung der Licht-Materie-Wechselwirkung auf der Nanoskala aus verschiedenen Perspektiven vorgestellt. Jedes Kapitel enthält eine kurze Einleitung, einen Theorieteil, Messdaten oder Simulationsergebnisse sowie eine Analyse; vervollständigt durch einen Schlussteil.

Kapitel 3 behandelt die direkte Beobachtung von geführten Modenresonanzen auf einer metallischen Metaoberfläche mit dem s-SNOM. In Kapitel 4 wird die s-SNOM-Technik auf eine TMDC-Monolage in Kombination mit einer resonanten Mikrokavität angewendet, um die Wirkung auf die Verstärkung der Photolumineszenz zu beleuchten. Für Kapitel 5 wird das c-AFM eingesetzt, um Tunnelströme durch vertikale TMDC- und Graphen-Heteroschichtstrukturen zu charakterisieren.

Kapitel 6 enthält einen Exkurs aus dem Bereich der Nanophotonik. Hier werden Zeitbereichssimulationen einzelner Ladungsträger zur Beschreibung von der Ladungsträgerdynamik in Experimenten zur Erzeugung höherer Harmonischer im Terahertzbereich in p-dotiertem Silizium genutzt. Der gemeinsame Nenner der Licht-Materie-Wechselwirkung bietet eine freie Verbindung zum zentralen Thema. Kapitel 7 schließt die Arbeit mit einer Zusammenfassung ab. Im Folgenden werden die Ergebnisse kurz zusammengefasst.

Die zentrale Arbeit an einer metallischen Metaoberfläche aus elliptischen Goldscheiben wird in Kapitel 3 vorgestellt. Der zugehörige Theorieteil führt in das Konzept von Oberflächen-Plasmon-Polaritonen (SPPs) ein, das für den Forschungsbereich der Plasmonik im Allgemeinen wesentlich ist. Verschiedene Methoden zur Berechnung der Dispersionsrelation dieser Oberflächenmoden an ein- und mehrschichtigen Grenzflächen werden auf die untersuchte Metaoberflächenprobe angewendet. Das Modell sagt drei verschiedene Moden voraus, die sich an der Grenzfläche ausbreiten. Eine teil-gebundene ins Substrat abstrahlende Oberflächenmode sowie zwei vergrabene stark gebundene anisotrope Moden. Eine auf der Probe platzierte Nanokugel aus Silizium wird als radiale Anregungsquelle verwendet. Der Vergleich mit s-SNOM-Nahfeldbildern, die mit Hilfe der räumlichen Fourier-Analyse interpretiert werden, zeigt, dass nur die schwach gebundene geführte Modenresonanz ausreichend angeregt wurde, um durch s-SNOM-Bildgebung nachgewiesen werden zu können. Die schwache Oberflächenbindung erklärt die scheinbar isotrope Ausbreitung auf der anisotropen Oberfläche. Die Beobachtung der verbleibenden stark eingegrenzten anisotropen vergrabenen Moden würde eine verbesserte tiefenempfindliche Auflösung des Systems erfordern, die im Prinzip für Schichtdicken von 20 nm möglich sein sollte. Darüber hinaus wirft die Beobachtung die Frage auf, ob die durch Impuls- und Modenvolumenanpassung der Nanokugel gegebene Anregungseffizienz einen ausreichenden Anregungsquerschnitt erzeugt, um nachweisbare vergrabene SPP-Moden zu erzeugen. Daraus werden Ideen für weitere Messungen abgeleitet, um auch die vergrabenen SPP-Moden abbilden zu können. Dies sind zum einen die Durchstimmbarkeit der Wellenlänge oder Nanokugeldimension, um die Resonanz und Güte der Anregung quantifizieren zu können, der Einsatz eines Substrats oder von Nanopartikeln mit verstärkendem Einfluss auf die Signalstärke aus dem oberflächennahen Volumen.

In Kapitel 4 wird die Idee der Visualisierung vergrabener elektrischer Felder mit s-SNOM fortgesetzt. Hier wird es auf die Untersuchung von WS_2 angewendet, einem zweidimensionalen TMDC-Material, welches Photolumineszenz zeigt. Durch die Strukturierung des Galliumphosphid-Substrats unter der hängenden Monolage, die von einer dünnen Schicht aus hBN getragen wird, wird die Photolumineszenzausbeute um den Faktor 10 erhöht. Dies wird durch den Entwurf einer lateralen DBR-Mikrokavität mit zusätzlich optimierter vertikaler Tiefe erreicht, die in das Substrat geätzt wurde. Die hochauflösende Abbildung der elektrischen Feldverteilung im Resonator wird durch den Einsatz von s-SNOM ermöglicht, um die Verbesserung der Einkopplung durch diese beiden Ansätze zu bewerten. Dabei wird die bedeckte Resonatorstruktur mit Messungen bei nicht-resonanter Anregung und in unbedecktem Zustand, folglich ohne vertikale Verstärkung, verglichen. Es konnte festgestellt werden, dass die laterale Struktur überwiegend zur verstärkten Photolumineszenzausbeute beiträgt, während für die Einkopplung keine offensichtliche Verstärkung auf die vertikale Strukturoptimierung zurückgeführt werden konnte. Weiterführende Ideen betreffen die direkte Messungen der Photolumineszenz durch messspitzenverstärkte Nahfeldmessungen und die Trennung von Materialkontrast und Feldverteilung, welche eine für s-SNOM typische Quelle für Messartefakte darstellt.

Das zweidimensionale Material WS_2 wird in Kapitel 5 erneut mit Hilfe von c-AFM untersucht. Unterschiedlich dicke Multilagen auf Graphen und Gold dienen als Tunnelbarrieren für vertikale Ströme zwischen Substrat und leitender c-AFM-Messpitze. Die nanoskopische Spitze wird im Kontaktmodus verwendet, um die Topografie der Probe abzubilden und Zugang zu den mikroskopischen Terrassen unterschiedlicher Dicke zu erhalten. Die Daten können mit einem Fowler-Nordheim-Modell mit Parametern für die Tunnelbreite und Schottky-Barrierenhöhen der beiden Grenzflächen erklärt werden. Die Messungen zeigen jedoch eine schwache Reproduzierbarkeit, was eine detailliertere Zusammenfassung

der relevanten Fehlerquellen erfordert. In der Schlussfolgerung des Kapitels werden mehrere Schlüsselaspekte vorgeschlagen, die bei künftigen Messungen berücksichtigt werden sollten. Entscheidend ist, dass c-AFM sehr empfindlich auf die Adsorption von Wasserfilmen an der Probenoberfläche reagiert, worunter WS_2-Oberflächen unter Umgebungsbedingungen leiden. Unzuverlässige c-AFM-Messungen sowie eine Verschlechterung der Oberfläche aufgrund einer starken Adhäsion zwischen Spitze und Probe werden mit der Bildung von Wassermenisken in Verbindung gebracht. Zusätzlich wird die Verwendung von zweidimensionalen Materialien, z. B. Graphen, als Substratelektrode vorgeschlagen, um eine gut definierte Grenzfläche zu gewährleisten. Die Unebenheit metallischer Substratkontakte führt zu einem inhomogenem elektrischen Kontakt und der Ausbildung unterschiedlicher Abstände sowie lokaler Fallenzustände. Diese Anmerkungen zu den vorläufigen Messungen dürften weitere Studien zu vertikalen Ströme durch zweidimensionale Heterostrukturen ermöglichen und den Weg für komplexere geschichtete Materialsysteme ebnen, wie in der Schlussfolgerung von Kapitel 5 vorgeschlagen.

Kapitel 6 befasst sich mit der Beschreibung der Erzeugung höherer Harmonischer im Terahertzbereich in p-dotiertem Silizium. Dies stellt eine Abweichung vom Thema der Oberflächenmessungen im Nanobereich dar und ist teilweise durch die spannenden experimentellen Daten der höheren Harmonischen aus Silizium bis zur neunten Harmonischen motiviert, die zum damaligen Zeitpunkt analysiert wurden. Weitere Verbindungen zu zweidimensionalen Materialien werden in der Einleitung von Kapitel 6 angedeutet, wo die aktuelle Forschung zur Erzeugung höherer Harmonischer in zweidimensionalen Materialien angesprochen wird. Das Kapitel skizziert ein eindimensionales Einzelteilchen-Zeitbereichsmodell, das zur Simulation der oszillierenden Bewegung von Lochladungsträgern infolge der Anregung durch einen intensiven Terahertz-Puls verwendet wurde. Von den beiden nichtlinearen Effekten, von denen erwartet wird, dass sie zur Erzeugung höherer Harmonischer in p-dotiertem Silizium beitragen, nämlich der nichtparabolischen Bandstruktur und der energieabhängigen Impulsstreuung, wurde festgestellt, dass die relative Dominanz von der Temperatur abhängt. Für die Messung bei Tieftemperatur von 10 K ist die Nichtparabolizität der Bandstruktur maßgeblich, bei Raumtemperatur hingegen dominiert der Einfluss der energieabhängigen Streurate. Dieser Unterschied liegt in dem starken Beitrag der nur gering bevölkerten leichten Lochladungsträger begründet, die unter Berücksichtigung der Spin-Orbit-Kopplung eine wesentlich stärker anharmonische Bandkrümmung aufweisen als die schweren Löcher. Das Ergebnis beschreibt qualitativ die experimentellen Daten und bietet einen Beitrag zur aktuellen Debatte über den Ursprung der Nichtlinearität bei der Erzeugung höherer Harmonischer in festen Kristallen.

Zusammengefasst stellen die dargestellten Ergebnisse Beiträge zur experimentellen Forschung auf der Grundlage des Nahinfrarot-s-SNOM und der Aufbauvariation des c-AFM dar. Die spitzenbasierten nanoskopischen Rastermessverfahren wurden eingesetzt, um die Oberfläche - und in erweitertem Sinne auch oberflächennahe Volumina - einer plasmonischen Metaoberfläche und von ein- und mehrschichtigen TMDC-Materialien zu untersuchen.

In diesem Zusammenhang lieferte die Nahfeldbildgebung Belege für die Oberflächenwellendispersion einer geführten Modenresonanz, die über eine dielektrische Nanokugel angeregt wurde. Darüber hinaus ermöglichte sie eine hochauflösende Abbildung des Feldes einer vergrabenen, substratintegrierten, die Photolumineszenz verstärkenden Mikrokavität und belegte deren verstärkende Wirkung auf die eingekoppelte Strahlung. Ein Vorhaben, das AFM im Kontaktmodus mit einer leitenden Spitze zur Messung von Quantentunnelströmen durch dünne WS_2-Flakes zu nutzen, zeigte vorläufige Ergebnisse und wurde mit einem Report über das weitere Vorgehen bei zukünftigen Studien abgeschlossen.

Schließlich schließen zusätzliche Arbeiten zur Debatte über den Ursprung der Erzeugung

höherer Harmonischer aus dem Valenzband von dotiertem Silizium die Arbeit ab. Obwohl sie nicht im Rahmen von zweidimensionalen Oberflächen untersucht wurden, sind sie aufgrund ihrer Relevanz als untermauernder Beitrag zu aktuellen experimentellen Ergebnissen aus zwei Hochintensitäts-Terahertz-Anlagen in diese Arbeit aufgenommen worden.